DISS. ETH NO. 27320

TWO-WAY SPANNING TIMBER-CONCRETE COMPOSITE SLABS MADE OF BEECH LAMINATED VENEER LUMBER WITH STEEL TUBE CONNECTION

A thesis submitted to attain the degree of
DOCTOR OF SCIENCES of ETH ZURICH
(Dr. sc. ETH Zurich)

presented by
BENJAMIN JOHANNES KREIS
MSc ETH Civil Eng
born on 16.01.1989
citizen of
Ermatingen TG

accepted on the recommendation of
Prof. Dr. Andrea Frangi (ETH Zurich, Examiner)
Prof. Dr. Walter Kaufmann (ETH Zurich, Co-examiner)
Prof. Dr. Alfredo M.P.G. Dias (University of Coimbra, Co-examiner)

2021

Acknowledgements

This thesis is the outcome of my research activities at the Chair of Timber Structures at the Institute of Structural Engineering (IBK) of ETH Zurich. I have been privileged to work in a such a fantastic environment full of inspiring, open-minded, positive and supportive people.

I would like to express my sincere gratitude to *Prof. Dr. Andrea Frangi* for this opportunity and all the support, trust, inspiration and belief I have received from him during these years. The positive atmosphere that he has created in this research group and the appreciation that he shows for all the work and every single member of the team are truly outstanding and made this time an enjoyable and inspiring experience.

I would like to thank my co-supervisors *Prof. Dr. Walter Kaufmann* and *Prof. Dr. Alfredo M.P.G. Dias* for carefully reviewing this thesis.

The collaboration with the two partner companies *WaltGalmarini AG* and *Implenia Schweiz AG* was of irreplaceable value to the success of this project. The close interaction with them allowed me to look at my academic research work from a practice-oriented perspective. In particular, I thank *Wolfram Kübler* for his endless inspiration in the development of innovative solutions. Whenever a concept didn't work, he already had three new ideas that we could investigate next. I would like to thank the entire team of *WaltGalmarini AG*, in particular *Michael Büeler*, *Nils Schriber*, *Louis Trümpler* and *Tizian Haussener* for their valuable contributions in this project. I thank the entire team of *Implenia Schweiz AG*, in particular *Christian Kündig*, *Simon Beeler*, *Tobias Hohermuth*, *Jérôme Peter* and *Adrian Ulrich*. Without their input, I would never have ended up with a solution that is actually buildable on a construction site.

During all the experimental work that I carried out in the laboratory of ETH Zurich, I could always rely on the proficient support and the practical expertise of the *Bauhalle Team*. In particular, I would like to thank *Dominik Werne*, *Patrik Morf*, *Pius Herzog*, *Christoph Gisler*, *Thomi Jaggi* and *Martin Viertel*. Whatever problem I had with my test setup, specimens or measurement equipment, they always helped me to find a solution. Their calm and positive attitude made it a pleasure to work in this laboratory on a daily basis.

I would like to thank all students who contributed to this research project with a master thesis or a master project: *Raphael Stadelmann*, *Anick Imhof*, *Raphaël Schmutz*, *Anica Gamper*, *Senthuran Mohaneswaran*, *Anja Meier* and *Cyrill Laube*. Their company during many long working days in the laboratory, their interest and thirst for knowledge was always a great motivation for me.

A warm 'thank you' goes to all my colleagues of *Group Frangi* and former *Group Fontana*. All of you have made a big contribution to my work, with all the inspiring discussions, inputs, feedback, questions, answers and – most of all – the great atmosphere that you created in this team. I consider many of you as my mentors during this challenging project and I am grateful for your friendship.

I gratefully acknowledge the Swiss Innovation Agency *Innosuisse* for the financial support of this research project. I was fortunate enough to attend many workshops and meetings within the framework of *COST Action FP1402*. In particular, I thank *Prof. Dr. Alfredo M.P.G. Dias*, *Prof. Dr. Jörg Schänzlin* and all other members of *Working Group 4* for the numerous insightful discussions about the development of unified design guidelines for timber-concrete composite structures.

For more than ten years, I have been a proud member of the *ETH Big Band*. Playing music is one of the biggest passions in my life and I have been extremely privileged to be a part of so many fantastic projects with this incredible group of musicians. During a PhD project with countless highs and lows, for me, having such a reliable balance with all the rewarding projects of this band was of irreplaceable value on this journey.

Of course, I can't thank enough all my closest friends and my family for their unconditional support. First and foremost, my parents *Ursula* and *Erhard*, who have never stopped supporting and encouraging me in whatever I chose to pursue, and whose interest in my activities has always been a great motivation for me. I thank my sister *Fränzi*, my brother *Lukas*, my sister-in-law *Phuong Anh* and my two godchildren *Lena* and *Jakob* for all the support and the energy they have given me and for all the happy hours that we have spent together.

My last and greatest gratitude goes to *Irina*. Most couples don't write their PhD theses at the same time and in the middle of a global pandemic that confines everybody to their homes for most of the time. There are a couple of good reasons why they don't do that... Looking back at the past months, I am extremely happy and proud of how we tackled this ultimate challenge together, always working as a team and supporting each other. I truly don't know how I would have done any of this without your loving support and I can't thank you enough!

Zurich, 2021
Benjamin Kreis

Abstract

Timber-concrete composite (TCC) slabs play an essential role in modern timber construction. Consisting of a timber member in the tension zone, a concrete layer in the compression zone and a shear connection between the two parts, TCC slabs feature a number of advantages that make them ideally suitable for use in both office and residential buildings. However, currently used TCC slab systems carry loads only in one direction. This represents a restriction of architectural flexibility, as irregular floor plans are difficult to realise and columns cannot be used as direct point supports. As a contribution towards overcoming these limitations and thus expanding the application field of TCC slabs, a novel two-way spanning TCC slab system was developed and investigated in this research project.

The developed TCC slab uses beech laminated veneer lumber (LVL), an engineered wood product providing high strength and stiffness in both load-bearing directions. It was found that an optimised stiffness-to-mass ratio can be achieved if the core of the slab between the timber and concrete layers is filled with a light-weight material such as cellulose fibres or stone wool. As a direct consequence of this concept choice, TCC connectors with a high bending stiffness have to be used. Therefore, a solution using steel tubes as connectors was developed.

The local behaviour of this steel tube connection was investigated in an extensive experimental campaign, providing information about the stiffness, shear capacity and ductility of the connection. The results show that a sufficient stiffness can only be achieved if a grouting system is used in the connection of the steel tubes with the timber layer. A ductile failure mode was observed in the connection tests due to inelastic compression deformations in timber and a redistribution of internal forces in concrete.

Based on these results, the load-bearing behaviour of the novel TCC slab was investigated in uniaxial bending tests. These tests showed that the connection behaviour governs the global load-bearing behaviour. Cross-sectional failures in timber or concrete were not observed. A ductile failure mode in the connectors led to a remarkably ductile global load-bearing behaviour.

Two calculation models are provided in this thesis that can be used for a prediction of the uniaxial load-bearing behaviour of the TCC slab. A comparison of the test results with the corresponding predictions showed that the deformations under service loads, the fundamental frequency and the load-bearing capacity can be predicted with high accuracy.

The biaxial load-bearing behaviour of the novel TCC slab was investigated in an elaborate large-scale experiment. A modular test setup was developed that allowed to perform static and dynamic tests on the same specimen in different support conditions. A substantial increase in stiffness and fundamental frequency in biaxial versus uniaxial support conditions was observed. Two calculation models were developed that represent well the observations made in the experiments.

In conclusion, the great potential of the novel two-way spanning TCC slab for the application in practice was demonstrated in this research project. Calculation models were developed that allow for an accurate prediction of the load-bearing behaviour in uniaxial and in biaxial bending.

Kurzfassung

Holz-Beton-Verbunddecken (HBV-Decken) spielen eine wichtige Rolle im modernen Holzbau. Eine Vielzahl von Vorteilen haben in den vergangenen Jahrzehnten zu einem zunehmenden Einsatz dieses Deckensystems in Büro- und Wohngebäuden geführt. Gegenwärtig sind die verfügbaren HBV-Deckensysteme einachsig tragend. Dies stellt eine Einschränkung der architektonischen Flexibilität dar, da unregelmässige Grundrisse schwierig zu realisieren sind und eine Punktlagerung der Decken auf Stützen nicht möglich ist. Um diese Einschränkungen zu überwinden und somit den Einsatzbereich von HBV-Decken zu erweitern, wurde in diesem Forschungsprojekt ein neuartiges, zweiachsig tragendes HBV-Deckensystem entwickelt und untersucht.

Die entwickelte HBV-Decke verwendet Buchenfurnierschichtholz, ein Holzwerkstoff, der eine hohe Festigkeit und Steifigkeit in beide Tragrichtungen aufweist. Das Verhältnis zwischen Deckensteifigkeit und -masse lässt sich optimieren, wenn zwischen Holz- und Betonschicht eine Lage aus einem leichten Material wie Zellulosefasern oder Steinwolle eingefügt wird. Als direkte Konsequenz dieses Konzeptes müssen HBV-Verbinder mit einer hohen Eigenbiegesteifigkeit eingesetzt werden. Daher wurde eine Lösung mit Stahlrohren als Verbinder entwickelt.

Das lokale Tragverhalten dieser Stahlrohrverbindung wurde anhand eines umfangreichen Versuchsprogramms untersucht. Die Ergebnisse zeigen, dass eine ausreichende Steifigkeit nur erreicht werden kann, wenn in der Verbindung der Stahlrohre mit der Holzschicht ein Vergusssystem verwendet wird. In den Verbindungsversuchen wurde ein duktiler Versagensmodus beobachtet, der auf inelastische Druckverformungen im Holz und eine Umverteilung der inneren Spannungen im Beton zurückzuführen ist.

Basierend auf diesen Erkenntnissen wurde das Tragverhalten der neuartigen HBV-Decke in einachsigen Biegeversuchen untersucht. Dabei zeigte sich, dass das globale Tragverhalten primär durch das Verbindungsverhalten bestimmt wird. Ein duktiler Versagensmodus in den Verbindungen führte zu einem bemerkenswert duktilen Tragverhalten des HBV-Deckensystems.

Im Rahmen dieser Arbeit werden zwei Berechnungsmodelle präsentiert, die eine Prognose des einachsigen Tragverhaltens der HBV-Decke ermöglichen. Ein Vergleich der jeweiligen Ergebnisse mit den Versuchsresultaten zeigt, dass die Modelle eine zutreffende Prognose der Verformungen unter Gebrauchslasten, der Eigenfrequenz und der Tragfähigkeit erlauben.

In einem umfangreichen Grossversuch wurde das biaxiale Tragverhalten der neuartigen HBV-Decke untersucht. Um statische und dynamische Tests am selben Prüfkörper unter verschiedenen Auflagerbedingungen durchführen zu können, wurde ein spezieller modularer Versuchsaufbau entwickelt. Eine wesentliche Erhöhung der Steifigkeit und der Eigenfrequenz bei zweiachsiger gegenüber einachsiger Tragwirkung wurde beobachtet. Zwei Berechnungsmodelle wurden entwickelt, deren Resultate gut mit den Beobachtungen aus den Experimenten übereinstimmen.

Die in der vorliegenden Arbeit vorgestellten und diskutierten Untersuchungen zeigen das grosse Potential des neuartigen, zweiachsig tragenden HBV-Deckensystems auf. Die vorgestellten Berechnungsmodelle erlauben eine zuverlässige Prognose des Tragverhaltens und eine einfache, praxistaugliche Bemessung des HBV-Deckensystems.

Contents

Chapter 1

Introduction

1.1 Motivation and background

Timber-concrete composite (TCC) slabs play an essential role in modern timber construction. Consisting of a timber member in the tension zone, a concrete layer in the compression zone and a shear connection between the two parts, they show a number of advantages that make them ideally suitable for use in both office and residential buildings. Compared to traditional timber slabs, TCC slabs show increased stiffness and load-bearing capacity, better dynamic behaviour and seismic resistance, improved sound insulation and higher fire resistance. Compared to conventional solid reinforced concrete slabs, a significant reduction of self-weight is achieved when using TCC slabs. In addition, reducing the necessary amount of concrete and steel leads to a more sustainable solution with lower CO_2 emissions and grey energy consumption. The ceiling soffit can be kept in wood, which is appreciated by many architects, investors and residents.

However, using TCC slabs also imposes certain limitations to architectural flexibility. Currently used TCC slab systems carry loads only in one direction, which means that walls or beams are always necessary as continuous supports and columns cannot be used as direct point supports. Furthermore, this characteristic of the system makes it difficult to realise irregular floor plans with openings. As a contribution towards overcoming these limitations and thus expanding the application field of TCC slabs, a novel two-way spanning slab system was developed and investigated in this research project.

Most TCC slab systems consist of a relatively thick timber section and a thin concrete slab. In these structures, concrete cracking can often be neglected since the concrete section is almost entirely in compression, as shown e. g. by Müller [59]. In these TCC slab systems, the coniferous timber species Norway spruce (*Picea abies* Karst.) is typically used. Using engineered wood products with higher strength, such as beech laminated veneer lumber (beech LVL), allows for a substantial reduction of the timber layer thickness. However, in order to achieve a sufficient bending stiffness of the composite member, the total height has to remain in a similar range, leading to an increased ratio of concrete to timber height. Boccadoro [4] developed and investigated such a system consisting of 40 mm thin beech LVL plates and a concrete layer approximately four times as thick. As a consequence, more than half of the concrete section cracks and therefore does not significantly contribute to the bending stiffness of the composite member while substantially increasing the self-weight. To optimise the ratio between weight and stiffness, a large part of the cracked concrete section can be replaced with a lightweight material. However, introducing such an interlayer between the timber and concrete sections makes it impossible to use notches as a connection system. Also, thin dowel-type fasteners (e. g. screws) are not applicable because they do not provide enough stiffness to connect the timber and concrete sections in this case. Therefore, a solution using steel tubes as connectors was developed and investigated in this research project.

Floor slabs are responsible for a large part of the total mass of buildings and, thus, contribute substantially to the forces acting on vertical load-bearing members such as columns, walls and the foundation. Horizontal forces generated during an earthquake are directly influenced by the floor slab mass. Especially in large-volume buildings, using optimised light-weight slab solutions leads to significant savings in the design of vertical members and the foundation. This is not only an economical advantage but also allows to save resources and reduce the total environmental impact of construction projects. At the same time, reducing the mass of floor slabs may affect its dynamic behaviour and acoustic insulation properties negatively. Therefore, these aspects have to be studied as well.

This thesis is the result of a research project initiated by the Institute of Structural Engineering (IBK) of ETH Zurich in collaboration with the construction company *Implenia Schweiz AG* and the engineering office *WaltGalmarini AG*. The project was funded by the Swiss Innovation Agency *Innosuisse* (former *Commission for Technology and Innovation, CTI*).

1.2 Objectives

The objectives pursued in this research project can be divided into two categories. Firstly, the concept of a novel two-way spanning TCC slab system is developed with the following goals:

- A two-way spanning TCC slab shall be developed that (a) has no visible supporting beams, (b) offers the possibility of using columns as direct point supports and (c) allows for a comparable degree of design flexibility as a reinforced concrete flat slab.
- The TCC slab should be applicable as one-way or two-way spanning slab and enable a seamless combination of both options (slab with one-way and two-way spanning areas).
- An efficient and economical construction process is pursued, either using cast-in-situ concrete or full prefabrication of TCC elements.
- The self-weight of the TCC slab shall be minimised, without violating the requirements regarding dynamic behaviour and sound insulation.

Secondly, the load-bearing behaviour of the developed slab is studied in detail, pursuing the following objectives:

- A profound understanding of the load-bearing mechanisms in the slab is to be developed with regard to the local connection behaviour, uniaxial bending and biaxial bending, using experimental and analytical approaches.
- The most important parameters of the system and their influence on the stiffness, load-bearing capacity and ductility of the TCC slab should be identified.
- Practice-oriented calculation methods shall be developed that allow for a safe design of the TCC slab in both serviceability and ultimate limit states.

1.3 Concept of the developed TCC slab system

The two categories of objectives explained above cannot be pursued independently. For example, experimental investigations are necessary to understand the load-bearing behaviour of different connection types. The findings of the same experiments, however, serve also as a basis for the decision about which connection type suits best the requirements of the pursued slab concept. Therefore, concept development and investigation of the load-bearing behaviour are closely related and influence each other.

As a consequence, the different test series carried out in the scope of this research project are not all based on the exact same final version of the concept. Covering the entire development process in detail, including all concept approaches that were abandoned along the way, would exceed the scope of this thesis. Therefore, only the final concept is described below. Any resulting differences between test specimens and the final concept are addressed in the respective chapters covering the experimental investigations (Chapters 3 – 5).

The final concept of the TCC slab features a steel tube connection and is depicted in Fig. 1.1. The structure consists of three layers:

- **Concrete layer:** On top, the compression zone of the composite member consists of a concrete layer of 80 – 120 mm thickness. A steel reinforcement mesh is placed in the middle of the concrete section to prevent any extensive shrinkage cracks.
- **Interlayer:** The core of the TCC slab is filled with a light-weight material such as cellulose fibres or stone wool and is approximately 100 – 200 mm thick. This layer does not serve any structural purpose other than ensuring a constant distance between the load-carrying timber and concrete sections. Installations such as electrical lines or a sprinkler system can be arranged in this layer, which is an advantage compared to conventional TCC slab systems.
- **Timber layer:** At the bottom, the tension zone of the composite member consists of 60 mm thick plates made of beech laminated veneer lumber (beech LVL). The material used in this project (*BauBuche Q*, Chapter 2.1) contains cross-layers (veneers oriented perpendicular to the main direction), providing strength and stiffness in both directions.

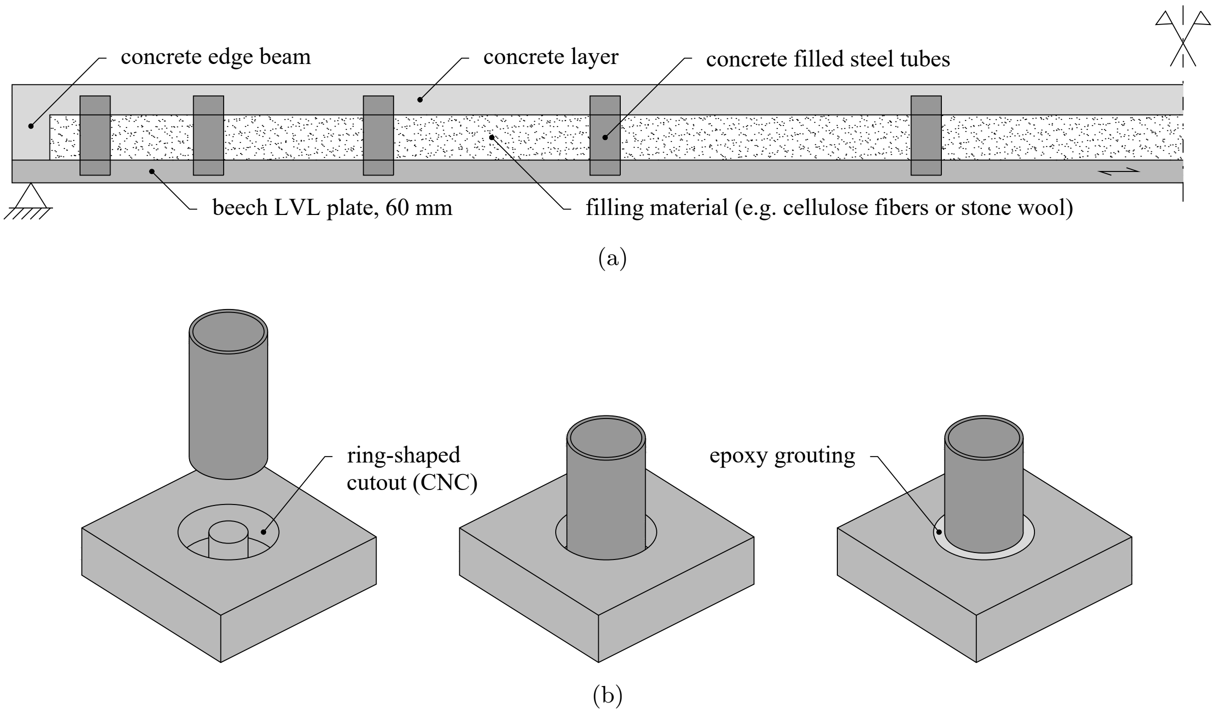

Fig. 1.1: Concept (a) longitudinal section and (b) connection of the steel tube in the beech LVL plate.

The load-carrying timber and concrete sections are connected using steel tubes that can be arranged according to the shear forces. Fig. 1.1a shows a possible arrangement for a simply supported beam subjected to uniformly distributed load. The connection of the steel tubes is illustrated in Fig. 1.1b. Ring-shaped cutouts are milled in the beech LVL plate using CNC machining. The thickness of the cutouts is chosen such that gaps are left both inside and outside the steel tube. These gaps are filled with a high performance epoxy grouting system (*Sikadur®-42 HE*), creating a stiff and slip-free connection.

After placing the interlayer and reinforcement mesh, concrete is poured on top of the interlayer and inside the steel tubes. In this way, the concrete layer and its connection with the steel tubes is created in the same production step.

At the location of the supports, high shear forces have to be introduced into the composite slab. In this area, the interlayer is replaced by concrete, creating an edge beam (Fig. 1.1a). This conceptually prevents a local shear force peak in the timber section and high normal forces in the first row of steel tubes.

Different versions of the TCC slab with steel tube connection

The general slab concept as described above can be adapted to different project boundary conditions as follows:

- Full prefabrication of TCC elements or on-site construction using cast-in-situ concrete
- Conception as a one-way or two-way spanning slab

This leads to the following versions of the slab:

- **Full prefabrication:** In this case, TCC elements of max. 1.82 m width (max. production width of *BauBuche Q* plates) are fully prefabricated as explained above. Any electrical cables or pipes for a sprinkler system are installed in the factory. Precambered elements can be produced by placing spacers of varying height under the beech LVL plate before concreting. On site, the concrete layers of neighbouring elements have to be connected to enable transmission of membrane forces (e. g. horizontal forces from earthquake or wind action).

- **On-site construction using cast-in-situ concrete:** In some projects, using cast-in-situ concrete may be more economical than connecting prefabricated elements on site. In this case, formwork elements are prepared in the factory or on site, with additional upper beech LVL beams connected to the steel tubes (Fig. 1.2). These beams help to increase the stiffness of the formwork elements during concreting, allowing a construction process without the need for extensive propping. Depending on the span, propping may be omitted entirely. The connection of the steel tubes with the upper beams is achieved by drilling precisely fitting holes in the beams, inserting the steel tubes and securing the position with a self-tapping dowel from the side. The steel tubes protrude from the upper timber beam to achieve a connection with the concrete layer in the final state (Fig. 1.2). The interlayer including installations can be placed on site in one step for an entire storey, eliminating many interface and connection issues compared to the prefabrication option.

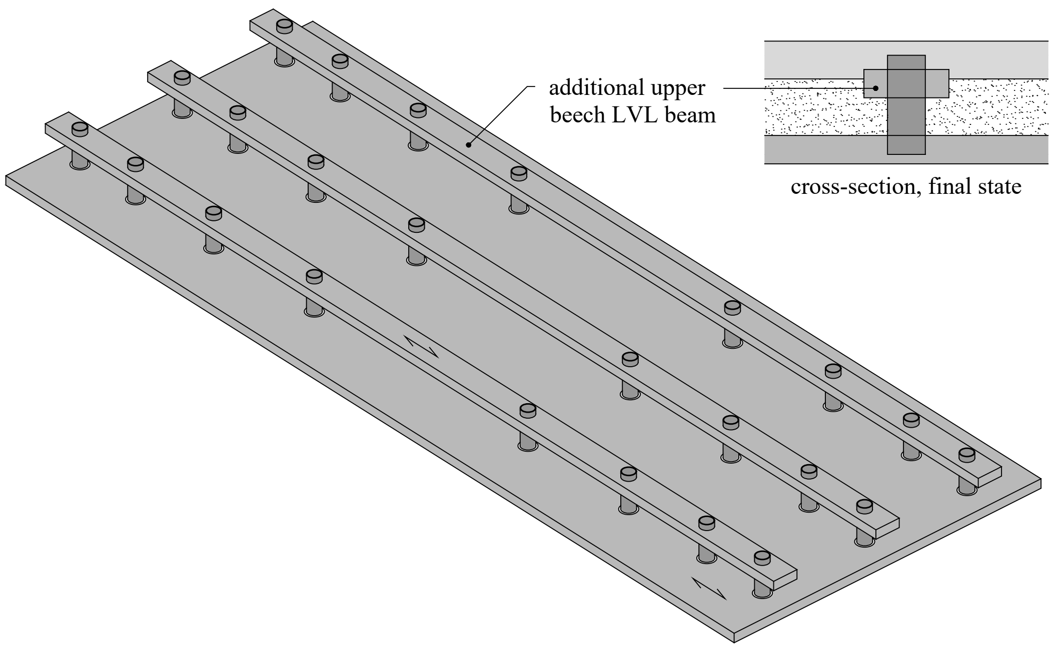

Fig. 1.2: Formwork element with additional upper beech LVL beams and connection in the final state.

- **Two-way spanning slab:** In order to achieve a biaxial load-bearing behaviour, the beech LVL plates have to be connected along their side edges. This connection is referred to as 'side connection' hereinafter and enables the transmission of tensile forces in transversal direction of the beech LVL plate (perpendicular to the main veneer orientation). Fig. 1.3 illustrates the developed side connection concept using glued-in rods. The steel box on the right side is produced either as a cast iron part or using a standard RRW steel profile, welded together with a base plate. The steel box is connected to the beech LVL using several glued-in rods in the factory. On the left side, a steel plate is connected analogously. On site, standard steel bolts are used to connect the two elements. A conical groove is milled into the side edge of the beech LVL plate to ensure the vertical alignment of the elements on site. In horizontal direction, production tolerance is accommodated with a slotted hole in the steel box. These side connections can be arranged according to the expected transversal bending moment, based on the project boundary conditions. In areas where the slab carries loads only in the main direction, they can be omitted. Experiments on alternative side connection concepts have been carried out in an early stage of this research project. However, the examined alternative side connections are not compatible with the final slab concept described in this thesis.

  The two-way spanning TCC slab can be designed such that from below, it looks like a point-supported flat slab without any visible beams. However, this is only possible if in the location of the point supports, the interlayer is replaced by concrete (Fig. 1.1a). The resulting beams can be designed in reinforced concrete, acting as integrated linear supports for the two-way spanning TCC slab. The corresponding load-bearing mechanism differs from that of a flat slab where point support forces are directly introduced into the slab with torsional moments. In this system, point support forces can only be introduced indirectly using internal beams.

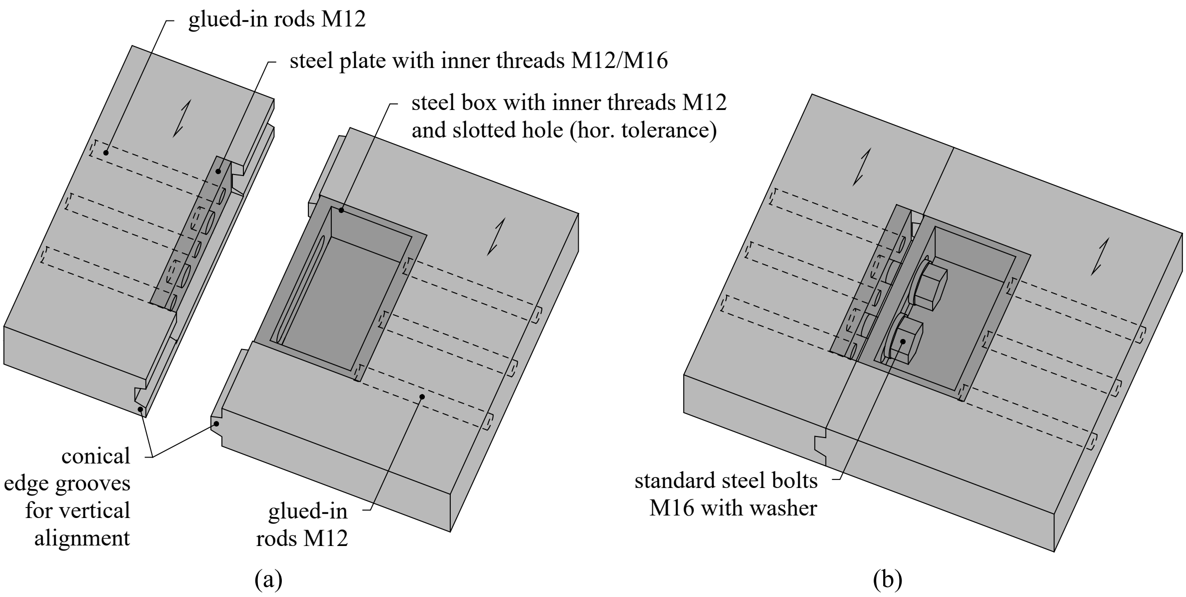

Fig. 1.3: Concept for the side connection, (a) element prefabrication and (b) connection on site.

In the beginning of this research project, the concept version using cast-in-situ concrete was the favoured option. In this scenario, introducing a weight-saving interlayer is a logical consequence for the following reasons:

- A connector with high bending stiffness is necessary in any case, to effectively activate the stiffness of the additional timber beams during the construction state.
- Limiting the formwork deflections during concreting is one of the main design challenges in this scenario (propping is undesired). Reducing the amount of concrete to a necessary minimum is therefore a priority.

During the project, investigations by *Implenia Schweiz AG* and *WaltGalmarini AG* led to the conclusion that in most cases, prefabrication is expected to be the more economical construction process than casting concrete on site. Therefore, this thesis focuses mainly on this version of the concept.

1.4 Outline and overview

The structure of this thesis is illustrated in Fig. 1.4. Following this introduction, **Chapter 2** provides a brief overview on the state of the art regarding beech LVL and the field of timber-concrete composite (TCC) slabs. Currently available TCC slab systems and calculation models are discussed. A special focus is placed on studies exploring the use of beech LVL or steel tubes in TCC slabs and research projects investigating two-way spanning TCC slabs.

Chapters 3 – 5 present the experimental investigations that were carried out within the scope of this research project. Three series of connection shear tests were conducted to develop an optimised connection concept. The main results of these tests were the connection stiffness, shear capacity and deformation capacity. These results are used as input parameters for the calculation models for uniaxial and biaxial bending (Fig. 1.4). Two further experimental campaigns investigated the load-bearing behaviour of the TCC slab with steel tube connection in uniaxial and biaxial bending.

Chapter 6 presents two different calculation models that can be used to predict the uniaxial load-bearing behaviour of the investigated TCC slab. Based on a comparison with the results of the uniaxial bending tests, these models are discussed in detail with regard to their accuracy and their applicability in a practical design process.

In **Chapter 7**, the two calculation models from Chapter 6 are extended to represent the biaxial bending behaviour of the novel two-way spanning TCC slab. In these models, the results of the connection shear tests and the uniaxial bending models are used as input parameters (Fig. 1.4). The performance of the two calculation models is assessed on the basis of a comparison with the results of the biaxial bending test.

Chapter 8 provides a summary of the most important conclusions of this research project. The limitations of the presented results are discussed and an outlook is given regarding possible further research on the novel TCC slab with steel tube connection.

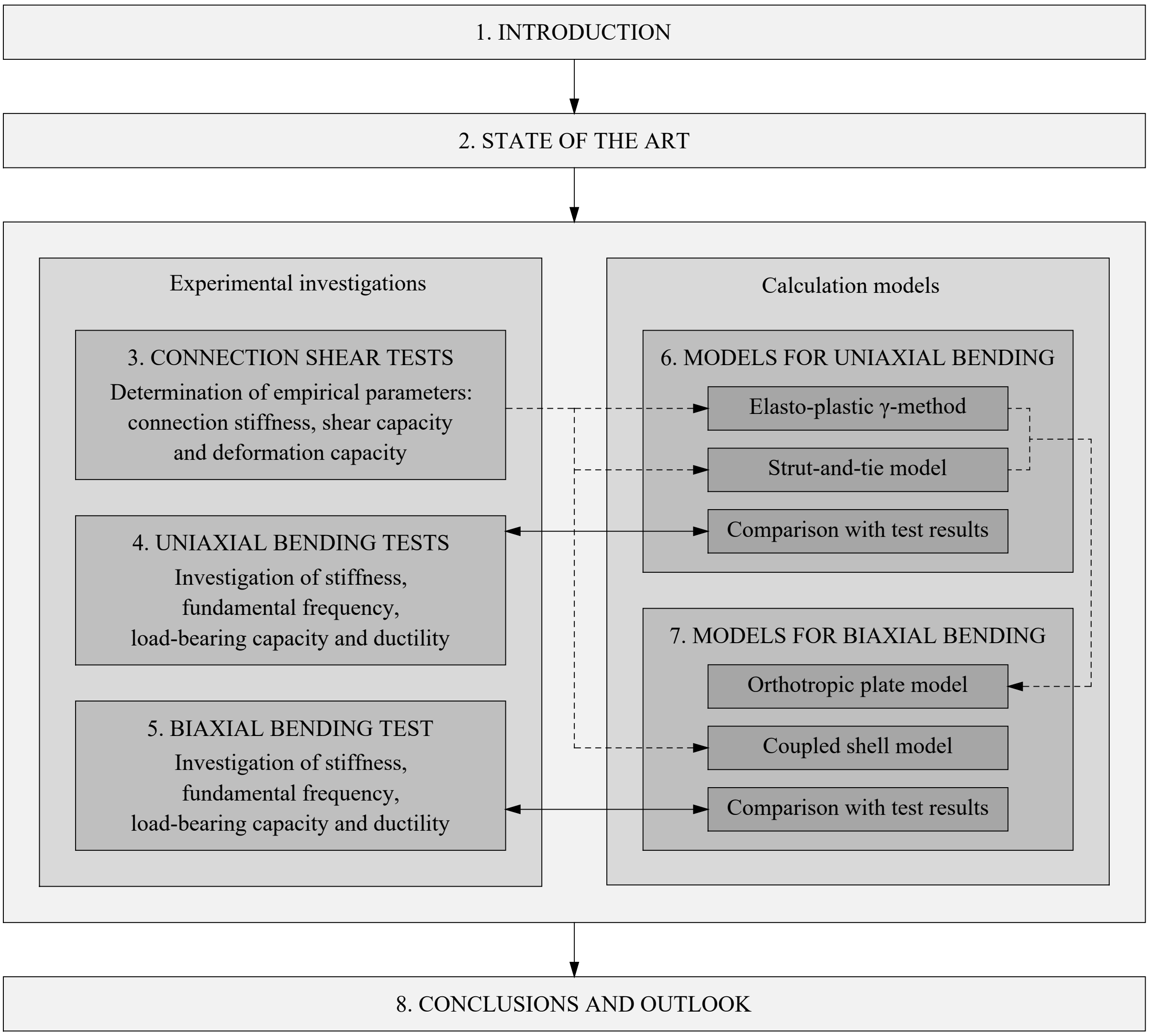

Fig. 1.4: Overview of the structure of this thesis.

Chapter 2

State of the art

2.1 Beech laminated veneer lumber

Beech (*Fagus sylvatica* L.) is one of the most common wood species in Central Europe. In Switzerland, Germany and Austria, beech accounts for 10 – 18% of the total wood stock and for 56 – 68% of hardwood resources [2; 69]. Although its potential for structural use was recognised already in 1884 by Sarrazin & Schäfer [68], beech wood is still mostly used as firewood or for other non-structural purposes, e. g. in the furniture industry [42; 43]. For structural applications, beech is processed into a number of wood-based products, either consisting of lamellas (thickness greater than 20 mm, for glued laminated or cross laminated timber) or 2 – 4 mm thin, rotary-peeled veneers. A comprehensive summary of the research work published on the topic of beech glued laminated timber (glulam) is presented by Ehrhart [28].

Using thin veneers rather than lamellas as a basis for engineered wood products leads to a more homogeneous material and consistent, reliable mechanical properties. In addition, the production process for rotary-peeled veneers results in lower material losses than sawing rectangular lamellas out of circular logs. Laminated veneer lumber (LVL) is produced either with all veneers oriented in the same direction, or including cross-layers. The latter option allows to overcome some of the limitations caused by the strong anisotropy of wood such as its low tensile strength and stiffness perpendicular to the grain. Early studies on the mechanical properties of beech LVL were published by Kolb [40] in 1968 and Ehlbeck & Colling [25; 26; 27] in the 1980's. The technological advancements in the industrial production of beech LVL by the German company *Pollmeier GmbH* since the beginning of the 21st century transformed beech LVL from a niche product to an economically competitive solution used in many modern timber construction projects [34]. Extensive tests for the determination of all relevant mechanical properties have been carried out by van de Kuilen & Knorz [88; 89]. Based on the results of these studies, a National Technical Approval was obtained in Germany for glulam made of beech LVL [22] (replaced by a European Technical Assessment [61] in 2015), as well as for beech LVL plates with and without cross-layers (*BauBuche S* and *BauBuche Q*) in 2013, updated in 2016 and 2018 [24]. All relevant mechanical properties of the beech LVL plates that were used in this research project can be obtained from the latest version of the manufacturer's declaration [63].

Since the initial tests in 2012/13 [88; 89], the range of available plate thicknesses and their corresponding veneer layouts have been adjusted. The cross-layer ratio n_{90}/n_{tot} (with n_{90} and n_{tot} being the number of cross-layers and total layers, respectively) varies depending on the plate thickness (Fig. 2.1) and strongly influences the mechanical properties, especially in the direction perpendicular to the grain. This dependence is addressed in a simplified way in the National Technical Approval [24] and the manufacturer's declaration [63] with conservative strength and stiffness values for two thickness categories. A selection of these values is given in Tab. 2.1. More information on the statistical distribution of the mechanical properties is provided by van de Kuilen & Knorz [88; 89] for *BauBuche S* and *BauBuche Q* with a cross-layer ratio of 22%.

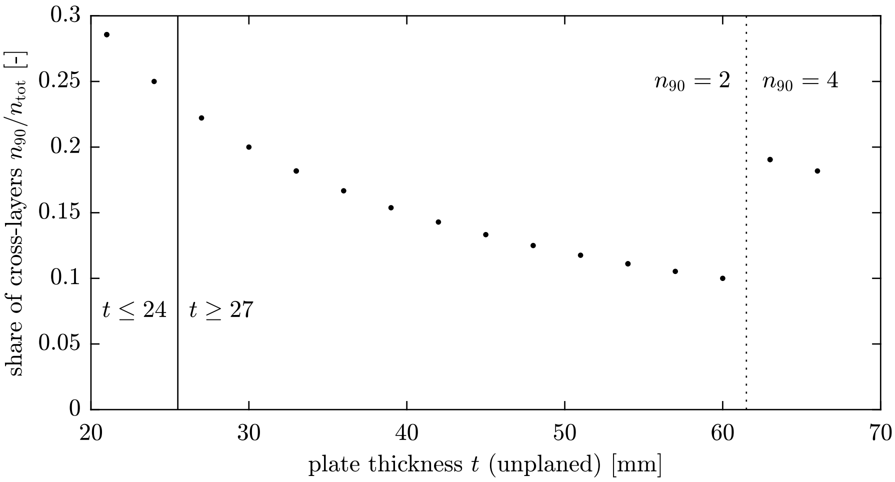

Fig. 2.1: Cross-layer ratio in *BauBuche Q*.

Tab. 2.1: Selection of material properties of *BauBuche*, strength and stiffness values in [MPa] and densities in [kg/m^3], as declared in [63].

Property		*BauBuche S*	*BauBuche Q* $t \leq 24$ mm	*BauBuche Q* $t \geq 27$ mm
char. plate bending strength ‖ to grain	$f_{\mathrm{m,0,flat,k}}$	80	70	81
char. plate bending strength ⊥ to grain	$f_{\mathrm{m,90,flat,k}}$	–	34	21
char. tensile strength ‖ to grain	$f_{\mathrm{t,0,k}}$	60	46	49
char. tensile strength ⊥ to grain	$f_{\mathrm{t,90,edge,k}}$	1.5	15	8.0
char. compressive strength ‖ to grain	$f_{\mathrm{c,0,k}}$	57	57	62
char. compressive strength ⊥ to grain	$f_{\mathrm{c,90,edge,k}}$	14	40	22
char. plate shear strength ‖ to grain	$f_{\mathrm{v,0,flat,k}}$	8.0	3.8*	3.8*
mean MOE ‖ to grain	$E_{0,\mathrm{mean}}$	16'800	11'800	12'800
mean MOE ⊥ to grain	$E_{90,\mathrm{mean}}$	470	3500	2000
mean density	ρ_{mean}	800	770	800

* rolling shear in the cross-layers

2.2 One-way spanning timber-concrete composite slabs

2.2.1 Timber-concrete composite systems

Timber-concrete composite (TCC) slabs consist of a timber member, a concrete layer and a shear connection in between. The two materials are typically arranged in such a way that timber and concrete are subjected to tensile and compressive stresses, respectively. This combination leads to a number of advantages such as high stiffness and load-bearing capacity, as already discussed in Chapter 1.1.

Comprehensive summaries of the history and development of TCC slabs have been written by many authors, e. g. Blass et al. [3], Müller [59] and Yeoh et al. [91]. A large variety of different TCC systems have been developed in the past three decades. They can be divided into two main groups, based on the chosen type of timber element:

- Linear TCC systems (Fig. 2.2a), using beams made of timber or glulam. The space between the timber beams can be used for installations, which makes these systems suitable especially for industrial or office buildings.
- Planar TCC systems (Fig. 2.2b), using timber elements that cover the entire lower surface of the structure, such as *Brettstapel* elements, cross laminated timber (CLT) or LVL plates. In many residential buildings, this is the preferred system due to its visually calmer soffit and because less space for installations is needed.

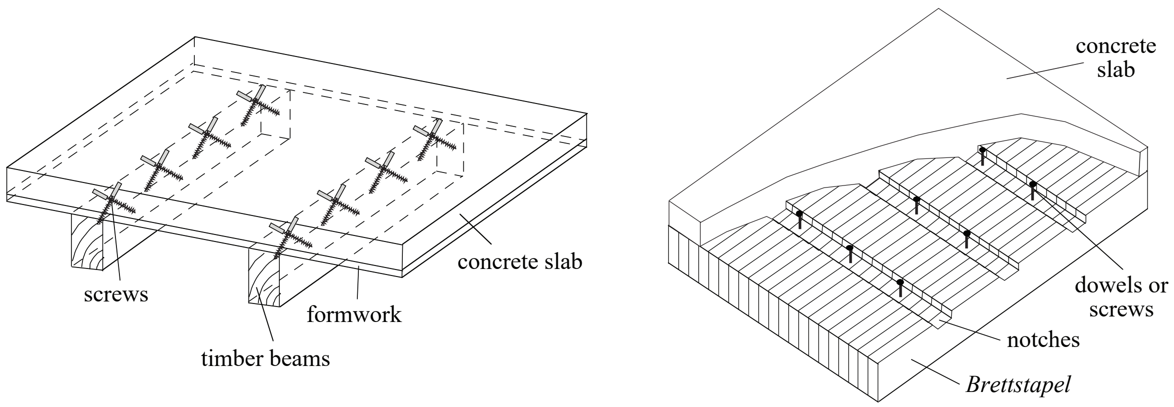

(a) (b)

Fig. 2.2: (a) Linear and (b) planar TCC systems, adapted from [30].

TCC slabs can be produced in different ways:

- Full prefabrication of TCC elements. In this case, an industrialised element production in controlled factory conditions and rapid erection on site is possible. At the same time, transportation costs are high and some concrete or mortar is still necessary on site to connect the elements.

- Erecting the timber structure and casting the concrete on site. I this case, the timber elements act both as formwork in the construction state and as tensile and bending member in the final state. Propping is often necessary to limit deflections during concrete casting.

- Connecting the timber structure with a prefabricated concrete slab on site. Compared to cast-in-situ concrete, this option has the advantage that deformations due to concrete shrinkage can be omitted.

The structural behaviour of TCC slabs is strongly influenced by the load-slip behaviour of the used connection system. Therefore, many research projects have focused on the development of efficient TCC connection systems, pursuing three main goals:

- High connection stiffness: This allows for an effective activation of the composite action, leading to high bending stiffness and load-bearing capacity of the TCC member.

- Ductility: A brittle failure of the structure without any warning can be avoided if the connection is ductile. The robustness of the TCC slab improves if the connection system allows for a force redistribution.

- High load-bearing capacity: The connectors have to be strong enough to transmit the shear forces at the interface between timber and concrete.

A comprehensive literature research on all available connection systems for TCC slabs was carried out within the framework of COST Action FP1402 / WG 4 [21], partly based on a publication by Monteiro et al [58]. Approximately 60 publications were grouped in the following three categories, using the number of publications per category to quantify how much research had been done in the respective fields:

- Dowel-type fasteners (45%)

- Notches or notches combined with steel fasteners (33%)

- Other connection systems (22%)

The first category includes screws and glued-in rods (both vertical and inclined), dowels, nails, bolts, staples and other metallic connectors. Most research within this category has focused on screws, nails and dowels, as the use of these fasteners was already well-established in timber-to-timber connections. Dowel-type fasteners typically show low to medium connection stiffness and load-bearing capacity and often exhibit relatively high ductility. Dowel-type fasteners were tested and described by many authors, e. g. Dias [17], Dias et al. [19; 20], Frangi [30], Gelfi et al. [32] and van der Linden [90]. A frequently observed characteristic of dowel-type fastener is their pronounced nonlinear load-slip behaviour [18].

Notched connections are usually produced by milling cutouts in the timber section. They show very high stiffness and load-bearing capacity. However, their failure mode is brittle in many cases and they provide no resistance against vertical gap opening. Therefore, notches are often combined with vertical steel fasteners to mitigate these issues, which has been a subject of controversial discussion among researchers in the past decade. Ductile failure of notches has been observed by Frangi & Fontana [31] and Boccadoro [4]. Among others, Michelfelder [54] and Kudla [46] investigated the structural behaviour of notches in TCC structures.

A large variety of other connection systems have been investigated such as friction based connections [48], direct gluing of timber and concrete [8; 41; 70; 75; 85] or other special proprietary systems. The numbers of publications per connection category given above do not necessarily reflect the use of these connection systems in practice but they can be used as a rough indicator for that [21].

TCC systems using beech LVL

Most well-established TCC systems use timber elements made of standard-strength spruce. This typically results in a structure with a relatively thin concrete slab, i.e. a ratio of concrete to timber height $h_1/h_2 < 1$. In general, if linear timber elements are chosen (Fig. 2.2a), the ratio h_1/h_2 is lower than with planar elements (Fig. 2.2b). In both cases, the relatively thin concrete section is almost entirely subjected to compressive stresses and therefore, concrete cracking does not play a significant role in these systems.

For a long time, the use of high performance wood-based materials such as beech LVL in TCC slabs was not a focus in research because such a system would not have resulted in an economically competitive solution. Only in the past decade, with the start of industrial production of *BauBuche* on a large scale, the cost of beech LVL dropped substantially and researchers started investigating the use of this material in TCC slabs.

A planar system with beech LVL plates (*BauBuche Q*) and notches as connectors was developed by Boccadoro [4]. This research project strongly focused on the development of a notched connection that is able to exhibit plastic deformations at failure. The geometry of the notches was chosen such that a ductile timber compressive failure in the notch front is governing and any other brittle failures can be excluded. This ductile failure mechanism was shown both in local shear tests as well as in bending tests [6] and an analytical model was developed for predicting the load-bearing behaviour of a single-span beam [7]. Large global plastic deformations in the bending tests (mid-span deflection) were only observed if vertical gap opening was prevented by installing external vertical end-to-end reinforcement [6]. Furthermore, the local shear transfer close to the notches was investigated [5]. Other aspects relevant for the use in practice such as the prediction of deformations and dynamic behaviour were not studied in detail.

A similar system with notched connection was tested by Mönch [57], using glulam made of beech LVL, resulting in a vertical orientation of the laminations. The same notch depth of 15 mm as in [4] was used and additional vertical screws were installed in the notches. Ductile timber compressive failure in the notches was observed, accompanied by vertical gap opening and followed by a brittle combined bending-shear failure in concrete after small global plastic deformations.

Linear TCC systems using beech LVL were investigated by Yeoh et al. [93; 92] and later by Sebastian et al. [73; 74]. While in the former study vertically oriented 60 – 120 mm thin LVL boards were used, the latter investigated the use of glulam joists made of beech LVL with a horizontal orientation of the laminations. In both research projects, the structural behaviour was examined in double-shear push-out tests and bending tests. Yeoh et al. investigated three different connection types: rectangular and triangular notches combined with a vertical screw as well as staggered toothed metal plates. In contrast, Sebastian et al. focused on a connection using screws, varying several parameters such as different inclinations of the screws, arrangement as single screws or as pairs in X-formation, using fully threaded or partially threaded screws and different push-out test setups with concrete in compression or in tension, corresponding to the situation in sag and hog zones in a continuous TCC beam.

The superior strength of beech LVL compared to glulam made of spruce allows for a significant reduction of the timber cross-section. In the case of a design with linear timber elements, the concrete section is still thin compared to the timber height ($h_1/h_2 < 1$). However, the ratio h_1/h_2 increases substantially if planar elements made of beech LVL are used, ranging from 2.0 [57] up to 4.0 [6]. While the bending and tensile strength of beech LVL is around $2.5-3$ times higher than in spruce glulam GL24, its MOE is only $10-20\%$ higher. Therefore, the necessary bending stiffness can only be achieved with a certain total height of the TCC member. However, in TCC slabs with high h_1/h_2 ratios, typically more than half of the concrete section is cracked. While cracked concrete does not significantly contribute to the bending stiffness, it makes the structure relatively heavy, similar as in classical reinforced concrete slabs.

The fact that the use of high performance wood-based materials in TCC slabs has been studied only in recent years explains why concepts with a lightweight interlayer between timber and concrete have not been a focus of research so far. Adding such an interlayer is a promising strategy especially in TCC slabs with a high-strength timber section. This is because, in these cases, the lightweight interlayer replaces a part of the cracked concrete section.

TCC systems with steel tube connection

The french construction company *Paris Ouest* started developing a proprietary TCC system called *Sylvabat* in the late 1980's, using linear timber members and steel tubes as a connector. The company obtained an *Avis Technique*, allowing them to use this system in construction projects in European and Overseas France. This document has been revised several times, most recently in 2018 [9]. Fig. 2.3 shows cross-section drawings of this TCC system. The steel tubes have a diameter of 30, 50 or 70 mm and a wall thickness of 2 mm. A vertically-guided drilling machine is used to mill ring-shaped cutouts of 40 mm depth and a diameter 0.4 mm smaller than the used steel tube to achieve a form-fitting connection without using any glue. This production step is done either on site or in the factory, where CNC machining can be used as an alternative. A formwork of max. 25 mm thickness is installed and concrete is always casted on site. The formwork is either continuous (Fig. 2.3a) or discontinuous (Fig. 2.3b), which has an influence on the connection stiffness and shear capacity. The structural behaviour of the connection system was studied experimentally. No detailed test report is publicly available, but design values are given for the connection stiffness and shear capacity (Tab. 2.2).

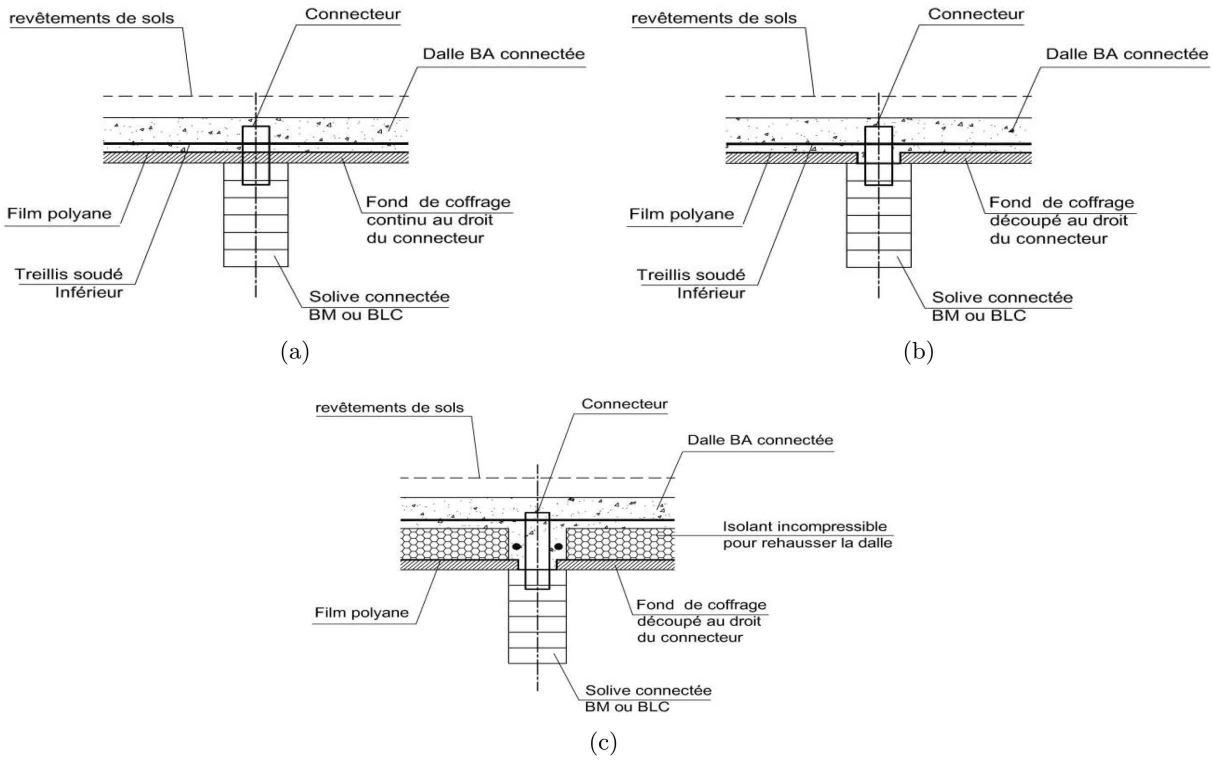

Fig. 2.3: TCC system *Sylvabat*, with (a) continuous and (b) discontinuous formwork at the location of the connectors, and (c) a design option with an insulation layer, reprinted from [9].

Tab. 2.2: Mechanical properties of the steel tube connection *Sylvabat* according to [9], valid for timber beams with a density $\rho \approx 450\,\mathrm{kg/m^3}$.

Steel tube diameter D [mm]	Formwork *	Stiffness K_{ser} [kN/mm]	Design shear capacity R_{d} [kN]
30	d	88.2	14.3
	c	29.4	10.3
50	d	49.0	25.0
	c	55.3	19.6
70	d	49.0	31.5
	c	–	–

* c = continuous (Fig. 2.3a), d = discontinuous (Fig. 2.3b)

An option including an interlayer made of isolation material is also mentioned in the document (Fig. 2.3c). According to the authors, this design may be chosen for the following reasons: (a) improved acoustic and thermal insulation properties and/or (b) increased stiffness to mass ratio. In this design, the insulation interlayer is disrupted at the location of the timber joists (Fig. 2.3c), leaving a concrete beam of the same width as the timber joist or at least 30 mm wider than the diameter of the steel tubes.

According to the *Avis Technique*, this TCC system has been used in over a thousand construction projects, building a total floor area of approximately 500'000 m^2. Applications covered the refurbishment of old timber slabs as well as the construction of new buildings.

Lukaszewska et al. [52] investigated a number of potential solutions for connecting off-site prefabricated concrete slabs to timber beams on the construction site. Among these, two connector types are similar to the steel tube connection investigated in the scope of this thesis:

- Connector 'SST + S' (Fig. 2.4a – 2.4c): A 20 mm diameter, 47 mm long steel tube with a welded flange is cast into the concrete slab and connected to the timber beam using a 20×120 mm hexagon head coach screw.
- Connector 'GDF' (Fig. 2.4d – 2.4f): A 20 mm diameter steel dowel with two flanges is cast into the concrete slab and connected to a hole in the timber beam using epoxy glue.

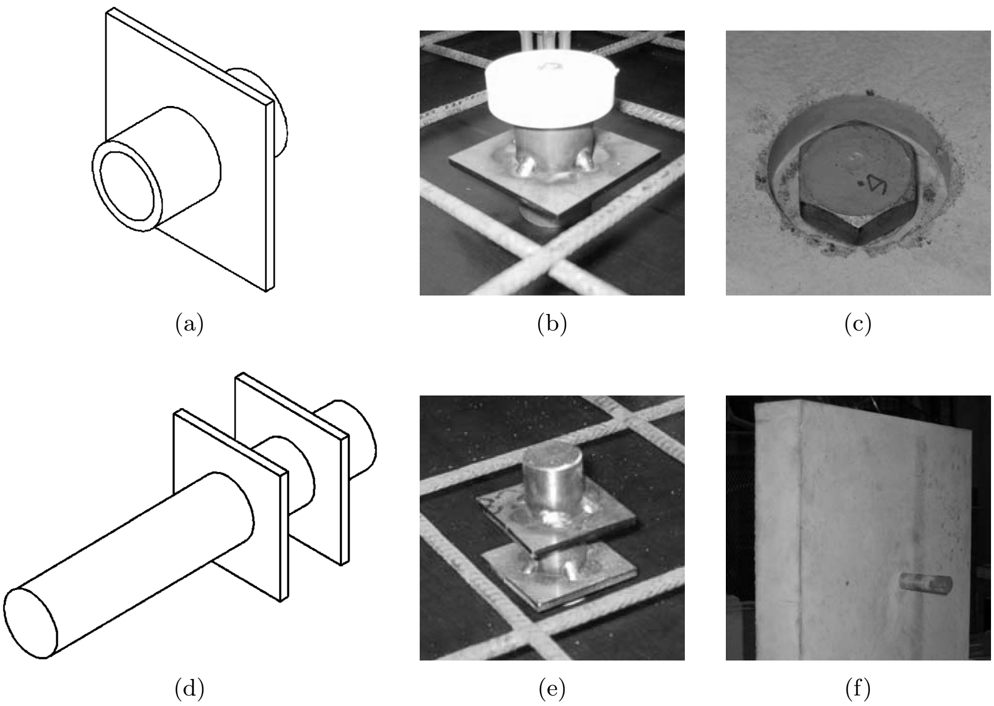

Fig. 2.4: Selection of connection systems investigated by [52], connector 'SST + S': (a) drawing, (b) in formwork before concreting and (c) after connection with timber beam; connector 'GDF': (d) drawing, (e) in formwork before concreting and (f) prefabricated concrete slab before connection with timber beam; reprinted from [52].

Push-Out tests were performed with all connectors to investigate their load-slip behaviour. Type 'SST + S' showed the lowest stiffness of all tested connectors whereas type 'GDF' showed a medium stiffness. Both connection types showed a pronounced nonlinear load-deformation curve, which is typical for dowel-type fasteners [18], and a very ductile failure. Despite its lower stiffness, type 'SST + S' was chosen for further testing rather than type 'GDF', mainly due to concerns about the quality of application and curing of epoxy glue on the construction site.

2.2.2 Calculation models

The load-bearing behaviour of TCC structures is strongly affected by the connection stiffness. Fig. 2.5 illustrates this influence using two limit cases. If no connection is present, no shear forces can be transmitted between the partial sections of the composite member and therefore, an external bending moment is carried entirely by the bending moments in the partial sections M_{i}. In the case of a rigid connection, no slip occurs between the partial sections and a significant portion of the external bending moment is carried by the pair of normal forces $N \cdot e$. Both maximum strain (and stress) as well as cross-section curvature are minimal in this structurally optimal case. However, in contrast to steel-concrete composite structures, such a rigid connection is difficult to implement in TCC structures. Therefore, flexible connectors are typically used, which results in a structural behaviour somewhere in between the two discussed limit cases, often described as 'partial composite action'. As a consequence of the connection flexibility, the assumption that plane sections remain plane after deformation (Bernoulli's hypothesis) is not valid for entire TCC members, but only for their individual components.

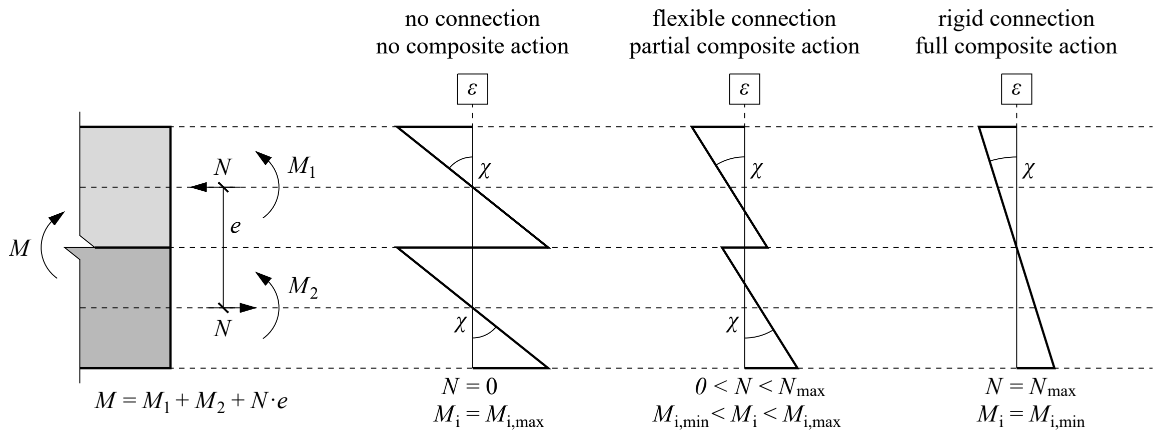

Fig. 2.5: Influence of connection stiffness on composite action.

Differential equation

The structural behaviour of composite members with a flexible connection can be described with a differential equation, as derived by Stüssi [83; 84] in 1943. Solutions for various boundary conditions have been published by many authors (e. g. Natterer & Hoeft [60] and Smith et al. [82]). While the differential equation allows deriving closed-form solutions, the effort increases substantially for cases with irregular material properties, loading and support conditions, connector layout etc.

The γ-method

For practical applications, a number of simplified calculation methods have been developed. The most widely used is the γ-method, which is closely related to Möhler's model [56] and described in Annex B of Eurocode 5 [13]. Its derivation is based on the solution of the differential equation for the case of a simple span beam under sinusoidally distributed load with constant cross-section geometry, material properties and connection stiffness across the entire span (uniform spacing of the connectors). For these boundary conditions, the solution of the differential equation is particularly simple and the reduction of the bending stiffness due to the flexible connection can be described using the γ-factor. As a simplification, the same definition can also be applied for other boundary conditions such as a simple span beam subjected to uniformly distributed load. All necessary formulas are given e. g. in Annex B of Eurocode 5 [13] and are applied and explained in Chapter 6.2 for the geometry of the system described in this thesis.

As discussed by Müller [59], different definitions of the γ-factor have been suggested and used. While all definitions lead to the same end results if consequently applied, this is a common source of confusion for engineers using this method. The definition suggested by Möhler [56] is used by most researchers and was adopted in Annex B of Eurocode 5 [13]. Furthermore, this definition is also the basis for the long-term models adopted in the final draft of the CEN/TC250/SC5 Technical Specification on the structural design of TCC structures (hereinafter called TS TCC) [15]. Therefore, this definition is used also in the scope of this thesis.

One of the most common discrepancies between the assumptions of the γ-method and TCC structures in practice is the distribution of the connectors along the span. While the γ-method assumes a uniform spacing of the connectors, these are almost always concentrated in areas with high shear forces (typically near the supports) to optimise the performance of the TCC member. Several methods of estimating an equivalent even spacing s_{ef} in such cases have been compared by Michelfelder [54]. She found that using different approaches can significantly influence the bending stiffness resulting from the γ-method. The most commonly used approximation is the following, as adopted in the TS TCC [15]:

$$s_{\mathrm{ef}} = 0.75 \cdot s_{\mathrm{min}} + 0.25 \cdot s_{\mathrm{max}} \tag{2.1}$$

with s_{min} and s_{max} denoting the minimum and maximum connector spacing, valid for cases where $s_{\mathrm{max}} \leq 4 \cdot s_{\mathrm{min}}$. A more precise definition of s_{min} and s_{max} is provided by Michelfelder [54], which is shown in Fig. 2.6 and was used in the scope of this thesis.

The main advantage of the γ-method for practical use is its simplicity and the fact that all design verifications can be done using analytical formulas. This allows for easy parametric design optimisation using spreadsheet calculations, as done in many engineering offices.

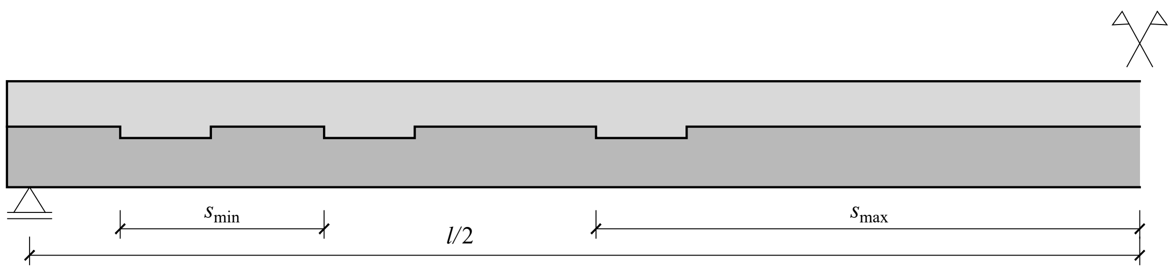

Fig. 2.6: Definition of minimum and maximum connector spacing according to [54].

Strut-and-tie models

With the increasing usability and popularity of FEM software, new calculation approaches were developed on this basis. A well-established and widely used method is the strut-and-tie model, which was first described by Grosse et al. [33] and Rautenstrauch et al. [65]. The term *strut-and-tie model* (presumably translated from the German *Stabwerkmodell*) is established in the TCC community [21], although the model actually is a frame, rather than a truss with struts and ties. Fig. 2.7 shows an example for a single span TCC beam with three notches per shear area. The timber and concrete chords are modelled as individual beams, connected with (a) beam elements representing the TCC connectors and (b) hinged rigid beam elements representing the vertical contact of the two members. A hinge is inserted in the connector beam element at the height of the interface between timber and concrete, to correctly model the eccentricity of the connection. The bending stiffness of the connector beam elements is calculated as follows:

$$EI^* = \frac{K}{3} \cdot \left(z_1^3 + z_2^3\right) \tag{2.2}$$

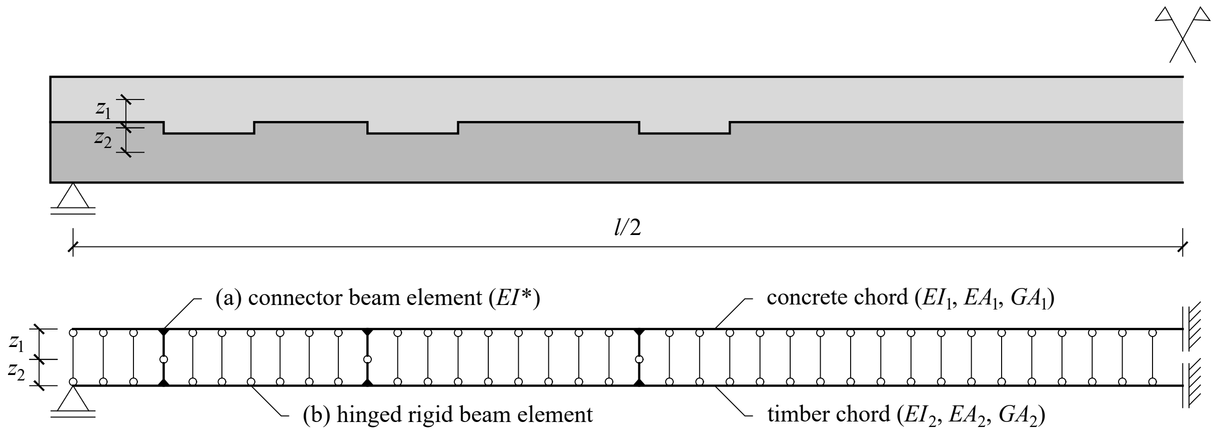

Fig. 2.7: Strut-and-tie model for a single span TCC beam with three notches per shear area.

The main advantages of strut-and-tie models are their flexibility and intuitive interpretation of the results. Engineers can model the connectors in their precise location and analyse arbitrary loading and support conditions. The internal forces resulting from the model can be used directly for the design verifications. In addition, strut-and-tie models are particularly useful for the following tasks:

- Iterative optimisation of the connector layout for a given loading situation, pursuing an even distribution of the shear forces in all connectors: Using this technique, both bending stiffness and load-bearing capacity of the TCC member can be maximised for a given number of connectors.
- Modelling of multi-span TCC beams: The situation in the hog zones can be accurately modelled by changing the properties of the concrete chord in these areas. For example, if

the concrete section is assumed to be fully cracked in the hog zone, the stiffness properties can be set to $EI_1 = 0$ and EA_1 according to the steel reinforcement. This is, however, an iterative procedure as these stiffness properties influence the distribution of internal forces and in turn, the resulting length of the hog zone. An example for this procedure is provided by Müller [59].

- Nonlinear analyses: Strut-and-tie models can be modified such that the nonlinear load-slip behaviour of the connectors can be considered. A corresponding approach is discussed in Chapter 6.3.

While the range of application is by far wider compared to the γ-method, strut-and-tie models require a higher effort and are not as convenient for parametric design optimisation. Further limitations concern TCC members where significant concrete cracking occurs under positive bending moments. This is often the case in TCC members with a high concrete to timber height ratio h_1/h_2. This topic is analysed in detail in Chapter 6.3.

Other calculation models

The γ-method and strut-and-tie models are by far the most used calculation methods in engineering practice. However, further models have been developed that may be needed in special situations. If more than two layers are connected with flexible connectors, the shear analogy is a useful model. This method was developed by Kreuzinger [45] and further work was done by Scholz [71]. In special cases, full 3D FE models can be used for the analysis of TCC structures. While this method offers almost unlimited possibilities, the complexity and time effort of such an analysis is substantial. Therefore, this approach is almost exclusively used in research. A comprehensive summary and comparison of all available calculation models is provided by Dias et al. [21].

2.3 Two-way spanning timber-concrete composite slabs

Up to date, almost all TCC slabs are one-way spanning. Only in recent years, a few research projects started focusing on the development of two-way spanning slabs. So far, all of these research projects focused on composite slabs using CLT made of spruce.

In 2013, the American company *Skidmore, Owings & Merrill, LLP (SOM)* started a research project with the goal to develop a structural system for high-rise buildings using mass timber as the main structural material [38; 80]. The concept development focused on architectural, structural, economical and ecological aspects and includes solutions for the vertical elements and the floor slabs. Based on a comparison of different floor slab types, the authors concluded that a two-way spanning CLT-concrete composite slab would be best suited to meet the requirements of such a building. The concept is intended to be used in multi-span systems to optimise the structural behaviour regarding deformations and vibrations. The structural behaviour of this TCC slab was investigated in an extensive experimental campaign by Higgins et al. [35] and SOM [81]. The following four test series were carried out in 2017:

- Uniaxial small scale 3-point bending tests to compare different TCC connection systems
- Biaxial small scale tests to determine the orthotropic stiffness values of the TCC slab
- Uniaxial full scale 4-point bending tests with clamped supports to investigate the load-bearing behaviour in multi-span systems
- Uniaxial full scale long-term tests to investigate the creep behaviour

The biaxial small scale tests were performed on three identical quadratic specimens of approximately 2.4 m side length. The CLT and concrete thickness was 171 and 57 mm, respectively. Inclined self-tapping screws were chosen as connectors. Two different test setups were used to determine all orthotropic stiffness parameters of each specimen under service loads. The bending stiffness in both load-bearing directions was measured in a uniaxial 3-point bending test setup. The torsional stiffness was obtained by supporting three corners of the specimen and applying a point load on the fourth corner. All stiffness parameters were determined under positive (concrete in compression) and negative (concrete in tension) bending moments, resulting in a total of six values per specimen.

For a prediction of the biaxial load-bearing behaviour of the CLT-concrete composite slab, the authors used an FE model with orthotropic plate elements. The bending stiffness values in both load-bearing directions for the orthotropic stiffness matrix were calculated independently, using the γ-method. This was done for both positive and negative bending moments, achieving good agreement with the test results. In the FE model, the positive and negative bending stiffness values were iteratively assigned to the sag and hog zones of the multi-span slab. The authors do not give any recommendations with regard to the calculation of the torsional stiffness.

A similar two-way spanning CLT-concrete composite slab was developed and investigated by Loebus & Winter [50]. The most important results of this research project are summarised by Loebus et al. [49]. Two different concepts for the shear connection between CLT and concrete were pursued: inclined self-tapping screws and rectangular notches.

In the biaxial stress field of a two-way spanning TCC slab, the direction of the principal shear force varies. Investigating the influence of this varying shear force direction on the connection behaviour was one of the main goals of the research project. Double-shear push-out tests and FEM analyses were carried out for both notches and inclined screws with varying force direction. In the case of notches, the authors concluded that it is important to always activate the CLT layers parallel to the grain, leading to different notch depths depending on the shear force direction. In the case of inclined screws, the conclusion was that all connectors should be aligned along the direction of the principal shear forces. A spring model was suggested to account for the directional dependency of the connection stiffness in the case of inclined screws.

The torsional stiffness was investigated in a test setup identical to the one used in the research project by *SOM* [35; 81], on quadratic specimens of 2.1 m side length. A significant reduction of the torsional stiffness was observed after concrete cracking occurred. No ultimate failure was reached as the experiments were stopped at a deflection of the loaded corner of 50 mm.

The global load-bearing behaviour of the two-way spanning TCC slab was investigated in a small scale biaxial test. Four quadratic specimens of 3.5 m side length were loaded in a test setup that is the biaxial equivalent of a 4-point-bending test setup (hinged line supports on all sides, point loads at 1/3 and 2/3 of the span). Both connection concepts (notches and inclined screws) were investigated. According to the authors, all specimens showed high stiffness and load-bearing capacity. Limited ductility was observed before ultimate failure occurred due to combined tension and bending in the CLT element. FEM analyses were performed to compare the load-bearing behaviour of the two-way spanning TCC slab with a one-way spanning equivalent. This comparison confirmed the high potential of two-way spanning TCC slabs.

Another similar two-way spanning CLT-concrete composite slab was developed by the Swiss companies *Pius Schuler AG* and *Schilliger Holz AG* [72]. The shear connection between CLT and concrete is achieved by gluing 20 mm thick timber blocks on the CLT surface. Brittle shear failure in the glue line between CLT and timber blocks was governing the load-bearing capacity of the TCC slab in experiments. This slab system has already been implemented in a few residential buildings in Switzerland.

In all of the above-mentioned studies on two-way spanning TCC slabs, a significant increase in stiffness was observed compared to a one-way spanning alternative. Given that the design of TCC slabs is typically governed by deformation or vibration criteria, this result confirms the great potential of two-way spanning TCC slabs.

Chapter 3

Connection shear tests

3.1 Introduction

This chapter covers the shear tests that were conducted to study the behaviour of the steel tube connection used in the considered TCC slab concept. The main objectives of these tests were:

- Investigating the stiffness, shear capacity and ductility of the connection
- Understanding the structural behaviour and the governing failure mechanisms
- Studying the influence of various parameters on the connection behaviour
- Providing empirical data as an input for the uniaxial and biaxial bending models

Three series of push-out tests were conducted. Series A (12 specimens) focused on the connection concept development. A considerable number of parameters were varied as an experimental basis to choose the best design for further tests. In series B (8 timber specimens) and C (8 concrete specimens), the structural behaviour of the final connection concept was further investigated. The main findings are presented and discussed in this chapter. A detailed report of all conducted experiments is provided in [44].

3.2 Materials and methods

3.2.1 Specimens

The investigated TCC slab concept contains three different connection types, which is shown in Fig. 3.1. All of these connection types were investigated in separate experiments. Connection type 2 only occurs if a construction process with cast-in situ concrete is chosen. In the case of full prefabrication, an upper beam is not necessary and thus, only types 1 and 3 occur in the structure. As towards the end of this research project, full prefabrication was considered to be the more economical option, this chapter focuses mainly on connection types 1 and 3.

The beech LVL boards used for all timber specimens were produced by the company *Pollmeier GmbH* in Creuzburg. At the time of the first test series (series A), plates thicker than 40 mm were not available. Therefore, the specimens were manufactured by block gluing several plates of 40 mm thickness. At the time of test series B, plates of 60 mm could be used for the side members without block gluing, which represents the situation in the TCC slab more accurately. Further details on the used materials are given in Tab. 3.1.

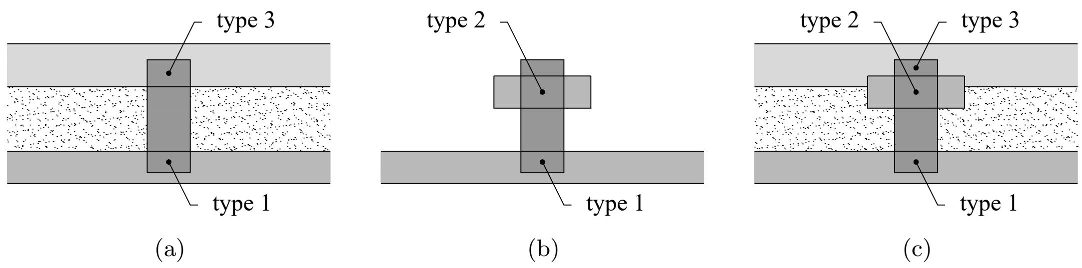

Fig. 3.1: Connection types in different concept versions of the TCC slab: (a) full prefabrication or (b) & (c) using cast-in-situ concrete (construction and final state); connection type 1: steel tube in beech LVL, type 2: steel tube penetrating upper beech LVL beam, type 3: steel tube in concrete.

For the specimens with type 3 connections, concrete was ordered according to the specifications given in Tab. 3.1. All other test series in the scope of this research project were done with concrete strength class C30/37. Time constraints made it necessary to test the specimens already after eight to nine days. Therefore, strength class C35/45 was chosen to compensate for the shorter hydration time. Concrete tests were performed to determine the MOE according to SIA 262/1 [77], the cylinder compressive strength according to EN 12390-3 [11] and the splitting tensile strength according to Chen [16]. A detailed report of these tests is provided in [44]. Tab. 3.2 shows that the measured strength values are as expected for concrete C35/45 at this age. However, the tested samples reached only a third of the expected MOE value, which will be discussed in Chapter 3.3.4.

The geometry of all specimens is depicted in Fig. 3.2 and the chosen set of specimen parameters is summarised in Tab. 3.3. The geometry was chosen such that symmetrical vertical loading was possible in the test setup (Chapter 3.2.2). Consequently, each specimen contained four identical steel tube-timber or steel tube-concrete connections. In the specimens with type 2 connections, the shape of the middle member was modified accordingly. Every specimen was given a name consisting of the test series (A,B,C), connection type (1,2,3) and an ascending number per test series, e. g. B-2-4. In order to get an overview of the influence of different parameters with as few specimens as possible, all test series were based on the following principle: In each specimen group, one reference configuration was chosen (marked with ° in Tab. 3.3). All other specimens were used to vary one of the parameters at a time (bold print in Tab. 3.3), while the other parameters remained unchanged with regard to the reference configuration.

Connection type 1 is usually fabricated using a CNC milling machine (Chapter 1.3). In this case, a ring is cut out of the LVL plate, leaving an inner tenon in place. The specimens of test series B were fabricated like this (Fig. 3.3a). Due to limitations in the fabrication facility at the time of test series A, an alternative construction process had to be chosen. Instead of removing only a ring, a full cavity was cut out (Fig. 3.3b). This modification allowed for a fabrication in two steps. First, a hole was drilled in one of the two LVL plates by means of core drilling. In a second step, this plate was block glued to the other LVL plate. Specimen A-1-3 presents an exception. In this case, the core was put aside, reduced to a smaller diameter and glued to the base of the cavity (Fig. 3.3c).

Tab. 3.1: Materials used in the push-out specimens.

Material	Description	Details
BauBuche Q (series A)	Thickness	40 mm
	Veneer layout	||| − ||||| − |||
	Cross-layer ratio	14%
BauBuche Q (series B)	Thickness	60 mm
	Veneer layout	||| − || − |||||| − || − |||
	Cross-layer ratio	19%
Concrete (series C)	Ordered quality	C35/45, self-compacting (SCC)
	Max. aggregate size	16 mm
	Admixture	MasterLife SRA 895 (2% of cement mass)
	Concrete age	8 (concrete tests) and 8 − 9 days (push-out)
Reinforcement	Standard mesh K335	B500A, ∅ 8 @ 150 mm
Steel tubes	ROR 60.3/2.0	S235, welded
	ROR 60.3/3.6	S235, welded
	ROR 60.3/8.0	E355
	ROR 82.5/3.6	E355, seamless
	ROR 82.5/8.0	E355
	ROR 101.6/3.6	S235, welded
	RRW 80×80/3.6	S355, hot-rolled
Grout types	Sikadur®-Pronto 12	Acrylic repair mortar and grout [78]
	Sikadur®-42 HE	High performance epoxy grouting system [79]

Tab. 3.2: Results of concrete tests, 8 days after production.

		Mean value [MPa]	COV	n
Modulus of elasticity	E_1	9'800	5%	3
Cylinder compressive strength	$f_{1,\mathrm{c}}$	34.6	9%	3
Splitting tensile strength	$f_{1,\mathrm{t,sp}}$	2.6	13%	4

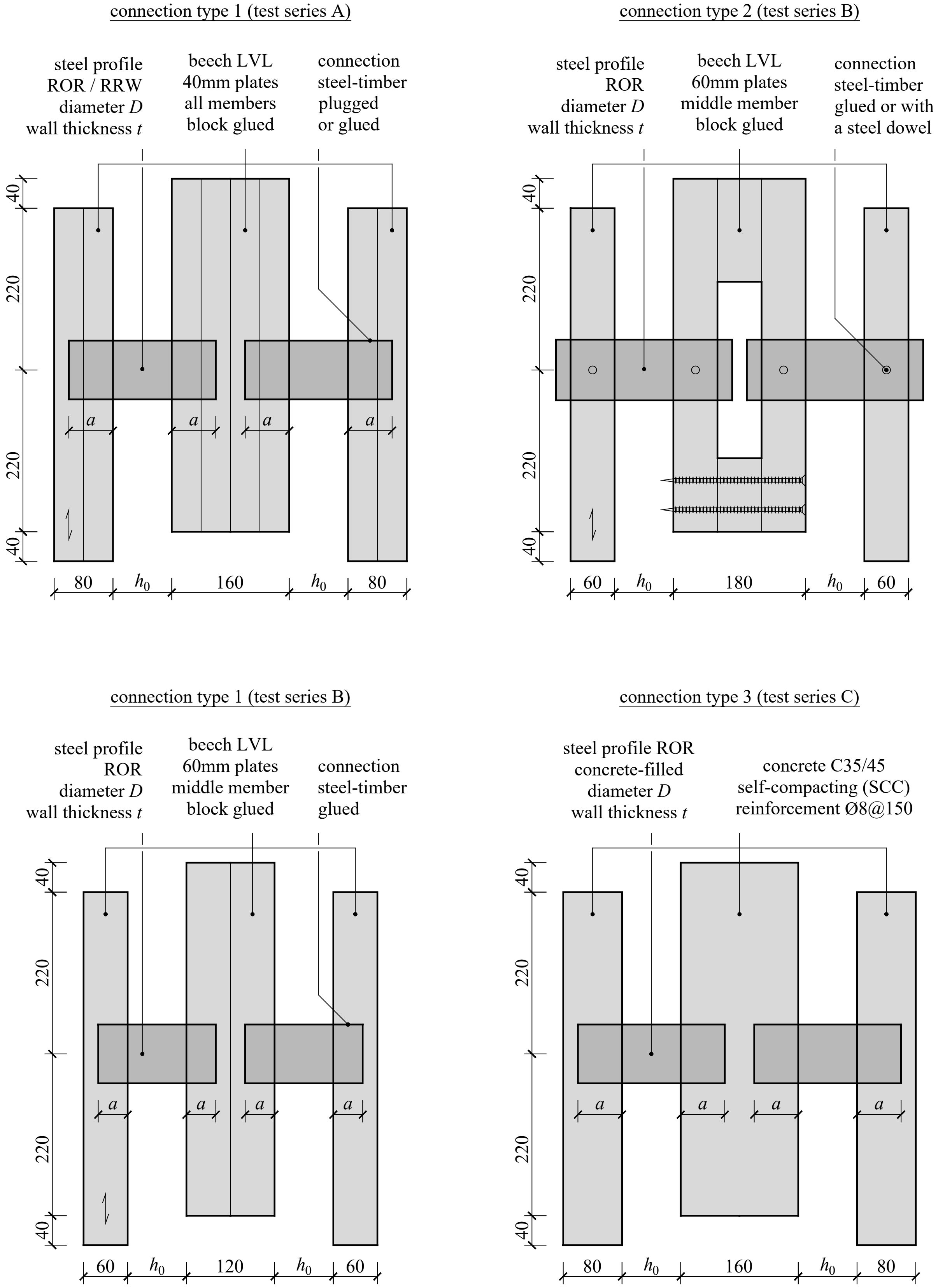

Fig. 3.2: Geometry of the push-out specimens, depth (out of plane) of all specimens: 220 mm.

Tab. 3.3: Parameters of the push-out specimens.

Name	Conn. type	Grout type *	Embed-ment depth	Space between members	Steel tube dimensions	Inner tenon	Add. hor. support
			a [mm]	h_0 [mm]	$D\,/\,t$ [mm]		
A-1-1.1 °	1	none	40	80	ROR 82.5/3.6	no	no
A-1-1.2 °	1	none	40	80	ROR 82.5/3.6	no	no
A-1-2.1	1	**g1**	40	80	ROR 82.5/3.6	no	no
A-1-2.2	1	**g2**	40	80	ROR 82.5/3.6	no	no
A-1-3	1	none	**60**	80	ROR 82.5/3.6	yes	no
A-1-4	1	none	40	**0**	ROR 82.5/3.6	no	no
A-1-5	1	none	40	**40**	ROR 82.5/3.6	no	no
A-1-6	1	none	40	**120**	ROR 82.5/3.6	no	no
A-1-7	1	none	40	80	ROR **60.3**/3.6	no	no
A-1-8	1	none	40	80	ROR **60.3**/**2.0**	no	no
A-1-9	1	none	40	80	ROR **101.6**/3.6	no	no
A-1-10	1	none	40	80	**RRW** 80/3.6	no	no
B-1-1.1 °	1	g2	40	80	ROR 82.5/8.0	yes	yes
B-1-1.2 °	1	g2	40	80	ROR 82.5/8.0	yes	yes
B-1-1.3 °	1	g2	40	80	ROR 82.5/8.0	yes	no
B-1-2	1	g2	40	**120**	ROR 82.5/8.0	yes	yes
B-1-3	1	g2	40	80	ROR **60.3**/8.0	yes	yes
B-2-4	2	**g2**	60	80	ROR 82.5/8.0	no	yes
B-2-5 °	2	none	60	80	ROR 82.5/8.0	no	yes
B-2-6	2	none	60	80	ROR **60.3**/8.0	no	yes
C-3-1.1 °	3	-	40	80	ROR 82.5/3.6	-	yes
C-3-1.2 °	3	-	40	80	ROR 82.5/3.6	-	yes
C-3-1.3 °	3	-	40	80	ROR 82.5/3.6	-	no
C-3-2	3	-	**30**	80	ROR 82.5/3.6	-	yes
C-3-3	3	-	**50**	80	ROR 82.5/3.6	-	yes
C-3-4	3	-	**60**	80	ROR 82.5/3.6	-	yes
C-3-5	3	-	40	**120**	ROR 82.5/3.6	-	no
C-3-6	3	-	40	80	ROR **60.3**/3.6	-	yes

* Grout types: g1 = Sikadur®-Pronto 12, g2 = Sikadur®-42 HE

° Reference configuration

After the preparation of the timber members (connection types 1 and 2), the specimens were assembled. In the case of a grouted connection, the assembly had to be split up into several phases to ensure that the connection is fabricated in the same way as in a real structure, with the steel tubes always in a vertical position. In contrast to the timber specimens, the concrete specimens (connection type 3), were produced with the steel tubes in a horizontal position. A formwork was fabricated with openings for the steel tubes (Fig. 3.4). To make sure that the concrete would fill the steel tubes, a self-compacting concrete (SCC) was used.

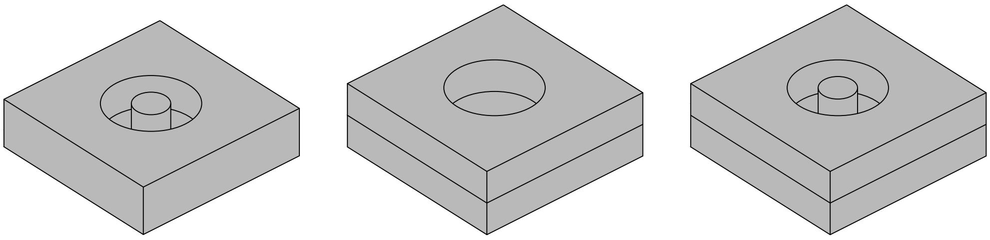

(a) (b) (c)

Fig. 3.3: Production differences of connection type 1 specimens in (a) test series B, (b) test series A and (c) specimen A-1-3.

(a) (b) (c)

Fig. 3.4: Production of concrete push-out specimens: (a) formwork and concrete cylinders, (b) close-up of one specimen before casting, (c) formwork and concrete cylinders after casting of concrete.

3.2.2 Test setup

The double-shear push-out test is a well-established method to determine the load-bearing behaviour of TCC connectors [15]. In conventional connection systems, there is no or only a very small gap between the two structural members ($h_0 \approx 0$). The investigated TCC structure, however, includes a substantial gap. Therefore, the classical double-shear push-out test setup (described e. g. in the TS TCC [15]) had to be modified. Fig. 3.5 and 3.6 show the used test setup.

The experiments were conducted on the universal testing machine Schenck Hydropuls 1600 kN (Fig. 3.6a) in the laboratories of ETH Zurich. The vertical forces were introduced in such a way that potential shear failures in the timber member were not excluded by the boundary conditions of the test setup.

Due to the force eccentricity in the tested connection, horizontal supports for the outer members of the specimen were necessary. At the bottom, these were realised using square full steel profiles (45×45 mm) connected with two M13 threaded rods (⑦ and ⑧ in Fig. 3.5). At the top, horizontal displacements were prevented using steel profiles LNP 80×8 mm coated with PTFE plates (④). Similar PTFE plates were glued to the specimen in these locations to minimise friction forces. In test series A, these supports were installed only on the inner side, because this is where horizontal displacements were expected. During the tests, however, displacements towards the outside were observed in some cases. Therefore, additional outer supports were installed in test series B and C, preventing the outer members from tilting.

To investigate the influence of this modification, one of the three identical reference configuration specimens in both test series B and C was tested in the original test setup without the additional supports. No substantial influence on stiffness, load-bearing capacity or ductility was observed. Specimen C-3-5 was also tested in the original test setup (Tab. 3.3), because given its large width, the additional supports could not be attached to the steel base plate.

To ensure that the middle timber member would remain perfectly vertical throughout the test, four guiding supports were installed in the middle of the bottom base plate (⑥). This was important because an inclination of the middle timber member could have led to deviation forces and asymmetrical loading of the two steel tubes.

3.2.3 Measurements and test procedure

The cylinder force was measured using the internal load cell of the testing machine. Two NDI Optotrak Certus position sensors were installed to record the deformations on both front and rear side of the specimen. Strobers (Fig. 3.6) were glued to both the specimen and the testing machine, which allowed for a precise 3D tracking of these points throughout the experiments. Their locations are shown in Fig. 3.5. Depending on the specimen type, 16 – 24 strobers were used on each side. Additionally, the distance between the two steel base plates was measured using a linear variable differential transformer (LVDT), confirming the accuracy of the NDI measurement.

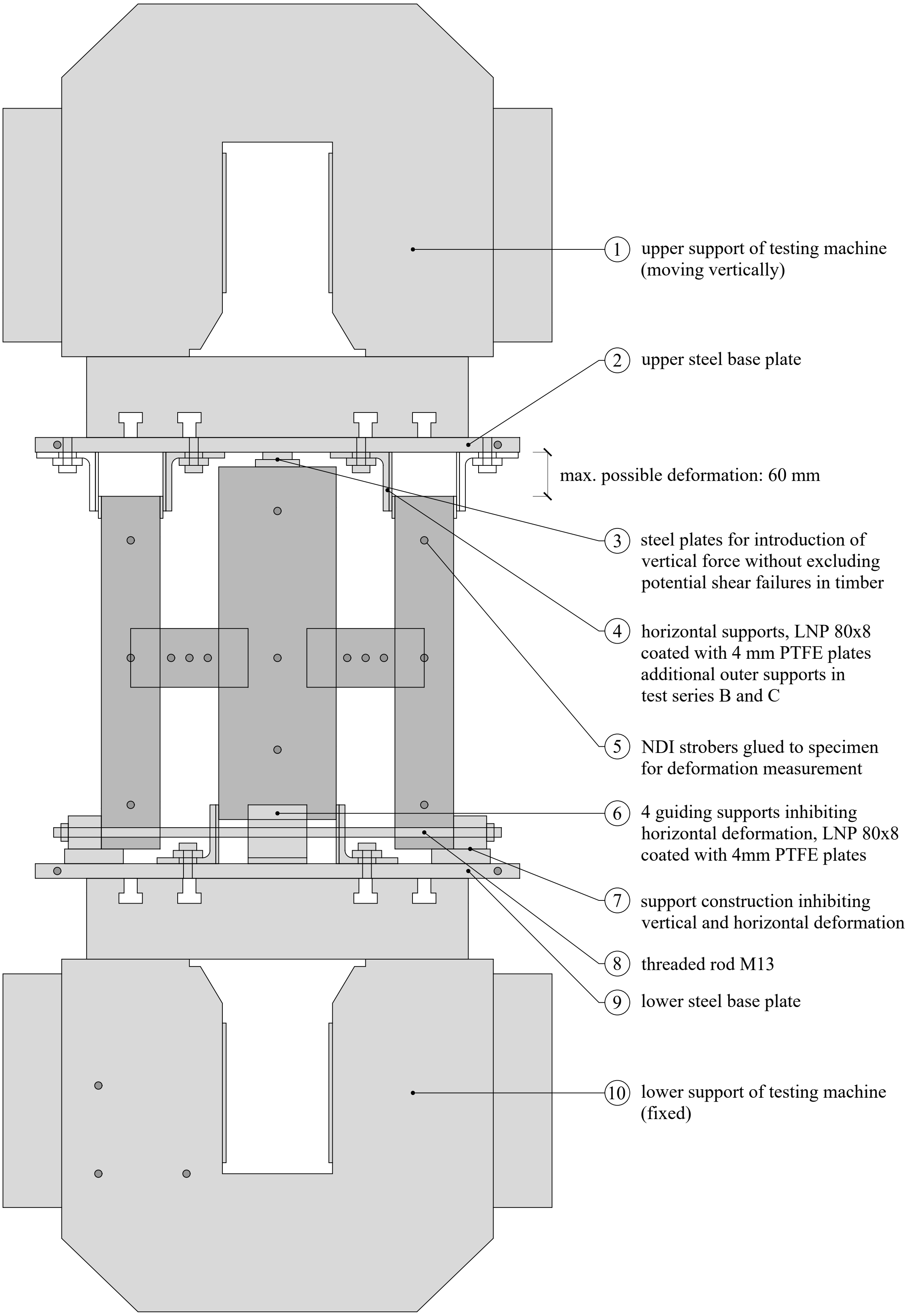

Fig. 3.5: Test setup used for double shear push-out experiments.

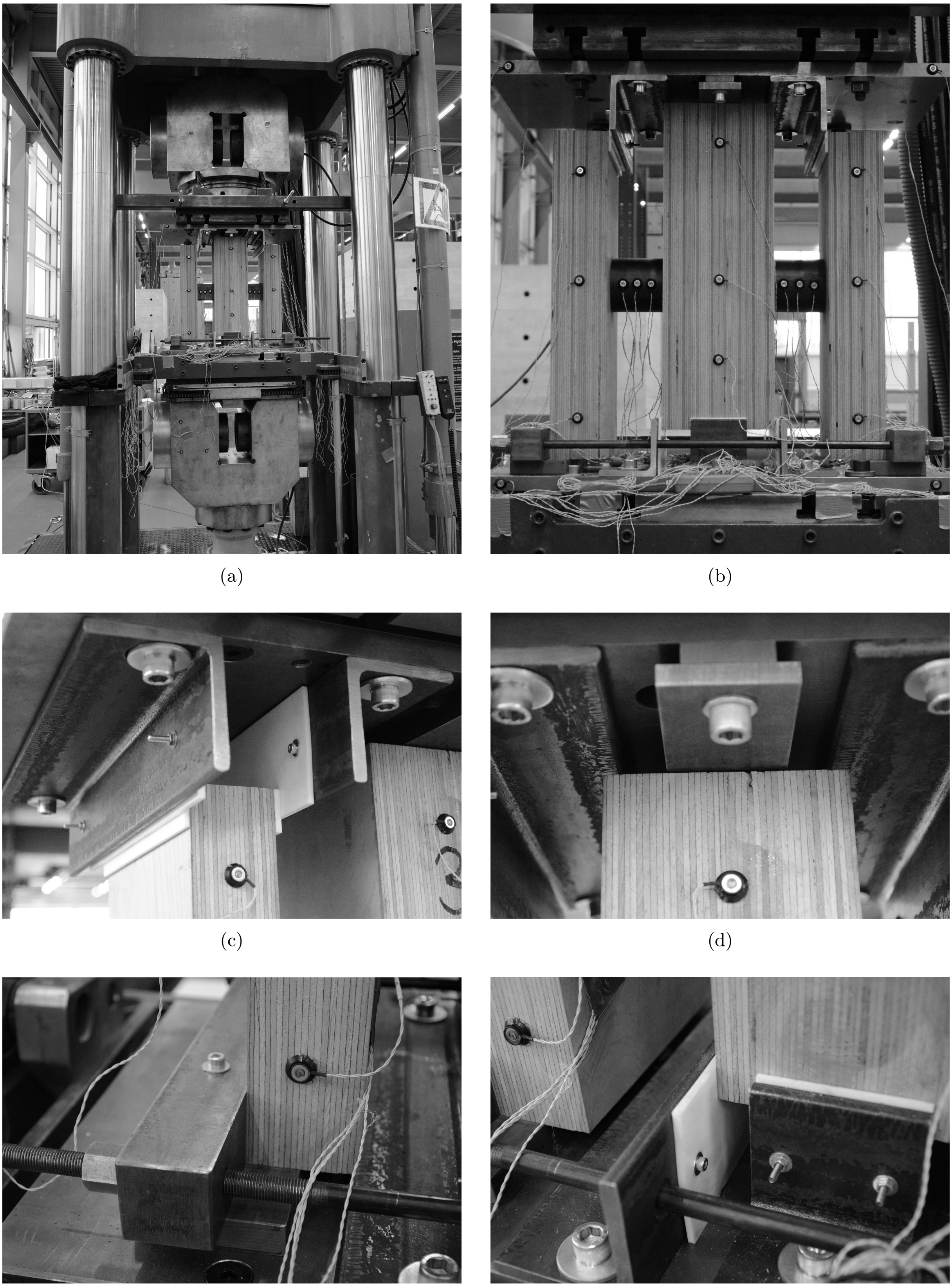

(a) (b)

(c) (d)

(e) (f)

Fig. 3.6: Photos of the test setup: (a) testing machine, (b) overview with specimen A-1-3, (c) ④ additional outer support in series B and C, (d) ③ introduction of the vertical force, (e) ⑦ bottom support construction and (f) ⑥ guiding supports for the middle member.

The tests were conducted according to the following procedure: After centering the specimen in the testing machine, all horizontal supports (4 and 6 in Fig. 3.5) were positioned and tightened. The lower support construction (8) was tightened. This was done by hand, making sure there would be no slip, however avoiding any substantial post-tensioning. The used loading protocol is based on the recommendations given in EN 26891 [10]. The specimen was loaded at a constant displacement rate (Fig. 3.7), so that the post-peak behaviour of the connection could be observed as well. Depending on the expected stiffness of the specimen, the displacement rate of the first loading/unloading cycle was 0.01 or 0.02 mm/s. For the second loading ramp, the displacement rate was doubled. In a few cases, additional unloading and reloading cycles were performed after the maximum force had been reached to assess the remaining elastic connection stiffness in this state. The experiment was stopped when either a brittle failure led to a significant force drop or when the capacity of the test setup was reached at a displacement of 60 mm.

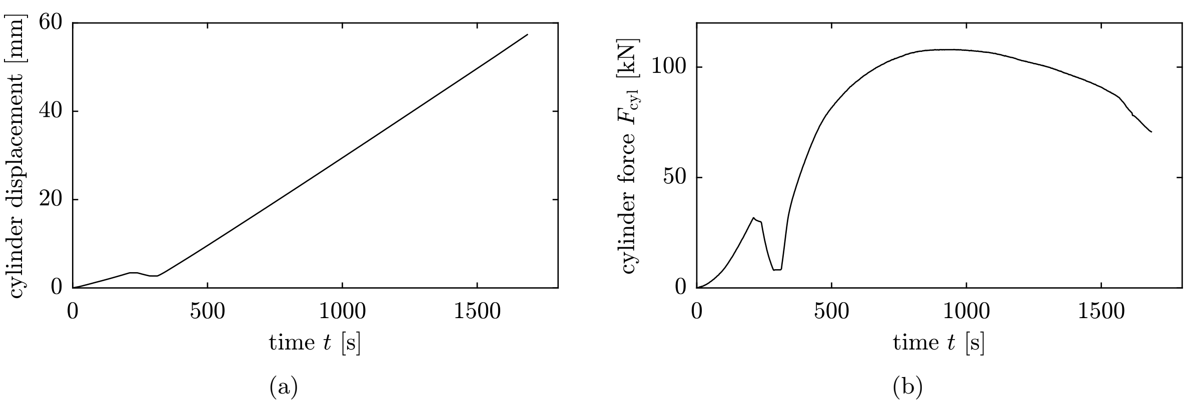

Fig. 3.7: Typical (a) displacement-time and (b) force-time diagrams.

3.2.4 Data evaluation

In the investigated TCC connector, a large part of the deformation occurs in the embedded part of the steel tube in the timber or concrete member. Using a rotational spring is the most practical way to account for the connection stiffness in a calculation model (e. g. for a TCC beam using this connection system). Therefore, describing the moment-rotation behaviour of the connection was one of the main goals of this test series. However, as neither the bending moment nor the rotation in the connection could be measured directly, they had to be calculated from the vertical force T and the relative vertical displacement between the middle member and the side members, hereinafter called relative displacement parallel to the beam axis Δu. Fig. 3.8 shows the mechanical model that was used for this calculation. The following simplifications were made to calculate the moment-rotation behaviour of the connection:

- The location of the rotational spring is assumed at the base of the steel tube (Fig. 3.8b) for connection types 1 and 3. Connection type 2 is always symmetrical, thus the spring location is assumed in the middle of the timber member.

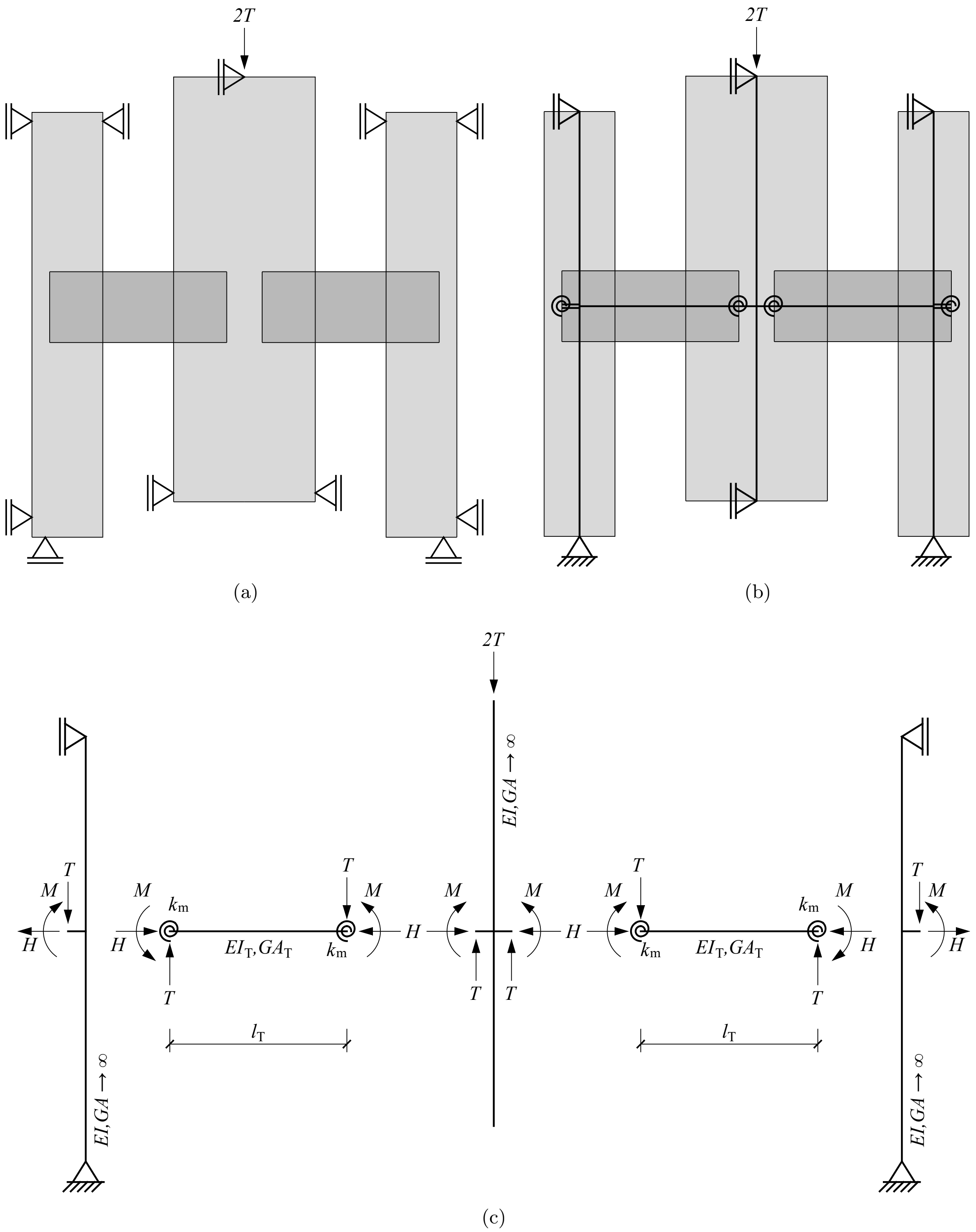

Fig. 3.8: Mechanical model used to calculate the moment-rotation behaviour of the tested connection: (a) position of the supports in the test setup, (b) simplified model and position of the rotational springs and (c) free body diagram.

- The force acting on the middle member is assumed to be equally distributed to the left and right connection (Fig. 3.8c).
- The part of the deformation that is caused by bending and shear in the steel tube is calculated using Timoshenko beam theory. In the case of concrete filled steel tubes (connection type 3), both steel and concrete sections are considered in the calculation of EI_T and GA_T. The shear area used in the calculation of the steel tube shear stiffness GA_T is estimated according to Eurocode 3 [14], section 6.2.6(3):

$$A_\mathrm{v} = 2A/\pi = 2t \cdot (D - t) \tag{3.1}$$

- The deformation of the outer timber or concrete members due to bending and shear is not accounted for in the calculation of the connection moment-rotation behaviour. This is equivalent to assuming that all timber or concrete members are rigid (Fig. 3.8c). Small deformations of the outer members were measured, mainly towards the end of the experiments (post-peak). These deformations could lead to a slight overestimation of the calculated rotation φ (Eq. 3.3). However, their influence on the moment-rotation behaviour in absolute terms is estimated to be negligible.

Based on the described mechanical model and its assumptions, the connection moment-rotation behaviour is calculated as follows:

$$M = T \cdot \frac{l_\mathrm{T}}{2} \tag{3.2}$$

$$\varphi = \frac{\Delta u}{l_\mathrm{T}} - \frac{T l_\mathrm{T}^2}{12 EI_\mathrm{T}} - \frac{T}{GA_\mathrm{T}} \tag{3.3}$$

Linear regression was performed in the linear part of the force-displacement and the moment-rotation curves (approximately between $0.1 - 0.4\,T_\mathrm{u}$) to calculate both global stiffness $k_\mathrm{s} = T/\Delta u$ and local rotational stiffness $k_\mathrm{m} = M/\varphi$ of the connection. This was done on both the initial loading and reloading curve, resulting in four linearised stiffness values $k_{\mathrm{s},1}$, $k_{\mathrm{s},2}$, $k_{\mathrm{m},1}$ and $k_{\mathrm{m},2}$. More details on the regression are given in [44].

3.3 Results and discussion

3.3.1 Introduction

The recorded NDI measurement data allowed for an in-depth analysis of the deformations that happened throughout the loading tests. A detailed report of each experiment including all the observations and analyses made is given in [44]. In the following part of this thesis, the most important results are presented and discussed separately for the three investigated connection types (Chapters 3.3.2 – 3.3.4), focusing on the observed structural behaviour and the influence of the studied parameters. In Chapters 3.3.5 – 3.3.7, additional aspects concerning all three connection types are discussed.

3.3.2 Connection type 1: steel tube in beech LVL

Structural behaviour and observed failure mechanisms

In the studied connection, a shear force T and a bending moment M have to be transmitted from the steel tube to the timber member. The shear force is transmitted via contact pressure at the interface with the timber (Fig. 3.9). In almost all specimens, the resulting compressive stresses in the timber led to inelastic deformations at the front side of the cutout (Fig. 3.10b). This **timber compressive failure** is the main reason for the nonlinear load-bearing behaviour and the ductility that was observed in most connection tests. Depending on the steel tube wall thickness t, **local buckling** was observed at the same location in the steel tube (Fig. 3.9a and 3.10a). Buckling is not expected to occur in the real structure when the steel tube is filled with concrete. Therefore, in test series B, the wall thickness t was increased in order to exclude this failure mechanism.

The bending moment from the steel tube is transmitted with a combination of two force pairs: a pair of contact forces (horizontal forces in Fig. 3.9) and a pair of shear forces at the interface (vertical forces in Fig. 3.9). In a form-fitting connection without grouting, shear forces can be transmitted only by friction and are therefore limited. In a grouted connection, a larger portion of the bending moment can be transmitted in this way, leading to a higher stiffness but also to higher tensile stresses perpendicular to the grain, especially on the rear side of the connection. In many cases, this resulted in a combined failure due to **shear and tension perpendicular to the grain on the rear side** of the connection (Fig. 3.10d). Another **shear failure** was observed **on the front side** of the connection due to the introduction of the main shear force from the steel tube (Fig. 3.9b and 3.10c). This failure usually occurred in a cross-layer, where the shear strength is lowest (rolling shear).

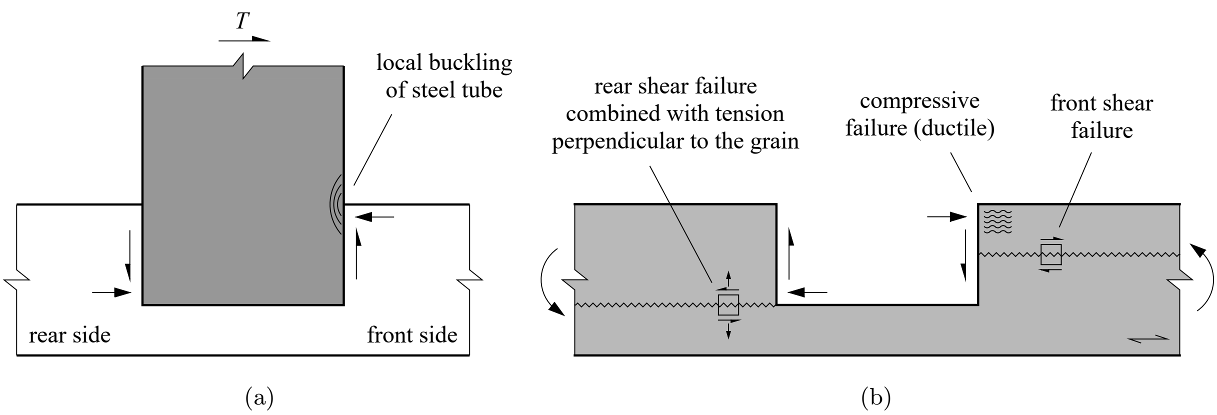

Fig. 3.9: Illustration of the forces acting in type 1 connections and observed failure mechanisms (a) in the steel tube and (b) in the timber part.

The typical force-displacement behaviour of test specimens with type 1 connections was linear at forces up to $0.3-0.5\,T_\mathrm{u}$, after some initial slip in case of a form-fitting connection without grouting. At this load level, inelastic compression deformations (and in some cases steel tube buckling) started occurring. These deformations increased gradually, leading to a pronounced nonlinear behaviour and eventually to a plateau in the force-displacement diagram. The above-described shear failures usually happened after reaching the maximum force, resulting in a force drop and limiting the deformation capacity of the connection. Tab. 3.4 lists the main results of all type 1 connection tests.

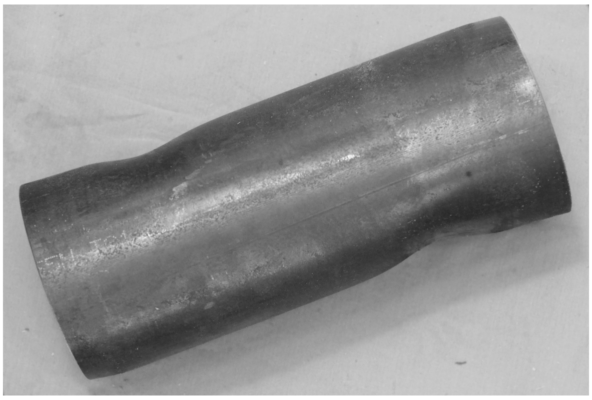

(a)

(b)

(c)

(d)

Fig. 3.10: Photos of observed failure mechanisms in push-out tests on type 1 connections: (a) local buckling of steel tube (specimen A-1-3), (b) timber compression deformation (A-1-1.2), (c) front shear failure (B-1-1.1) and (d) rear shear failure combined with tension perpendicular to the grain (B-1-3).

Form-fitting connection without grouting

Test series A focused on the investigation of a form-fitting type 1 connection without grouting. The main goal of this preliminary experimental campaign was to quantify the influence of several parameters on the stiffness, load-bearing capacity and ductility of the connection. The final

Tab. 3.4: Results of all type 1 connection tests.

Specimen name	Max. connection force and moment		Global stiffness 1st/2nd loading		Rotational stiffness 1st/2nd loading	
	T_u [kN]	M_u [kNm]	$k_{s,1}$ [kN/mm]	$k_{s,2}$ [kN/mm]	$k_{m,1}$ [kNm/rad]	$k_{m,2}$ [kNm/rad]
A-1-1.1	54.0	4.32	6.36	15.3	84.4	215
A-1-1.2	51.9	4.15	4.07	10.7	53.4	146
A-1-2.1	33.1	2.65	18.8	25.8	269	386
A-1-2.2	77.8	6.22	45.2	56.5	778	1’060
A-1-3	60.4	6.04	7.69	13.5	165	305
A-1-4	135	5.39	42.9	66.3	150	244
A-1-5	40.5 *	2.43*	10.8	28.0	80.5	223
A-1-6	45.8	4.58	3.84	9.37	79.4	204
A-1-7	33.3	2.66	4.32	10.7	58.0	154
A-1-8	18.1	1.45	2.41	9.19	32.4	142
A-1-9	49.5	3.96	7.05	22.6	92.8	317
A-1-10	33.9	2.71	3.05	13.1	39.7	181
B-1-1.1	95.0	7.60	62.0	68.2	956	1’070
B-1-1.2	100	8.02	67.0	70.0	1’050	1’110
B-1-1.3	92.6	7.40	76.3	75.4	1’230	1’220
B-1-2	75.4	7.54	31.2	36.5	720	864
B-1-3	71.1	5.69	32.4	44.9	506	767

* Premature shear failure due to insufficient quality of the timber block gluing. Specimen was reloaded to reach compressive failure in timber at $T_u = 77.5\,\mathrm{kN}$ / $M_u = 4.65\,\mathrm{kNm}$.

type 1 connection concept was chosen based on the results found in this test series and further investigated in test series B.

The influence of all studied connection parameters on both global force-displacement and local moment-rotation behaviour is shown qualitatively in Fig. 3.11. Specimens A-1-1.1 and A-1-1.2 correspond to the reference configuration and are therefore shown in all plots. Specimen A-1-1.2 had large differences in the production tolerance of the connections on the left and the right side of the specimen. This led to a significantly lower initial stiffness due to slip on one side (asymmetric loading). For better clarity in Fig. 3.11, the respective curve was shifted horizontally and the data before the unloading/reloading cycle are not plotted. The respective raw data are presented in [44].

Fig. 3.11a and 3.11b show the influence of the embedment depth a on both global force-displacement and local moment-rotation behaviour. Increasing the embedment depth by 50%

led to an approximately 40% higher M_u and doubled the rotational stiffness $k_{m,1}$. No significant influence on the ductility was observed.

The influence of the space between the members h_0 was investigated with a subset of five specimens. As expected, this parameter has a significant influence on the global force-displacement behaviour (Fig. 3.11c). Both stiffness and shear capacity increase with decreasing h_0. In specimen A-1-5, a premature shear failure occurred due to insufficient quality of the timber block gluing. The specimen was reloaded, reaching compressive failure in timber at $T_u = 77.5\,\text{kN}$, $M_u = 4.65\,\text{kNm}$ (not plotted in Fig. 3.11c and 3.11d).

Specimen A-1-4 was tested as a limit case of the connection system with $h_0 = 0$, allowing for a comparison with the values given in the *Avis Technique* describing the *Sylvabat* TCC system [9]. For a slightly smaller steel tube diameter of 70 mm and a significantly lower mean timber density of $\rho \approx 450\,\text{kg/m}^3$, the given stiffness value is $K_{ser} = 49.0\,\text{kN/mm}$ and the specified design shear capacity $R_d = 31.5\,\text{kN}$ (Tab. 2.2). The measured global stiffness of specimen A-1-4 is in a similar range ($k_{s,1} = 42.9\,\text{kN/mm}$, $k_{s,2} = 66.3\,\text{kN/mm}$). In terms of shear capacity, a comparison is difficult as the value given in [9] is a design value. It is, however, to be expected that the shear capacity of the connection tested in this study (135 kN) is higher than the experimental mean value determined for [9], due to the superior mechanical properties of beech LVL. Compared to all other specimens, almost no ductility was observed in specimen A-1-4, due to brittle shear failure in timber.

Fig. 3.11d and 3.12a show that the chosen mechanical model with rotational springs is able to decouple the influence of the parameter h_0 appropriately, as all specimens show similar rotational stiffness k_m, maximum moment M_u and ductility. For the sake of completeness, the moment-rotation behaviour of specimen A-1-4 ($h_0 = 0$) was also plotted. However, the model does not make much sense in this case, because the choice of the spring location (Fig. 3.8b) has a substantial influence on the result if h_0 is small. This is confirmed by the significant difference compared to the other specimens (Fig. 3.11d).

Fig. 3.11e and 3.11f show the results of six specimens with different steel tubes. The influence of the steel tube diameter on k_m and M_u is shown in Fig. 3.12b. While the stiffness increases continuously with larger steel tube diameters, the moment capacity could not be increased for $D > 80\,\text{mm}$. Increasing D with constant t reduces the resistance to local buckling. In contrast to the reference configuration, the steel tube in specimen A-1-9 ($D = 101.6\,\text{mm}$) buckled, which explains the lower moment capacity. In specimen A-1-8 with a lower wall thickness $t = 2\,\text{mm}$, strong local buckling was observed (Fig. 3.13a), which significantly reduced its load-bearing capacity and stiffness. The potential use of quadratic RRW profiles instead of round ROR profiles was investigated in specimen A-1-10. The results show that the connection behaviour is less advantageous in this case because of stress concentrations in the corners of the timber cutout (Fig. 3.13b) and early local buckling on the flat side of the steel profile. In addition, the connection behaviour of quadratic profiles is expected to depend substantially on the shear force direction, which is an important factor to be considered in two-way spanning slabs, as discussed by Loebus & Winter [50]. In contrast, the directional dependency in connections with point-symmetric profiles such as ROR is a function only of the veneer layout in the LVL plate.

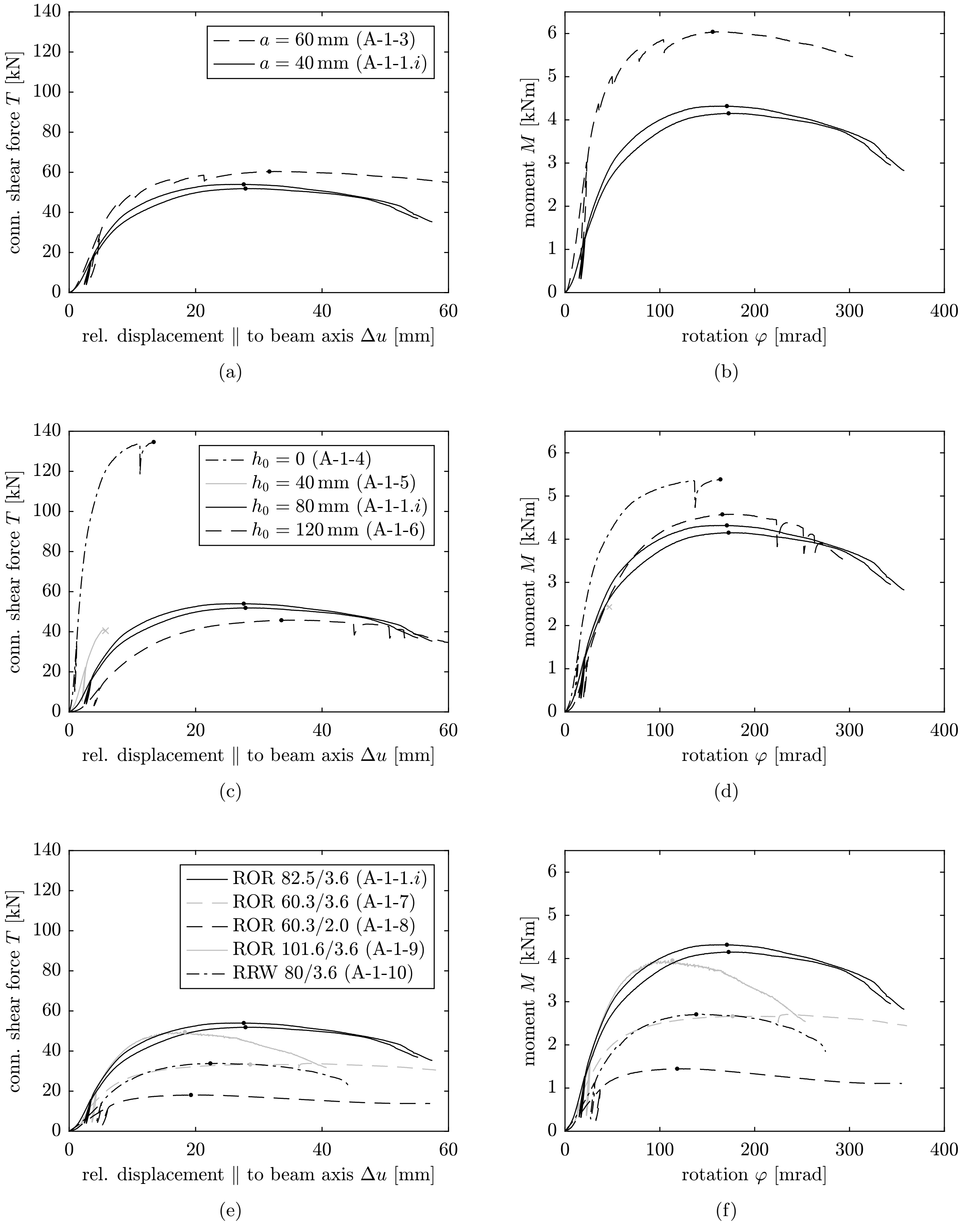

Fig. 3.11: Force-displacement and moment-rotation behaviour of type 1 connections without grouting: influence of (a) & (b) embedment depth, (c) & (d) space between the members and (e) & (f) different steel tubes.

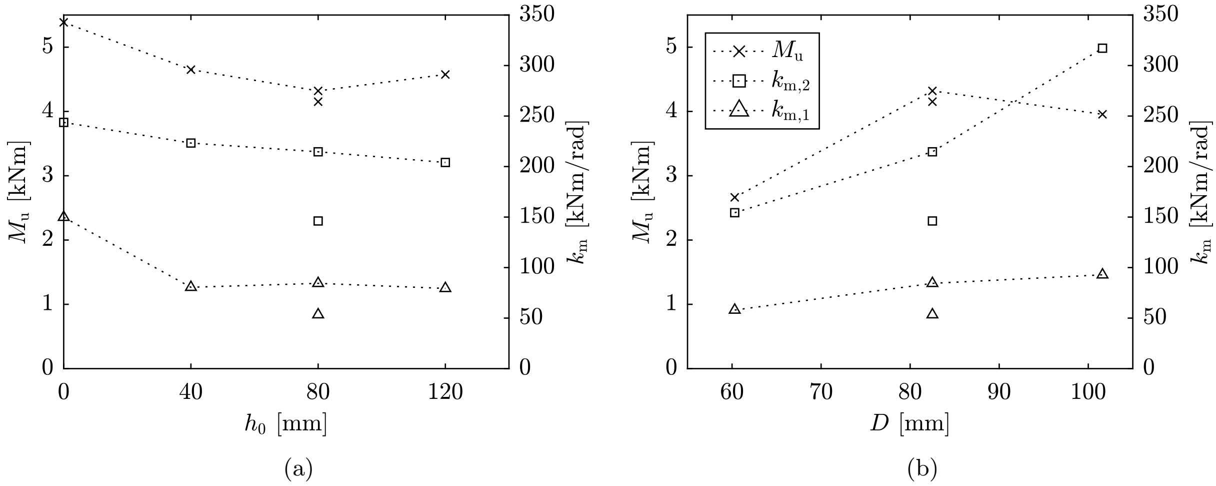

Fig. 3.12: Influence of (a) space between the members h_0 and (b) steel tube diameter D ($t = 3.6$ mm) on moment capacity and rotational stiffness. The data points that are off the trend line correspond to specimen A-1-1.2 where tolerance differences led to asymmetric loading and a significantly lower stiffness.

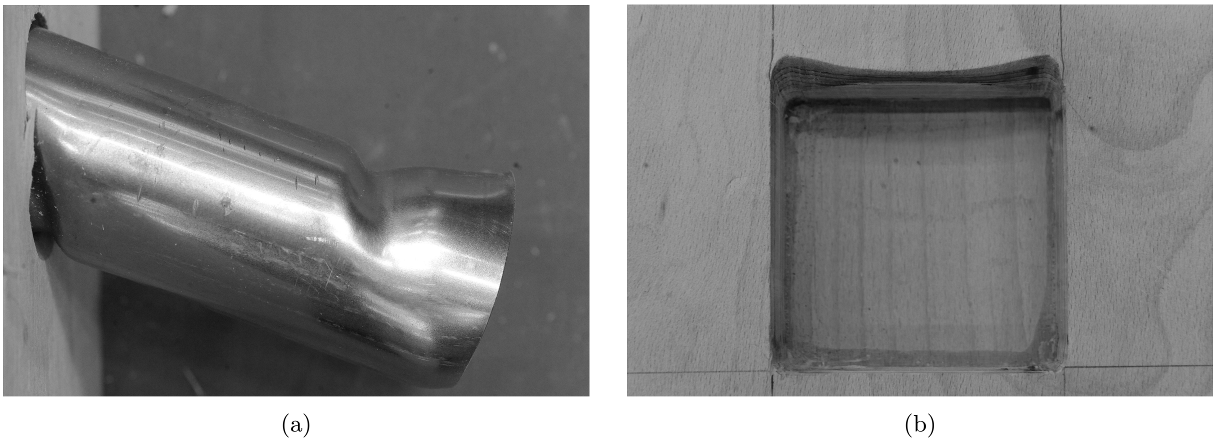

Fig. 3.13: (a) Strong buckling in specimen A-1-8 with reduced steel tube wall thickness and (b) stress concentrations in specimen A-1-10 with RRW steel profiles.

Comparison of grouting systems

In addition to investigating the influence of the geometric parameters discussed above, an important goal of test series A was to compare the form-fitting connection concept with the alternative of milling a larger cutout in the timber part and then filling the gap with a grouting system. Two different grout types were tested. Fig. 3.14 and Tab. 3.4 show the pronounced influence of grouting on the connection behaviour. The initial slip deformations, typical in form-fitting connections, are effectively eliminated with both of the two grouting systems. This is an important aspect, because initial slip deformations caused by production tolerances are difficult to quantify and control. As seen in specimen A-1-1.2, these deformations can also affect the effective connection stiffness. In addition to this improvement, significant adhesion between the grouting and the timber surface was achieved in the case of Sikadur®-42 HE. This was well visible after dismantling the specimen, which took a considerable effort and led to a timber tensile failure rather than adhesion failure of the grouting (Fig. 3.14d). This adhesion led to a substantial stiffness increase, with $k_{\mathrm{m},1}$ almost ten times higher and $k_{\mathrm{m},2}$ five times higher than in specimen A-1-1.1 without grouting. In addition, the load-bearing capacity was increased by 40%.

The grouting system Sikadur®-Pronto 12 allowed for a considerable increase in stiffness as well, but to a much lesser degree than in the case of Sikadur®-42 HE. The reason for this is that no significant adhesion with the timber part was achieved with this grouting system. Its main effect in the connection was the elimination of initial slip and an increase of the effective steel tube diameter compared to the form-fitting design. This was visible during the experiment when the entire grouting block was rotated out of the timber cutout together with the steel tube (Fig. 3.14c). In addition, a compressive failure was observed in the grouting layer, resulting in a load-bearing capacity 40% lower than in the corresponding form-fitting connection.

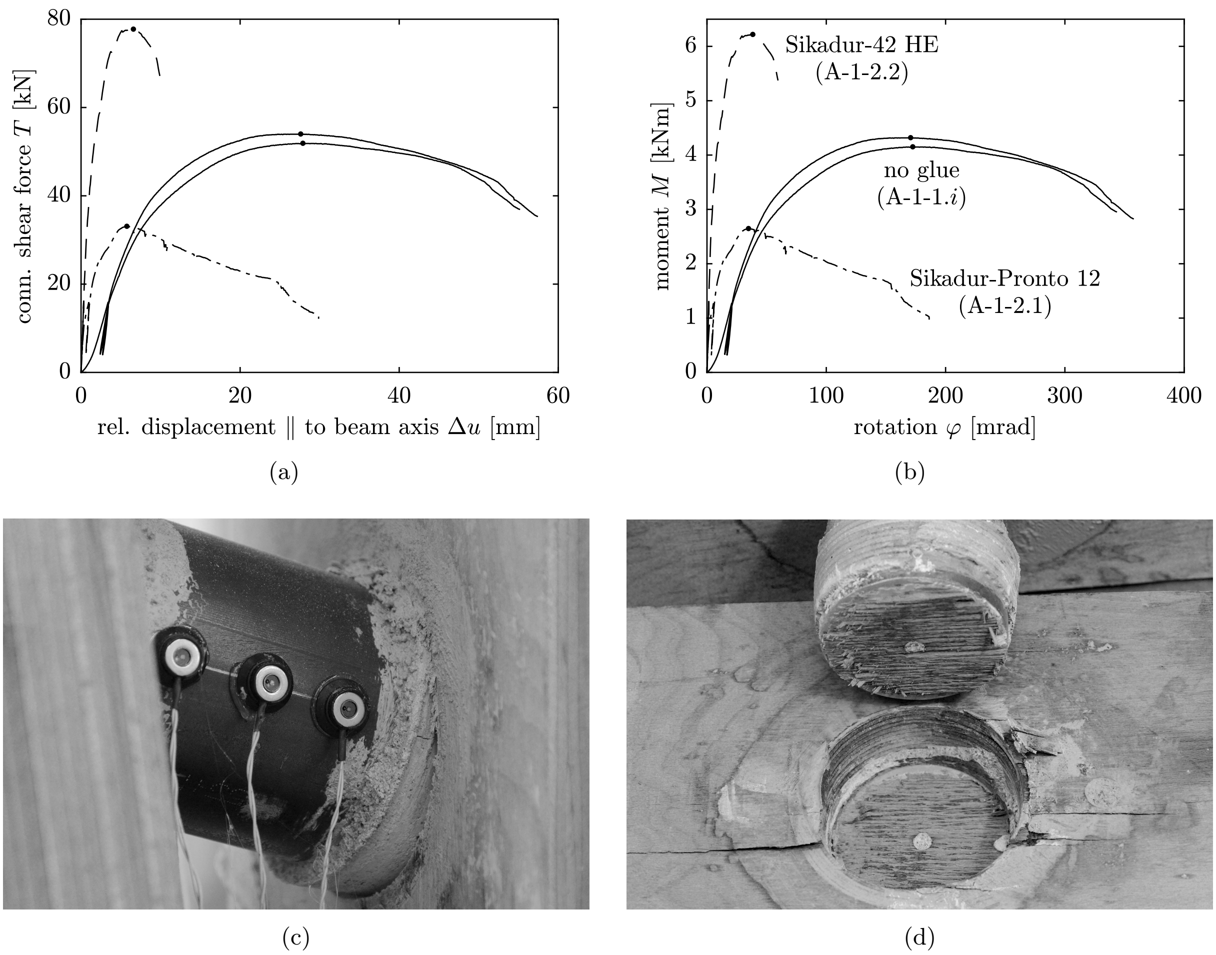

Fig. 3.14: Comparison of different grouting systems tested in series A: (a) force-displacement and (b) moment-rotation behaviour, (c) adhesion failure and compressive failure in the grouting of specimen A-1-2.1 and (d) timber tensile failure perpendicular to the grain after dismantling specimen A-1-2.2.

Final connection with grouting

Based on the findings in test series A, the final type 1 connection concept was defined as described in Chapter 1.3, using the Sikadur®-42 HE grouting system. The main reason for this decision was the high stiffness. In a TCC system with steel tube connection and direct contact between timber and concrete, such as in the *Sylvabat* system [9], grouting would not lead to an economical solution because the connection is already very stiff. In the TCC concept investigated in the scope of this thesis, however, the additional stiffness provided by the grouting system is extremely valuable because it allows for an efficient composite action despite the presence of a light-weight interlayer between timber and concrete.

A set of 5 specimens was tested, using the same material (60 mm thick beech LVL plates without block gluing close to the connections) and production process (Fig. 3.3a) as in a real structure. Fig. 3.15 shows the resulting force-displacement and moment-rotation behaviour of the tested specimens. The obtained stiffness values and load-bearing capacities are listed in Tab. 3.4. The three reference configuration specimens showed a consistent behaviour, with all values of M_u and k_m within ±5% and ±15% of the respective mean value. In all three tests, inelastic deformations were observed before shear failures occurred on the rear and/or front side of the connection (Fig. 3.9). These brittle shear failures led to force drops and, from a more global perspective, a linear softening post-peak behaviour (Fig. 3.15). Compared to a form-fitting connection without grouting, the deformation capacity was considerably lower. In specimen B-1-1.2, a post-peak unloading/reloading cycle was performed, showing that the remaining elastic stiffness in this damaged stage was around a third of the initial stiffness.

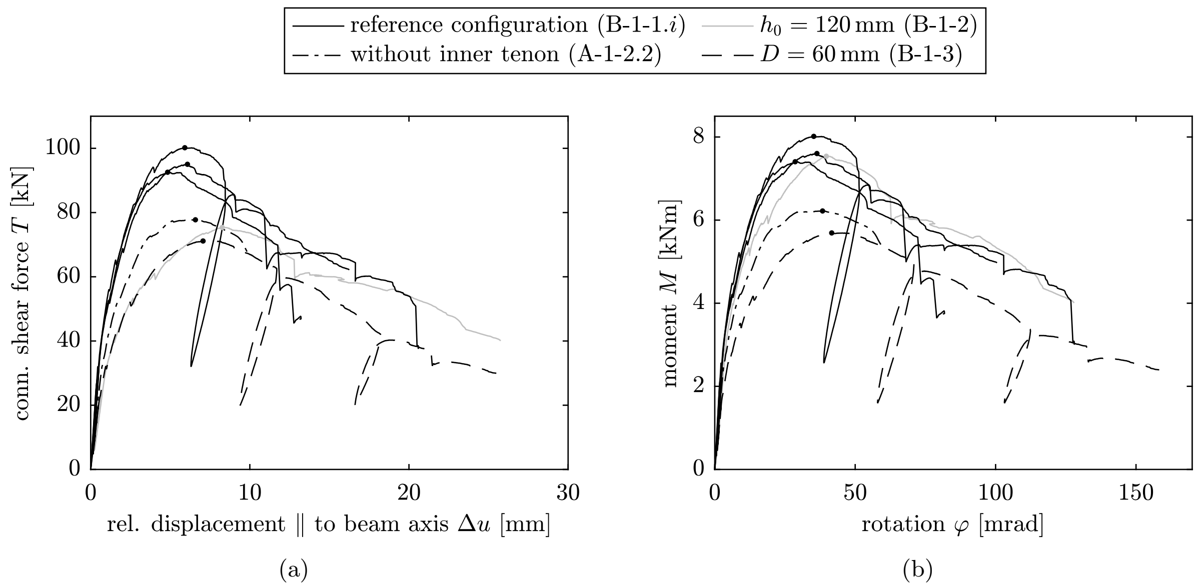

Fig. 3.15: (a) Force-displacement and (a) moment-rotation behaviour of connection type 1 with grouting.

In addition to the 5 specimens from test series B, specimen A-1-2.2 is plotted as well in Fig. 3.15. The different production procedure of the connection with a full cavity (Fig. 3.3b) led to a stiffness reduction of 25% in this case. The moment capacity was also lower (−20%), which can be explained with the shear failure occurring in the block gluing close to the base of the connection. The influence of the distance between the members h_0 and the steel tube diameter D was assessed with specimens B-1-2 and B-1-3. In both cases, a similar influence as in the specimens without grouting was observed.

3.3.3 Connection type 2: steel tube penetrating upper beech LVL beam

Connection type 2 is used only in case of a production process with cast-in-situ concrete. Given its main purpose is to reduce the deflections of the formwork elements during concrete casting, achieving a high stiffness is the primary goal in this connection type. Two specimens with form-fitting connections (as described in Chapter 1.3) were tested, with steel tube diameters of 80 mm (B-2-5) and 60 mm (B-2-6). As a comparison, one specimen was fabricated with grouted connections (B-2-4) and $D = 80$ mm. Fig. 3.16 shows the observed load-displacement and moment-rotation behaviour and Tab. 3.5 lists the main results.

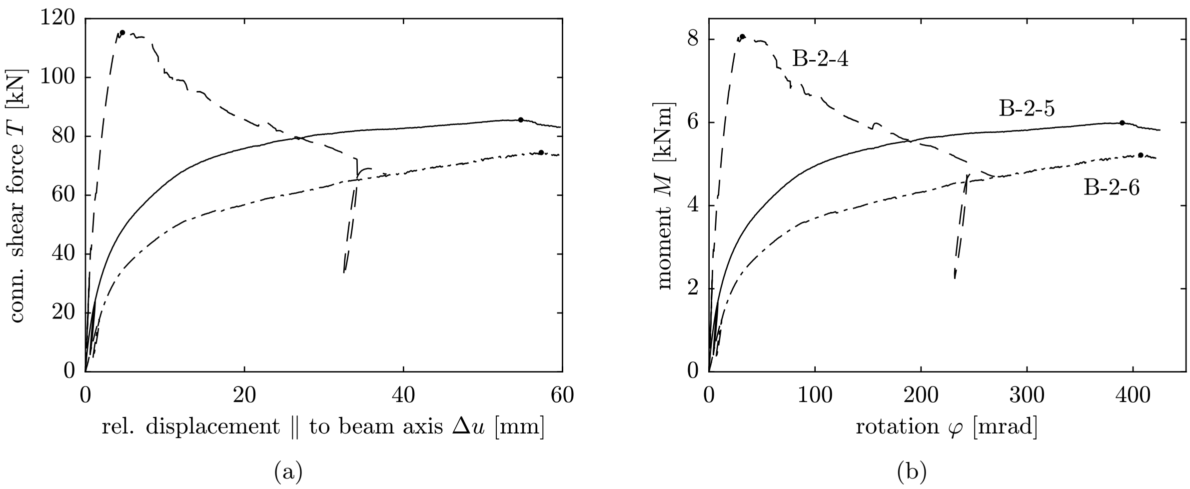

Fig. 3.16: (a) Force-displacement and (b) moment-rotation behaviour of connection type 2.

Tab. 3.5: Results of type 2 connection tests.

Specimen name	Max. connection force and moment		Global stiffness 1st/2nd loading		Rotational stiffness 1st/2nd loading	
	T_u [kN]	M_u [kNm]	$k_{s,1}$ [kN/mm]	$k_{s,2}$ [kN/mm]	$k_{m,1}$ [kNm/rad]	$k_{m,2}$ [kNm/rad]
B-2-4	115	8.07	53.5	70.2	592	809
B-2-5	85.6	5.99	13.1	27.9	132	290
B-2-6	74.5	5.21	8.08	15.9	81.9	167

Similar as in type 1 connections, grouting has a pronounced influence on the load-bearing behaviour. Initial slip is eliminated and adhesion leads to a rotational stiffness about 5 times as high as in the corresponding specimen without grouting. Nevertheless, grouted type 2 connections are not expected to be an economical solution because of their higher cost and time consumption in the production process.

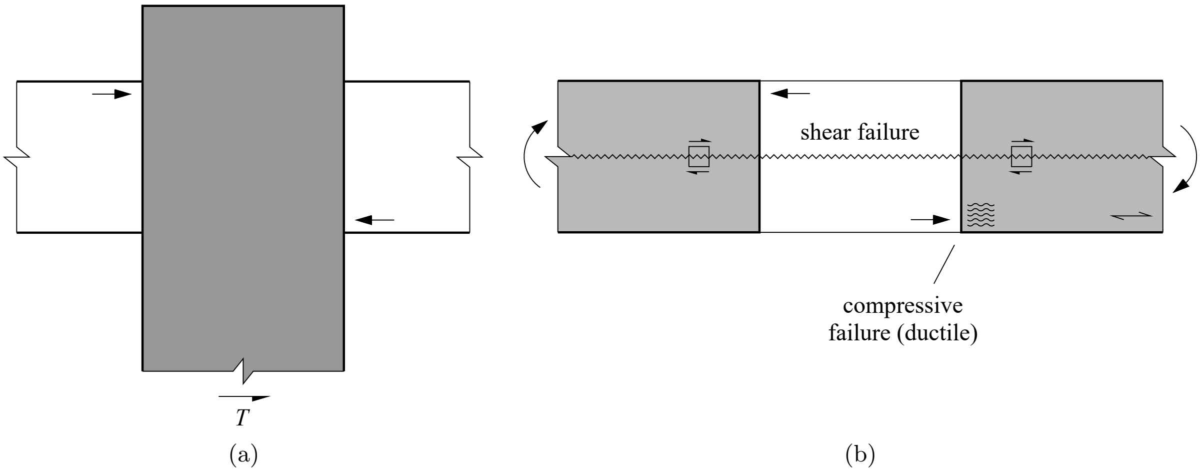

Fig. 3.17: Illustration of the forces acting in type 2 connections and observed failure mechanisms (a) in the steel tube and (b) in the timber part.

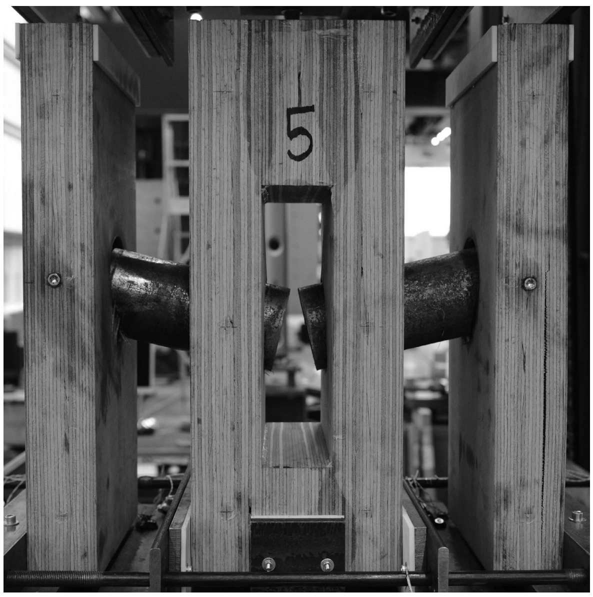

Fig. 3.18: Shear failure in the right timber member (specimen B-2-5).

The two specimens with form-fitting connections showed a very ductile behaviour due to compression deformation in the timber. A shear failure occurred only after large deformations (Fig. 3.17 and 3.18). Compared to a type 1 connection with the same steel tube diameter and embedment depth (A-1-3), specimen B-2-5 shows a 20% lower stiffness. While in type 1 connections the steel tube ends in a ring-shaped cutout, in type 2 connections it penetrates the timber member entirely. In the former case, this leads to higher embedment stiffness close to the steel tube base, which explains this difference in the test results. The influence of the steel tube diameter was similar as observed already in type 1 connections.

3.3.4 Connection type 3: steel tube in concrete

Structural behaviour and observed failure mechanisms

In all type 3 connection specimens, a ductile failure mode was observed. The following chapter describes the observed structural behaviour and explains the load-bearing mechanisms.

The used test setup with horizontal supports both at the lower and upper end of the side members is statically indeterminate (Fig. 3.8). Equilibrium is achieved with or without a compressive normal force in the steel tube H, leading to different horizontal support reactions H_S and $H_\mathrm{S} - H$ and different bending moments in the side member. Fig. 3.20a shows the forces acting on the right side member of a push-out specimen, rotated by 90° counter-clockwise, and the bending moments for the two limit cases $H = 0$ and $H = H_\mathrm{S}$. Because of the symmetry of the test setup, the middle member of the push-out specimen is not exposed to any significant bending moments. The boundary conditions in the side members are similar to the situation in a bending beam in the left half of a simple span setup, as shown in Fig. 3.20d. Therefore, the observations and analyses in this chapter generally focus on the side members of the push-out specimens.

Fig. 3.19 gives an overview on the observed crack propagation in the concrete side members. The first crack occurred when the tensile stresses reached the concrete tensile strength in the location where the maximum bending moment is expected for $0 < H < H_\mathrm{S}$ (Fig. 3.20a). After this, the observed stiffness decreased, leading to an almost horizontal plateau in the force-displacement diagram (Fig. 3.21). During this phase, additional cracks developed perpendicular to the initial crack, as shown in Fig. 3.19b and 3.19e. Eventually, a compressive failure in concrete occurred, which led to a substantial force-drop, limiting the connection deformation capacity and denoting the end of the experiment (Fig. 3.19c and 3.19f).

After the first crack forms, the reinforcement bars (placed centrally in the concrete member), have to take over the tensile force that was carried by concrete tensile stresses before cracking. In order to explain the structural behaviour of the connection in cracked reinforced concrete, several truss models have been developed. Fig. 3.20b shows a theoretical truss model, assuming $H = 0$. The introduction of the bending moment from the steel tube is idealised with two point forces ζT and $(\zeta - 1)T$, where ζ is a factor depending on:

- the embedment depth a, defining the lever arm between the two point forces
- the distance between the members h_0, defining the ratio of the shear force T and bending moment M that have to be transmitted in the connection

The models show both the geometry of the compression and tension struts as well as the graphical force equilibrium of each node, illustrating the magnitude of all forces in relation to the connection shear force T.

The theoretical truss model shown in Fig. 3.20b is not compatible with the observations made during the experiment, because one of the compression struts is oriented perpendicular to the crack shown in Fig. 3.19a and 3.19d. Furthermore, relatively large vertical tensile stresses in concrete are needed to achieve equilibrium. Redirecting the mentioned compression strut in the truss model to avoid the cracked area would increase the vertical tensile force even more. This tensile force explains the second crack that forms in the concrete side member (Fig. 3.19b and 3.19e).

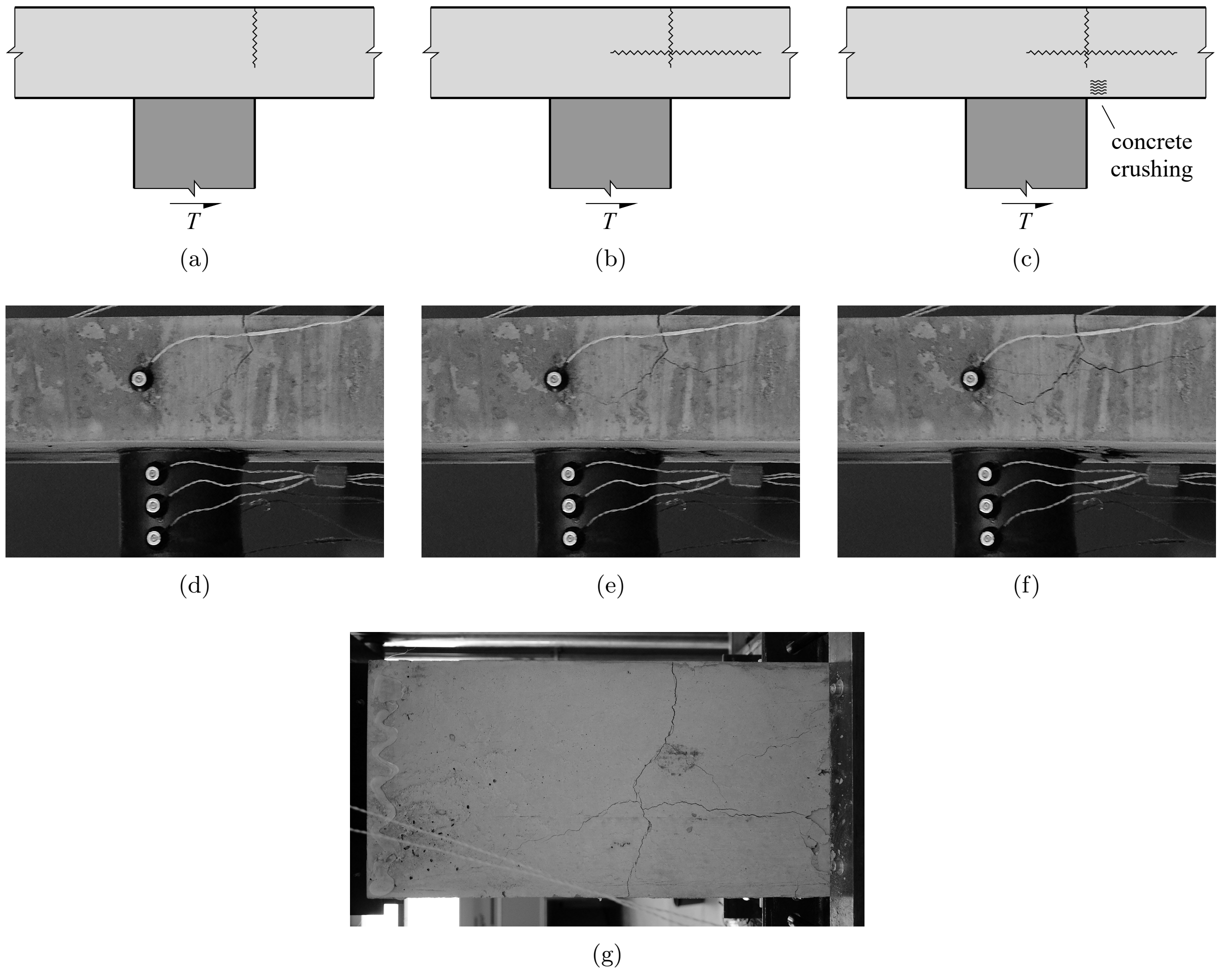

Fig. 3.19: Typical observed crack propagation and failure in concrete side member, schematic and photos of right side member rotated by 90° counter-clockwise: (a) & (d) cracks due to tensile stresses from bending moment, (b) & (e) additional cracks due to transversal tensile stresses, (c) & (f) concrete crushing and (g) longitudinal crack due to splitting tensile stresses.

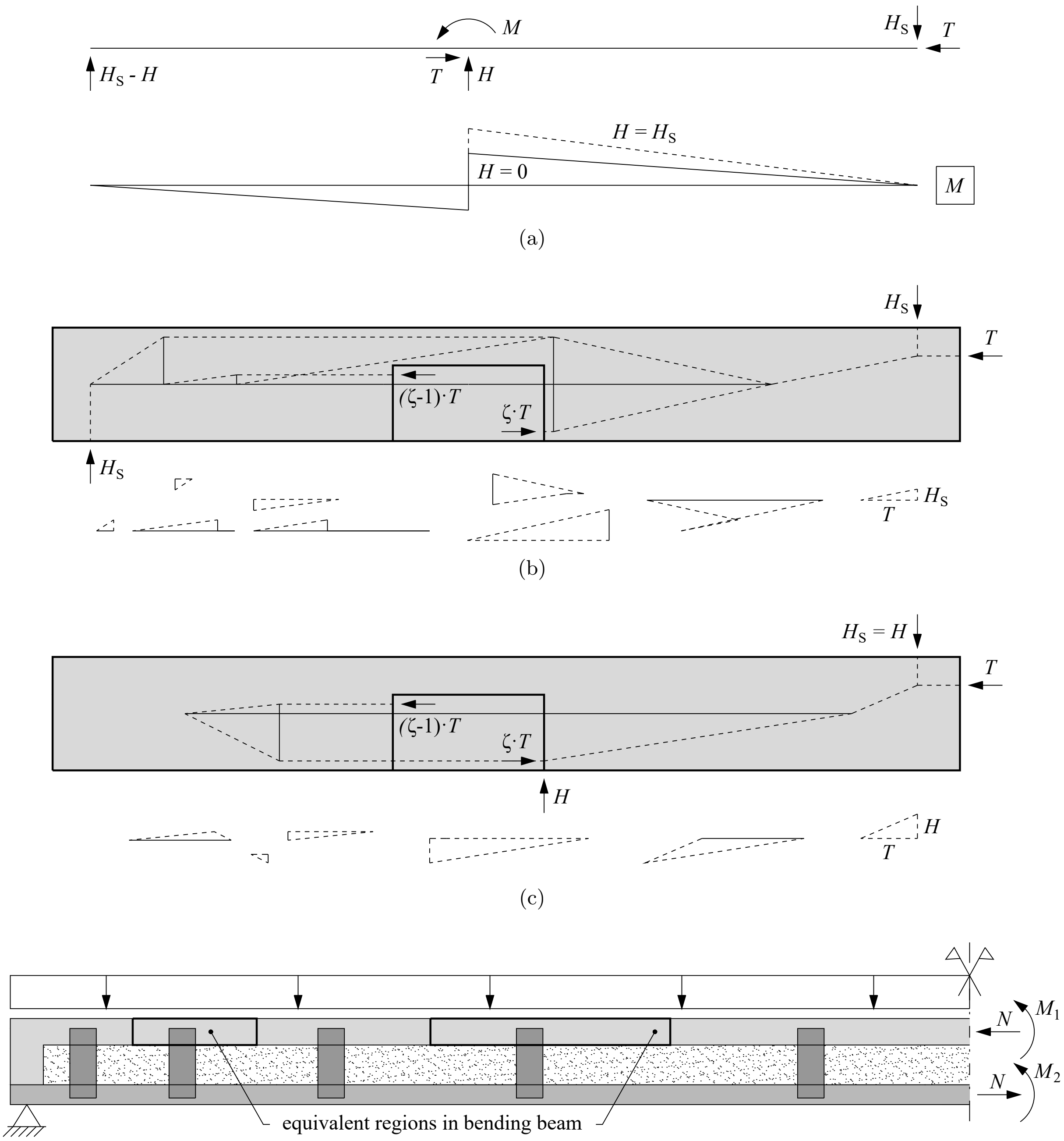

Fig. 3.20: Illustration of the compressive (- - -) and tensile (—) forces acting in the side member of a type 3 connection specimen: (a) beam model representing the uncracked state, (b) theoretical truss model explaining the cracked state if $H = 0$ is assumed, (c) truss model representing the cracked state, for $H = H_S$, with the typology and graphical force equilibrium of all nodes, (d) equivalent situation in a bending beam.

A new equilibrium state without compression struts in the cracked area can only be found for $H \neq 0$. Fig. 3.20c shows a possible truss model for the limit case $H = H_S$. In the perspective of Fig. 3.20, the main longitudinal reinforcement bars are placed in front and behind the steel tube (visible in Fig. 3.3). Therefore, the forces ζT and $(\zeta - 1)T$ from the steel tube have to be redirected outwards, to reach the plane of the reinforcement bars, which is not visible in the perspective of Fig. 3.20. The resulting transversal tensile forces led to a longitudinal crack in the side members shown in Fig. 3.19g. After cracking, the respective tensile forces are taken over by the transversal reinforcement bars.

When the longitudinal reinforcement reaches its yielding force, the connection starts exhibiting plastic deformations. The deformation capacity is limited by a concrete compressive failure. The graphical force equilibrium of the respective node confirms that the largest concrete compressive force is indeed in the location where the respective failure was observed.

The magnitude of the steel tube normal force H is unknown in the push-out test and also in a full scale bending beam, because the system is always statically indeterminate. In the equivalent area in a bending beam (Fig. 3.20d), the support force H_S in the push-out test corresponds to the shear force in the concrete member. Arriving at the steel tube, this shear force can either remain in the concrete member, or it can be transferred to the timber beam below. This distribution of the shear force is difficult to estimate as it depends on the current stiffness of the connection and can change with increasing load. The crack patterns observed in the push-out tests, combined with the discussed truss models allow for a qualitative assessment of this behaviour. It can be assumed that at low loads, a large part of the shear force remains in the concrete member. Once cracks start to occur, the stiffness of the concrete beam decreases and a substantial part of the shear force is transmitted through the steel tube, leading to a new equilibrium as shown in Fig. 3.20c.

Influence of the studied connection parameters

Fig. 3.21 shows the force-displacement and moment-rotation behaviour and Tab. 3.6 lists the main results of all type 3 connection tests. The graphs in Fig. 3.21 are divided into two subsets, showing qualitatively the influence of the investigated connection parameters.

The influence of the embedment depth a was investigated with a subset of six specimens. Fig. 3.21a and 3.21b show that both the global stiffness and shear capacity as well as the rotational stiffness and moment capacity consistently increase with a larger embedment depth a. In Fig. 3.22 the main test results of the same subset of specimens are plotted as a function of a, confirming this influence quantitatively. It is clearly visible that the influence of the embedment depth a on the reloading stiffness $k_{\mathrm{m},2}$ is more pronounced than on the first loading stiffness $k_{\mathrm{m},1}$. This aspect will be discussed in the following Chapter 3.3.5. Looking at the truss model explaining the structural behaviour of the steel tube connection in cracked reinforced concrete (Fig. 3.20c), this observed influence of the embedment depth a makes sense. Increasing a leads to a larger lever arm between the point forces that are introduced in the connection, reducing the magnitude of these forces for constant T and M.

Tab. 3.6: Results of type 3 connection tests.

Specimen name	Max. connection force and moment		Global stiffness $1^{st}/2^{nd}$ loading		Rotational stiffness $1^{st}/2^{nd}$ loading	
	T_u [kN]	M_u [kNm]	$k_{s,1}$ [kN/mm]	$k_{s,2}$ [kN/mm]	$k_{m,1}$ [kNm/rad]	$k_{m,2}$ [kNm/rad]
C-3-1.1	52.3	4.18	56.7	138	906	3'440
C-3-1.2	56.1	4.49	58.1	180	935	6'250
C-3-1.3	55.8	4.47	56.7	143	907	3'710
C-3-2	42.7	2.99	54.0	107	621	1'480
C-3-3	60.2	5.42	63.5	164	1'440	9'900
C-3-4	62.8	6.28	87.9	144	3'460	15'000
C-3-5	40.0	4.00	40.9	87.4	1'060	3'420
C-3-6	29.8	2.38	27.7	62.8	482	2'010

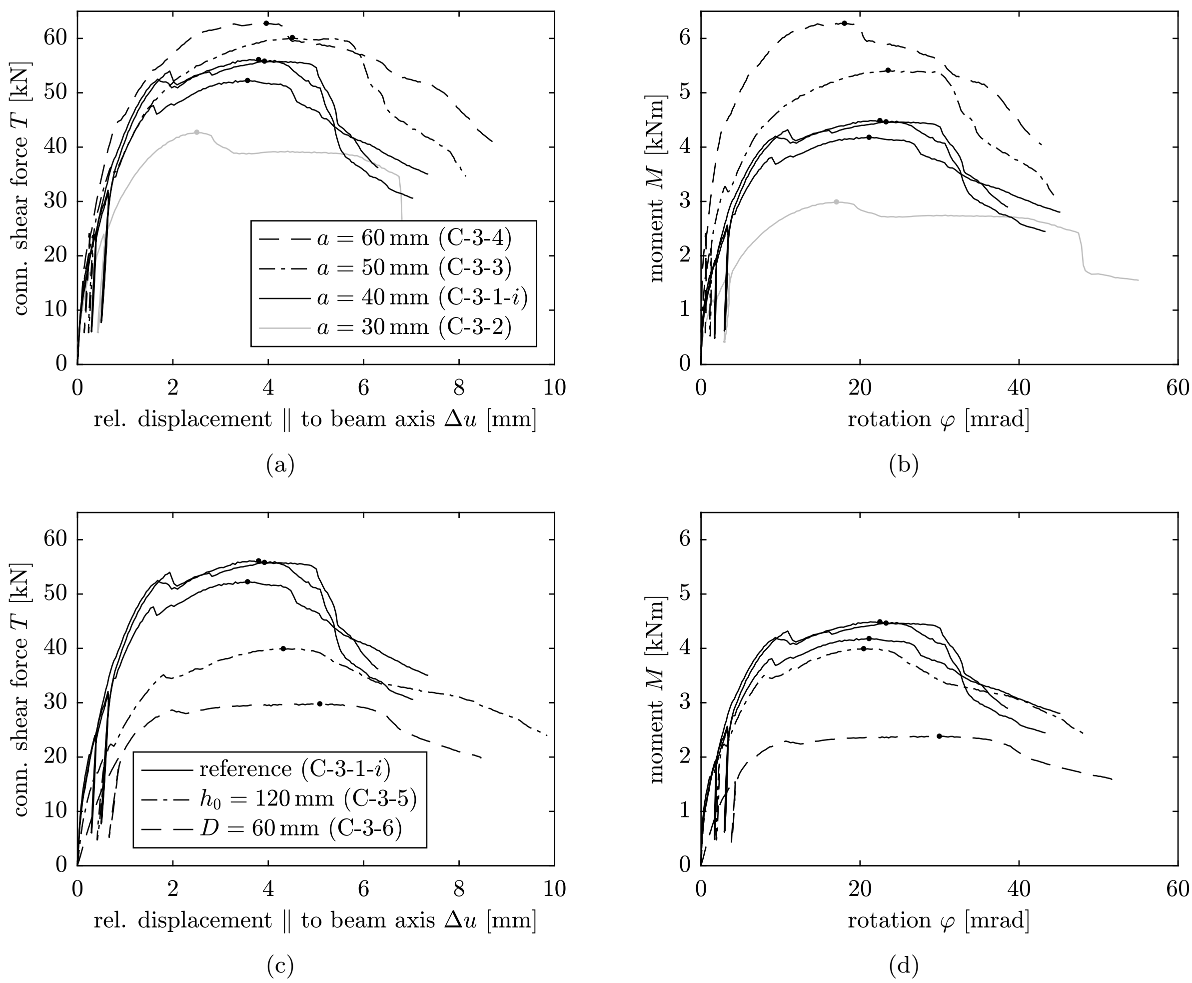

Fig. 3.21: Force-displacement and moment-rotation behaviour of connection type 3: Influence of (a) & (b) embedment depth and (c) & (d) space between the members and steel tube diameter.

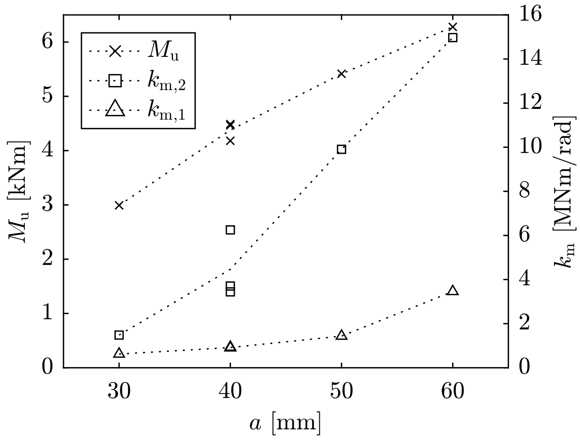

Fig. 3.22: Influence of embedment depth a on the moment capacity and the rotational stiffness.

The influence of the steel tube diameter D and the distance between the concrete members h_0 was investigated with one specimen each. The results are shown qualitatively in Fig. 3.21c and 3.21d. Reducing D to 60 mm led to a reduction of rotational stiffness and moment capacity of around 50%, which is in a similar range as the respective reduction observed in type 1 connections. The specimen with increased $h_0 = 120$ mm showed significantly lower global stiffness and shear capacity, while rotational stiffness and moment capacity remained similar as in the reference specimens. This confirms that the chosen mechanical model with rotational springs is able to decouple the influence of the parameter h_0 appropriately, as already observed in the investigations on type 1 connections.

While the material tests on the used concrete showed a normal compressive strength, the measured MOE of 9'800 MPa was very low, which was most likely due to poor concrete mixing. This was observed both during the production of the specimens (liquid and inhomogeneous fresh concrete) and during the tests (most of the aggregates were at the bottom of the specimens). It is to be expected that the connection stiffness would be higher if a standard concrete with an MOE according to the specifications was used. However, further experimental campaigns are needed to quantify this influence. The connection shear capacity is not expected to be significantly affected by the low MOE.

3.3.5 Difference between first loading and reloading stiffness

In all connection shear tests, an unloading/reloading cycle was performed after reaching approximately 40% of the expected shear capacity. While in some specimens the observed stiffness during reloading was substantially higher than during first loading, other specimens showed no significant difference in stiffness. In this chapter, these differences and their relevance in the assessment of the structural behaviour of TCC slabs with steel tube connection are discussed.

Tab. 3.7 lists the ratio $k_{m,2}/k_{m,1}$ for the different connection types investigated in this experimental campaign. The results show that in type 1 and 2 connections with grouting, the stiffness increase caused by pre-loading was relatively small. In contrast, type 1 and 2 connec-

Tab. 3.7: Ratio of rotational stiffness during first loading and reloading.

Connection type	n	$k_{m,2}/k_{m,1}$		
		min	mean	max
Type 1 with grouting	7	0.99	1.24	1.52
Type 2 with grouting	1	–	1.37	–
Type 1 without grouting	10	1.63	2.91	4.56
Type 2 without grouting	2	2.04	2.12	2.20
Type 3	8	2.38	4.45	6.88

tions without grouting as well as type 3 connections exhibited a substantial stiffness increase. This is also well visible in the moment-rotation plots shown in Fig. 3.23.

The large stiffness increase after pre-loading in type 1 connections without grouting may be explained with the production tolerance leading to a small gap between the steel tube and the timber (Fig. 3.24a). When the connection is loaded, some initial rotation is needed for the steel tube to reach the horizontal contact points at the edge of the timber cutout (Fig. 3.24b), which is the reason for the low initial stiffness in Fig. 3.23a for $\varphi < 10\,\mathrm{mrad}$. Assuming the steel tube to be rigid, the contact area in the situation illustrated in Fig. 3.24b is infinitely small. Additional rotation leads to compression deformation in timber and, as a consequence, to an expansion of the contact height as illustrated in Fig. 3.24c and 3.24d. Because a part of the compression deformation in timber is inelastic, this contact height is primarily a function of the maximum force T that the connection has been exposed to. In other words, the contact height is not significantly reduced during the unloading and reloading cycle, which explains the higher stiffness in that phase. In Fig. 3.24, the tolerance is chosen much larger than it would be in a real connection, for illustrative purposes. As a consequence, the rotations are exaggerated, leading to a large vertical displacement of the left base corner of the steel tube in Fig. 3.24d and a significant reduction of the lever arm between the two point forces. While this happens

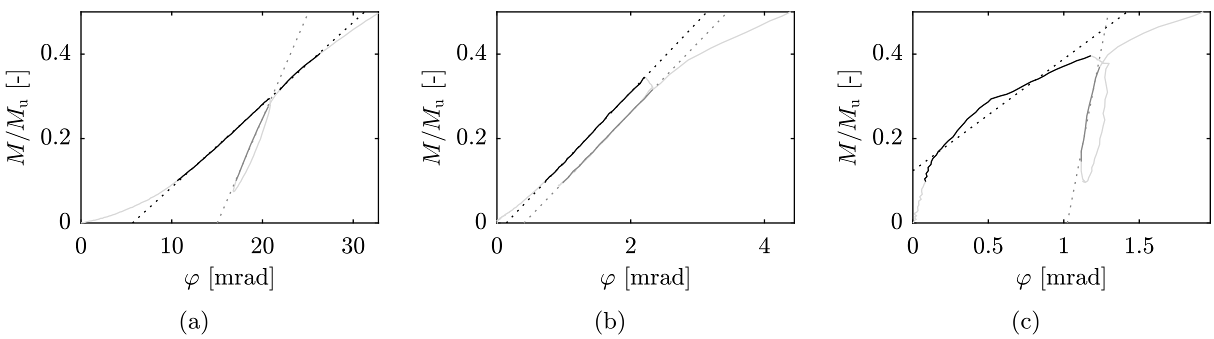

Fig. 3.23: Typical moment-rotation behaviour in the range $M < 0.5 \cdot M_u$, linear regression with considered data range for $k_{m,1}$ and $k_{m,2}$ plotted in black and dark grey, respectively, (a) type 1 without grouting (A-1-1.1), (b) type 1 with grouting (B-1-1.3), (c) type 3 (C-3-3).

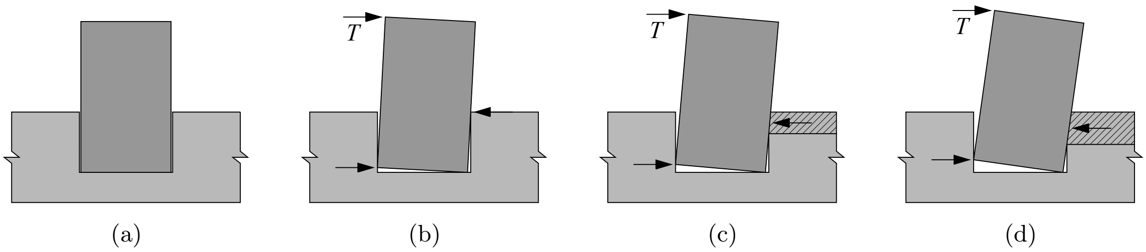

Fig. 3.24: Influence of production tolerance on the behaviour of type 1 connections: (a) situation before loading, (b) deformation needed for contact of the steel tube with the timber, (c) & (d) expansion of activated contact height in the timber depending on the current maximum shear force T_{max}.

also in a connection with realistic tolerance (or even no tolerance), the effect is much smaller, especially under service loads.

The same explanation for the stiffness differences is valid also for type 2 connections without grouting. In grouted connections (both type 1 and 2), the gap between the steel tube and timber is filled. Therefore, the mechanism described in Fig. 3.24 does not apply to these connections, explaining why pre-loading has no significant effect on the connection stiffness (Fig. 3.23b). In the case of type 3 connections, it can be assumed that small cracks develop around the steel tube as a consequence of concrete shrinkage, which leads to a similar situation as in type 1 connections without grouting.

The above-described influence of pre-loading on the connection stiffness is relevant especially in the assessment of the dynamic behaviour of the presented TCC structure. For the estimation of deformations (SLS) and load-bearing capacity (ULS), the assumed connection behaviour should be based on the first loading curve (Fig. 3.25), because in these cases, the absolute connection deformation is relevant. In dynamic calculations, a small cyclic load is considered that typically does not lead to a new maximum force in the connection (Fig. 3.25). Therefore, the reloading stiffness applies in these cases, describing the relative connection deformation during the load cycles.

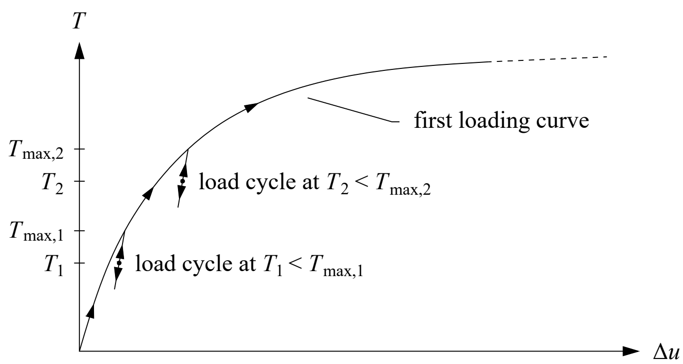

Fig. 3.25: Influence of the current maximum shear force T_{max} on the connection behaviour.

3.3.6 Displacements in the direction of the steel tube axis

In most connection shear tests, displacements in the direction of the steel tube axis Δw were observed. In the test setup (Fig. 3.5), Δw manifested as a horizontal displacement of the mid-point of the side members, oriented towards the outside. This displacement can be explained by the fact that the used steel tubes are not slender enough to be idealised as beams with no width. Rotating the tube around one of its base corners (Fig. 3.26) leads to the following displacements:

$$\Delta u = D \cdot (1 - \cos\varphi) + l_{\mathrm{T}} \cdot \sin\varphi \tag{3.4}$$

$$\Delta w = D \cdot \sin\varphi + l_{\mathrm{T}} \cdot (\cos\varphi - 1) \tag{3.5}$$

The initial slope of the displacement path (Fig. 3.26) is:

$$(\Delta w/\Delta u)_0 = \lim_{\varphi \to 0} \frac{D \cdot \sin\varphi + l_{\mathrm{T}} \cdot (\cos\varphi - 1)}{D \cdot (1 - \cos\varphi) + l_{\mathrm{T}} \cdot \sin\varphi} = \cdots = D/l_{\mathrm{T}} \tag{3.6}$$

The maximum displacement perpendicular to the beam axis is reached when $\Delta u = D$:

$$\Delta w_{\max} = \sqrt{D^2 + l_{\mathrm{T}}^2} - l_{\mathrm{T}} \tag{3.7}$$

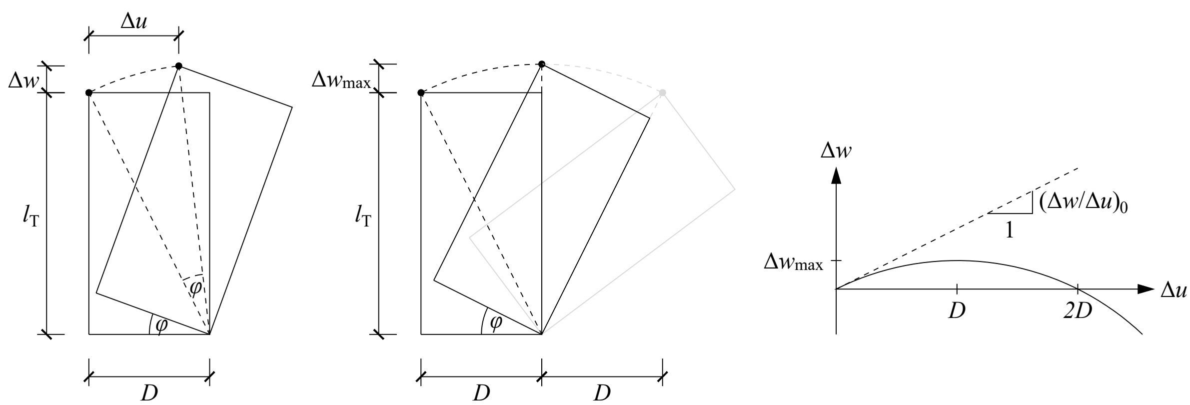

Fig. 3.26: Geometry of the steel tube rotation and parameters of the displacement path.

The displacement Δw reaches 0 again at $\Delta u = 2D$. Fig. 3.27 shows a parametric study of the displacement path for different steel tube dimensions. As shown already in Eq. 3.6 and 3.7, the displacements perpendicular to the beam axis become relevant especially for short steel tubes with a large diameter. In a real structure, the rotation of the steel tube is generally small, remaining in the quasi-linear part of the theoretical displacement path. Fig. 3.28a shows typical displacement paths observed in grouted type 1 and type 3 connections. The observed ratio $(\Delta w/\Delta u)_0$ was nearly linear in most cases. Fig. 3.28a also shows that the simplified geometrical model presented above significantly overestimates the displacement perpendicular to the beam axis. The model neglects the following deformations in the connection:

- compression deformations in the timber (perpendicular to the grain) or in the concrete close to the rotation point

- bending and shear (and buckling) deformations in the steel tube

All of these deformations reduce the real ratio $(\Delta w/\Delta u)_0$, explaining the observed deviations. Fig. 3.28b shows all collected data points from grouted type 1 and type 3 connections, obtained by linear regression. While the model consistently overestimates $(\Delta w/\Delta u)_0$, the influence of the steel tube dimensions seem to be correctly represented. The deformations mentioned above may be accounted for with an empirical correction factor using a linear fit as follows:

$$(\Delta w/\Delta u)_{0,\mathrm{corr}} = 0.63 \cdot D/l_{\mathrm{T}} \tag{3.8}$$

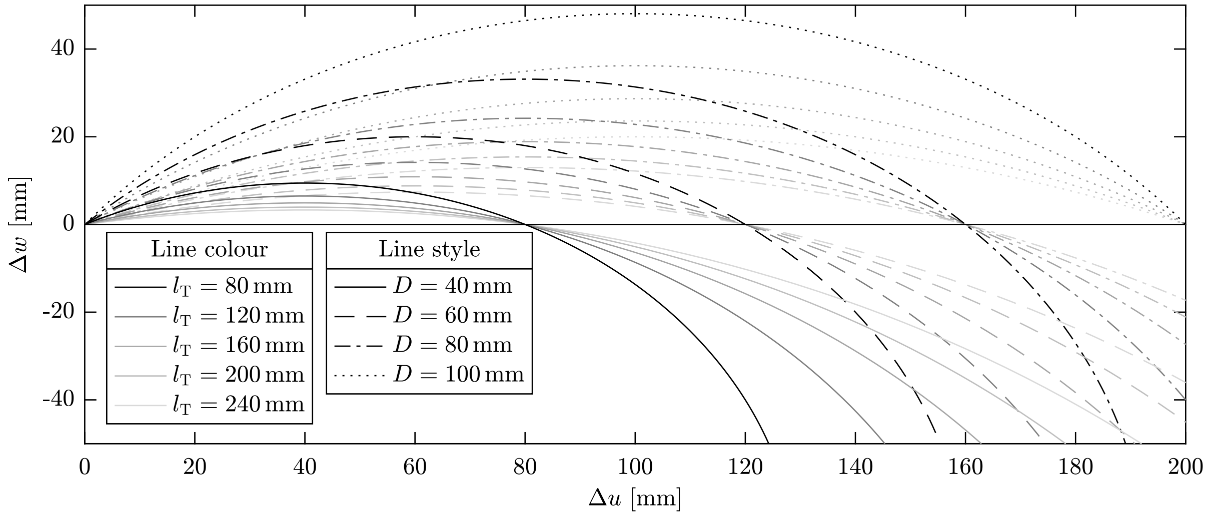

Fig. 3.27: Displacement path for different steel tube dimensions.

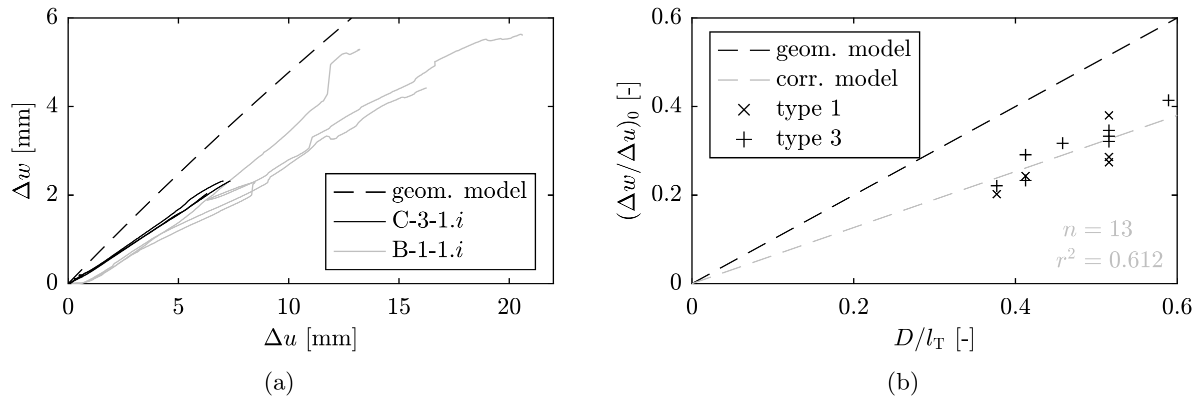

Fig. 3.28: Comparison of theoretical model with test results: (a) displacement path and (b) initial slope of the displacement path, data points with original and corrected model.

3.3.7 Empirical data for models with nonlinear rotational springs

One of the main goals of test series B and C was to obtain empirical data as an input for the calculation models for uniaxial and biaxial bending (Chapters 6–7). For simplified calculations, the connection behaviour is often linearised. However, this may lead to inaccurate results, as discussed by Dias [18]. Therefore, the nonlinear moment-rotation behaviour of the most important connection configurations tested in this experimental campaign is assessed in this chapter.

Various authors have suggested mathematical functions for this purpose (e. g. Ramberg & Osgood [64], Foschi [29], Richard & Abbott [67]). These functions can be fitted to experimental data using 3 – 4 parameters. While this allows for a relatively simple description of the nonlinear connection behaviour and potential use in analytical models, fitted curves never perfectly represent the experimental data.

Most modern FEM software solutions allow for nonlinear calculations based on multi-linear curves as an input, rather than using parametric mathematical functions. Therefore, a more direct approach was chosen in the assessment of the nonlinear connection behaviour than fitting mathematical functions. A set of moment-rotation values is provided in Tab. 3.8 for the most important connection configurations that are used in the final concept of the TCC slab. The resulting multi-linear functions were fitted visually to the test data. Fig. 3.29 shows the results of this approximation as well as the corresponding linear fit with $k_{\mathrm{m},1}$. In most cases, the yield moment M_{y} was set equal to the maximum moment from the push-out test M_{u} (exception: specimen C-3-2, Fig. 3.29b). For the configurations where more than one test result was available, $k_{\mathrm{m},1}$ and M_{y} were averaged. The maximum rotation $\varphi_{\max}$ was defined at the point where the first significant force drop occurred. The multi-linear functions provided in Tab. 3.8 and Fig. 3.29 can directly be used as an input in suitable FEM software.

Tab. 3.8: Moment-rotation values for empirical multi-linear functions representing the behaviour of type 1 and 3 connections with $D = 82.5$ mm, M in [kNm], φ in [mrad].

Type 1 $a = 40$ mm		Type 3 $a = 30$ mm		Type 3 $a = 40$ mm		Type 3 $a = 50$ mm		Type 3 $a = 60$ mm	
M	φ	M	φ	M	φ	M	φ	M	φ
0	0	0	0	0	0	0	0	0	0
2.10	1.80	0.50	0.20	0.80	0.24	0.80	0.12	1.40	0.12
3.00	3.19	1.07	1.20	1.40	0.82	1.33	0.36	2.33	0.55
3.46	4.00	1.68	3.50	1.90	1.60	1.59	0.52	3.90	1.98
4.25	6.00	2.16	6.00	2.50	2.90	2.52	1.80	4.85	4.00
5.30	10.0	2.45	8.00	3.00	4.20	2.99	2.90	5.42	6.39
6.36	15.0	2.63	9.70	3.45	6.00	4.23	7.00	5.98	10.0
7.03	20.0	2.73	13.0	3.90	9.00	4.83	11.0	6.28	15.0
7.39	25.0	2.73	40.0	4.15	13.0	5.28	18.0	6.28	20.0
7.59	30.0			4.38	20.0	5.39	23.0		
7.68	35.0			4.38	30.0	5.39	30.0		
7.68	40.0								
5.60	80.0								

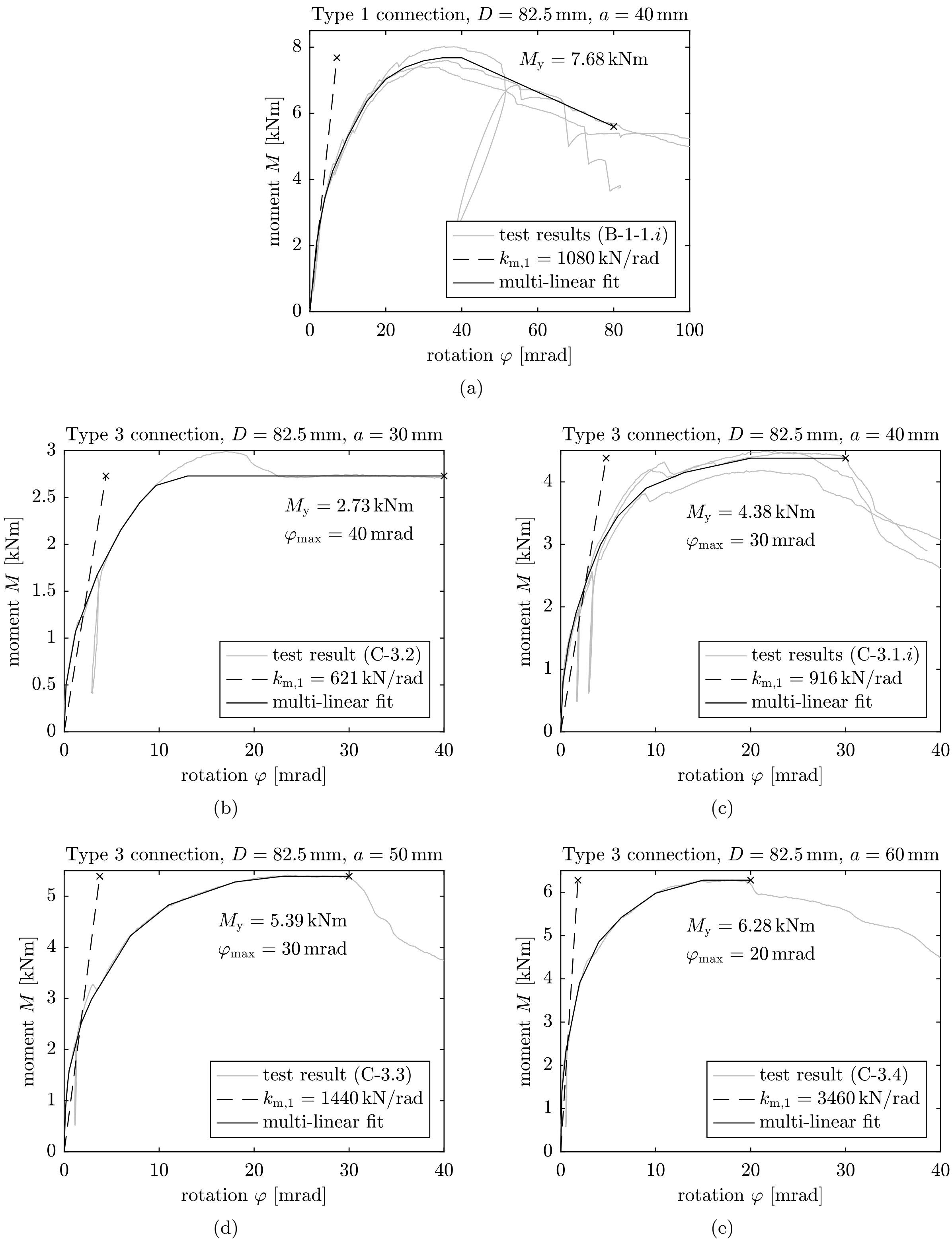

Fig. 3.29: Moment-rotation behaviour of the most important connection types that are used in the final concept of the TCC slab, with linear approximation and multi-linear fit according to Tab. 3.8.

3.4 Conclusions

The load-bearing behaviour of the steel tube connection used in the investigated TCC slab system was studied in a test campaign with a total of 28 specimens. The connection shear capacity and linearised stiffness values as well as empirical nonlinear moment-rotation curves have been obtained for different parameter configurations. These can be used as a basis for the analysis of the load-bearing behaviour of the TCC slab with steel tube connection in uniaxial and biaxial bending. Below, the main conclusions drawn from this experimental campaign are summarised:

- The most important parameter influencing the stiffness and shear capacity of type 1 connections is the use of a grouting system to fill the gap between the steel tube and the timber cutout. Compared to the form-fitting connection concept, the stiffness is up to 10 times higher and the shear capacity is increased by 40%. Based on these results, the final type 1 connection concept was defined, using the Sikadur®-42 HE grouting system.
- The steel tube diameter D and the embedment depth a are the main connection design parameters and have a similar influence in all connection types.
- The used mechanical model with rotational springs representing the connection stiffness is able to decouple the influence of the interlayer height h_0.
- The shear capacity of type 1 connections is governed by inelastic compression deformations, leading to a ductile behaviour. The deformation capacity is limited by shear failures in timber.
- A ductile failure mechanism was observed in all type 3 connections, which is achieved through force redistribution and eventually reinforcement yielding. The deformation capacity is limited by concrete crushing close to the steel tube.
- Further tests are necessary on type 3 connections to quantify the influence of the MOE, which was very low in the investigated specimens. Increased connection stiffness is expected if a standard concrete with normal MOE is used.
- A significant influence of pre-loading on the connection stiffness was observed in type 3 and type 1 and 2 connections without grouting. The first loading curve should be the basis for calculations regarding deformations (SLS) and load-bearing capacity (ULS). The higher reloading stiffness is relevant for dynamic analyses.

Chapter 4

Uniaxial bending tests

4.1 Introduction

This chapter covers the uniaxial bending tests that were conducted in the scope of this research project. At the time when these experiments were planned, the concept of the TCC slab with steel tube connection mainly focused on a production process using cast-in-situ concrete. The specimens were therefore based on this version of the concept, including an upper LVL beam in order to increase the bending stiffness in the construction state, as described in Chapter 1.3. The experimental campaign was divided into two phases: In a first step, formwork elements were produced and their bending stiffness was tested. Subsequently, the production of the specimens was completed and the stiffness and ultimate load-bearing capacity of the TCC slab elements were determined by means of destructive tests. The main objectives of this experimental campaign were:

- Investigating the stiffness, natural vibration frequency, load-bearing capacity and ductility of the TCC slab in uniaxial bending
- Understanding the structural behaviour and the governing failure mechanisms
- Studying the influence of various parameters on the load-bearing behaviour
- Providing experimental data as a basis to validate the calculation models for uniaxial bending (Chapter 6)

The main findings are presented and discussed in this chapter, with a focus on the second phase of the experimental campaign where the TCC slab in the final state was investigated. A detailed report of all conducted experiments is provided in [44].

4.2 Materials and methods

4.2.1 Specimens

In the scope of this experimental campaign, eleven bending specimens with a length of 5.46 m were produced and tested. The design of the specimens is based on the concept with a production process using cast-in-situ concrete, including three upper LVL beams per formwork element of 1.82 m width as illustrated in Fig. 1.2. The test specimens correspond to a third of the width of one formwork element, resulting in a width of 0.6 m.

The geometry of all specimens is depicted in Fig. 4.1 and 4.2 and the chosen set of parameters is summarised in Tab. 4.1. Specimens 1 – 8 were used to investigate the uniaxial bending behaviour in the main (longitudinal) direction of the TCC slab. Specimens 1.1 and 1.2 correspond to the reference configuration. In specimens 2 – 8, either the number of connectors per shear area m, the interlayer height h_0 or the connector stiffness (with or without grouting, or smaller steel tube diameter D) was varied. In Tab. 4.1, the respective varied parameter is highlighted in bold print. The first letter of the specified connection concept (e. g. 'g – f') refers to the lower connection (type 1) whereas the second letter describes the connection with the upper LVL beam (type 2).

The interlayer was fabricated using stone wool plates with cutouts for the steel tubes and the upper LVL beam. The relative position of the upper LVL beam is shown in Fig. 4.1 and was identical in all specimens. The concrete layer was reinforced with a steel mesh ⌀8 @ 150 mm placed directly on the upper LVL beam as shown in Fig. 4.1. In specimens 1 – 8, the steel tubes were arranged according to the expected shear forces as shown in Fig. 4.2.

Tab. 4.1: Parameters of the uniaxial bending specimens.

Name	Connection concept *	Connectors per shear area m [-]	Interlayer height h_0 [mm]	Steel tube dimensions D / t [mm]
1.1	g – f	4	120	ROR 82.5/3.6
1.2	g – f	4	120	ROR 82.5/3.6
2	g – **g**	4	120	ROR 82.5/3.6
3	g – f	**3**	120	ROR 82.5/3.6
4	g – f	**6**	120	ROR 82.5/3.6
5	g – f	4	**100**	ROR 82.5/3.6
6	g – f	4	**160**	ROR 82.5/3.6
7	**f** – f	4	120	ROR 82.5/3.6
8	**f** – f	4	120	ROR **60.3**/3.6
T1	g – f	4	120	ROR 82.5/3.6
T2	g – f	5	120	ROR 82.5/3.6

* g = grouted connection, f = form-fitting connection without grouting

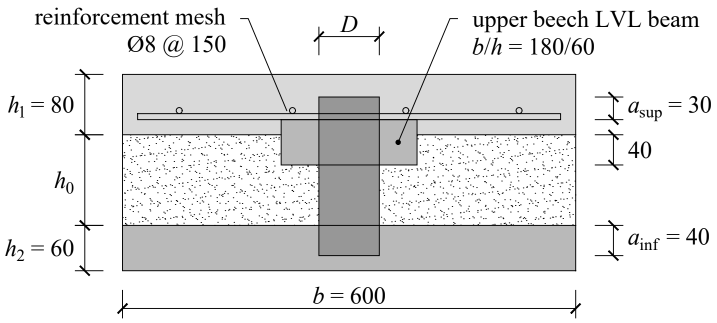

Fig. 4.1: Cross-section of specimens 1 – 8, dimensions in [mm].

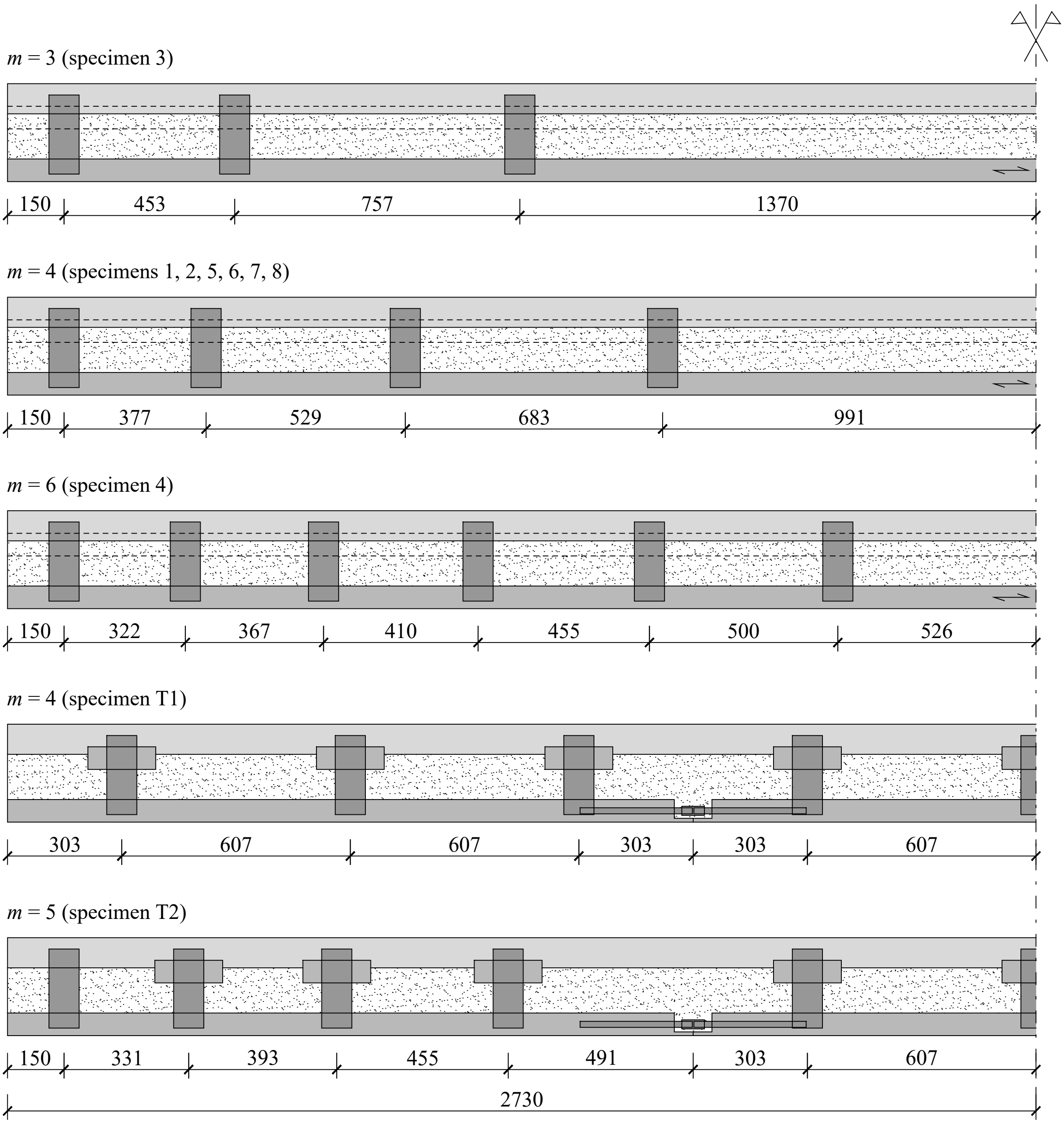

Fig. 4.2: Longitudinal section of specimens, dimensions in [mm].

Specimens T1 and T2 represent the transversal load-bearing direction of a two-way spanning version of the slab. In this concept, the weight of the fresh concrete during construction is carried mainly in the longitudinal direction of the slab. The slab shows a biaxial load-bearing behaviour only in the final state, after hardening of the concrete layer. The idea behind specimens T1 and T2 was to 'extract' a transversal stripe from this two-way spanning slab to investigate the uniaxial bending behaviour in this direction. Consequently, the main veneer direction was perpendicular to the span direction in these specimens and the timber layer was assembled from three beech LVL elements of 1.82 m length. The concept of the side connection as described in Chapter 1.3 was not yet developed at the time of this test series. A different connection concept was applied, using glued-in rods (GIR) with opposite threads, connected with a coupling nut as shown in Fig. 4.3. After gluing the threaded rods, the coupling nut was tightened with a torque of 100 Nm to achieve a slip-free connection. The reason why this connection concept was eventually abandoned is discussed in Chapter 5.

In specimen T1, the steel tubes and upper LVL beams were arranged with uniform spacing, in accordance with the formwork element concept depicted in Fig 1.2. In specimen T2, one additional steel tube close to the supports was added to investigate the respective influence on the structural behaviour in transversal direction.

The beech LVL parts needed for specimens 1 − 8 (longitudinal direction) were cut out of five LVL boards of 5.5 m length and 1.82 m width. In addition, two specimens for tensile tests were cut out of each board. All five LVL boards were marked with a colour, ensuring that the respective material used in the bending specimens could be identified. The parts needed for specimens T1 and T2 (transversal direction) were all cut out of the same LVL board, along with five pieces for tensile tests. The concrete was ordered according to the specifications listed in Tab. 4.2. Concrete tests were performed to determine the MOE according to SIA 262/1 [77], the cylinder compressive strength according to EN 12390-3 [11] and the splitting tensile strength according to Chen [16]. A detailed report of all material tests is provided in [44]. Tab. 4.3 and 4.4 show the main results of the material tests.

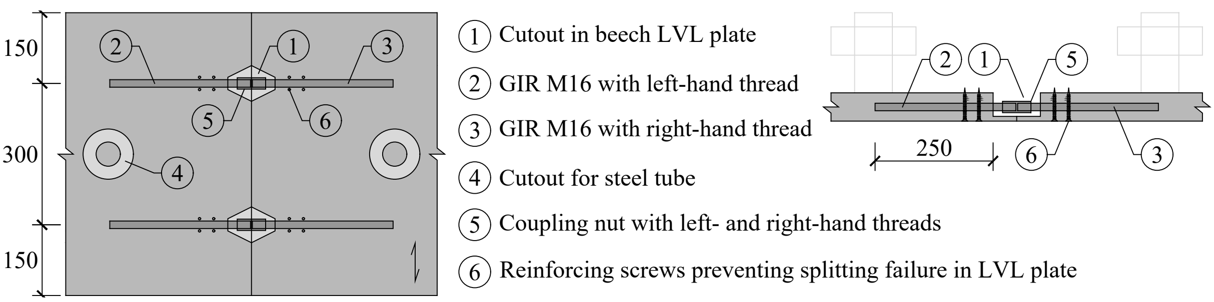

Fig. 4.3: Side connection in specimens T1 and T2, top view (left) and longitudinal section (right), dimensions in [mm].

Tab. 4.2: Materials used in the uniaxial bending specimens.

Material	Description	Details
Beech LVL (*BauBuche Q*)	Thickness Veneer layout Cross-layer ratio	60 mm $\vert\vert\vert - \vert\vert - \vert\vert\vert\vert\vert\vert - \vert\vert - \vert\vert\vert$ 19%
Stone wool	Flumroc MEGA Plate thickness	Insulation plates for interlayer 120 mm
Concrete	Ordered quality Max. aggregate size Admixture	C30/37 16 mm MasterLife SRA 895 (2% of cement mass)
Steel tubes	ROR 82.5/3.6 ROR 60.3/3.6	E355, seamless S235, welded
Grout type	Sikadur®-42 HE	High performance epoxy grouting system [79]
Glued-in rods	Threaded rods M16 Resin and hardener	Strength grade 8.8 WEVO EP 32 S / B22 TS [23]

Tab. 4.3: Results of material tests, production group 1 (specimens 1 – 8).

Material	Property		Mean value [MPa]	COV	n
Concrete (age: 25 days)	Modulus of elasticity	E_1	35'000	8%	3
	Cyl. compressive strength	$f_{1,c}$	44.1	2%	3
	Splitting tensile strength	$f_{1,t,sp}$	3.3	4%	4
Beech LVL (*BauBuche Q*)	MOE ∥ to grain	$E_{2,0}$	15'200	10%	10
	Tensile strength ∥ to grain	$f_{2,t,0}$	63.4	12%	10

Tab. 4.4: Results of material tests, production group 2 (specimens T1 and T2).

Material	Property		Mean value [MPa]	COV	n
Concrete (age: 40 days)	Modulus of elasticity	E_1	31'000	5%	3
	Cyl. compressive strength	$f_{1,c}$	38.0	7%	3
	Splitting tensile strength	$f_{1,t,sp}$	2.7	13%	4
Beech LVL (*BauBuche Q*)	MOE ⊥ to grain	$E_{2,90}$	4'930	9%	5
	Tensile strength ⊥ to grain	$f_{2,t,90}$	14.2	24%	5

4.2.2 Test setup

All experiments were conducted in the laboratories of ETH Zurich. The stiffness of the formwork elements was measured in a 4-point bending test setup with a span of $l = 5.24\,\text{m}$ and a distance between the two applied forces at mid-span of 1.6 m. Three loading cycles were performed in the linear-elastic range of the load-deflection curve. A detailed description of the used test setup is given in [44].

The tests in the final state were performed in a 10-point bending setup as depicted in Fig. 4.4 and 4.5. The force applied by the hydraulic cylinders (8 in Fig. 4.4) was distributed to eight points of equal distance along the span using steel beams (9). This was done to represent as accurately as possible the loading conditions of a simply supported beam subjected to uniformly distributed load. All cylinders were connected to the same hydraulic circuit with the oil pressure controlled by a manually operated pump.

4.2.3 Measurements and test procedure

The oil pressure in the hydraulic circuit was measured using the internal manometer of the manually operated pump. Based on this measurement, the cylinder forces were calculated. Two NDI Optotrak Certus position sensors were installed to record the deformations on the front side of the specimen. Strobers (visible e. g. in Fig. 4.5c) were glued to both the specimen and the supporting construction allowing for a precise 3D tracking of these points throughout the experiments. The strober locations are shown in Fig. 4.4. They were chosen according to the position of the steel tubes in the respective specimen, allowing for a calculation of the relative displacements between the timber and concrete sections at these points. Additional strobers were used to record the bending line of the specimen. Furthermore, one LVDT was installed to measure the deflection at mid-span, for live monitoring during the experiments and to confirm the accuracy of the NDI measurement.

After centering the specimen in the test setup and before the hydraulic cylinders were lowered, dynamic tests were conducted. Impulse excitation was achieved with a hammer hit at $x = L/4$, $L/2$ and $3L/4$, which was repeated three times. The free vibration response of the specimen to each of the nine impulse excitations was recorded at a rate of 1'200 Hz with an acceleration sensor glued to the top of the concrete layer at mid-span (Fig. 4.5e).

After the dynamic tests, the acceleration sensor was removed and the load-distribution construction was lowered and positioned on the specimen with the hydraulic cylinders. The oil pressure was relaxed and all measurements were tared. The loading protocol was similar as in the connection shear tests (Chapter 3) and is based on the recommendations in EN 26891 [10], including an unloading and reloading cycle after 40% of the estimated failure load was reached. The manual control with the hand operated oil pump is comparable to force based control in the elastic range and displacement based control in the plastic range of the experiment. Typical force-time and deflection-time graphs are shown in Fig. 4.6. The experiment was stopped when either a brittle failure led to a significant load drop or when the displacement capacity of the hydraulic cylinders was reached at a mid-span deflection of approximately 300 mm.

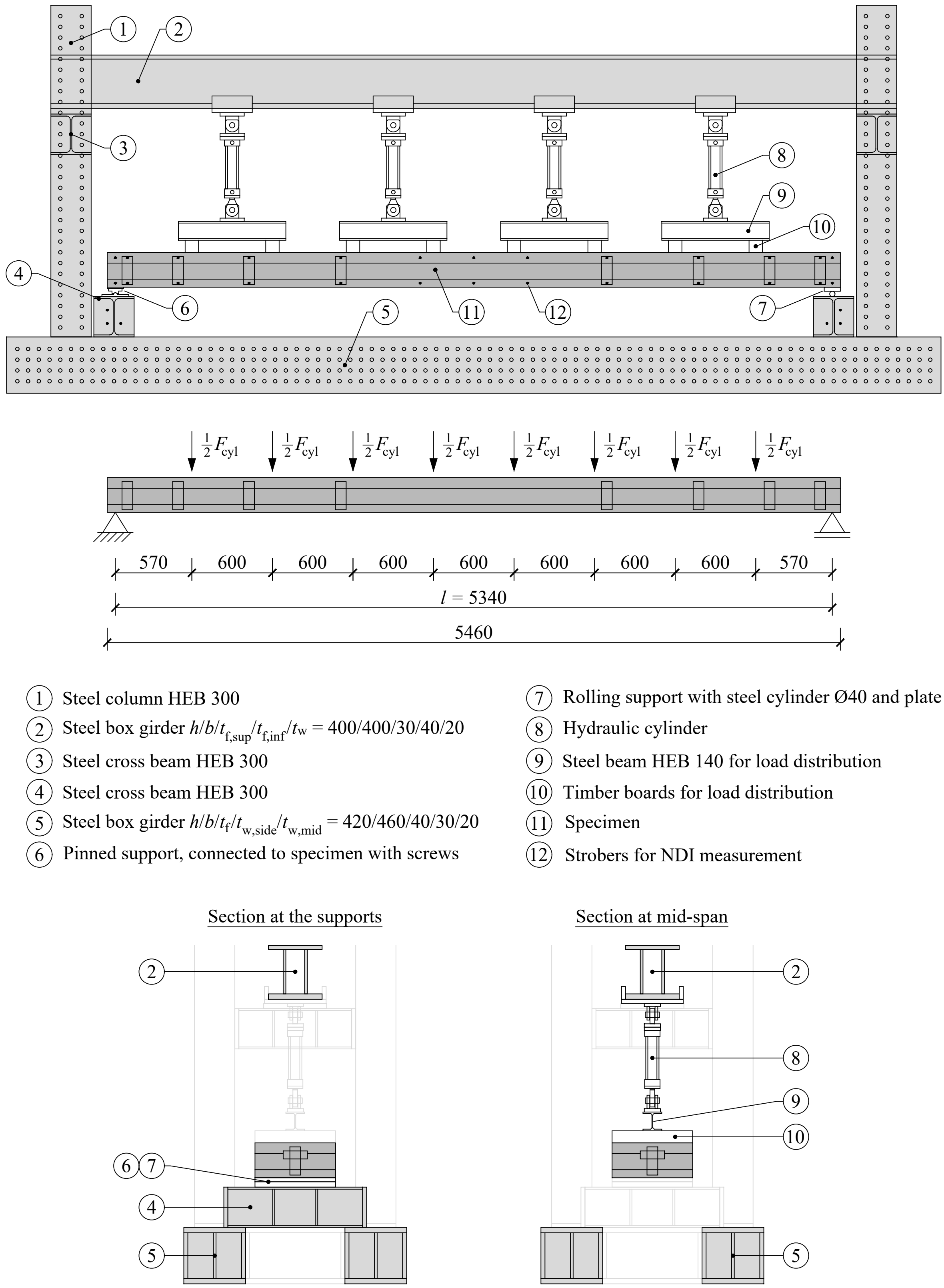

Fig. 4.4: Test setup for the uniaxial bending experiments in the final state, dimensions in [mm].

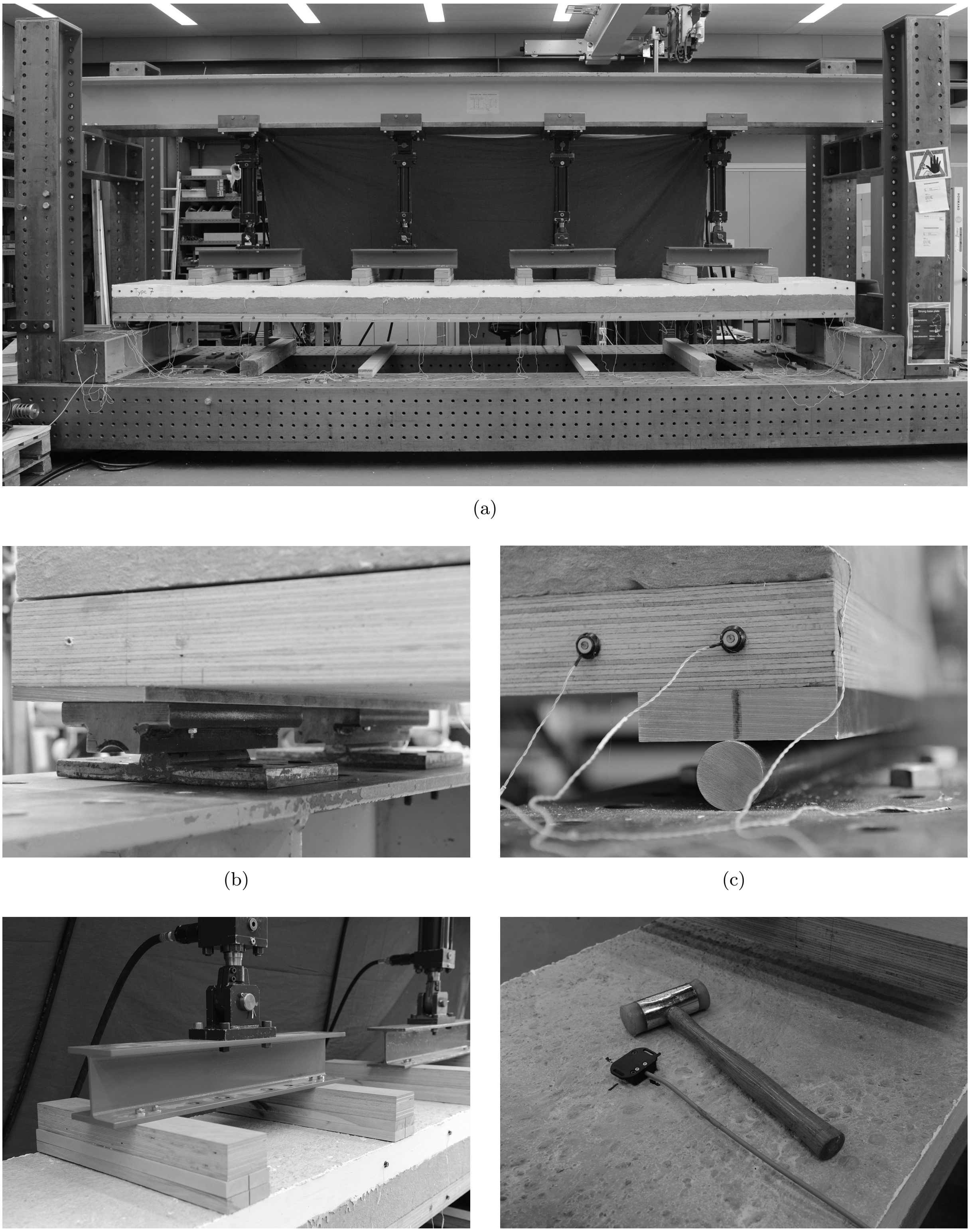

(a) (b) (c) (d) (e)

Fig. 4.5: Photos of the test setup (a) overview, (b) 6 pinned and (c) 7 rolling support, (d) load distribution construction and (e) hammer and acceleration sensor used for dynamic tests.

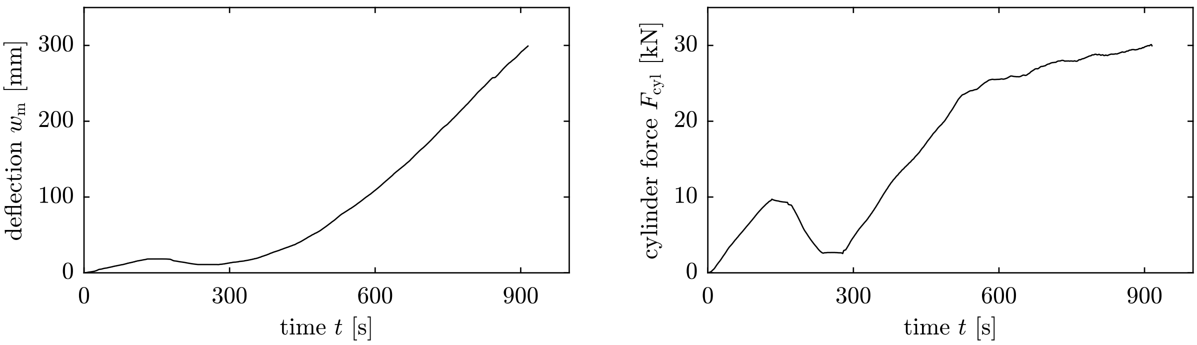

(a) (b)

Fig. 4.6: Typical (a) deflection-time and (b) force-time diagrams.

4.2.4 Data evaluation

This chapter covers briefly the most important steps of the data evaluation. More detailed information on each step is given in [44]. The bending stiffness of the formwork elements was calculated based on the measured cylinder forces, mid-span deflection and the geometry of the test setup. Linear regression was performed on all three loading cycles to obtain $EI_{con,1}$ and $EI_{con,2}$, the latter being the mean value from the second and third loading cycle.

The acceleration measurements recorded in the dynamic tests (Fig 4.7a) were transferred to the frequency domain with a fast Fourier transform (FFT). Fig. 4.7b shows a typical resulting plot from which the fundamental frequency was obtained.

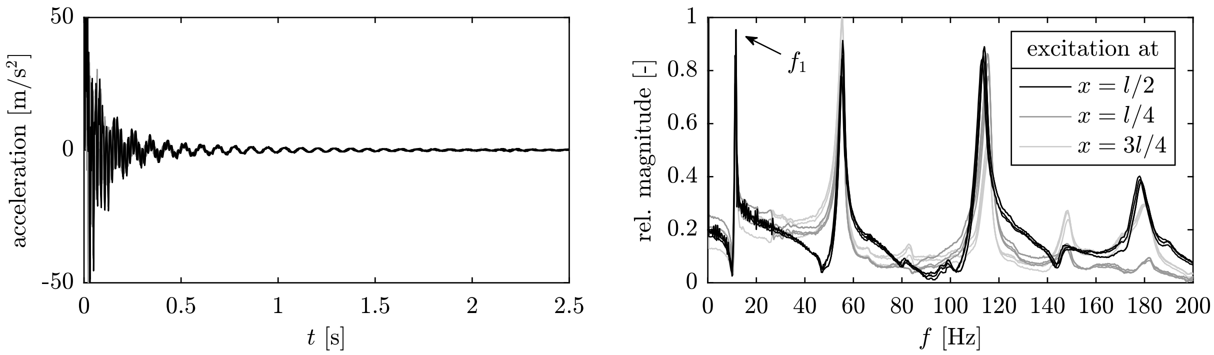

(a) (b)

Fig. 4.7: Typical result of dynamic test (a) time domain and (b) frequency domain (specimen 5).

Using the NDI measurement data, the bending line of both timber and concrete layers could be reconstructed at every point in time throughout the static loading tests. Fig. 4.8 shows the bending line of specimen 4 before test start and at maximum load, as an example. Of particular interest were the mid-span deflection w_m as well as the relative displacements of the timber and concrete layers, parallel and perpendicular to the beam axis Δu and Δw, respectively. Δu, also referred to as slip displacement, and Δw were calculated at the location of each connector by projecting the horizontal and vertical relative displacements to the current bending line at the considered point. The connectors are identified as shown in Fig. 4.8.

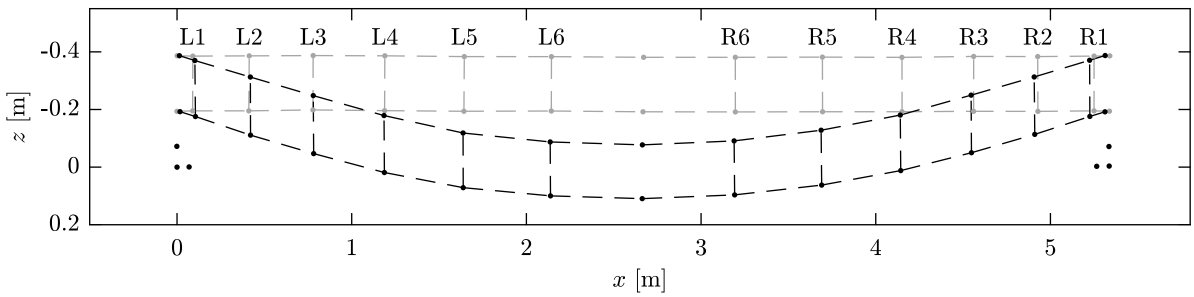

Fig. 4.8: Bending line before test start and at maximum load (specimen 4).

A linearised stiffness was calculated for both first loading and reloading cycle, using linear regression similar as in the connection shear tests (Fig. 3.23). The respective bending stiffness EI_1 and EI_2 was calculated based on the measured cylinder forces F_{cyl}, mid-span deflection w_{m} and the geometry of the test setup (static system depicted in Fig. 4.4).

To allow for an easier interpretation of the test results, an equivalent distributed load q was calculated as follows:

$$q = \frac{4 \cdot F_{\mathrm{cyl}}}{b \cdot l} \tag{4.1}$$

For the calculation of the load-bearing capacity, the self-weight of the specimen (measured with the integrated scale of the laboratory crane, $m_{\mathrm{s}} = 850 - 945\,\mathrm{kg}$ depending on the specimen) and the load distribution construction ($m_{\mathrm{LDC}} = 140\,\mathrm{kg}$) were added as follows:

$$q_{\mathrm{u}}^{*} = q_{\mathrm{u}} + \frac{(m_{\mathrm{s}} + m_{\mathrm{LDC}}) \cdot g}{b \cdot l} \tag{4.2}$$

4.3 Results

4.3.1 Load-bearing behaviour in the longitudinal direction

This chapter summarises the load-bearing behaviour and the main failure mechanisms that were observed in specimens 1 – 8, representing the longitudinal direction of the TCC slab. A detailed report of each individual experiment is given in [44]. Fig. 4.13 – 4.15 show the load-deflection diagrams of each test, along with the slip displacement Δu at the location of each connector in the specimen.

In almost all of the longitudinal specimens, no significant load drop due to a brittle failure was observed until the end of the experiment, when the displacement capacity of the hydraulic cylinders was reached at a mid-span deflection of approximately 300 mm. The only exception was specimen 2 with a stiffer, grouted connection in the upper LVL beam, which had a distinct influence on the connection ductility. This aspect will be discussed in Chapter 4.4.1. It is likely that the load could have been further increased in most cases, until a brittle failure in the connectors or in the cross-section, such as concrete crushing or timber tensile-bending failure, would have occurred. However, given the very flat slope (almost horizontal) of the load-deflection curve at the end of the experiments, it is not to be expected that the true load-bearing capacity would have been substantially higher than the maximum measured load during the tests.

In the beginning of the experiments, the load-deflection behaviour was approximately linear up to roughly 40% of the maximum load. After that, a non-linear phase followed. The behaviour in this second phase is related to the loss of stiffness in the connection starting at the same load level, which can be seen in the plots showing the slip displacements Δu. Furthermore, bending cracks started occurring in the concrete section (Fig. 4.9), which may also explain a part of the observed continuous decrease in bending stiffness during this phase. In all specimens, a longitudinal crack on the top of the concrete section opened up along the entire span during this phase. This likely happened because the timber beam in the middle of the section provided a stiffer support for the concrete than the stone wool on the sides of the section. Thus, the concrete section was subjected to a negative transversal bending moment.

After this non-linear phase, a plastic phase was observed, during which the deflections substantially increased at a small, but positive q/w_{m} gradient. An overview of the failure mechanisms observed during this phase is given in Fig. 4.9. On the timber side of the connectors, the following three failure types were identified:

- Front block shear failure (FBS): block shear failure between the connector closest to the support (L1 and R1) and the end of the specimen (Fig. 4.10a and 4.10b)
- Local front shear failure (LFS): local shear cracks on the front side of the connector, towards the support (Fig. 3.9b and 4.10c)
- Rear shear/tensile failure (RST): local cracks due to shear and and tension perpendicular to the grain on the rear side of the connector, towards mid-span (Fig. 3.9b and 4.10d)

In some cases (e. g. specimen 1.1, Fig. 4.13a), these shear failures led to small load drops in the global load-deflection diagram, but the load could be further increased afterwards. In other cases (e. g. specimen 4, Fig. 4.14e), they only led to additional deformations without any noticeable load drop.

Front block shear failures (FBS) were visible already during or directly after the experiments (Fig. 4.10a) and were observed in all specimens (exception: specimen 8), in most cases only on one side. The other two failure types were noticed only acoustically or suspected due to small load drops during the experiment. They were visually detected only after removing the stone wool, which was done for specimens 1.1, 2, 4 and 6. In specimen 6, the beech LVL plate was cut with a circular saw to confirm both failure types LFS and RST (Fig. 4.10c and 4.10d). These failures typically occurred on the same side of the span as the FBS, close to connector 2. Close to connector 3, only small cracks were visible in some cases.

Removing the stone wool from the specimens further revealed that in some connectors, the grouting had failed, such as in specimen 4 (Fig. 4.11a). However, it could not be determined if this had happened before or after the other failures.

In most specimens, during the plastic phase of the experiment, several cracks on top of the concrete section were observed close to the first steel tube on the side (L1 and R1), as shown in Fig. 4.11b. Similar cracks had already been observed and discussed in the connection shear tests (Chapter 3.3.4).

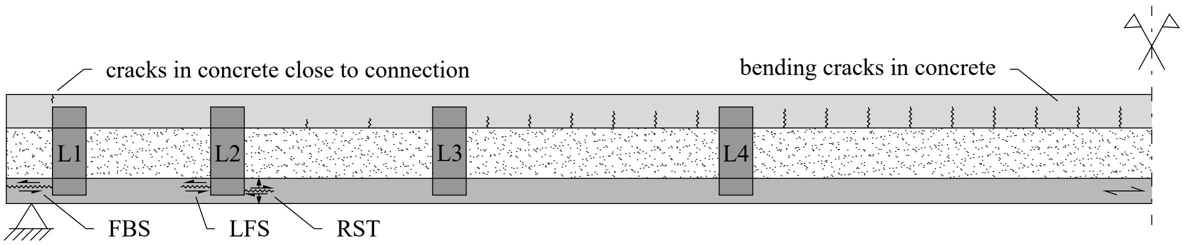

Fig. 4.9: Overview of main failure mechanisms observed in longitudinal specimens.

(a)

(b)

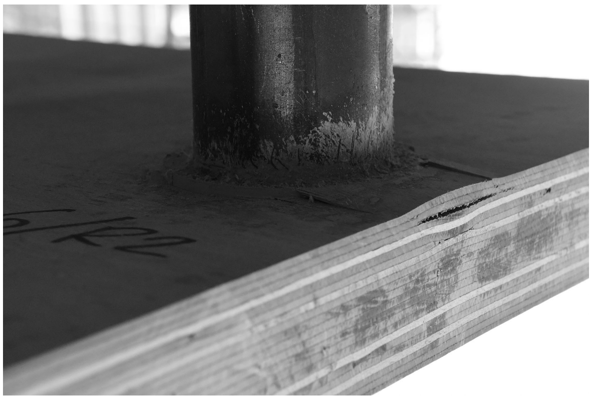

(c)

(d)

Fig. 4.10: Photos of connection shear failures in timber (a) front block shear failure (FBS) in specimen 4 close to connector L1, directly after the test and (b) after removing the stone wool layer, (c) local front shear failure (LFS) in specimen 6 close to connector R2, visible cut oriented towards the support, (d) rear shear/tensile failure (RST) in specimen 6 close to connector R1, visible cut oriented towards mid-span.

In specimen 4, a local concrete compressive failure was observed close to mid-span, shortly before the end of the experiment (Fig. 4.11c). However, this did not lead to any noticeable load drop. No cross-sectional failures such as bending tensile or shear failures were observed neither in the main timber section nor in the upper LVL beam (exception: specimen 2). In all specimens, the load-bearing behaviour was governed by the connection behaviour, not by cross-sectional failure modes.

(a)

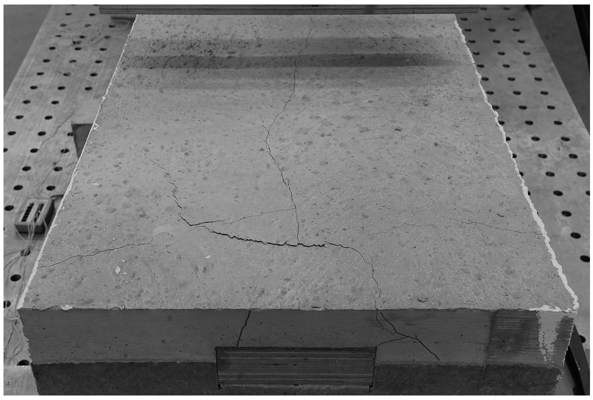

(b)

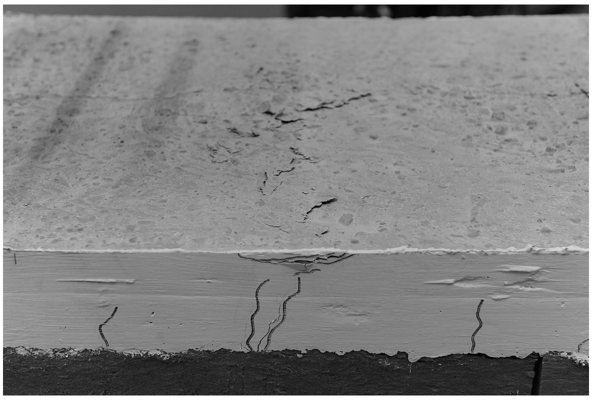

(c)

Fig. 4.11: Photos of (a) failure in grouting (specimen 4, connector R1), (b) cracks on top of the concrete section (specimen 1.1, connector L1) and (c) local concrete compressive failure in specimen 4 close to mid-span.

Opening specimen 2 (with a stiffer, grouted connection in the upper LVL beam) revealed additional failure types that were not observed in any of the other specimens:

- Timber compressive failure close to the connector (buckling of the fibers, Fig. 4.12a)
- Failures in the upper LVL beam close to connectors L1 – L4 due to shear and tension perpendicular to the grain (Fig. 4.12b)
- Distinct vertical pulling out of the steel tube in the lower connections during the post-peak phase of the experiment, along with crushing of the grouting (Fig. 4.12b)

The difference in failure mechanism of specimen 2 compared to the other specimens will be discussed in Chapter 4.4.1.

(a) (b)

Fig. 4.12: Failures in specimen 2: (a) timber compressive failure close to connector L2, (b) failures in the upper LVL beam due to shear and tension perpendicular to the grain, vertical pulling out of the steel tubes and crushing of the grouting.

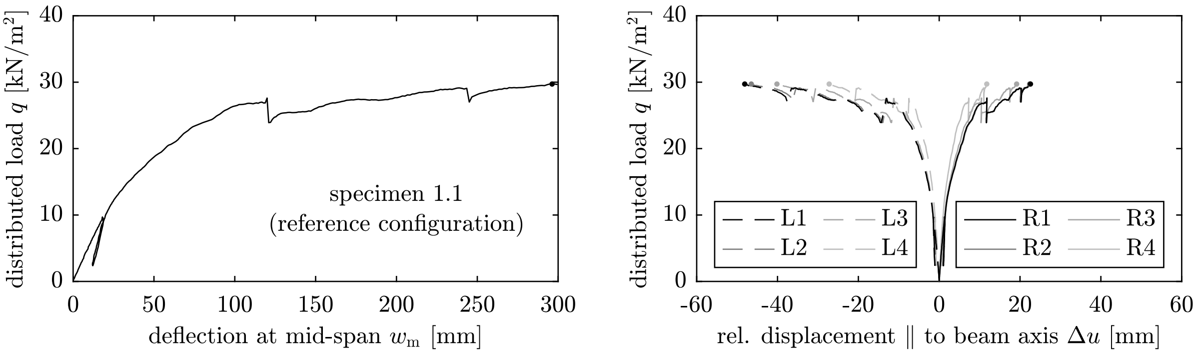

(a) (b)

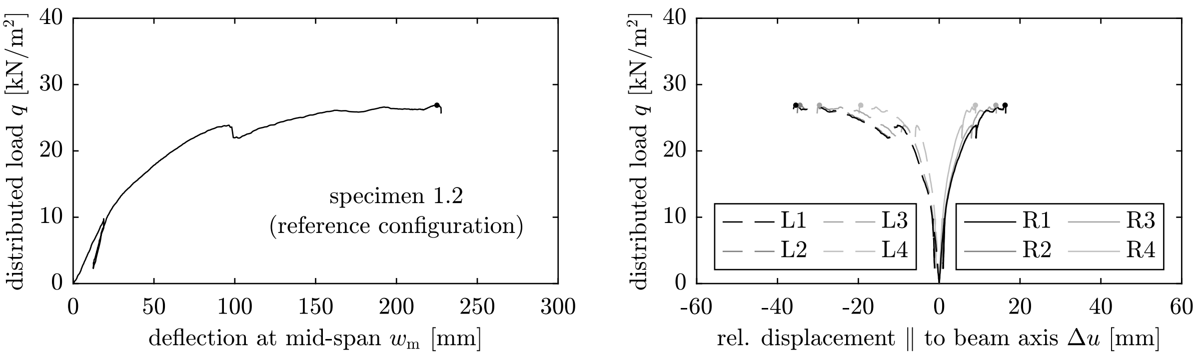

(c) (d)

Fig. 4.13: Test results of specimens 1.1 and 1.2.

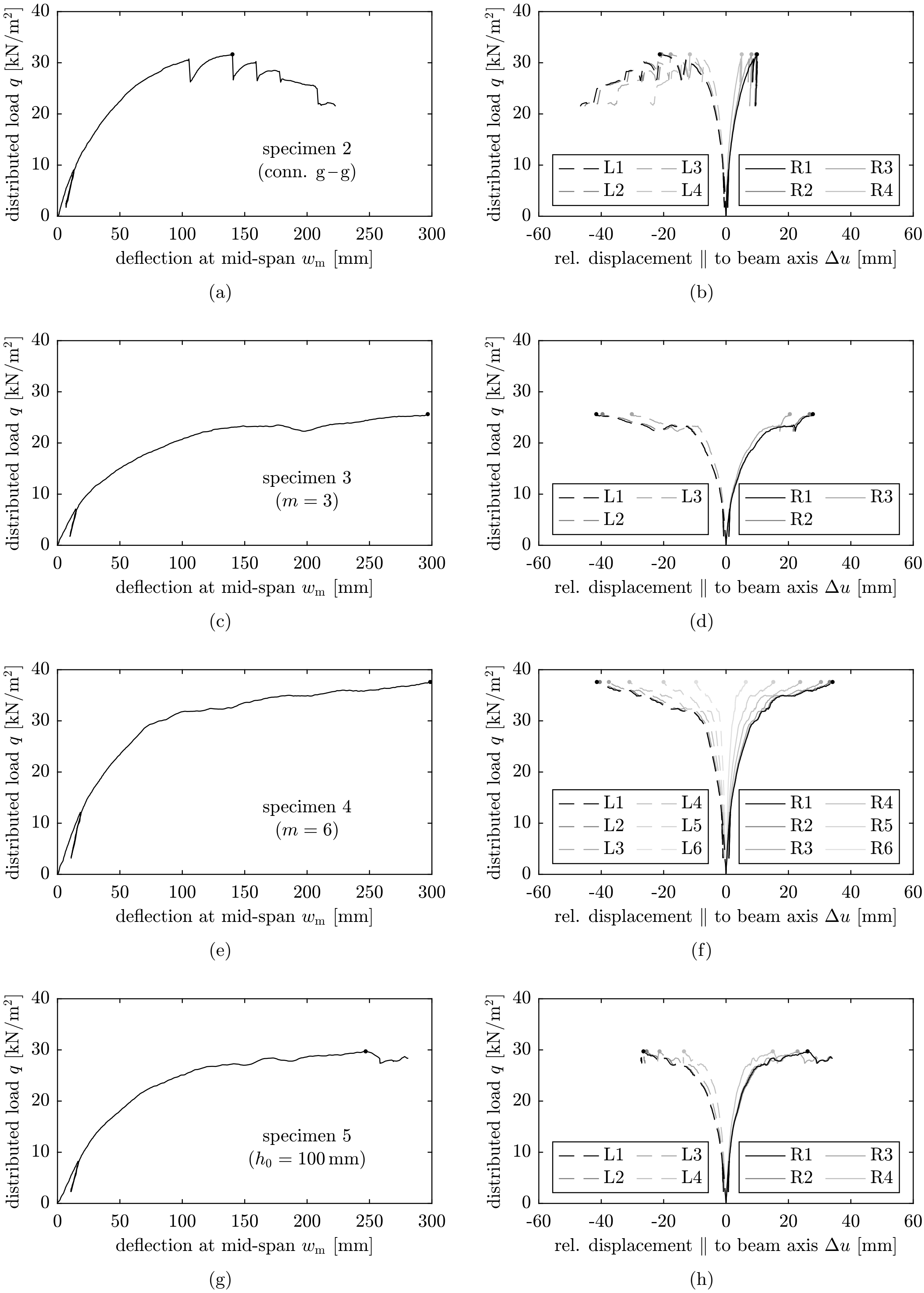

Fig. 4.14: Test results of specimens 2 – 5.

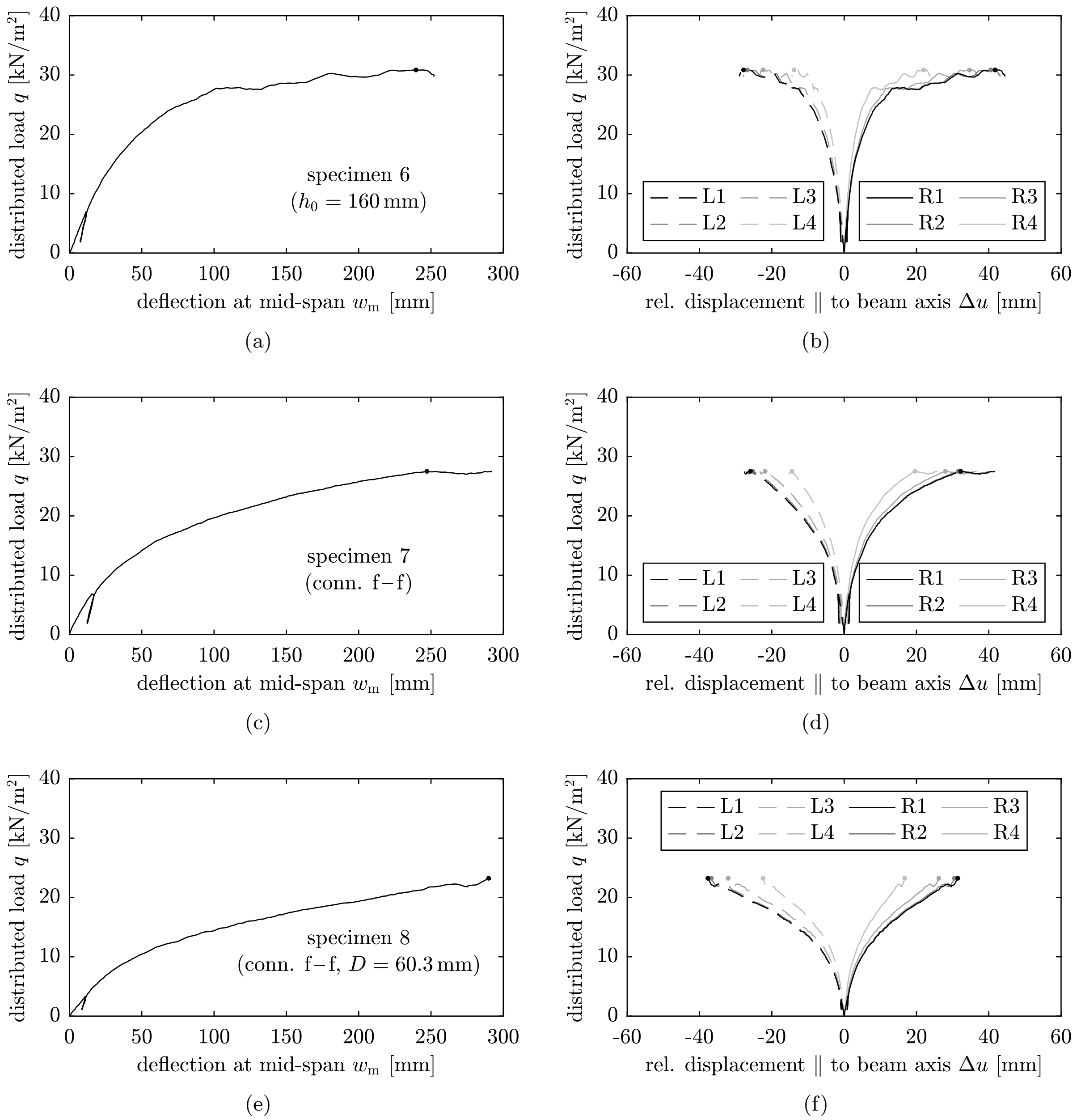

Fig. 4.15: Test results of specimens 6 − 8.

4.3.2 Load-bearing behaviour in the transversal direction

The load-bearing behaviour of the transversal specimens T1 and T2 was governed by the connection behaviour, similar as in the longitudinal specimens. Fig 4.16 shows the main results of these two experiments. Compared to specimens 1 − 8, the following differences were observed:

- After reaching the maximum load q_u, a substantial load drop was observed. The failure mechanism was less ductile than in the longitudinal specimens.

- The orientation of the upper LVL beams was rotated by 90° compared to specimens 1 – 8, which had a distinct influence on the behaviour of the steel tube – concrete connection. Whereas in the longitudinal specimens, the upper LVL beam likely provided some resistance for the connection, this was not the case in specimens T1 and T2. On the contrary, in these specimens, the upper LVL beams imposed a kinematic constraint to the connection that led to a pulling out of the steel tube from the concrete with increasing rotation of the steel tubes (visible in Fig. 4.17a). To a lesser extent, this effect was already observed in the connection shear tests and discussed in Chapter 3.3.6. Translated to these considerations, the presence of the upper LVL beam would be equivalent to an increased steel tube diameter D.
- No shear failures were observed in the timber. After opening specimen T2, cracks in the grouting in connector L1 were visible (Fig. 4.17b).
- In specimen T2 (with an additional connector close to the support, without upper LVL beam), the non-linear phase started at a higher load level than in all other specimens. The load-deflection behaviour remained approximately linear up to a load of roughly 70% of the maximum load. The two load drops at 11.0 and 12.2 kN/m^2 visible in Fig. 4.16c were due to cracking of the concrete above connectors L1 and R1, leading to a significant stiffness reduction.

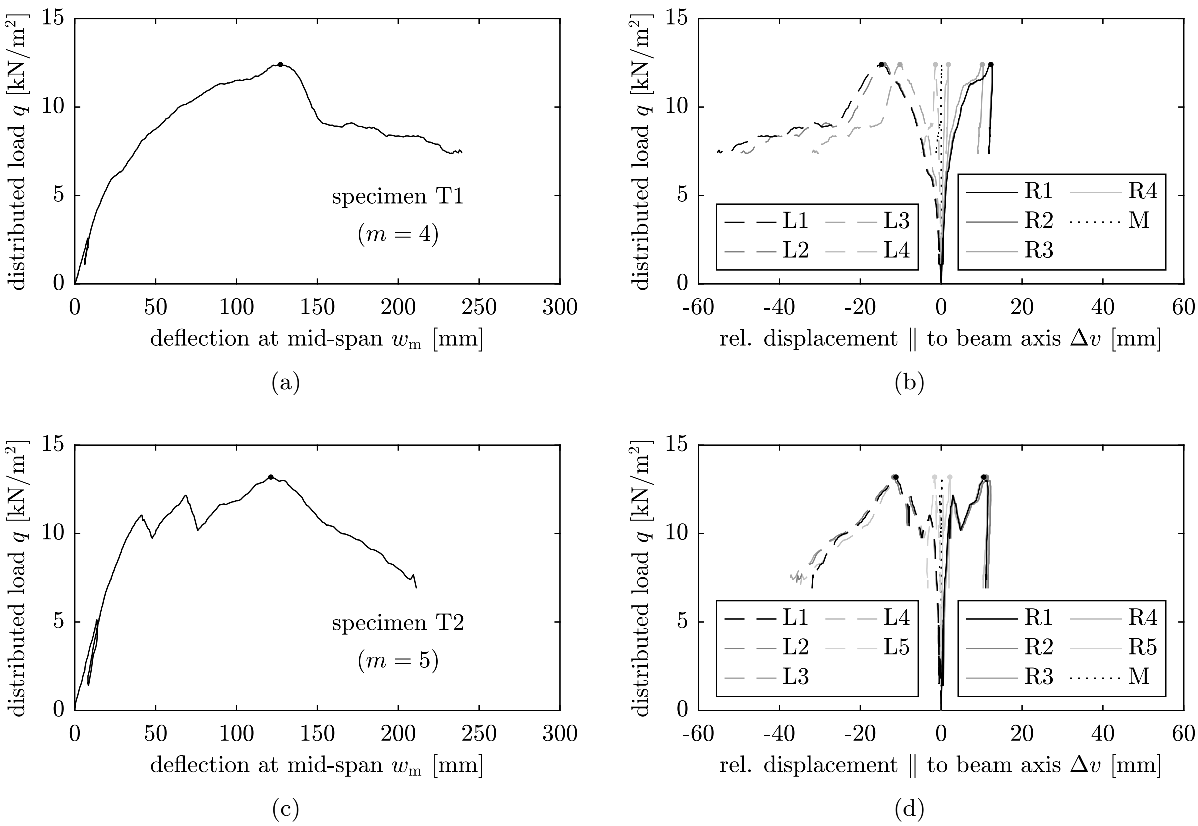

Fig. 4.16: Test results of specimens T1 and T2 (transversal direction).

(a) (b)

Fig. 4.17: Specimen T2 (a) pulling out of the steel tube from the concrete due to kinematic constraint of upper LVL beams (L2 and L3), (b) cracks in the grouting of connector L1.

During the linear phase of the experiments, no significant influence of the two side connections (i.e. the two GIR connections located at 1/3 and 2/3 of the span) was observed. With increasing load, however, the bending line was not as continuous as in the longitudinal tests anymore, but slightly polygonal. Fig. 4.18 shows the bending line of specimen T1 reconstructed from the NDI measurement at different load levels, illustrating this observation. Attempting to quantify these kinks in the bending line at the location of the side connections, the inclination of the timber plate on both sides of the connection (shown in Fig. 4.18) was derived from the measurement data. The difference of the inclination was then calculated according to Eq. 4.3 and plotted in Fig. 4.19.

$$\Delta\vartheta = |\vartheta_{\mathrm{s}} - \vartheta_{\mathrm{m}}| \tag{4.3}$$

Fig. 4.19a (specimen T1) shows a noticeable change in the slope of the $\Delta\vartheta$ curve at $q \approx 5\,\mathrm{kN/m^2}$. It is likely that this was due to a loss of stiffness in the side connections, starting at this load level. Fig. 4.19b (specimen T2) shows a similar change at $q \approx 3.5\,\mathrm{kN/m^2}$, however the data are less clear in this case.

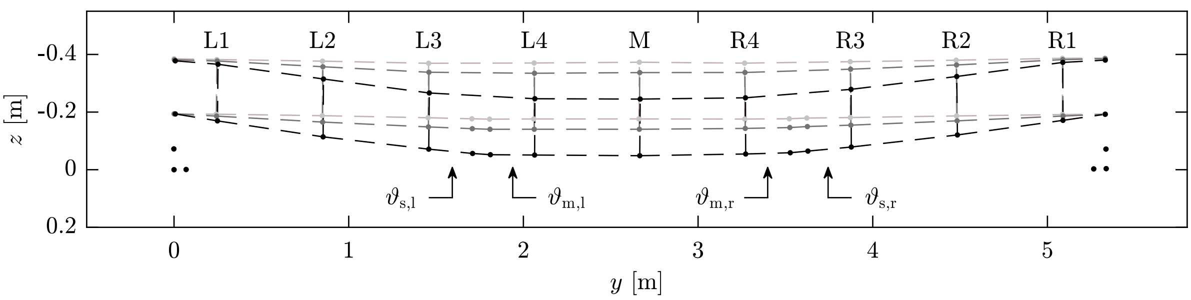

Fig. 4.18: Bending line of specimen T1 before test start, at $q = 0.8 \cdot q_{\mathrm{u}}$ and $q = q_{\mathrm{u}}$.

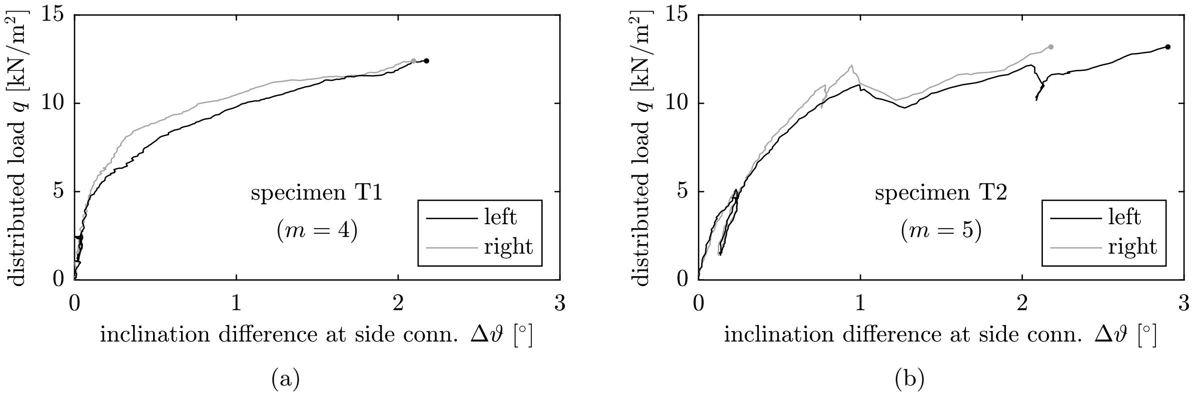

Fig. 4.19: Difference of the bending line inclination at the side connections in (a) specimen T1 and (b) specimen T2 (post-peak behaviour not plotted).

In specimen T1, a local failure in the timber section occurred close to L3 (Fig. 4.20), shortly before the experiment was stopped. It is likely that this failure was significantly influenced by the glued-in rods at this location, leading to tensile stresses perpendicular to the grain. However, this failure occurred at large deformations after the load had already dropped to roughly 65% of the maximum load.

Fig. 4.20: Local failure due to tensile stresses perpendicular to the grain close to connector L3 in specimen T1.

4.3.3 Summary of the test results

A summary of the main results is given in Tab. 4.5. All values were derived according to the procedure described in Chapter 4.2.4.

Tab. 4.5: Main results of all uniaxial bending tests.

Spec.	Formwork stiffness $1^{st}/2^{nd}$ loading		Mass	Fund. freq.	Bending stiffness $1^{st}/2^{nd}$ loading		Max. test load excl./incl. self-weight	
	$EI_{con,1}$ [kNm^2]	$EI_{con,2}$ [kNm^2]	m_s [kg]	f_1 [Hz]	EI_1 [kNm^2]	EI_2 [kNm^2]	q_u [kN/m^2]	q_u^* [kN/m^2]
1.1	1'290	1'320	915	12.0	4'090	8'750	29.7	33.0
1.2	1'330	1'350	870	11.6	4'270	8'420	26.9	30.0
2	1'820	1'810	880	13.0	5'130	9'130	31.7	34.8
3	970	1'120	900	11.6	3'360	8'720	25.6	28.8
4	1'500	1'460	905	12.8	5'240	9'760	37.6	40.8
5	1'070	1'170	850	11.4	4'040	8'080	29.7	32.7
6	1'460	1'600	940	12.0	4'630	9'620	30.9	34.2
7	740	930	915	11.2	2'630	8'130	27.5	30.7
8	720	930	890	10.0	1'910	7'120	23.2	26.4
T1	–	–	945	9.2	2'460	4'670	12.4	15.7
T2	–	–	935	8.8	3'140	4'320	13.2	16.5

4.4 Discussion

4.4.1 Comparison with the results of the connection shear tests

Ductility and connection deformation capacity

In all specimens representing the longitudinal load-bearing direction of the investigated TCC slab, considerable ductility was observed. Fig. 4.21 shows the load-deflection curves of all tests and, as a reference, two limit predictions based on the minimum and maximum possible bending stiffness of the composite section. Using the measured MOE values (Tab. 4.3) and the reference cross-section geometry ($h_0 = 120\,\text{mm}$), the following two limit cases were assessed:

- $EI_{I,\gamma=1}$
  with a rigid connection and uncracked concrete (calculation with the n-method)
- $EI_{II,\gamma=0} = EI_{1,II} + EI_2$
  with no connection and cracked concrete. The bending stiffness of the cracked concrete section $EI_{1,II}$ was calculated considering the steel reinforcement bars as shown in Fig. 4.1.

Fig. 4.21 shows that the bending stiffness in the elastic phase was substantially lower than $EI_{I,\gamma=1}$ in all specimens. As expected, a good prediction of the bending stiffness can only be achieved if the flexibility of the connection is considered. However, this leads to an individual prediction for each specimen that will be presented and discussed in Chapter 6.4.

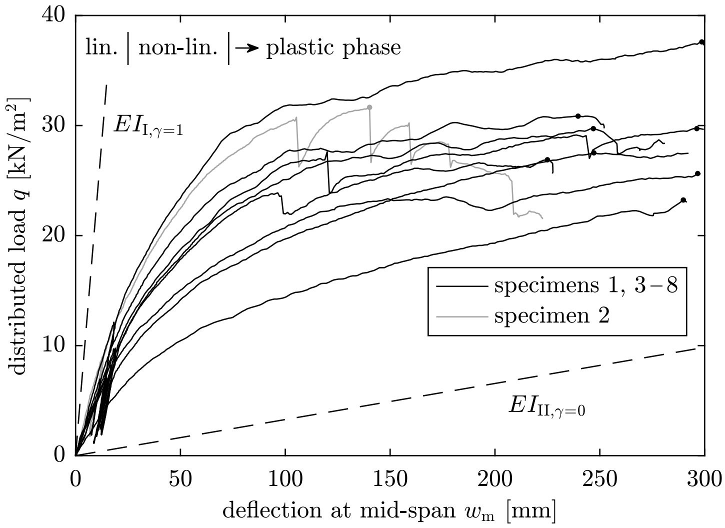

Fig. 4.21: Load-deflection curves of all longitudinal specimens and limit predictions based on the minimum and maximum possible bending stiffness of the composite cross-section.

Fig. 4.21 further shows that after the non-linear phase, all curves (exception: specimen 2) approach an asymptote that is approximately parallel to the prediction using $EI_{\mathrm{II},\gamma=0}$. This means that, after the connectors reach their shear capacity at the end of the non-linear phase, all additional load is carried by increasing bending moments in the partial cross-sections (cracked concrete section and timber section). The part of the load carried by composite action is equivalent to the vertical distance between the line based on $EI_{\mathrm{II},\gamma=0}$ and the respective load-deflection curve. This part remains approximately constant during the plastic phase, meaning that the shear force in the connectors did not significantly decrease throughout the experiment. Fig. 4.22 illustrates the amount of deformation that specimen 4 was able to accommodate during the plastic phase while the load was still increasing at the end of the experiment.

While also in the connection shear tests some ductility was observed, the connection deformation capacity was limited (Chapter 3). Except for type 1 and 2 connections without grouting, a brittle failure or a softening post-peak behaviour was always observed. However, the results of the bending tests indicate that the shear force in the connectors did not significantly decrease after reaching the shear capacity, even at large slip displacements up to $\Delta u \approx 40\,\mathrm{mm}$. In the following paragraphs, possible reasons for this difference in the observed deformation capacity are discussed.

In the specimens produced for the bending tests, an upper LVL beam was included, leading to a combined type 2/3 connection in the final state (Fig. 3.1c). In the connection shear tests, connection types 2 and 3 were investigated only separately and therefore, no direct information regarding a potential interaction between these two connections is available. However, a comparison of the results of push-out specimens B-2-5 and C-3-2 (geometry corresponding to the connections in the bending specimens) shows that the connection in concrete (type 3) is almost five times stiffer. In addition, the cross-section area and MOE of the concrete section are significantly higher than in the case of the upper LVL beam. Therefore, the contribution of the

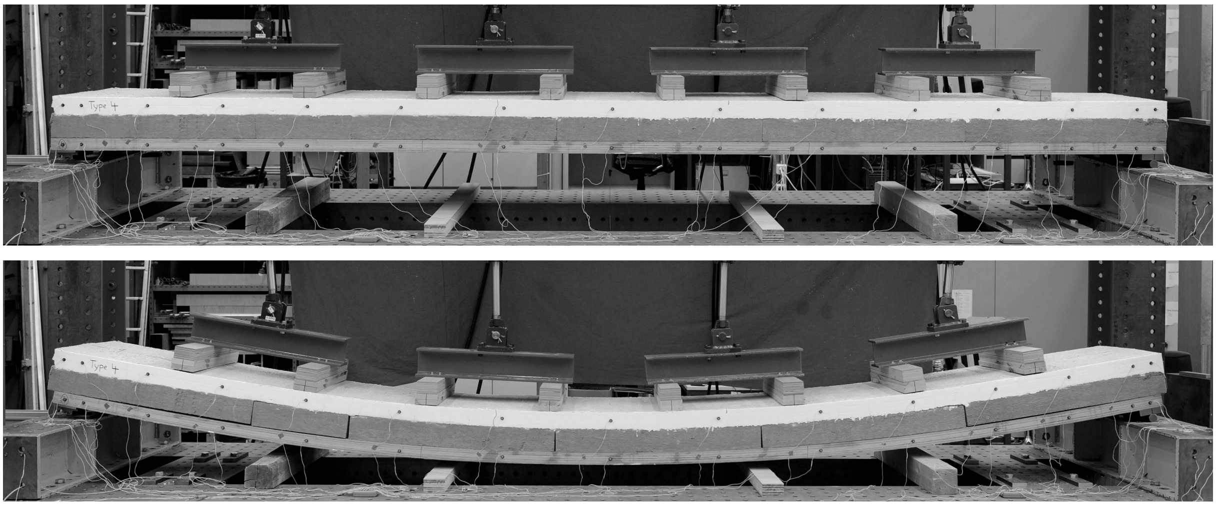

Fig. 4.22: Photos of specimen 4 before the test and at $q_\mathrm{u} = 37.6\,\mathrm{kN/m^2}$, $w_\mathrm{m} = 299\,\mathrm{mm}$.

upper LVL beam to the bending stiffness of the composite member is expected to be negligible. Specimen 2 presents an exception, with a substantially stiffer, grouted type 2 connection. In this specimen, a higher stiffness was observed in the bending test. Furthermore, opening this specimen after the test revealed shear failures in the upper LVL beam, confirming that this member had been subjected to higher stresses than in the other specimens, where no such failures were observed. The plastic phase was not as extended as in the other specimens and a softening post-peak behaviour with several load drops was observed. This indicates that the presence of the upper LVL beam may indeed have had an influence on the connection deformation capacity. It is possible that in the other specimens, the upper LVL beam, while being negligible during the linear phase, had a positive influence on the connection behaviour in the plastic phase of the experiment. The upper LVL beam may have offered additional load paths in the connection of the steel tube with the concrete, acting as a flange on the steel tube. However, based on the collected data it is not possible to clearly verify or quantify this influence. Further bending tests on specimens without an upper LVL beam would be necessary as a comparison.

On the timber side, the connections were built identically for both push-out and bending tests. However, the observed shear failures were different in the two experimental campaigns. While in the push-out tests the shear failures always developed over the full specimen width of 220 mm, this did not happen in the bending tests because the LVL plate was significantly wider (600 mm). Therefore, block shear failures were often observed instead, as shown in Fig. 4.10b. Given that the shear failures were the main factor limiting the deformation capacity in the push-out tests, this may explain a part of the observed difference in ductility between the two test campaigns. Further push-out tests with an increased specimen width could be carried out to achieve a similar block shear mechanism and to further investigate the connection deformation capacity in this case.

In the push-out tests on type 3 connections, the deformation capacity was limited by a concrete compressive failure close to the steel tube. The quality of the used concrete was not ideal. Especially the mix between aggregates and matrix was not sufficiently homogeneous, which was visible during casting and when preparing the concrete cylinders, resulting in low MOE values (Tab. 3.2). Even though the measured compressive strength reached the required values, it is possible that the poor mixing led to a lower local compressive strength and thus to a reduced deformation capacity of the connection. In further push-out tests, particular attention should be paid to the concrete quality in order to avoid this possible influence.

Furthermore, it should be mentioned that push-out tests can never perfectly replicate the mechanical situation in a bending beam. A push-out test setup is always subject to simplifications and often, discrepancies concerning the lateral forces acting on the push-out specimen (equivalent to vertical forces in the bending beam) have to be accepted. Therefore, the results of bending tests are often considered to be more significant when differences compared to push-out tests are observed. For example, Müller [59] adjusted the connection stiffness and shear capacity values determined in push-out tests after observing a slightly different behaviour in corresponding bending tests, so that they correctly represent the latter. In the present case, however, a similar adjustment of the connection deformation capacity would not be on the safe side. The main reason for this is that, based on the conducted experiments, it cannot be excluded that the upper LVL beam had a positive influence on this property. Therefore, the connection deformation capacity should be based on the results of the push-out tests until further bending tests without an upper LVL beam allow for more concise conclusions. The observed connection deformation capacity in the bending tests will be further discussed in Chapter 6.4, based on a comparison of model calculations with the measured test data.

Difference between first loading and reloading stiffness

In the connection shear tests, a substantial difference of the stiffness during first loading and reloading cycles was observed for connections of type 1/2 without grouting and type 3 (Chapter 3.3.5). The results of the bending tests confirm these observations. Tab. 4.6 shows the ratio of the bending stiffness EI_1/EI_2 in the formwork elements and in the final state, grouped based on the connection types. The specimens with standard connection type configuration 'g − f' showed almost no difference in stiffness in the construction state. This is because in these cases, the grouted type 1 connection is around eight times stiffer than the form-fitting type 2 connection. The stiffness of the entire steel tube connection is therefore mainly provided by the

Tab. 4.6: Ratio of bending stiffness during first loading and reloading.

Connection types*	n	$EI_{con,2}/EI_{con,1}$			EI_2/EI_1		
		min	mean	max	min	mean	max
g − f	6	0.97	1.06	1.15	1.86	2.11	2.60
g − g	1	–	0.99	–	–	1.78	–
f − f	2	1.26	1.27	1.29	3.09	3.41	3.73

* g = grouted connection, f = form-fitting connection without grouting

former, which showed no significant pre-loading dependency in the push-out tests. In the final state, this changes because a significant contribution to the stiffness is made by the type 3 connection, which showed the strongest dependency in the push-out tests. While in the specimens with connection types ‘g−g’ the values of EI_1/EI_2 are lower, they increase in the case of connection types ‘f−f’, which is in agreement with the results of the push-out tests. The coherence of these static bending stiffnesses and the measured fundamental frequencies is further investigated in Chapter 6.4 by means of model calculations.

4.4.2 Influence of parameter variation in the longitudinal specimens

Number of connectors

The influence of the number of connectors per shear area m was investigated with a subset of four specimens in longitudinal direction. The load-deflection curves of these specimens are plotted in Fig. 4.23a and the main results in the final state as a function of m are shown in Fig. 4.23b and 4.23c. The results clearly show that a higher number of connectors leads to a consistent

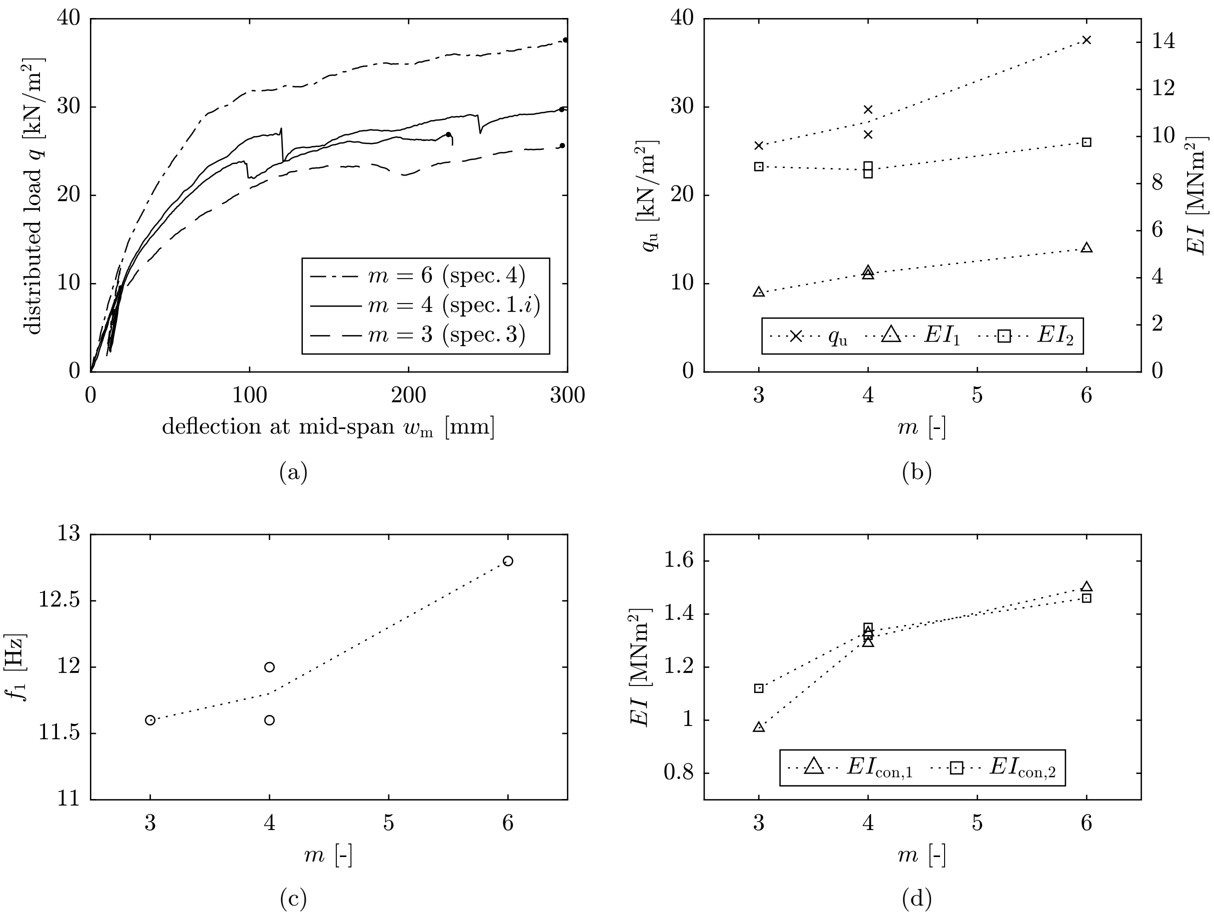

Fig. 4.23: Influence of the number of connectors per shear area m on (a) load-deflection curves in the final state, (b) maximum test load q_u and bending stiffness EI in the final state, (c) fundamental frequency in the final state, (d) bending stiffness of the formwork elements in the construction state.

increase in bending stiffness, load-bearing capacity and fundamental frequency. This is according to the expectations, as a higher number of connectors increases the connection efficiency of the composite structure. The same conclusion is also valid for the formwork elements in the construction state (Fig. 4.23d). Regarding ductility, no influence of the number of connectors was observed.

Interlayer height

The influence of the interlayer height h_0 was investigated with a subset of four specimens in longitudinal direction. The load-deflection curves of these specimens are plotted in Fig. 4.24a and the main result values in the final state as a function of h_0 are shown in Fig. 4.24b and 4.24c. The influence of the interlayer height h_0 is more complex than the number of connectors m. Increasing h_0 leads to a larger static height of the composite member, which generally leads to a higher bending stiffness and load-bearing capacity, if the connection system is sufficiently stiff. However, increasing h_0 also leads to a larger lever arm of the steel tubes and therefore to a lower

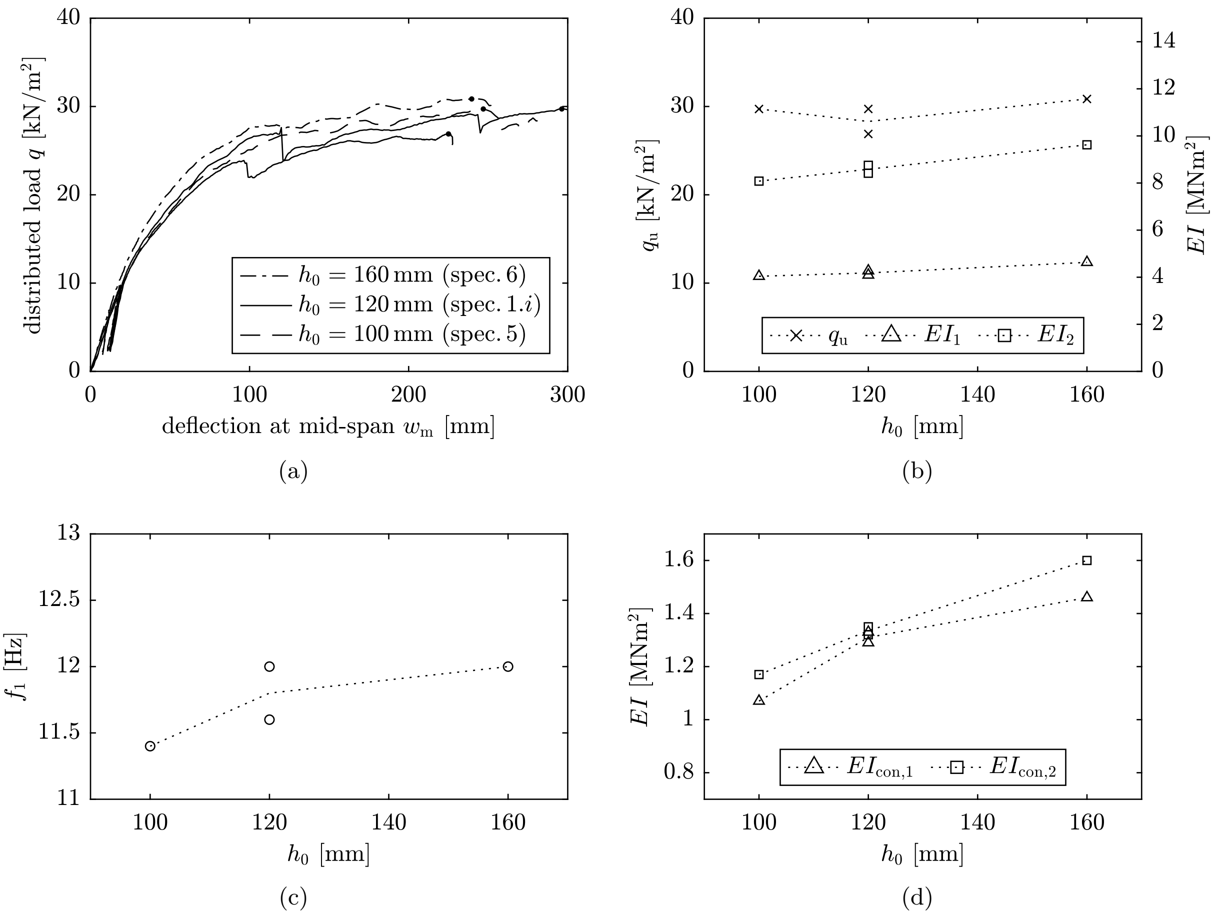

Fig. 4.24: Influence of the interlayer height h_0 on (a) load-deflection curves in the final state, (b) maximum test load q_u and bending stiffness EI in the final state, (c) fundamental frequency in the final state, (d) bending stiffness of the formwork elements in the construction state.

connection stiffness K per connector. In the tested specimens, these two influences neutralised each other, leading to a similar first loading bending stiffness EI_1 and load-bearing capacity q_u in all cases. Increasing h_0 by 60% (from 100 to 160 mm) resulted in an only 15% higher EI_1 and 4% higher q_u.

However, this does not mean that a higher bending stiffness and load-bearing capacity can generally not be achieved by increasing h_0 in the TCC slab with steel tube connection. Whether this is possible or not depends mainly on the following two factors:

- The connection efficiency in the composite member before changing h_0: If the connection efficiency is low from the beginning, the part of the external load carried by composite action (pair of normal forces in the partial sections) is low, and therefore, increasing h_0 will not significantly influence the structural behaviour.

- The rotational stiffness k_m of the steel tube connections: High values of k_m allow to minimise the loss of connection stiffness K with increasing h_0.

The γ-method, described in Chapter 2.2.2, is the simplest and most widely used model to describe the load-bearing behaviour of TCC structures and is based on the definition of the γ-factor (Eq. 4.4). While this factor should not be used to assess the efficiency of a given composite structure in absolute terms, it is a useful indicator to qualitatively compare the connection efficiency in different composite systems and it shows the main influencing parameters.

$$\gamma_1 = \frac{1}{1 + \frac{\pi^2 E_1 A_1 s_\mathrm{ef}}{K l^2}} \tag{4.4}$$

Combining Eq. 4.4 with the considerations made above, it can be concluded that the following boundary conditions are favourable for achieving a higher bending stiffness and load-bearing capacity by increasing h_0:

- low stiffness EA of the partial cross-sections

- large span l

- large number of connectors m (low distance between the connectors s_ef)

- high rotational stiffness k_m of the steel tube connections

This explains why the increase of bending stiffness in the formwork elements during construction is substantially larger than in the final state (Fig. 4.24d). The stiffness EA of the upper partial cross-section is much lower in the construction state (LVL beam 180 × 60 mm) than in the final state (concrete 600 × 80 mm). Furthermore, Fig. 4.24b shows that the increase of the reloading stiffness EI_2 is larger than for EI_1, which can be explained with the higher rotational stiffness k_m in this case. The noticeable increase in the measured fundamental frequency (Fig. 4.24c) can be explained in the same way, as it depends on the reloading stiffness of the connection. Regarding ductility, no influence of the interlayer height was observed.

Connection stiffness

Different connection types were tested in a subset of five specimens to assess the influence of the stiffness per connector K on the structural behaviour. The main purposes of these tests were:

- Re-evaluating and confirming the chosen connection concept with a grouted type 1 connection and, in case of a production process using cast-in-situ concrete, a form-fitting type 2 connection, as described in Chapter 1.3.
- Providing a broader experimental basis for the validation of the corresponding calculation models (Chapter 6), covering a wider range of connection efficiencies.

Fig. 4.25 shows that the choice of the connection type has a distinct influence on the structural behaviour. The absence of grouting in the type 1 connection ('f−f') leads to a substantial loss in bending stiffness and a lower fundamental frequency and load-bearing capacity. Using grouting in all connections ('g−g') allows to consistently improve these properties with respect to the standard configuration. However, as discussed already in Chapter 4.4.1, the failure mechanism in this specimen was substantially less ductile than in all other cases.

The results confirm that the chosen connection concept with grouted type 1 connections is the best option for practical use in TCC slabs with an interlayer. Form-fitting type 1 connections are not promising due to their substantially lower stiffness and using grouting in type 2 connections does not seem to justify the higher production cost. While in the latter case stiffness and load-bearing capacity are improved, the failure mode is less ductile, which would lead to an overall loss of robustness in the system.

4.4.3 Transversal load-bearing behaviour

The load-deflection curves of the two specimens investigating the transversal load-bearing direction of the TCC slab are plotted in Fig. 4.26, along with the longitudinal reference specimens. The load-bearing capacity of specimens T1 and T2 was similar and reached around 45% of the corresponding longitudinal specimens 1.1 and 1.2. In terms of bending stiffness EI_1, specimens T1 and T2 reached 60% and 75% of the longitudinal pendant, respectively. This confirms that one additional steel tube connector can increase the bending stiffness substantially. Not only the regression value EI_1 was higher in specimen T2, but also the linear phase lasted longer, up to a load of almost $0.7 \cdot q_\mathrm{u}$, which is clearly visible in Fig. 4.26.

With increasing load, a visible influence of the side connection was observed in both experiments. During the linear phase in the beginning of the tests, no significant influence was visible. However, the recorded measurement data did not allow for a quantification of the side connection stiffness during this phase.

Considering that the used beech LVL plates have a cross-layer ratio of only 19%, the measured bending stiffness of $60-75\%$ of the longitudinal direction is an encouraging result. Based on these findings, it can be expected that in a quadratic two-way spanning TCC slab, activating the transversal load-bearing direction significantly improves the structural behaviour, especially regarding vibrations and deflections under service loads.

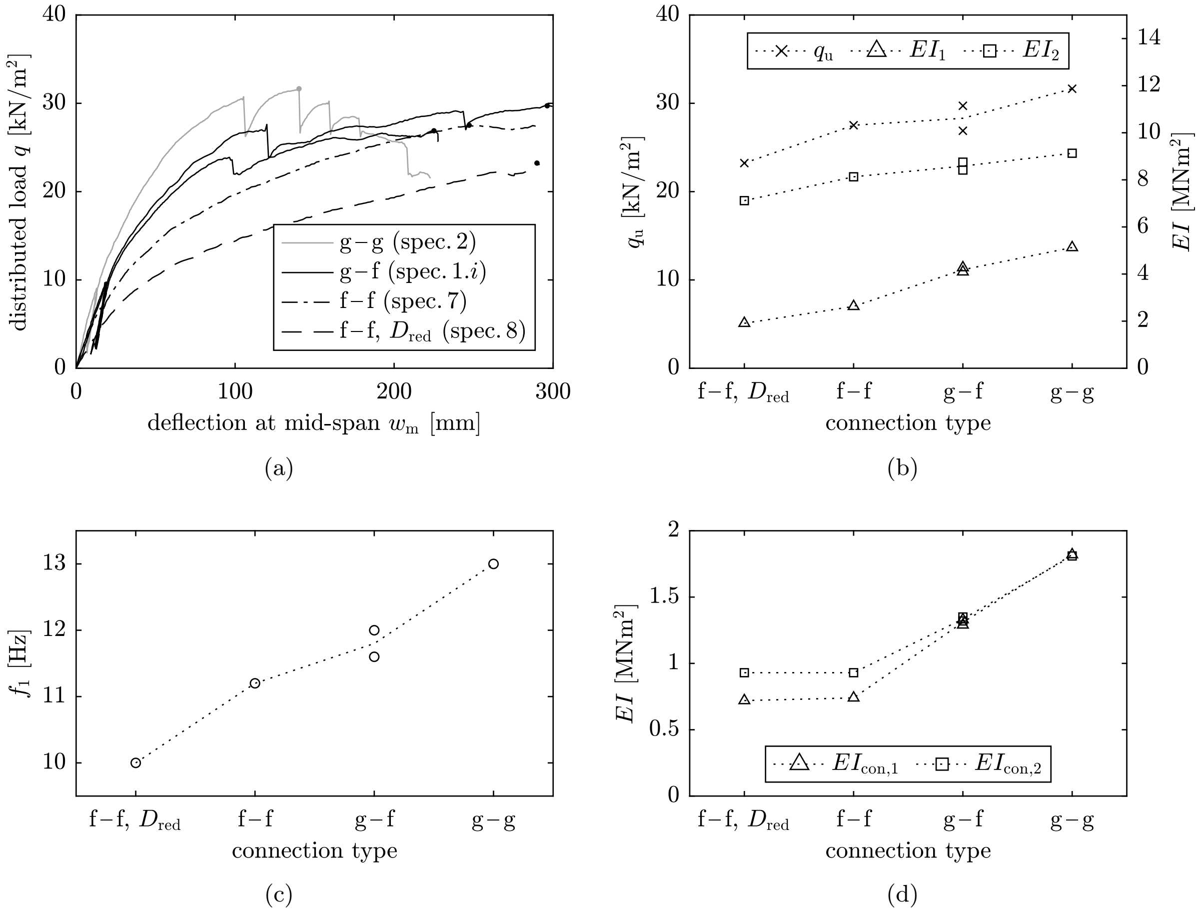

Fig. 4.25: Influence of the connection type on (a) load-deflection curves in the final state, (b) maximum test load q_u and bending stiffness EI in the final state, (c) fundamental frequency in the final state, (d) bending stiffness of the formwork elements in the construction state.

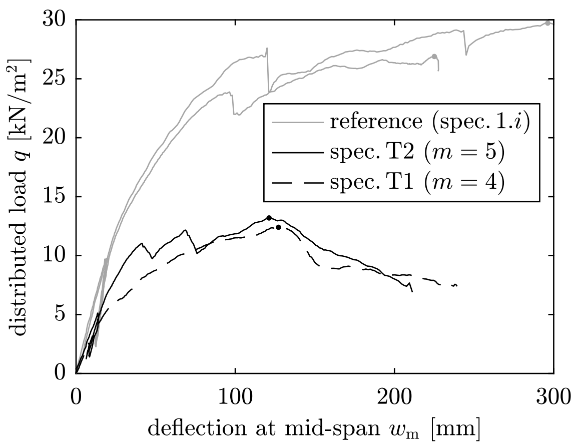

Fig. 4.26: Load-deflection curves of the two transversal specimens, compared to the longitudinal reference specimens.

4.5 Conclusions

The load-bearing behaviour of the TCC slab with steel tube connection was studied in a series of uniaxial bending tests comprising eleven specimens. The collected experimental data provide a sound basis for the validation of the calculation models for uniaxial bending (Chapter 6), covering a wide range of different connection efficiencies. Below, the main conclusions drawn from this test campaign are summarised:

- The observed load-bearing behaviour can be divided into three phases: a linear phase up to $0.4 \cdot q_\mathrm{u}$, a non-linear phase up to $0.8 \cdot q_\mathrm{u}$ and a plastic phase, during which the deflections increase substantially. In almost all specimens, no significant load drop due to a brittle failure was observed throughout the experiment, reaching a mid-span deflection of $w_\mathrm{m} \approx l/18 \approx 300\,\mathrm{mm}$.

- The structural behaviour of the TCC slab is governed by the connection behaviour, not by cross-sectional failure modes. A ductile failure mode with limited deformation capacity was already observed in the connection shear tests. The results of the bending tests, however, indicate a plastic connection behaviour up to slip displacements of $\Delta u \approx 40\,\mathrm{mm}$, which is significantly more than what would be expected based on the connection shear tests. A part of this difference may be explained by poor concrete quality and premature shear failures reducing the deformation capacity in the connection shear tests. However, it cannot be excluded that also the upper LVL beam that was integrated in the bending specimens, had a positive effect on the connection ductility.

- The chosen connection concept with a grouted type 1 connection and, in case of a production process using cast-in-situ concrete, a form-fitting type 2 connection, as described in Chapter 1.3, was confirmed to be the optimal solution for practical use in TCC slabs with an interlayer.

- The results consistently show that a higher number of connectors leads to a significant increase in bending stiffness and load-bearing capacity.

- In the tested specimens, increasing the interlayer height h_0 did not lead to a substantially higher bending stiffness or load-bearing capacity. The positive effect of a larger static height of the composite beam is compensated by a reduced connection stiffness K due to the larger lever arm of the steel tubes.

- The two specimens in transversal direction reached a bending stiffness of $60-75\%$ of the corresponding longitudinal specimen. Based on this result, a significant contribution of the transversal load-bearing direction can be expected in the two-way spanning version of the TCC slab with steel tube connection (Chapters 5 and 7).

Chapter 5

Biaxial bending test

5.1 Introduction

This chapter covers the experiments that were conducted to study the biaxial load-bearing behaviour of the TCC slab with steel tube connection. Several static and dynamic tests were performed on one quadratic specimen of 5.46 m side length. The main objectives of this experimental campaign were:

- Determining the orthotropic stiffness parameters of the two-way spanning TCC slab
- Investigating the stiffness, natural vibration frequency, load-bearing capacity and ductility of the TCC slab in biaxial bending
- Understanding the structural behaviour and the governing failure mechanisms
- Providing experimental data as a basis to validate the calculation models for biaxial bending (Chapter 7)

Fig. 5.1 shows an overview of this experimental campaign, which was divided into two main phases. The first phase was dedicated to the determination of the orthotropic stiffness parameters in static loading tests under service loads. For this purpose, a test setup was developed that allowed to vary the support conditions of the slab (Chapter 5.2.2). Fig. 5.2a, 5.2b and 5.2c illustrate the concept of the three static loading tests conducted in this phase. The bending stiffness in x- and y-direction EI_{x} and EI_{y} were determined in uniaxial bending tests (two line supports on the respective opposite edges of the slab). For the third test, point supports were installed in all four corners. One of the supports was lowered while measuring its support force and vertical displacement, which allowed for a calculation of the torsional stiffness EI_{xy}.

The maximum load in all static loading tests during phase 1 was chosen such that no irreversible deformations due to concrete cracking or a connection failure should occur in the specimen. Dynamic tests were performed to determine the fundamental frequency before and after each experiment (Fig 5.1). A comparison of the respective measurement results allowed to detect a possible change in the specimen stiffness due to unwanted cracks or connection failures.

As shown in Fig. 5.1, the fundamental frequency in the biaxial test setup was determined before and after phase 1. A comparison of these results confirmed that no significant change in stiffness occurred in the static loading tests and during the test setup modifications.

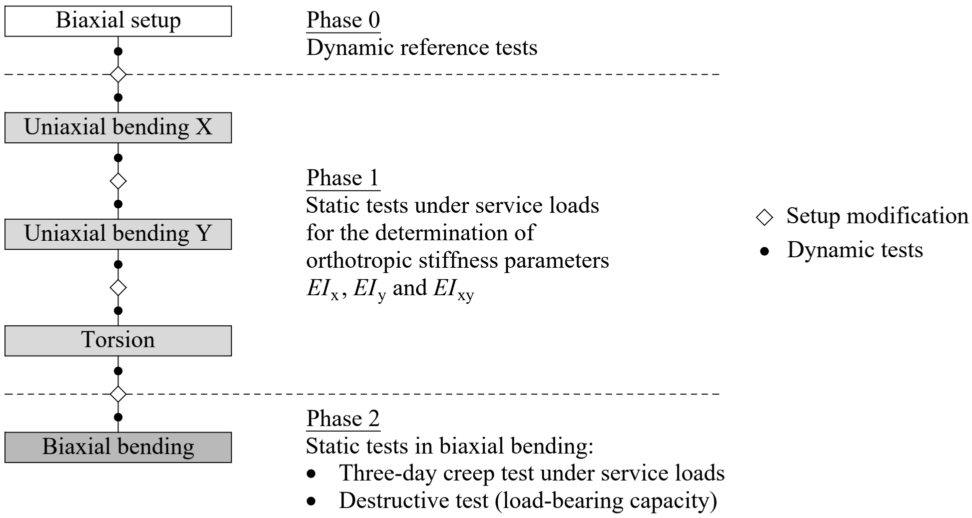

Fig. 5.1: Overview of the experimental campaign on a two-way spanning TCC slab including static and dynamic tests in different support conditions.

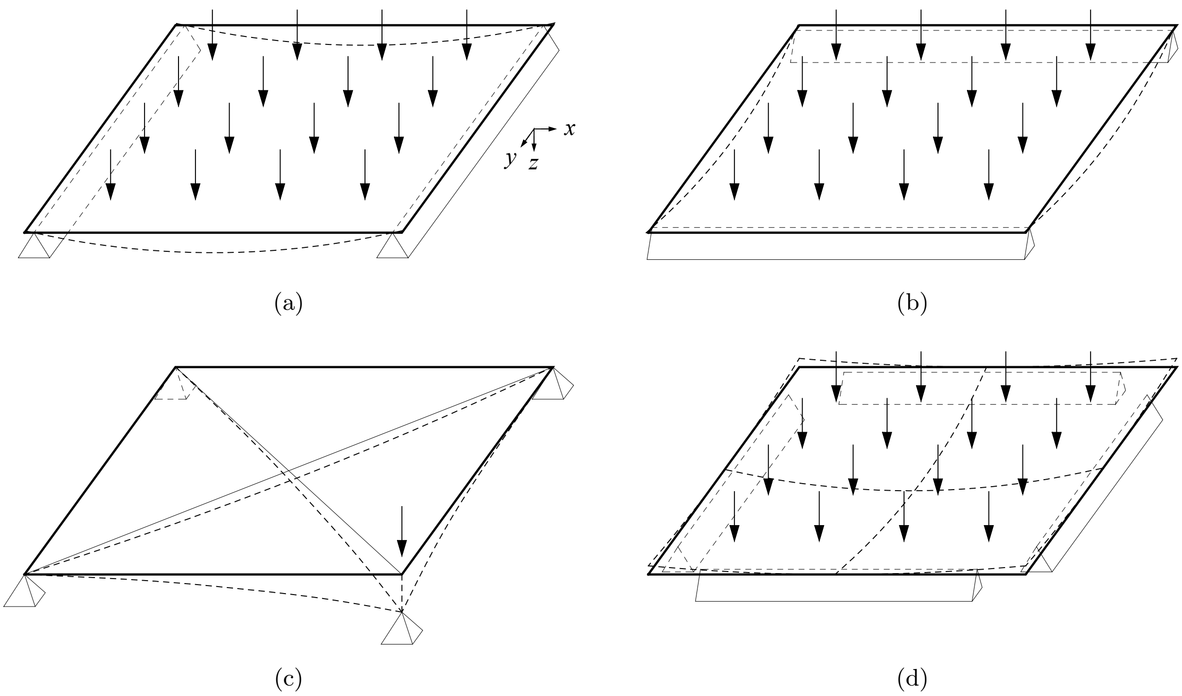

Fig. 5.2: Test concept for the determination of the orthotropic stiffness parameters: (a) bending stiffness in x-direction EI_x, (b) bending stiffness in y-direction EI_y, (c) torsional stiffness EI_{xy} and (d) load-bearing behaviour in biaxial bending.

The second phase focused on the investigation of the global load-bearing behaviour of the slab in a two-way spanning setup. Line supports were installed on all four sides of the slab (Fig. 5.2d). After a three-day creep test under service loads, the load-bearing capacity of the two-way spanning TCC slab was determined by means of a destructive test.

The main findings of this experimental campaign are presented and discussed in this chapter. A detailed report of all conducted experiments is provided in [44].

5.2 Materials and methods

5.2.1 Specimen

The specimen for the biaxial bending test consisted of three elements of 5.46 m length and 1.82 m width (maximum width of *BauBuche Q* plates). The element length was chosen as three times the width so that a quadratic specimen would result after assembly. These elements were fully prefabricated in the production facilities of *Implenia Schweiz AG*. In contrast to the specimens tested in uniaxial bending (Chapter 4), no upper LVL beam was included. After transporting the three elements to the testing laboratory at ETH Zurich, the specimen was assembled directly in the test setup. Fig. 5.3 shows the geometry of the assembled specimen and Tab. 5.1 lists all materials that were used in the production. Concrete tests were performed to determine the MOE according to SIA 262/1 [77], the cylinder compressive strength according to EN 12390-3 [11] and the splitting tensile strength according to Chen [16]. A detailed report of these tests is provided in [44]. Tab. 5.2 shows the main results of the material tests.

A concrete edge beam (① in Fig. 5.3) was included along the four sides of the specimen for the introduction of the support reaction forces. The edge beams contained no longitudinal reinforcement and they were not connected at the interface between the elements. Fig. 5.4a shows a photo of one of the two side elements before concreting.

The steel tubes (④) were arranged in a 9×9 grid with a uniform distance of 600 mm. This corresponds to the simplest possible way of arranging the steel tubes in a two-way spanning slab. This connector layout was chosen in the expectation that this would simplify the comparison with the model predictions. Four steel tubes in this grid were omitted because holes in the test specimen were necessary at these positions (⑤) due to the design of the test setup (Chapter 5.2.2). The standard connection concept with a grouted type 1 connection was applied (Fig. 3.1a). The embedment depth of the steel tube in concrete was 50 mm, leaving a concrete cover of 30 mm.

Four anchor points were installed on each of the three elements (③), which allowed to move them using a crane. Furthermore, four anchor points were installed in the concrete edge beam (②), which allowed to lift the entire specimen during the modification of the test setup. The location of all anchor points was chosen such that no significant tensile stresses would occur in the concrete layer during this process.

The side connections (⑨) were planned in analogy to the specimens tested in uniaxial bending (Fig. 4.3). In contrast to those specimens, the cutout in the LVL plate was done such that the connections could be accessed and inspected from below. An attempted assembly of the three elements revealed that the planned side connection concept is not applicable for elements of this size. The envisioned direct connection with a coupling nut does not allow for any production tolerance. This led to a blocking of the nuts and eventually the destruction of the threads of the GIR. Based on this experience, an improved concept for the side connections was developed as described in Chapter 1.3.

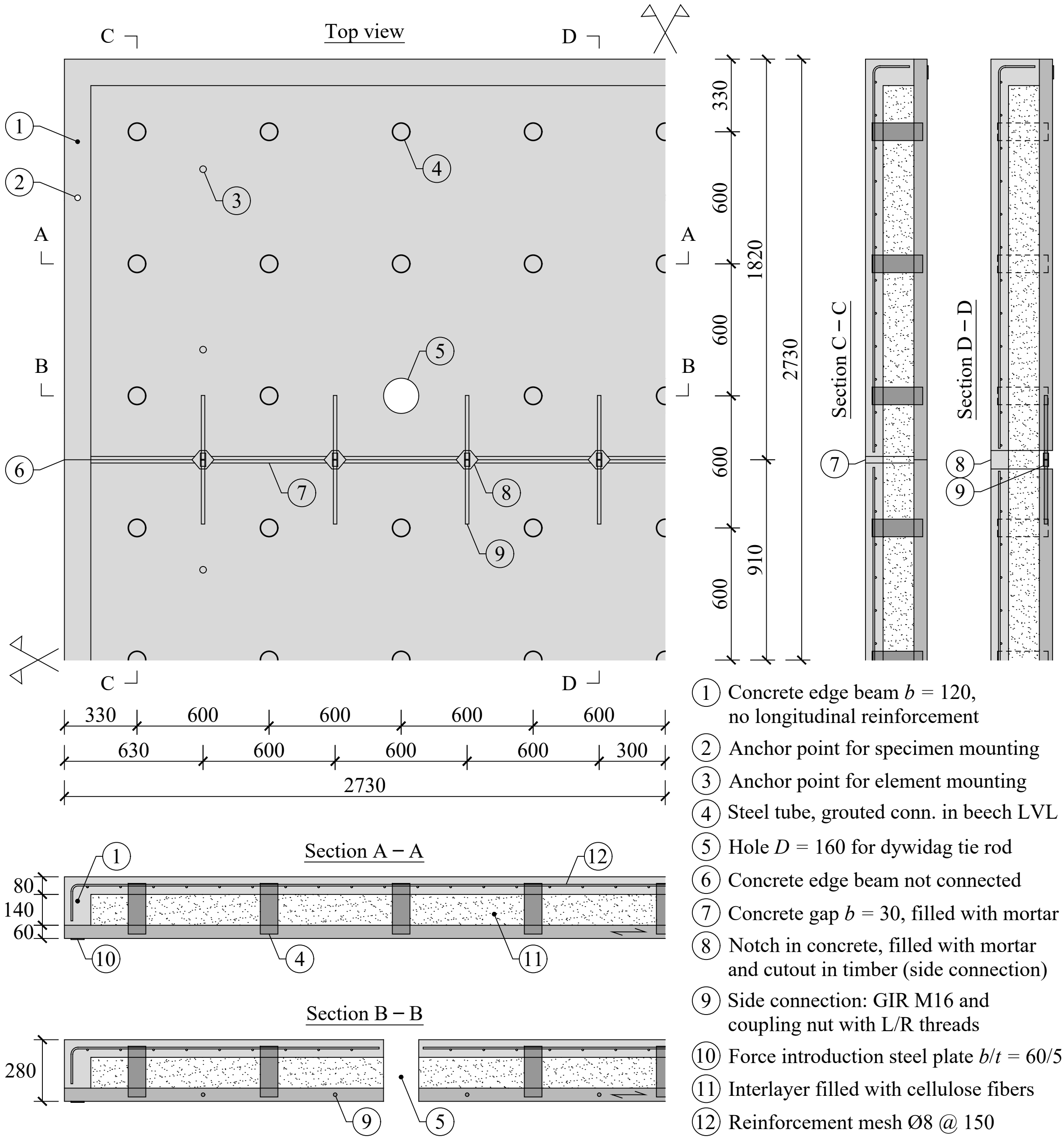

Fig. 5.3: Biaxial bending specimen: top view of one quarter of the symmetric quadratic specimen and sections in both directions, dimensions in [mm].

For the side connection in the test specimen, an alternative concept had to be found based on the given boundary conditions. Fig. 5.5 shows the chosen solution using a custom made oversized nut that was placed on the GIR and filled with an epoxy adhesive anchoring system. A rubber sealing ring ensured a central position of the GIR. Two holes were drilled in the nut to avoid any air inclusions during the injection. The adhesive was injected from below until it exited the upper hole. The load-bearing capacity of this connection was determined in six tensile tests. A mean value of 69.1 kN was measured, which corresponds to 55% of the tensile strength of the M16 threaded rod. A detailed report of these experiments is provided in [44].

The three prefabricated elements were positioned with the laboratory crane (Fig. 5.4b) and pulled together with two ratchet lashing straps (Fig. 5.4d). After injecting the side connections (Fig. 5.6a), the interlayer in these locations was filled with styrofoam. The gap in the concrete layer between the elements was filled with mortar, creating a form-fitting joint (Fig. 5.6b). The concrete edge beams were flush with the LVL plate, resulting in a contact joint at the element interfaces (Fig. 5.6c).

Tab. 5.1: Materials used in the biaxial bending specimen.

Material	Description	Details
Beech LVL	Thickness	60 mm
(*BauBuche Q*)	Veneer layout	||| − || − |||||| − || − |||
	Cross-layer ratio	19%
Cellulose fibres	Isocell	Compressed to approx. 60 kg/m^3
Concrete	Ordered quality	C30/37
	Max. aggregate size	16 mm
	Admixture	MasterLife SRA 895 (2% of cement mass)
Jointing mortar	ProOne GROUT 4	For concrete joints between the elements
Steel tubes	ROR 82.5/3.2	P235TR1, welded
Grout type	Sikadur®-42 HE	High performance epoxy grouting system [79]
Glued-in rods	Threaded rods M16	Strength grade 8.8
	Resin and hardener	WEVO EP 32 S / B22 TS [23]
	Connection injection	Hilti HIT-RE 500 V3 [62]

Tab. 5.2: Results of concrete tests, 89 days after production.

		Mean value [MPa]	COV	n
Modulus of elasticity	E_1	37'200	5%	3
Cylinder compressive strength	$f_{1,c}$	50.4	2%	3
Splitting tensile strength	$f_{1,t,sp}$	3.9	5%	4


(a)

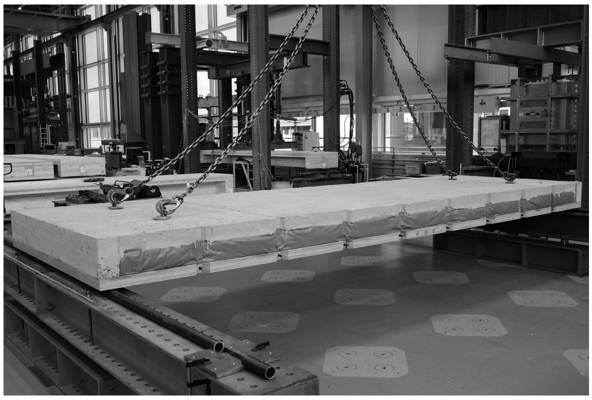
(b)


(c)

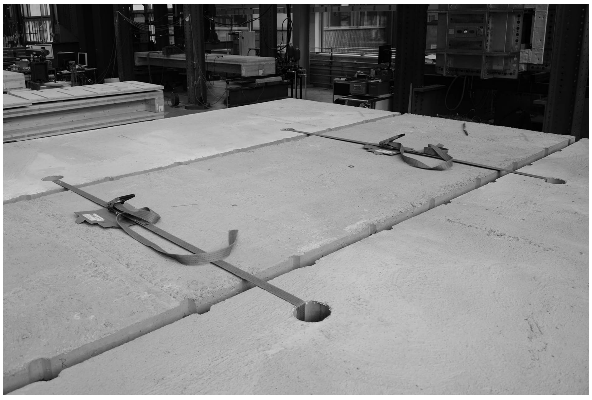
(d)

Fig. 5.4: (a) Prefabrication of one of the two side elements with concrete edge beam, cellulose fibres (packed in plastic), reinforcement bars, steel tubes, four anchorage points and placeholders for the two holes in the element, (b) & (c) positioning of the prefabricated elements with the laboratory crane and (d) with two ratchet lashing straps during the assembly of the specimen in the test setup.

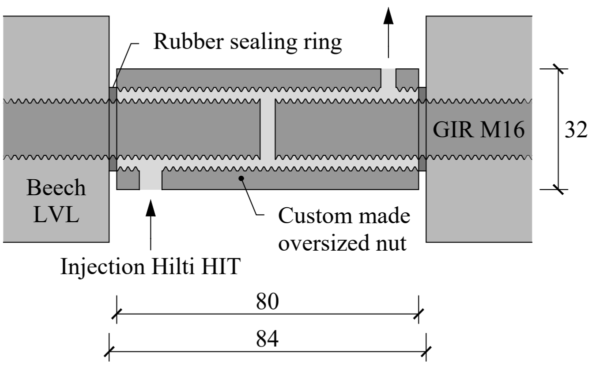

(a)

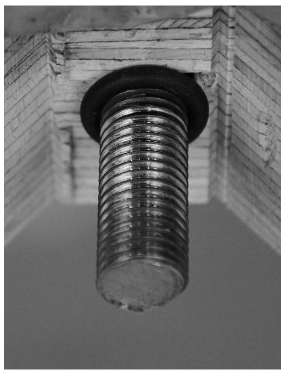
(b)


(c)

Fig. 5.5: Solution for the side connection in the specimen after the initial concept failed: (a) geometry and injection concept, (b) GIR with rubber sealing ring, (c) custom made oversized nut with two holes for the injection and an inner thread for optimal adhesive bonding.

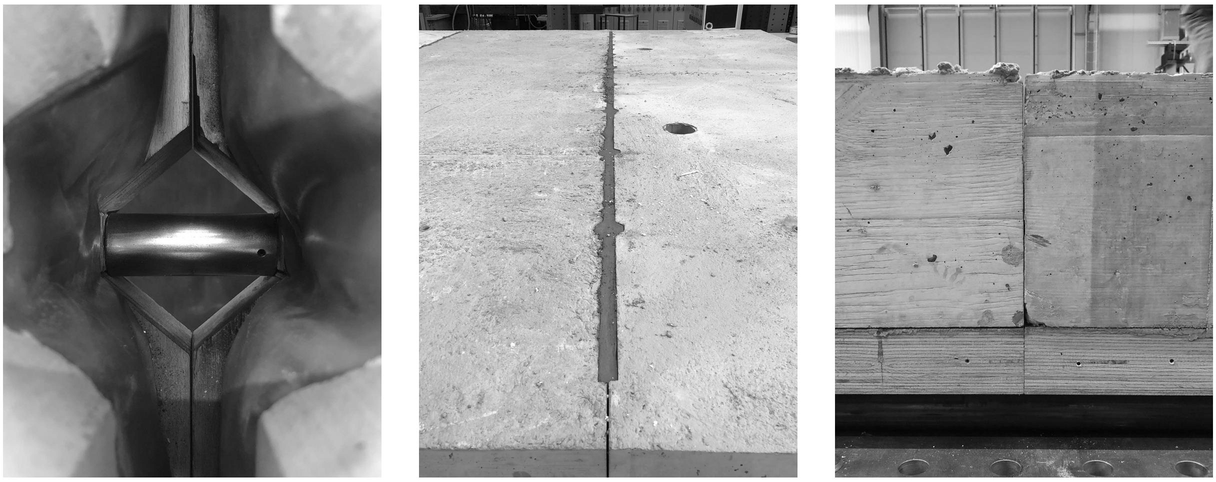

(a) (b) (c)

Fig. 5.6: (a) Assembled side connection before injection, (b) form-fitting joint of the concrete layer at the element interfaces filled with mortar and (c) contact joint of the concrete edge beam.

5.2.2 Test setup

The concept of this experimental campaign (Fig. 5.1 and 5.2) involved static loading tests on the same specimen in four different support conditions. A special test setup had to be designed to accomplish this with a specimen of this size and weighing approximately ten tons. The developed solution is illustrated in Fig 5.7. In a classical test setup with hydraulic cylinders mounted on a frame above the specimen (such as in Fig. 4.4), access to the specimen by crane is not easily possible. Therefore, the setup was inverted. Four hydraulic hollow piston cylinders (11 in Fig. 5.7) were installed beneath the strong floor (13 and Fig. 5.9a), suspended using dywidag tie rods (10). These rods passed through the holes in the test specimen and were connected to a load distribution construction on top of the specimen. This connection was constructed using a steel support cone and a spherical nut (5 and Fig. 5.9d) to avoid the transmission of any bending moments. An additional nut (11) was installed beneath the specimen so that the hydraulic cylinders could be mounted directly on the strong floor whenever they were not needed during an experiment. All cylinders were connected to the same hydraulic circuit with the oil pressure controlled by a manually operated pump. The four load distribution constructions led to a total of 16 point forces in the bending tests. Thick elastomer mats (6) were placed between the cross beams (3) and the specimen to compensate for uneven deformation and to avoid local force concentrations. The resulting situation with 16 point loads is comparable to a slab subjected to a uniformly distributed load.

Four line supports and four point supports were constructed to cover all required test configurations. All of these support constructions could be moved either manually (point supports) or using two manual pallet jacks (line supports) while the specimen was suspended on the laboratory cranes (Fig. 5.9b). This allowed for a relatively easy modification of the test setup. Fig. 5.8 shows the resulting four support configurations used in this experimental campaign.

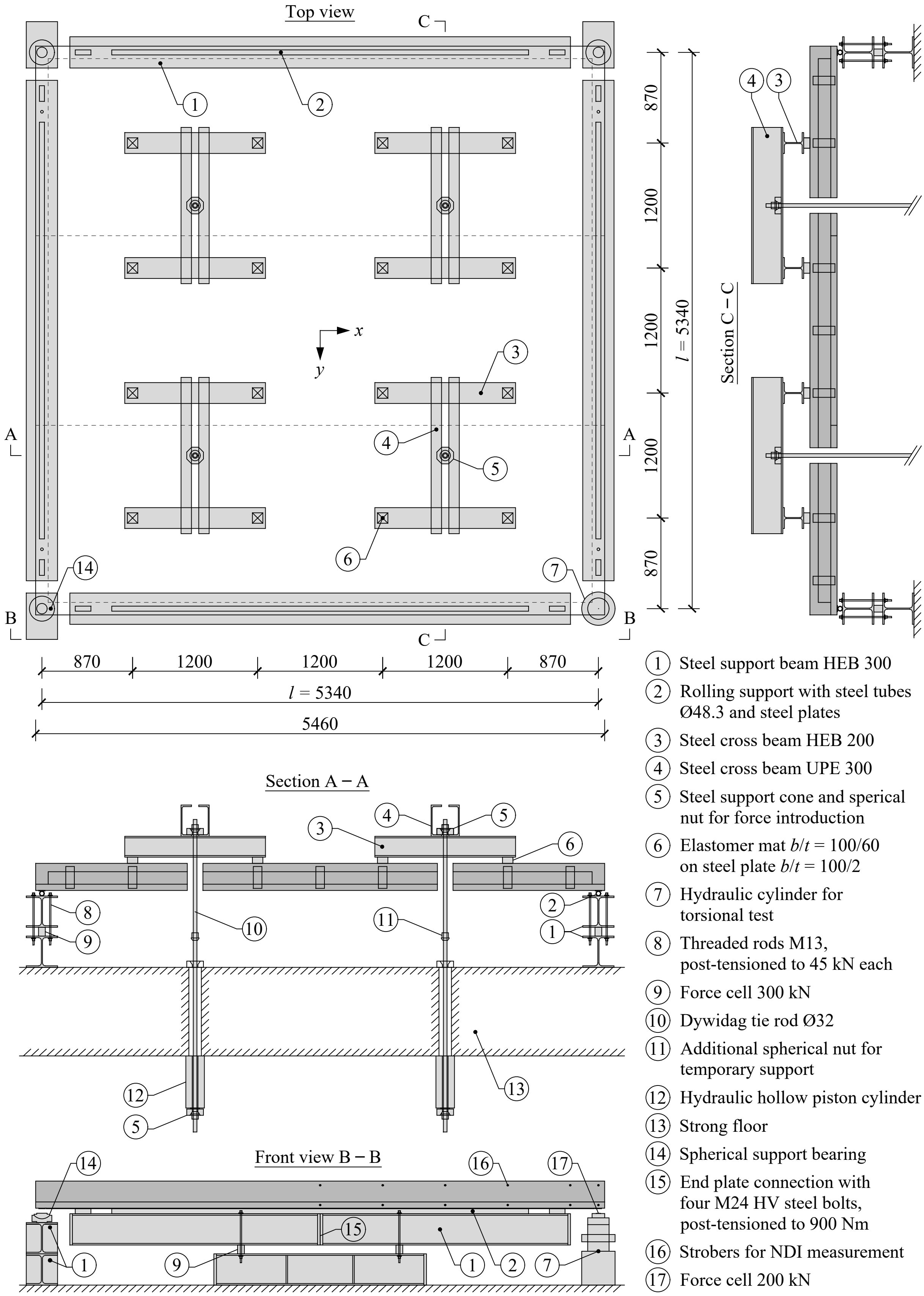

Fig. 5.7: Test setup used for the biaxial bending experiments, all dimensions in [mm].

Each of the line supports (Fig. 5.9c) had two built-in force cells (9 in Fig. 5.7), allowing to measure the support reactions during the experiments. Each force cell was post-tensioned to approximately 90 kN with two threaded rods (8 and Fig. 5.9e) to provide the necessary stability of the support construction. Steel tubes (2) of 4 m length minimised the transmission of any horizontal support forces. For the uniaxial stiffness tests during phase 1, additional short tubes were added, increasing the effective length of the line supports to 4.7 m.

Three point supports were built using HEB 300 steel profiles (1) and spherical support bearings (14 and Fig. 5.9f). A hydraulic cylinder with a locking nut and a force cell was used as the fourth point support (7 and Fig. 5.9g). In the torsional tests performed by Higgins et al. [35] and by Loebus & Winter [50], an external load was applied in one of the specimen corners. This was not necessary in the present study. A controlled lowering of one point support led to a reduction of the reaction force in this support and in the one diagonally opposite. Due to the 2.5 times larger span than in the mentioned experiments, this differential point force was sufficient to assess the torsional stiffness. Furthermore, the complete removal of one point support would already have led to substantial concrete cracking, which was unwanted in this phase of the experimental campaign.

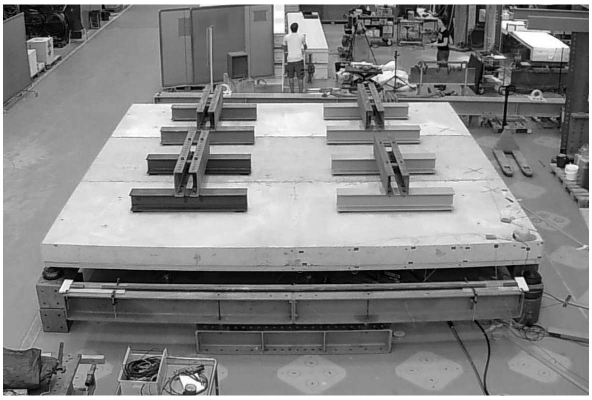

(a)

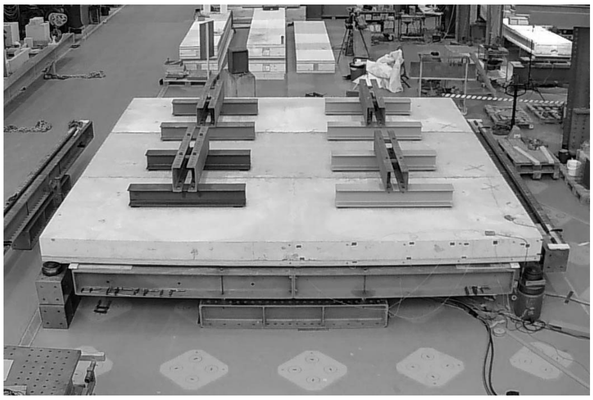

(b)

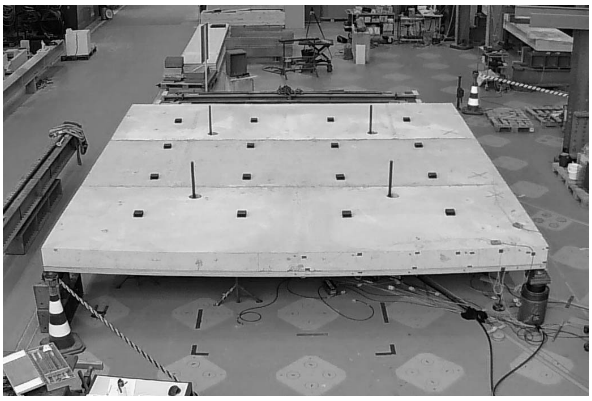

(c)

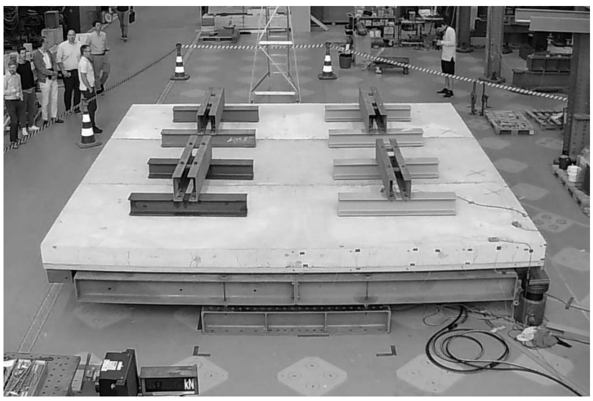

(d)

Fig. 5.8: Test setup configurations from the bird's eye view: (a) uniaxial bending in x-direction, (b) uniaxial bending in y-direction, (c) torsion and (d) biaxial bending.

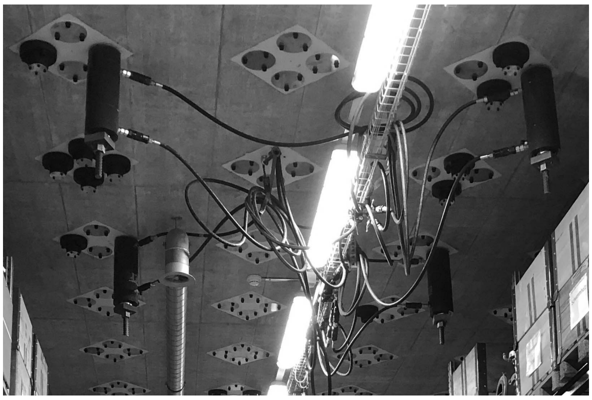

(a)

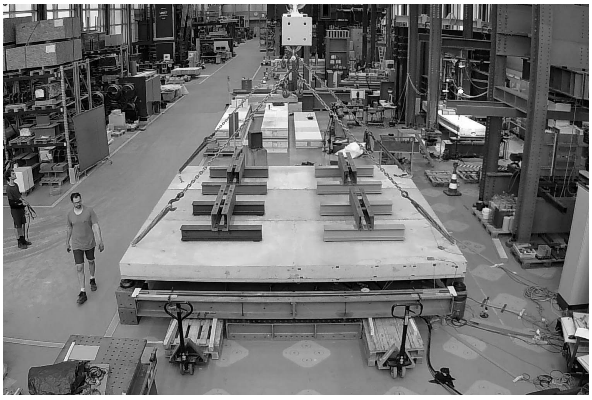

(b)

(c)

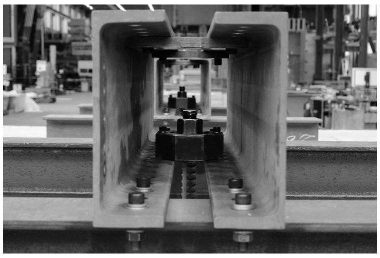

(d)

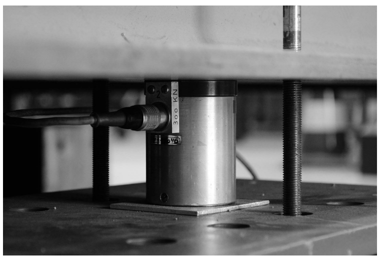

(e)

(f)

(g)

Fig. 5.9: Photos of the test setup: (a) hydraulic hollow piston cylinders installed beneath the strong floor, (b) modification of the support conditions with the specimen suspended on the laboratory cranes, (c) line support construction, (d) connection of the dywidag tie rods with the load distribution construction using a steel support cone and a spherical nut, (e) built-in force cells in the line support with post-tensioned threaded rods, (f) point support with spherical support bearings and (g) lowerable point support with force cell.

5.2.3 Measurements and test procedure

Various measurement sensors were installed in the test setup to record displacements, forces and accelerations. Fig. 5.10 shows their positions on the specimen. The oil pressure in the hydraulic circuit was measured using the internal manometer of the manually operated pump. Based on this measurement, the cylinder forces could be calculated. Two NDI Optotrak Certus position sensors were installed to record the deformations on the side of the specimen in the area marked in Fig. 5.10. Strobers (visible e. g. in Fig. 5.9g) were glued to both the specimen and the supporting construction allowing for a precise 3D tracking of these points throughout the experiments. The strober locations on the specimen are shown in Fig. 5.7. They were chosen according to the position of the steel tubes, allowing for a calculation of the relative displacements between the timber and concrete sections at these points.

The LVDTs measuring vertical displacements (Fig. 5.11a) at the edge of the specimen $w_{6,7,8,9}$ were installed only during the experiments where no line support was present in that position. During the torsional test, the reaction force of the lowerable point support F_9 was measured with a force cell (Fig. 5.9g) and w_{11} was used for live monitoring. The LVDT measuring w_{10} was installed only during the biaxial bending tests at the end of the experimental campaign. Six additional LVDTs s_i were installed at the interface of the specimen elements to measure the relative horizontal displacements in these locations (Fig. 5.11b).

Five acceleration sensors a_i (Fig. 5.11a) were installed in the locations shown in Fig. 5.10 for the dynamic tests that were performed at several time points during this experimental campaign (Fig. 5.1). Impulse excitation was achieved with a heel drop at all five sensor locations. This

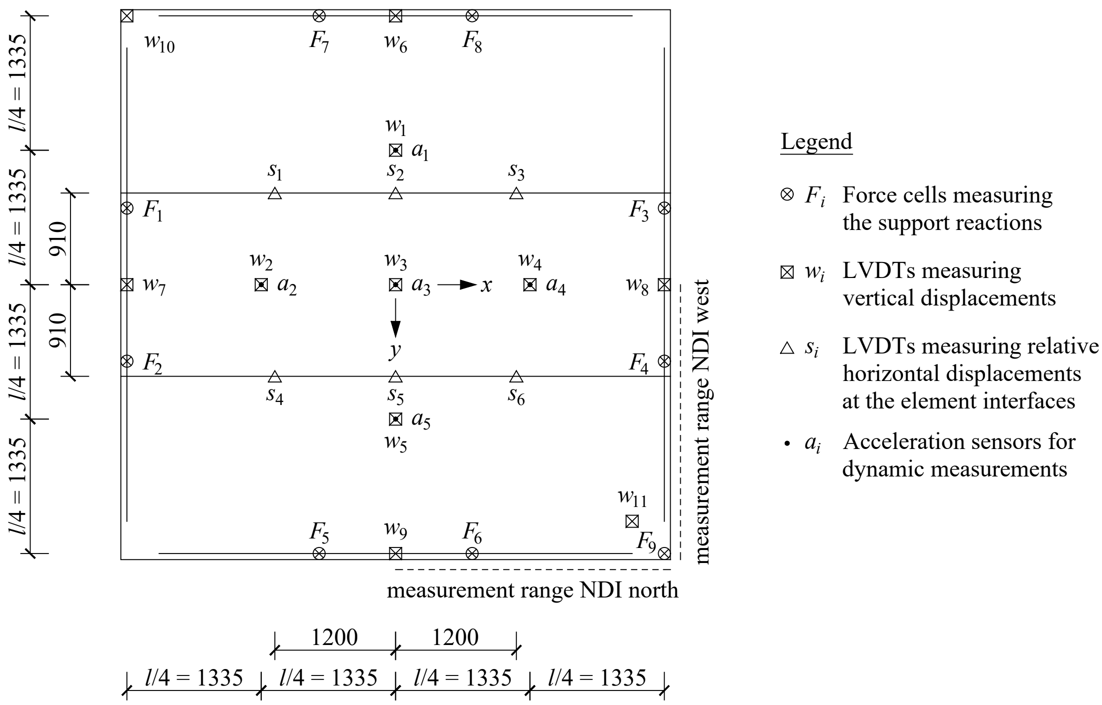

Fig. 5.10: Measurement setup in the biaxial bending experiments, all dimensions in [mm].

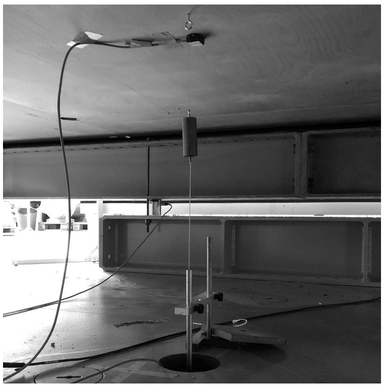

(a)

(b)

Fig. 5.11: (a) LVDT measuring the vertical displacements of the slab w_i and acceleration sensor used during the dynamic tests, (b) LVDT measuring the relative horizontal displacements s_i at the element interfaces.

was repeated three times and the free vibration response was recorded at a rate of 1'000 Hz. The load distribution construction (LDC) was not removed for the dynamic tests during phase 1.

An overview of the tests conducted in the scope of this experimental campaign is shown in Fig. 5.1. The three static loading tests during phase 1 were performed at low load levels in order to avoid any irreversible deformations in the specimen. For the uniaxial bending tests in x- and y-direction, predictions of the uniaxial load-bearing capacity were made using the calculation model presented in Chapter 6.2. The maximum load during the test was set at 35% of the predicted failure load including the specimen self-weight. In the uniaxial bending tests, three loading and unloading cycles were performed. The torsional test was started with the hydraulic cylinder set at the same height as the other point supports. Starting from this neutral position, two cycles were performed in each direction until a differential support reaction of $\pm 10\,\mathrm{kN}$ was reached (Fig. 5.15a).

In the biaxial setup, the specimen was loaded to approximately 20% of its load-bearing capacity for 69 hours. This load level was chosen assuming a non-structural permanent load of $2\,\mathrm{kN/m^2}$ and a live load of $3\,\mathrm{kN/m^2}$, adding up to $5\,\mathrm{kN/m^2}$. Because of a technical problem with the measurement hardware, the experiment had to be aborted after two hours. Three days later, the load was applied again and was then held constant for 69 hours. This was the only experiment where the load was not applied using a manually operated oil pump. Instead, a pendulum manometer was used to hold a constant load level throughout the time of the experiment.

The loading protocol of the final test was similar as in the connection shear tests (Chapter 3) and the uniaxial bending tests (Chapter 4). Based on the recommendations given in EN 26891 [10], an unloading and reloading cycle was performed after 40% of the estimated failure load was reached. The manual control with the hand operated oil pump is comparable to force based control in the elastic range and displacement based control in the plastic range of the test. The experiment was stopped when the deformation capacity of the test setup was reached.

5.2.4 Data evaluation

During all experiments, the oil pressure in the hydraulic system was measured with a manometer and the sum of support reactions was measured with force cells. Comparing these measurement data from the uniaxial bending test in x-direction showed that the total friction force in the hydraulic cylinders was approximately 12 kN. During the experiments in phase 1, the total applied force never exceeded 150 kN, which means that the friction forces were not negligible ($> 8\%$ of the total force) in these tests. The total force acting on the specimen was therefore computed from the force cell measurements:

$$F_{\mathrm{tot}} = \sum_{i=1}^{8} F_{\mathrm{i}} \tag{5.1}$$

In the final biaxial bending test, the specimen was loaded until failure and therefore the forces were up to five times higher than in all previous experiments. A comparison of the oil pressure measurement (accuracy of $\pm 0.5\%$) with the force cell measurements showed that the latter measurements were approximately 10% too low. The most likely reason for this deviation is that the larger forces and deformations in the test setup led to eccentric loading of the force cells. The used force cells are sensitive to such eccentric loading. At lower load levels, the pre-stressed threaded rods in the line supports were able to prevent any significant rotations that would lead to eccentric loading of the force cells. It is likely, however, that this was not the case anymore at the higher load levels in this experiment.

Therefore, for the final biaxial bending test, the total force acting on the specimen was computed from the oil pressure measurement. The friction forces ($< 2\%$ of the total force) were deducted from the total force:

$$F_{\mathrm{tot}} = 4 \cdot F_{\mathrm{cyl}} - 12\,\mathrm{kN} \tag{5.2}$$

As all four line supports were constructed identically, it can be assumed that the measurement error due to eccentric loading was similar in all force cells. Based on this assumption, the ratio between the force cell measurements was used despite the measurement errors. In particular, the ratio of the support reactions in x- and y-direction with regard to the total force were computed:

$$\frac{F_{\mathrm{x}}}{F_{\mathrm{tot}}} = \frac{\sum_{i=1}^{4} F_{\mathrm{i}}}{\sum_{i=1}^{8} F_{\mathrm{i}}} \quad \text{and} \quad \frac{F_{\mathrm{y}}}{F_{\mathrm{tot}}} = \frac{\sum_{i=5}^{8} F_{\mathrm{i}}}{\sum_{i=1}^{8} F_{\mathrm{i}}} \tag{5.3}$$

To allow for an easier interpretation of the test results, an equivalent distributed load q was calculated as follows:

$$q = F_{\mathrm{tot}}/l^2 \tag{5.4}$$

For the calculation of the load-bearing capacity, the self-weight of the specimen (measured with the integrated scale of the laboratory crane, $m_{\mathrm{s}} = 9750\,\mathrm{kg}$), the load distribution construction ($m_{\mathrm{LDC}} = 1250\,\mathrm{kg}$) and the hydraulic cylinders ($m_{\mathrm{cyl}} = 440\,\mathrm{kg}$) were added as follows:

$$q_{\mathrm{u}}^{*} = q_{\mathrm{u}} + (m_{\mathrm{s}} + m_{\mathrm{LDC}} + m_{\mathrm{cyl}}) \cdot g/l^2 \tag{5.5}$$

The relative displacements of the timber and concrete layers in x-direction Δu and in y-direction Δv were derived from the NDI measurements in analogy to the procedure described in Chapter 4.2.4. All steel tube connectors and side connections were given a name as shown in Fig. 5.12.

In the uniaxial bending tests during phase 1, the mean mid-span deflection was calculated with Eq. 5.6, from w_i as depicted in Fig. 5.10.

$$w_{\mathrm{m}} = \begin{cases} (w_6 + w_1 + w_3 + w_5 + w_9)/5 & \text{for bending in x-direction} \\ (w_7 + w_2 + w_3 + w_4 + w_8)/5 & \text{for bending in y-direction} \end{cases} \tag{5.6}$$

A linearised stiffness value was calculated for each loading cycle, using linear regression similar as in the connection shear tests (Fig. 3.23). The respective bending stiffness EI_{x} and EI_{y} was calculated based on the cylinder forces F_{cyl}, mid-span deflection w_{m} and the geometry of the test setup (Fig. 5.7). The data range used for the linear regression is shown in the respective result plots in the subsequent chapters.

The torsional stiffness was derived directly from the differential cylinder force F_{cyl} and displacement w_{cyl} in the specimen corner according to Eq. 5.7. For each loading cycle, linear regression was applied to obtain a linearised value of the orthotropic stiffness parameter EI_{xy}.

$$EI_{\mathrm{xy}} = \frac{F_9 \cdot l^2}{4 \cdot w_{\mathrm{cyl}}} \tag{5.7}$$

The acceleration measurements recorded in the dynamic tests were transferred to the frequency domain with a fast Fourier transform (FFT). This was done in analogy to the uniaxial bending tests (Fig. 4.7).

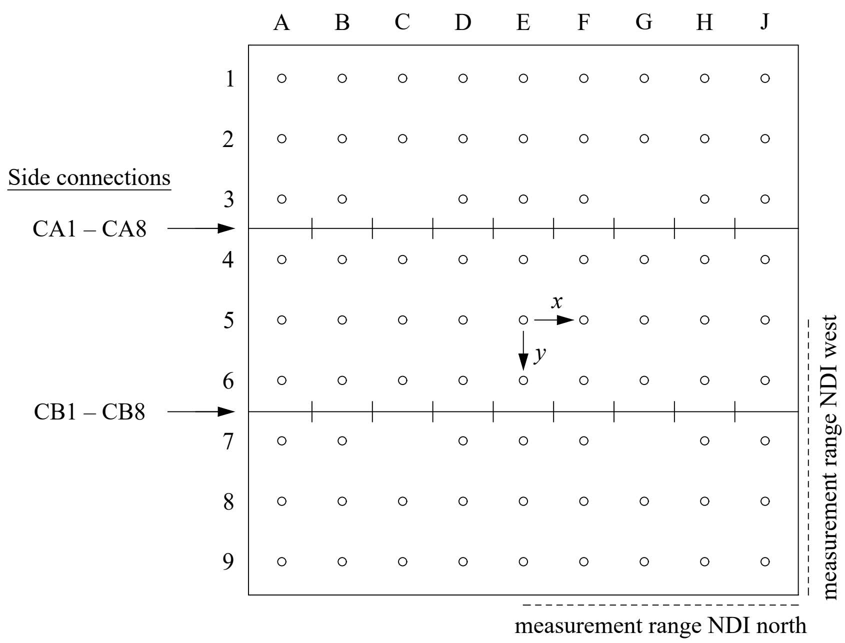

Fig. 5.12: Identification of the steel tube connectors and the side connections.

5.3 Results

5.3.1 Uniaxial bending in x- and y-direction and torsion

Fig. 5.13 – 5.15 show the main result plots of the two uniaxial bending tests and the torsional test. The orthotropic stiffness values determined from all three experiments are summarised in Tab. 5.3.

Before the first static loading test, the entire specimen had already been suspended on the laboratory crane during a test setup modification (Fig. 5.9b). This process led to visible bending cracks in the unreinforced concrete edge beams, especially on the two sides where this beam was continuous (spanning in x-direction). These cracks were visually assessed throughout phase 1 of the experimental campaign and no significant growth was observed.

In the uniaxial bending test in x-direction, three main loading cycles were performed. The first one was split in two sub-cycles due to a technical issue with the manually operated oil pump. Fig. 5.13b shows the load-deflection diagram that was used to calculate the bending stiffness EI_{x} with linear regression. The bending line along the span was symmetrical (Fig. 5.13c), with slightly larger mid-span deflections on the positive y-side (Fig. 5.13d).

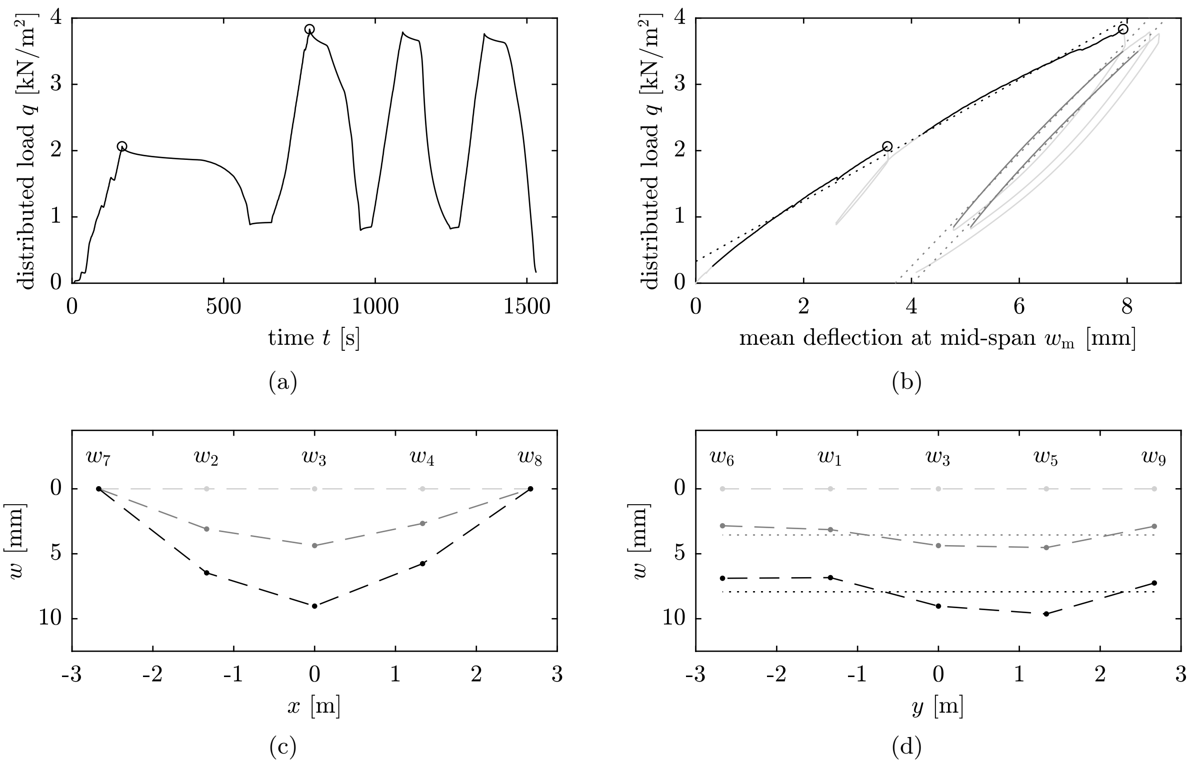

Fig. 5.13: Result plots from the uniaxial bending test in x-direction: (a) force-time, (b) force-deflection and linear regression of bending stiffness with the considered data range for 1st and 2nd/3rd loading stiffness values plotted in black and dark grey, respectively, (c) & (d) measured bending line in x- and y-direction, before test start and at the points in time marked in (a) and (b) (dotted line: w_{m}).

In the uniaxial bending test in y-direction, three loading cycles were performed as shown in Fig. 5.14a. The measured bending line along the span was slightly asymmetrical (Fig. 5.14d). Fig. 5.14c shows that the deflections at mid-span were similar across the width of the slab.

Fig. 5.15a shows the loading protocol of the torsional test. The observed stiffness was approximately equal for both loading directions. The cylinder force and displacement was defined as positive for an extension of the hydraulic cylinder (raising of the point support).

Tab. 5.3: Experimentally determined orthotropic stiffness values in [kNm^2/m].

		Loading cycle i		
		1	2	3
Bending stiffness in x-direction	$EI_{x,i}$	5’310	9’850	9’860
Bending stiffness in y-direction	$EI_{y,i}$	2’380	4’160	4’050
Torsional stiffness, pos.	$EI^{+}_{xy,i}$	3’090	3’640	–
Torsional stiffness, neg.	$EI^{-}_{xy,i}$	2’960	3’590	–

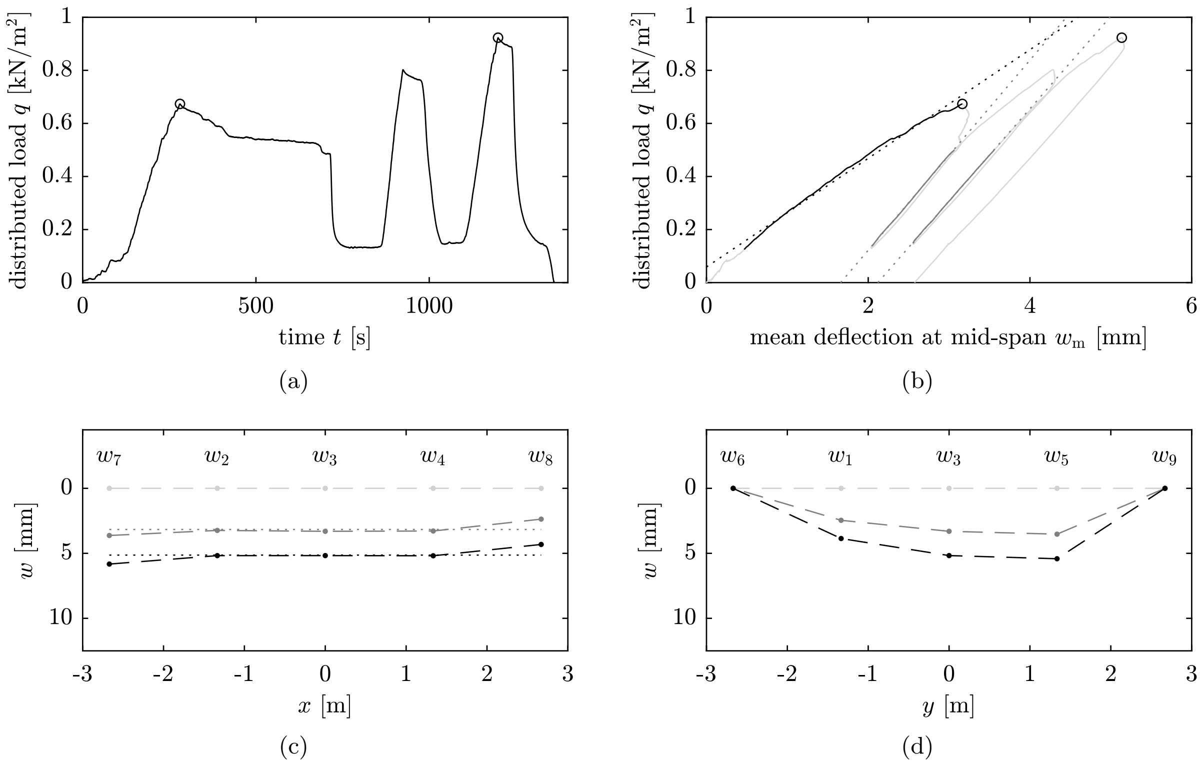

Fig. 5.14: Result plots from the uniaxial bending test in y-direction: (a) force-time, (b) force-deflection and linear regression of bending stiffness with the considered data range for 1st and 2nd/3rd loading stiffness values plotted in black and dark grey, respectively, (c) & (d) measured bending line in x- and y-direction, before test start and at the points in time marked in (a) and (b) (dotted line: w_m).

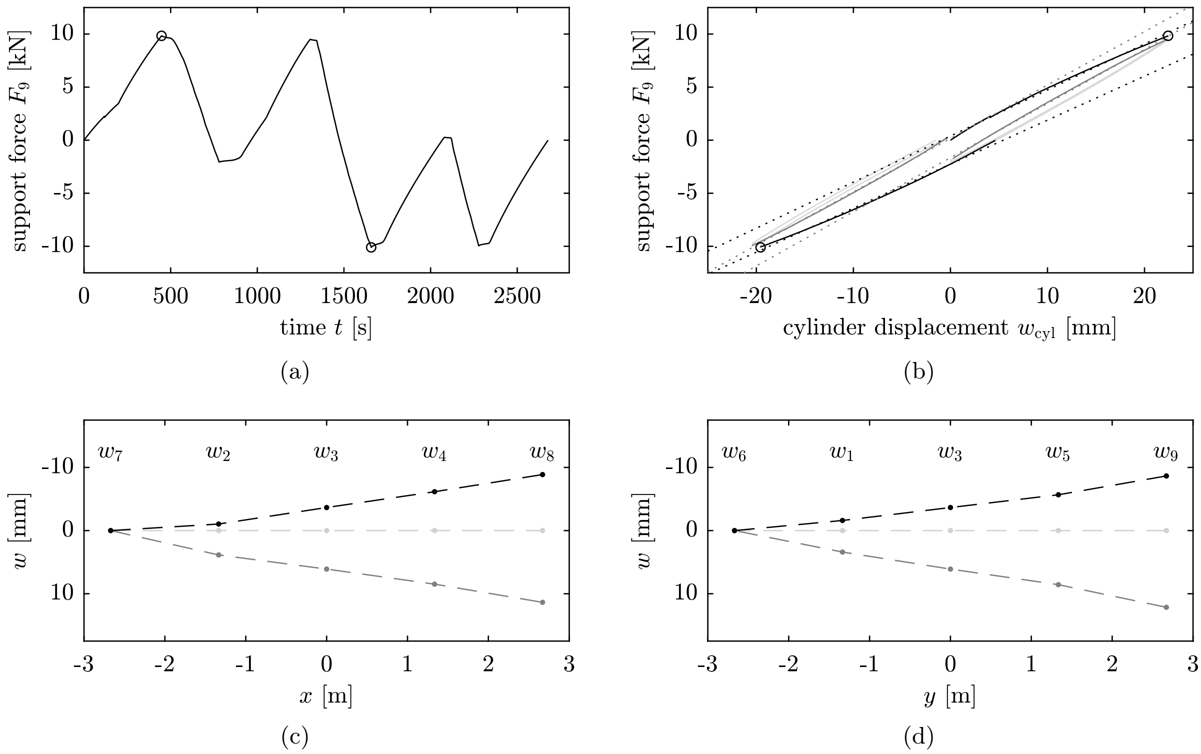

Fig. 5.15: Result plots from the torsional test: (a) force-time, (b) force-displacement and linear regression of torsional stiffness with the considered data range for 1st and 2nd loading stiffness values in both directions, plotted in black and dark grey, respectively, (c) & (d) measured bending line in x- and y-direction, before test start and at the points in time marked in (a) and (b).

5.3.2 Dynamic tests

Fig. 5.16 shows the frequency spectra of all dynamic tests and Tab. 5.4 lists the obtained fundamental frequencies. The experiment with a heel drop excitation at the centre of the slab was performed identically before and after the respective static loading test (Fig. 5.1). A comparison of Fig. 5.16a and 5.16b shows that in the uniaxial bending setup in x-direction, the first mode split into two modes after the static loading test. No mechanical explanation was found for this observation. In all other support conditions, the fundamental frequency was similar before and after the static loading tests.

Tab. 5.4: Experimentally determined fundamental frequency in [Hz], with heel drop excitation at the centre of the slab and load distribution construction installed, before and after the static loading test.

Support conditions	$f_{1,\text{before}}$	$f_{1,\text{after}}$
Uniaxial bending in x-direction	10.1	(9.0/12.0)
Uniaxial bending in y-direction	6.3	5.9
Point supports in the slab corners	5.9	5.9
Biaxial bending (before and after phase 1)	14.4	14.4

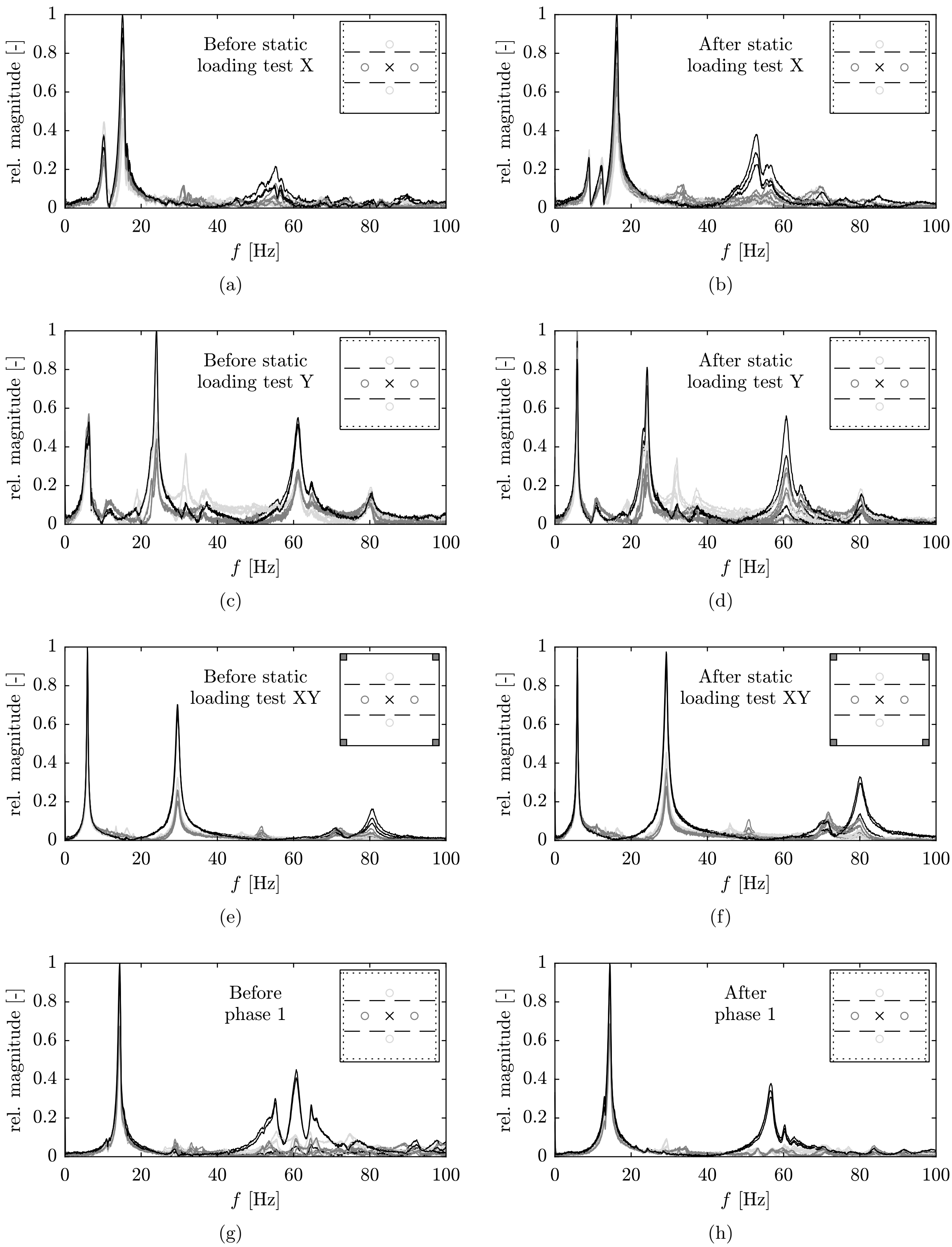

Fig. 5.16: Frequency spectra of all dynamic tests with heel drop excitation at the centre of the slab in different support conditions: (a) & (b) uniaxial bending in x-direction, (c) & (d) uniaxial bending in y-direction, (e) & (f) point supports in the slab corners, (g) & (h) biaxial bending.

5.3.3 Biaxial bending

Three-day creep test

The main result plots of the three-day creep test are shown in Fig. 5.17. The first attempt of this test had to be aborted after two hours due to a technical problem with the measurement hardware. The load-deflection curve of this test (grey line in Fig. 5.17b) corresponds to the first loading path of the slab in biaxial bending. At the beginning of the second test, another loading cycle was performed (second and third loading). Tab. 5.5 shows that during second and third loading, the global stiffness was similar, around 25% higher than during first loading. After the last loading cycle, the load was held at a constant level for 69 h (Fig. 5.17a). During this time, the deflection at the slab centre w_3 increased from 6.35 to 7.69 mm (+21%). Fig. 5.17c and 5.17d show no significant change in the shape of the bending line during the test.

Tab. 5.5: Global stiffness of the slab in biaxial bending, calculated with linear regression.

	1st loading	2nd loading	3rd loading
q/w_3 [kN/m^2/mm]	0.613	0.756	0.781

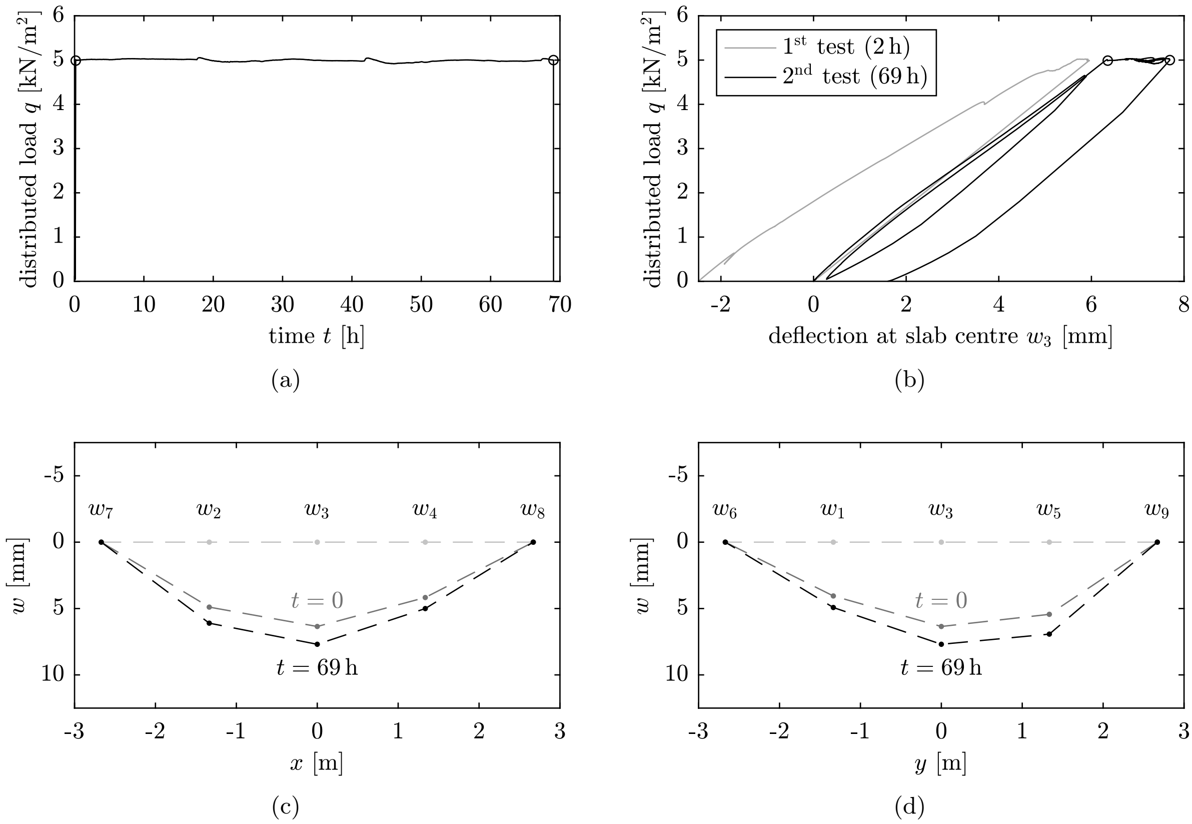

Fig. 5.17: Result plots from the 69 h creep test: (a) force-time, (b) force-deflection from the first test, which had to be aborted after 2 h, and the second test with a duration of 69 h, (c) & (d) measured bending line in x- and y-direction, before start of the second test and at the points in time marked in (a) and (b).

Destructive test

The main result plots of the last test of this experimental campaign are shown in Fig. 5.18. A distinct stiffness decrease is visible in Fig. 5.18a at $q \approx 7\,\mathrm{kN/m^2}$. This is likely due to the preloading that was performed during the three-day creep test. During the unloading and reloading cycle, the inclination of the load-deflection curve corresponds to the initial (reloading) stiffness again, which supports this explanation. Fig. 5.18c shows that during this phase of the test under service loads, the ratio of the support reactions in x- and y-direction was 60% and 40%, respectively.

At $q = 17\,\mathrm{kN/m^2}$, a sudden increase in relative displacements occurred at the element interface with side connections CA1 – CA8 (sensors $s_{1,2,3}$ in Fig. 5.18e), which also manifests in the load-deflection curve (1 in Fig. 5.18a). It is possible that one or several glue line failures in the side connections occurred at this time. However, this could not be confirmed as the connections were not visible during the test.

Starting at a load level of $q \approx 23\,\mathrm{kN/m^2}$, several minor load drops are visible in the load-deflection curve (2 in Fig. 5.18a). At the same time, local punching failures in the concrete cover above connectors A4, A5, A6, J4, J5 and J6 were observed (Fig. 5.20b, 5.21a and 5.21b). It is likely that the load drops were caused by these local failures. The total load further increased up to $q_\mathrm{u} = 25.5\,\mathrm{kN/m^2}$ ($q^*_\mathrm{u} = 29.5\,\mathrm{kN/m^2}$ including self-weight according to Eq. 5.5) and the deflection at the slab centre reached $w_3 = l/58 = 92\,\mathrm{mm}$ at this point.

A brittle failure of several side connections among CA1 – CA8 led to a vertical offset between the two adjacent slab elements and a load drop of $5\,\mathrm{kN/m^2}$ (3 in Fig. 5.18a, Fig. 5.20c and 5.20d). As a consequence of this failure, the ratio of the support reactions in x- and y-direction changed (Fig. 5.18c). During the following post-peak phase of the experiment, 75 – 80% of the load was carried in x-direction. Fig. 5.18d shows no significant change of the bending line shape in x-direction. In y-direction (Fig. 5.18f), the ratio w_3/w_1 substantially increased during the post-peak phase due to the vertical offset between the elements. The load level remained approximately constant between $q \approx 20 - 22\,\mathrm{kN/m^2}$ while the deflections further increased up to $w_3 = l/35 = 152\,\mathrm{mm}$. Further local punching failures were observed during the post-peak phase (4 in Fig. 5.18a). The test was stopped when the dywidag rods (10 in Fig. 5.7) were close to touching the edge of the holes in the specimen because of the large deformations at this point.

The measurements of the relative displacements between the timber and concrete sections Δu and Δv were not as conclusive as in the uniaxial bending tests (Chapter 4). However, Fig. 5.19 shows that the relative displacements in y-direction Δv were around two times higher than the corresponding displacements in x-direction Δu before the maximum load was reached. A substantial increase of Δv was observed during the post-peak phase. Relative displacements in both directions were larger at the centre of the slab edges than in the slab corner.

Throughout the entire experiment, the slab corners exhibited an upward displacement (lifting). This lifting was more pronounced in the concrete edge beam than in the beech LVL plate, which led to a gap opening between the two layers, visible in Fig. 5.20a. This gap opening in the slab corners increased at higher loads, reaching a maximum of around 15 mm.

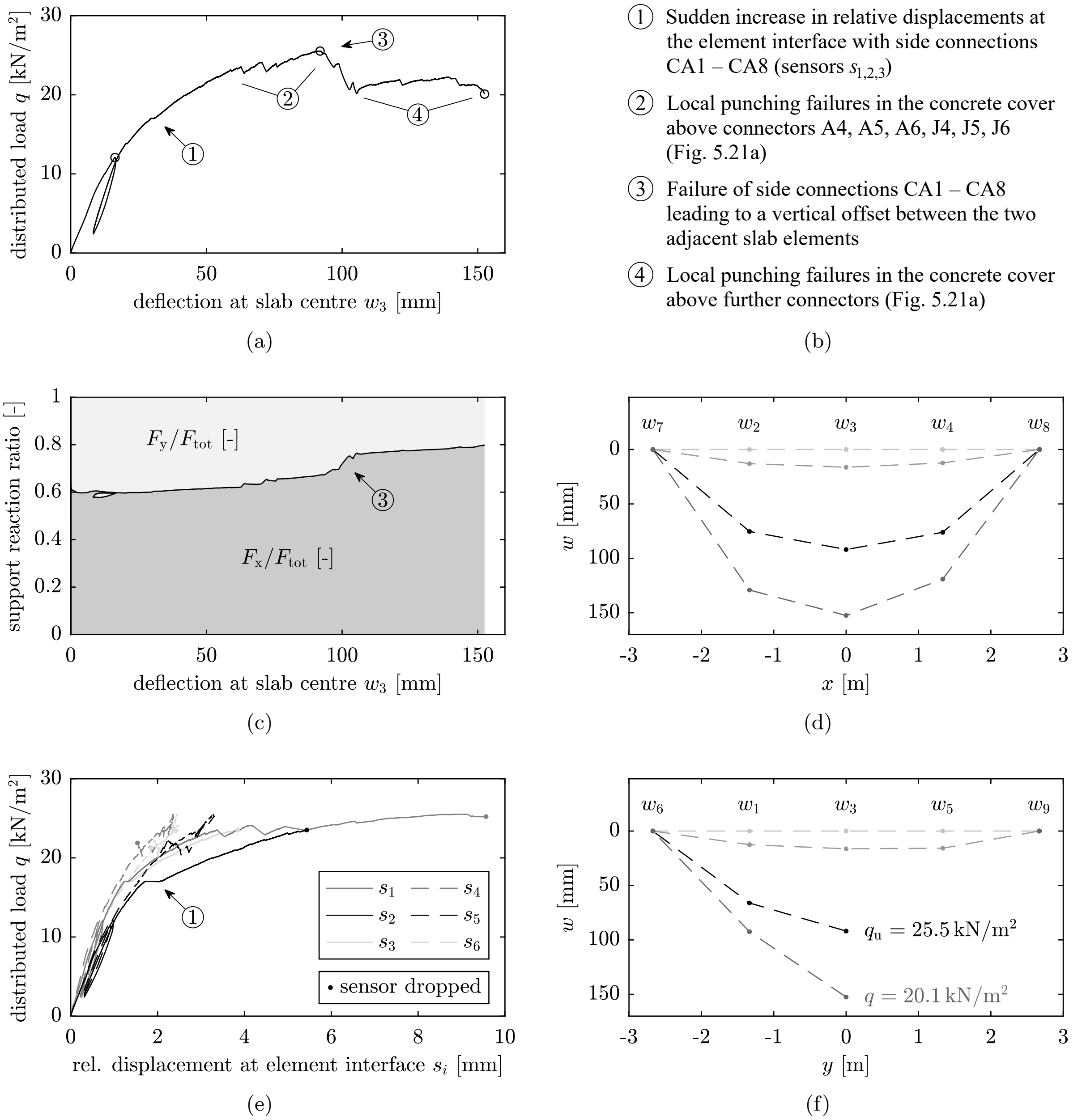

Fig. 5.18: Results of the final biaxial bending test: (a) force-deflection, (b) observations, (c) ratio of the support reactions in x- and y-direction, (d) & (f) measured bending line in x- and y-direction, before test start and at the points in time marked in (a) (sensor w_5 dropped shortly after the reloading cycle), (e) deformation at the side connections.

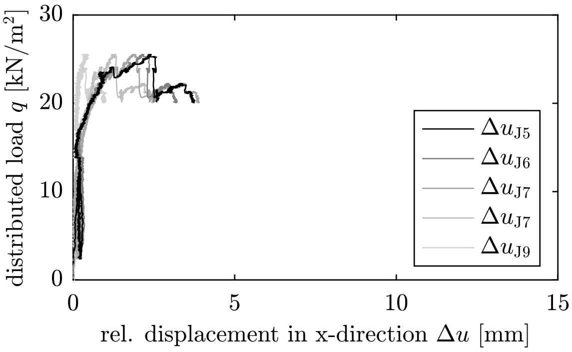

(a)

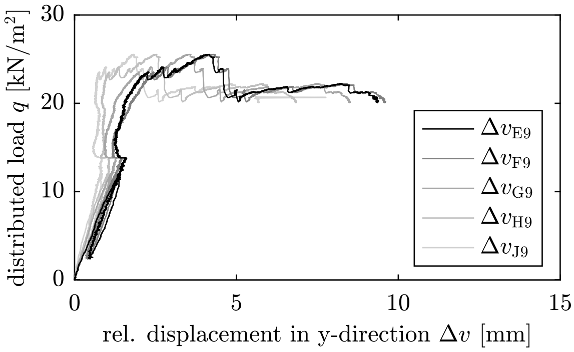

(b)

Fig. 5.19: Relative horizontal displacements between the timber and concrete sections at the connector positions (a) in x- and (b) y-direction.

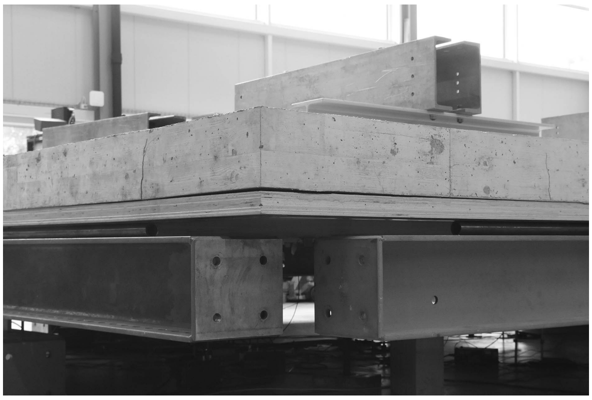

(a)

(b)

(c)

(d)

Fig. 5.20: Photos taken during the final biaxial bending test: (a) lifting and gap opening at the slab corner close to J1, at $q \approx 20\,\mathrm{kN/m^2}$, (b) ② local punching failures in the concrete cover above connectors J4, J5 and J6 at $q \approx 24\,\mathrm{kN/m^2}$ shortly before ③, (c) & (d) post-peak phase with vertical offset between two slab elements after ③ failure of several side connections among CA1 – CA8.

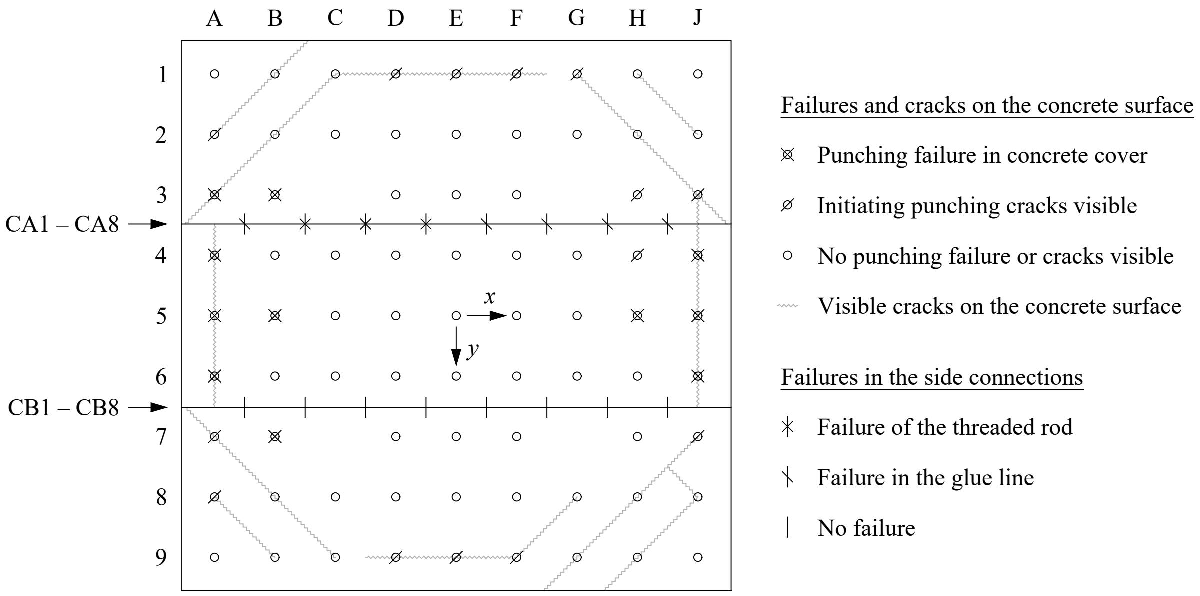

(a)

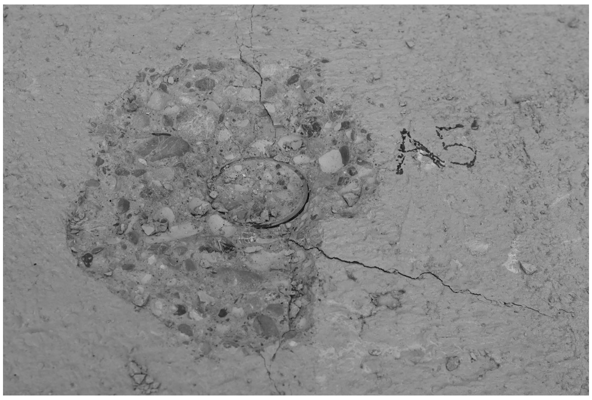

(b)

(c)

(d)

(e)

Fig. 5.21: Inspection of the specimen after the test: (a) overview of the visible failures on the concrete surface and in the side connections, (b) steel tube A5 after effortless removal of the concrete cover (slab edge towards the left side), (c) failure in the glue line between nut and GIR (left) and plastic bending deformation of the threaded rod (right) in side connection CA5, (d) & (e) failure of the threaded rod in side connection CA2.

5.4 Discussion

Serviceability criteria regarding deformations and vibrations often govern the design of TCC slabs in practice. Therefore, increasing the slab stiffness is the main motivation for choosing a two-way spanning TCC slab over a one-way spanning alternative. The results of this experimental campaign allow for a direct comparison of the stiffness and the fundamental frequency of the same TCC slab in uniaxial and in biaxial support conditions. Tab. 5.6 shows that activating the second load-bearing direction leads to a substantial increase in both stiffness and fundamental frequency. This result is supported by the measurement of the support force ratio in the biaxial bending test, which showed a load distribution of 60% in x-direction and 40% in y-direction.

The measured stiffness values can be further discussed using a theoretic comparison with an isotropic slab. The static stiffness of a quadratic, isotropic slab with hinged line supports on all four sides is expected to be around 200% higher than in uniaxial support conditions. However, this is only the case if the supports are built in a way that prevents uplift of the slab corners. For the geometry of the used test setup with unconstrained slab corners, the expected stiffness increase would be 150%. This is still substantially more than what was observed in the experiment. The same theoretical comparison can also be drawn with regard to the expected fundamental frequency. For a quadratic, isotropic slab with hinged line supports on all sides, an increase of 100% would be expected if uplift of the slab corners is not prevented. The main reason for these differences in static stiffness and fundamental frequency is the low bending stiffness of the tested slab specimen in transversal direction $EI_\mathrm{y} = 0.45 \cdot EI_\mathrm{x}$. It is likely that this stiffness value was affected by the alternative side connection concept that had to be used in the test specimen (Fig. 5.5).

Tab. 5.6: Comparison of the global slab stiffness q/w_m (1^st loading) and the fundamental frequency f_1 in uniaxial (x-direction) and in biaxial support conditions.

		Uniaxial	Biaxial	Rel. difference
q/w_m	[kN/m^2/mm]	0.457	0.613	+34%
f_1	[Hz]	10.1	14.4	+43%

Even though the measured stiffness and the fundamental frequency are lower than what would be expected in an isotropic slab, the findings of this experimental campaign confirm the great potential of two-way spanning TCC slabs for the application in practice. The benefit of a two-way spanning slab compared to a one-way spanning alternative is greatest in the case of a quadratic slab geometry. Loebus & Winter [50] investigated the influence of other span ratios $l_\mathrm{y}/l_\mathrm{x}$ on the deflections of one-way and two-way spanning TCC slabs with a parametric study using numerical models. Their results show that for $l_\mathrm{y}/l_\mathrm{x} = 1.5$, the stiffness benefit is less than half compared to a situation with a quadratic slab. For $l_\mathrm{y}/l_\mathrm{x} > 2$, the deflections of the one-way and two-way spanning TCC slabs are almost identical.

A distinct difference between the first loading and reloading stiffness was measured in all static loading tests during this experimental campaign, confirming the respective observations in the connection shear tests (Chapter 3) and uniaxial bending tests (Chapter 4). Tab. 5.7 shows that the difference was more pronounced in the first two tests (uniaxial bending in x- and in y-direction) than in the following experiments. This is most likely because in these later experiments, the connectors had already been preloaded during the previous tests. It is to be assumed that these results would be different if an alternative order of the experiments had been chosen.

Tab. 5.7: Ratio of slab stiffness during first loading and reloading.

	$(q/w_{\mathrm{m}})_2/(q/w_{\mathrm{m}})_1$
Uniaxial bending test in x-direction	1.86
Uniaxial bending test in y-direction	1.72
Torsional test	1.20
Biaxial bending test	1.25

In the biaxial bending test, local punching failures occurred in the concrete cover above several steel tube connectors. Cracks on the concrete surface above the steel tubes were observed already in the connection shear tests (Chapter 3). It is to be assumed that the normal force in the steel tube was higher in the bending test than in the connection shear tests. Combined with the cracks due to the introduction of the connection moment, this higher normal force in the steel tube led to the observed punching failure. No similar failure was observed in the uniaxial bending tests (Chapter 4). This difference can be explained with the upper LVL beam that was included in the uniaxial bending specimens. This beam acted as a flange on the steel tube and thus increased the punching resistance.

In the biaxial bending test, these local punching failures led to small load drops in the load-deflection curve (2 in Fig. 5.18a). The total load could be further increased afterwards as the connection can transmit a moment also without the concrete cover. However, shear forces from the concrete layer can no longer be transmitted to the steel tube after a punching failure has occurred. In the experiment, this did not lead to any further failures because all 16 point loads were positioned directly above a steel tube. Thus, no large shear forces had to be transmitted from the concrete layer to the steel tube.

For applications in practice, these local punching failures should be kept in mind. Large normal forces in the steel tubes should be avoided conceptually, e. g. by including a concrete edge beam as it was done in the tested specimen. If necessary, the punching resistance could be increased by welding a steel ring to the connector tubes as illustrated in Fig. 5.22b.

The failure mechanism of the tested specimen was significantly influenced by the resistance of the side connections. As an assembly of the slab elements with the original side connection concept was not possible, an alternative solution had to be found within this experimental campaign. The chosen solution (Fig. 5.5) allowed to perform all experiments as originally planned. However, the connection resistance was reduced. In some connections, failure occurred in the

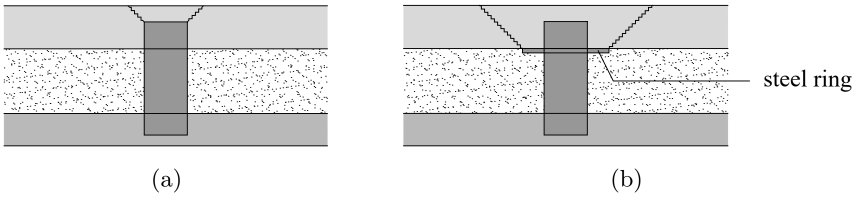

Fig. 5.22: (a) Original connection concept and (b) concept with a steel ring welded to the connector tube for improved punching resistance.

glue line (Fig. 5.21c) and in others, the threaded rod failed (Fig. 5.21d and 5.21e). This implies that there may have been differences in the quality of these glued connections.

The load-bearing capacity of the tested specimen was limited by the failure of the side connections (3 in Fig. 5.18a). However, before that, local punching failures were observed in the concrete cover above several steel tube connectors. It is therefore likely that the load-bearing capacity of the specimen would not have been substantially higher with a stronger side connection. The global ductility of the slab, however, was significantly affected by the failure of the side connection. It is likely that in a force controlled test, this failure would have led to a total collapse of the slab. As in this experiment, the load was applied with a manually operated oil pump (comparable to displacement control), a post-peak phase was observed. During this phase, a larger share of the total load was carried in x-direction of the slab, which was still intact. This redistribution of internal forces allowed for large deformations at 80% of the maximum load even though a brittle failure had occurred in the side connection.

It is likely that the side connection failure did not occur exclusively due to tensile forces in the GIR. Shear forces may have played an important role as well. This aspect has not been studied within the scope of this research project. The revised concept for the side connection described in Chapter 1.3 is expected to provide a higher shear resistance thanks to the conical edge grooves in the LVL plate. However, the resistance of the side connection to combined shear and tension should be investigated in further studies.

5.5 Conclusions

The load-bearing behaviour of the two-way spanning TCC slab with steel tube connection was studied in an extensive experimental campaign. Both dynamic and static loading tests were performed on the same specimen in different support conditions. Below, the main conclusions from these experiments are summarised:

- The tested quadratic specimen with a span of $l = 5.34\,\text{m}$ showed a 34% higher stiffness and 43% higher fundamental frequency in biaxial versus uniaxial support conditions. Even though these values are lower than what would be expected in an isotropic slab, they confirm the great potential of two-way spanning TCC slabs for the application in practice.

- In the biaxial bending test, 60% of the total load was carried in x-direction and 40% in y-direction. After the side connection failure, the load share in x-direction increased to 80%.
- A distinct difference between the first loading and reloading stiffness was measured in all static loading tests during this experimental campaign, confirming the respective observations in the connection shear tests (Chapter 3) and uniaxial bending tests (Chapter 4).
- Assembly of the specimen elements was not possible with the originally intended side connection concept. Therefore, an epoxy adhesive anchoring system was used to connect the GIR in the test specimen. A revised side connection concept was developed after this experimental campaign, which is described in Chapter 1.3).
- The load-bearing behaviour was not as ductile as in the uniaxial bending tests due to a brittle failure of the glued side connections. However, a redistribution of internal forces allowed for large deformations at 80% of the maximum load during a post-peak phase.
- Local punching failures occurred in the concrete cover above several connectors, which did not lead to a global collapse of the specimen. Nevertheless, this failure mode should be considered in the further development and in practical applications of this TCC slab.

Chapter 6

Models for uniaxial bending

6.1 Introduction

In this chapter, two models are presented that can be used to predict the uniaxial load-bearing behaviour of the investigated TCC slab. After a detailed description of both models, they are applied to the boundary conditions of the uniaxial bending tests performed within the scope of this research project. This allows for a comparison of the respective predictions with the test results. On this basis, the accuracy of the models is assessed with regard to the prediction of deformations, load-bearing capacity and dynamic behaviour. Recommendations regarding the application of the calculation models are provided.

6.2 Elasto-plastic γ-method

6.2.1 Introduction

This chapter presents an analytical model for timber-concrete composite members with ductile connections. The presented model is based on the work published by Frangi & Fontana [31] as well as Boccadoro [4] who extended the model focusing on its application for a TCC system with ductile notched connection.

Within the scope of this thesis, the model as described by Boccadoro [4] has been adapted to the novel TCC system with steel tube connection. The notations and conventions regarding the γ-method have been altered such that they are in accordance with Eurocode 5 [13] and the final draft of the CEN/TC250/SC5 Technical Specification on the structural design of TCC structures (TS TCC [15]). This should facilitate the application of the model for future analyses covering also the long-term behaviour of the novel slab system.

The model presented by Frangi & Fontana [31] and Boccadoro [4] assumes linear-elastic, perfectly plastic connection behaviour. This means that the connection is assumed to have unlimited deformation capacity. The experimental investigations on steel tube connectors (Chapter 3) have shown that this assumption may not be fully applicable in the presented structure. Although plastic deformations were observed, the connectors usually showed a brittle failure after a certain slip displacement $\Delta u_{\max}$. In the uniaxial bending tests (Chapter 4), a distinct ductile load-bearing behaviour was observed. No significant load drops due to brittle connection failures occurred even after large slip displacements of $\Delta u \approx 40\,\mathrm{mm}$. However, it cannot be excluded that the upper LVL beam integrated in these specimens had a positive effect on the connection ductility. Therefore, until experimental data are available also for specimens without an upper LVL beam, the connection deformation capacity should be regarded as limited. Consequently, the model has been extended for the case of such a connection system with limited deformation capacity. The main assumptions of the model regarding the concrete and the connection behaviour are illustrated in Fig. 6.1. The timber section is modelled as linear-elastic with brittle failure. Stress interactions are treated according to Eurocode 5 [13]. Furthermore, the connectors are assumed to be arranged such that the resulting elastic shear forces are equal in all connectors. This means that all connectors reach their shear capacity at the same time.

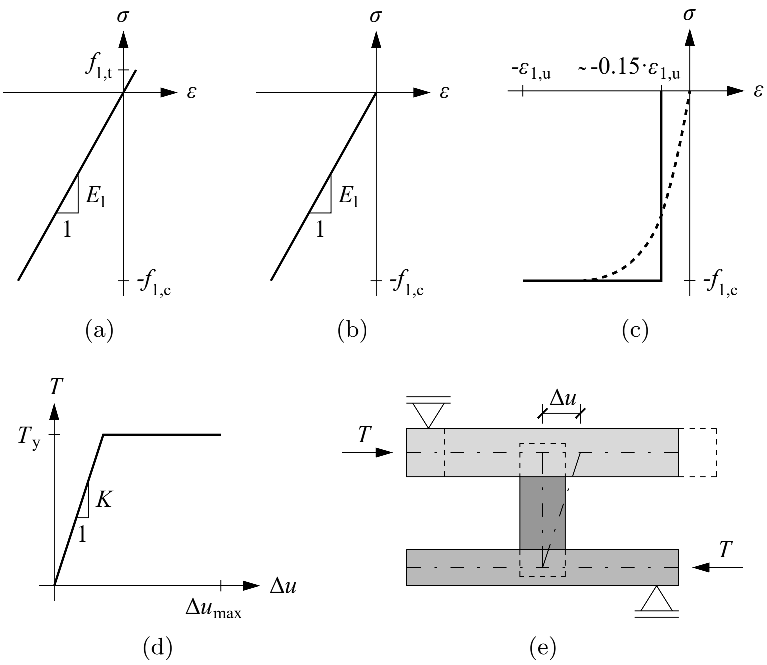

Fig. 6.1: Assumptions of the elasto-plastic γ-method: constitutive laws for concrete during (a) state I, (b) states II/III and (c) state IV; (d) & (e) connection behaviour.

The parameters of the connection behaviour used in the analysis (Fig. 6.1d) are derived directly from the results of the connection shear tests (Chapter 3). All considerations and calculation steps required for this are explained in Chapter 6.2.2.

The main part of the calculation model concerns the derivation of the moment-curvature behaviour of the composite cross-section at mid-span in Chapters 6.2.3 – 6.2.6. Fig. 6.2 shows an overview of the analysis, which is divided into four states, similar to the models typically used to describe the moment-curvature behaviour of reinforced concrete cross-sections. In state I, the concrete is uncracked and can carry tensile stresses. State I ends when the concrete tensile strength is reached. In state II, the concrete is cracked and assumed to have no tensile strength.

In the investigated TCC structure, the difference of the bending stiffness in state I and II is very small ($EI_{\mathrm{I}} \approx EI_{\mathrm{II}}$), because of the interlayer between the concrete and timber sections. However, concrete cracking has a distinct influence on the distribution of internal stresses. The load-bearing behaviour of the composite member is elastic during states I and II and can therefore be described with the elastic γ-method as described in Chapter 2.2.2. At the end of state II, all connectors reach their shear capacity, which marks the end of the elastic phase. During states III and IV, the theory of elastic composite action is not valid as there is no constant connection stiffness anymore. The moment-curvature behaviour in this elasto-plastic phase is described using analogies to the theories developed for the analysis of reinforced concrete cross-sections developed by Marti et al. [53] and implemented in the Swiss standard SIA 262 [76], combined with the suggested model by Frangi & Fontana [31]. These analogies were already described and used by Boccadoro [4].

In Fig. 6.2, the transition points (cr, y, cc) are marked with a circular frame and the corresponding geometry, axial strains and stresses are depicted on the left side. In all states, other failure modes are possible that would lead to a premature brittle failure of the composite member before having exhibited large deformations. These types of failures are marked with a rectangular frame on the right side in Fig. 6.2. The brittle failure modes caused by axial stresses in the timber and the concrete part of the composite cross-section are directly addressed in Chapters 6.2.3 – 6.2.6.

Potential failures caused by shear stresses in the partial sections are not discussed in this chapter. Local shear failures close to the connectors are accounted for with the empirical connection model that is used in the analysis (limitation of connection shear and deformation capacity). Shear failures in the timber or concrete section caused by global shear force were not observed in any of the uniaxial bending tests (Chapter 4) with a relatively short span of 5.34 m. As cross-sectional shear failures are less likely to occur with increasing span, this failure mode is not expected to be governing in practice and was therefore not investigated in detail. For practical applications, a simplified conservative design check can be performed by assigning the entire shear force to the timber section.

As the assumed connection behaviour is plastic during states III and IV, the slip displacements and deflections of the composite member cannot be calculated based only on the moment-curvature behaviour at mid-span. Chapter 6.2.7 covers the necessary additional considerations regarding the elastic and elasto-plastic areas of the composite beam and its boundary conditions. Therefore, for the cross-section analysis (Chapters 6.2.3 – 6.2.6) the connection behaviour is assumed to be linear-elastic, perfectly plastic. The slip displacement limit (connection deformation capacity) and the corresponding failure mode is then studied in Chapter 6.2.7 to complete the analysis.

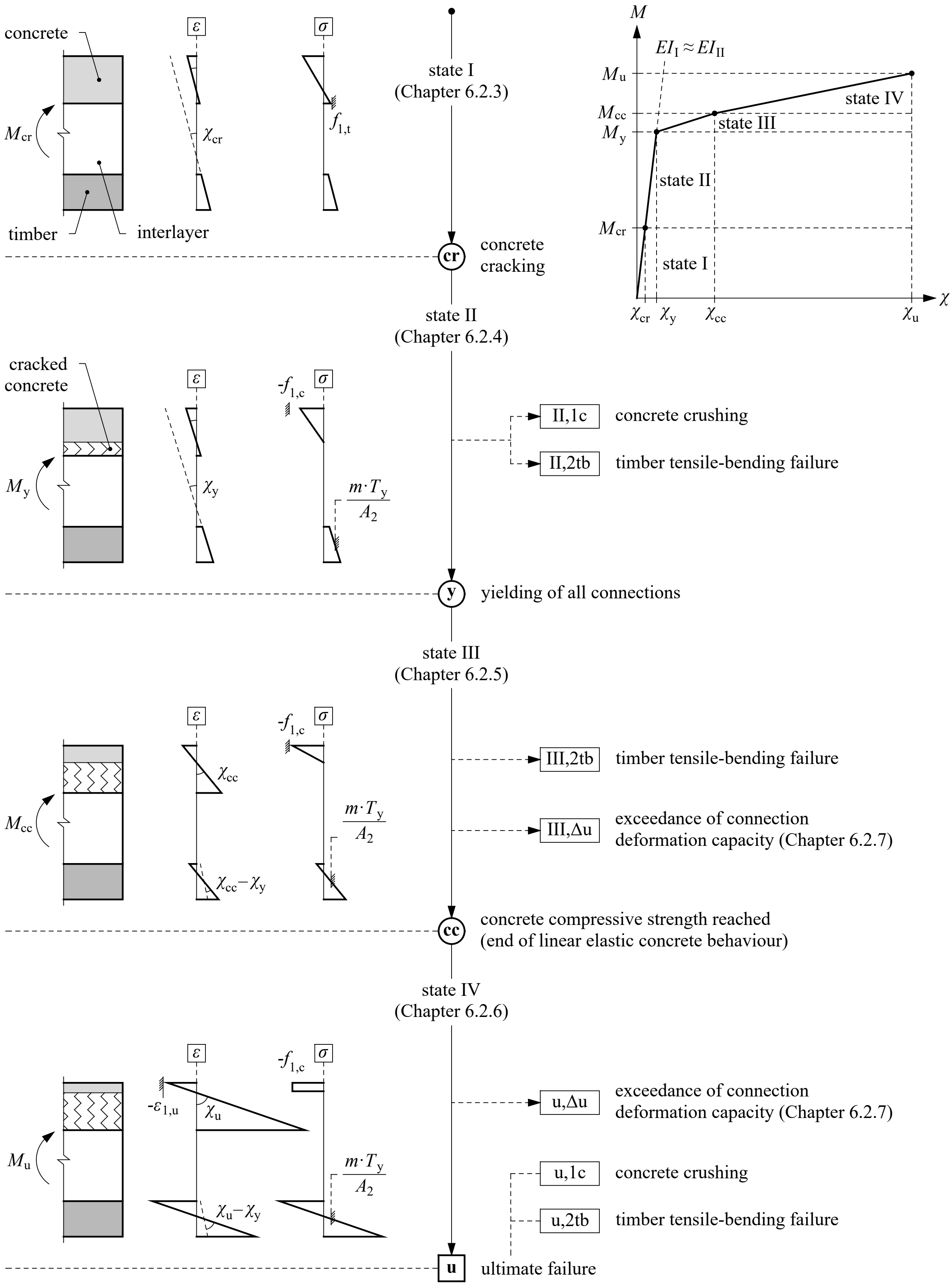

Fig. 6.2: Overview of the elasto-plastic γ-method: states of the composite cross-section, resulting moment-curvature diagram, considered failure modes and corresponding abbreviations and indices used in this chapter.

6.2.2 Connection behaviour

The parameters describing the connection behaviour as illustrated in Fig. 6.1d are derived directly from the results of the connection shear tests (Chapter 3). The clamping stiffness of the steel tube in the timber and concrete sections is represented by two different rotational springs. As the characteristics of these springs are investigated in individual experiments, deriving the elastic stiffness of the entire connection requires the use of a mechanical model, which is depicted in Fig. 6.3. Within the scope of the test evaluation, the position of the rotational springs was defined at the base of the steel tube (Chapter 3.2.4).

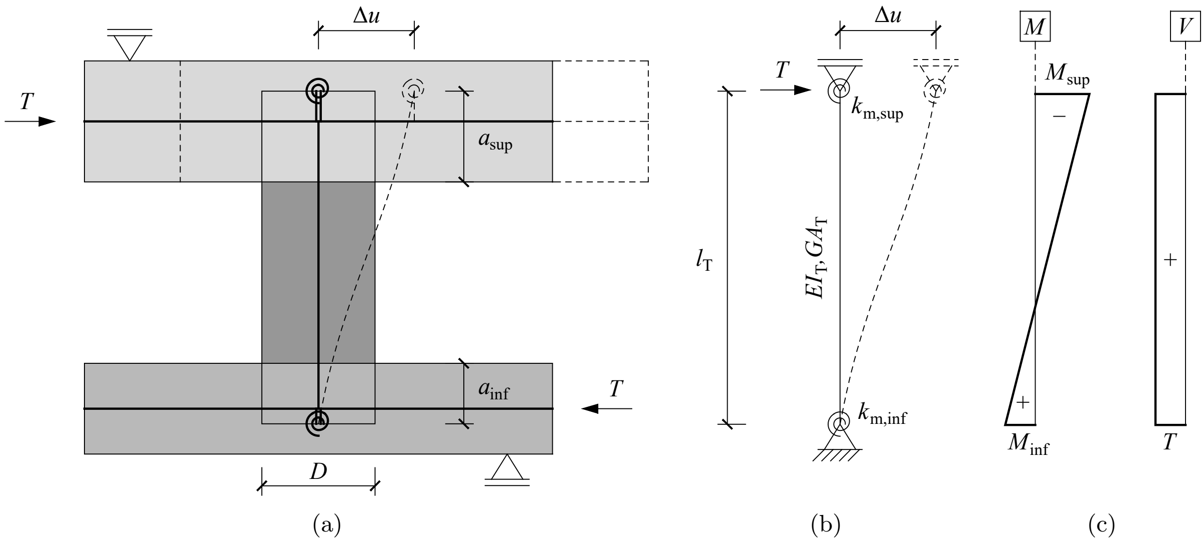

Fig. 6.3: Derivation of elastic connection stiffness from experimental results: (a) geometry of the connection, (b) mechanical model and (c) internal bending moments and shear forces in the steel tube.

Using the force method, the moments in the rotational springs are calculated:

$$M_{\text{sup}} = -\frac{l_{\text{T}}/2EI_{\text{T}} + 1/k_{\text{m,inf}}}{l_{\text{T}}/EI_{\text{T}} + 1/k_{\text{m,inf}} + 1/k_{\text{m,sup}}} \cdot Tl_{\text{T}} \tag{6.1}$$

$$M_{\text{inf}} = M_{\text{sup}} + Tl_{\text{T}} \tag{6.2}$$

The displacement Δu and the elastic connection stiffness follow:

$$\Delta u = (2Tl_{\text{T}} + 3M_{\text{sup}}) \cdot \frac{l_{\text{T}}^2}{6EI_{\text{T}}} + \frac{Tl_{\text{T}}}{GA_{\text{T}}} + (Tl_{\text{T}} + M_{\text{sup}}) \cdot \frac{l_{\text{T}}}{k_{\text{m,inf}}} \tag{6.3}$$

$$K = \frac{T}{\Delta u} \tag{6.4}$$

If brittle failure behaviour in the rotational springs is assumed, Eq. 6.1 and 6.2 can be used to determine a lower limit value of the connection shear capacity T_{y}. The nonlinear behaviour of both upper and lower rotational springs, however, allows for a redistribution of moments and therefore a higher connection shear capacity. If perfect plasticity is assumed in both rotational springs, an upper limit value of the connection shear capacity is obtained:

$$T_{\mathrm{y}} = \frac{M_{\mathrm{sup,y}} + M_{\mathrm{inf,y}}}{l_{\mathrm{T}}} \tag{6.5}$$

If experimentally determined moment-rotation ($M-\varphi$) curves are available for both rotational springs, finite element software can be used to perform a nonlinear push-over analysis (Fig. 6.4). This was done with the $M-\varphi$ curves described in Chapter 3.3.7, for all four possible connection combinations (embedment depth of the steel tube in timber $a_{\mathrm{inf}} = 40\,\mathrm{mm}$ and in concrete $a_{\mathrm{sup}} = 30, 40, 50, 60\,\mathrm{mm}$), steel tube diameter $D = 82.5\,\mathrm{mm}$ and varying length l_{T} between $150-300\,\mathrm{mm}$. The connection deformation capacity Δu_{max} was defined at the point where the first significant force drop occurs, as illustrated in Fig. 6.4. In all studied cases, this point coincides with the concrete connection reaching its maximum rotation $\varphi_{\mathrm{sup,max}}$. Neglecting the deformation of the steel tube ($EI_{\mathrm{T}}, GA_{\mathrm{T}} \to \infty$) allows for a simple hand calculation of a lower limit value of Δu_{max}:

$$\Delta u_{\mathrm{max}} = \varphi_{\mathrm{sup,max}} \cdot l_{\mathrm{T}} \tag{6.6}$$

Fig. 6.5 compares the results calculated from Eq. 6.5 and 6.6 with the results of the nonlinear push-over analysis. For $a_{\mathrm{sup}} = 30, 40, 50\,\mathrm{mm}$, T_{y} reaches more than 98% of the value calculated assuming perfect plasticity. For $a_{\mathrm{sup}} = 60\,\mathrm{mm}$, the values are slightly lower (95%).

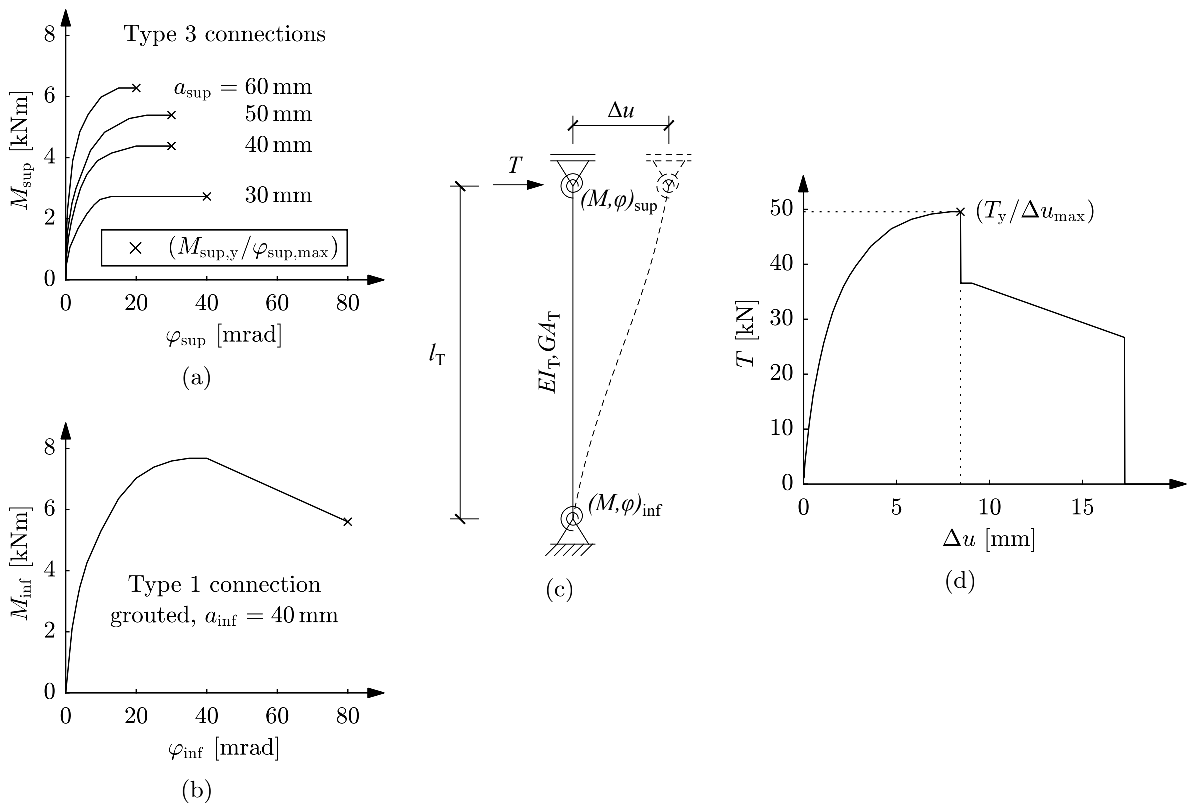

Fig. 6.4: Nonlinear push-over analysis: (a) & (b) input $M-\varphi$ curves, (c) static system and (d) resulting force-slip curve for $a_{\mathrm{sup}} = 30\,\mathrm{mm}$, $l_{\mathrm{T}} = 210\,\mathrm{mm}$ (reference configuration in the uniaxial bending tests).

Whether the connection can exploit its full plastic potential depends mainly on the maximum rotation that the concrete connection $\varphi_{\mathrm{sup,max}}$ can achieve before a brittle failure occurs. This parameter was determined based on three push-out tests with $a_{\mathrm{sup}} = 40\,\mathrm{mm}$ and based on only one test per configuration in the other cases. For $a_{\mathrm{sup}} = 60\,\mathrm{mm}$, the value was chosen conservatively because of a small force drop in the experiment (visible in Fig 3.29e), which has a direct influence on the result shown in Fig. 6.5a. Overall, the upper limit value according to Eq. 6.5 is a good approximation of the shear capacity T_y in the studied cases. Fig. 6.5b shows that the simplified calculation with Eq. 6.6 delivers good results on the conservative side. Also here, the results are a direct function of $\varphi_{\mathrm{sup,max}}$. Further test campaigns are necessary to extend the experimental basis for this parameter.

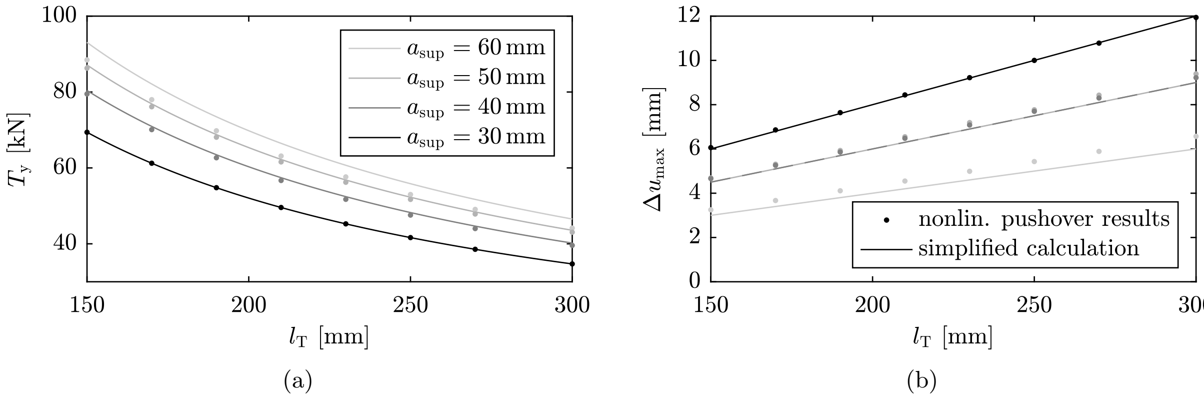

Fig. 6.5: Results of nonlinear pushover analysis and simplified calculations: (a) connection shear capacity T_y and (b) connection deformation capacity Δu_{max} (legends valid for both plots).

Tab. 6.1 summarises all experimentally determined input values necessary to calculate the connection stiffness K, shear capacity T_y and deformation capacity Δu_{max} for the most important cases. For static analyses the first loading stiffness $k_{m,1}$ should be used, while for dynamic calculations the higher reloading stiffness $k_{m,2}$ is applicable.

Tab. 6.1: Input values for calculation of connection properties, with steel tube diameter $D = 82.5\,\mathrm{mm}$ in all cases.

		$k_{m,1}$ [kNm/rad]	$k_{m,2}$ [kNm/rad]	M_y [kNm]	φ_{max} [mrad]
Type 1,	$a = 40\,\mathrm{mm}$	1’080	1’130	7.68	40
Type 3,	$a = 30\,\mathrm{mm}$	621	1’480	2.73	40
	$a = 40\,\mathrm{mm}$	916	4’470	4.38	30
	$a = 50\,\mathrm{mm}$	1’440	9’900	5.39	30
	$a = 60\,\mathrm{mm}$	3’460	15’000	6.28	20

6.2.3 State I: connection elastic, concrete uncracked and elastic

During state I, the concrete section is uncracked and can carry both compressive and tensile stresses. Fig. 6.6 illustrates the geometry of the composite cross-section and the axial strains, stresses and internal forces during state I. As the connection between the partial sections is not rigid, the strains along the height of the composite cross-section are discontinuous. The resulting offset between the partial sections is referred to as slip strain $\Delta\varepsilon$. As the vertical displacements of the partial sections are assumed to remain equal at all times, the curvature χ (inclination of the strain plane) has to be constant over the entire composite cross-section. The axial strains, stresses and internal forces are calculated using the γ-method introduced in Chapter 2.2.2. State I ends when the tensile stress at the bottom of the concrete section reaches the concrete tensile strength. No other failures are expected during state I.

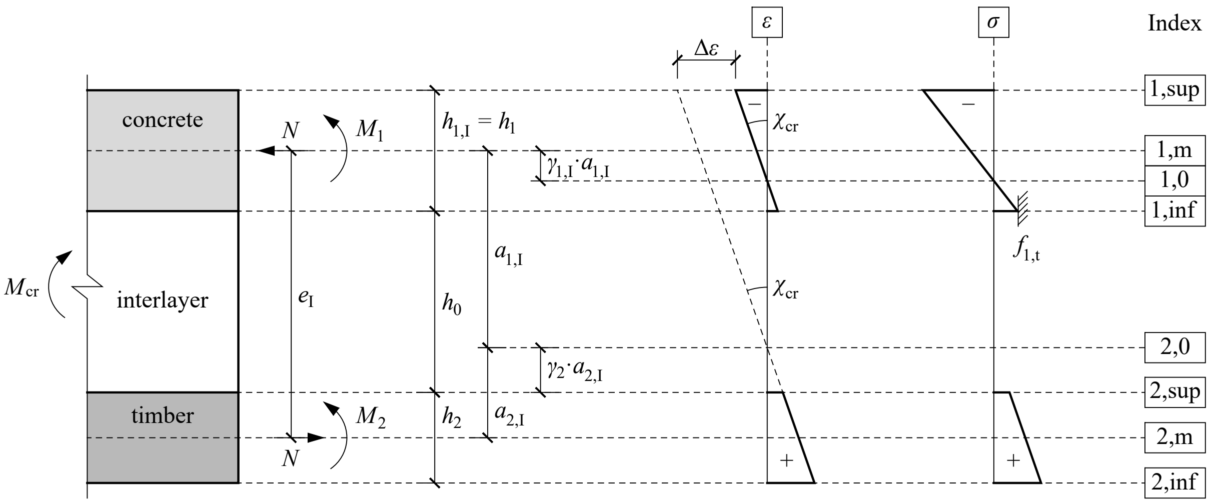

Fig. 6.6: Axial strains, stresses and internal forces at the end of state I (concrete cracking).

The cross-sectional areas and moments of inertia of the concrete and timber sections are:

$$A_{1,\mathrm{I}} = b_1 h_{1,\mathrm{I}} = b_1 h_1 \tag{6.7}$$

$$A_2 = b_2 h_2 \tag{6.8}$$

$$I_{1,\mathrm{I}} = \frac{b_1 h_{1,\mathrm{I}}^3}{12} = \frac{b_1 h_1^3}{12} \tag{6.9}$$

$$I_2 = \frac{b_2 h_2^3}{12} \tag{6.10}$$

The modulus of elasticity (MOE) of timber is chosen as the reference MOE. The different MOE of concrete and timber are taken into account with the following factors:

$$n_1 = \frac{E_1}{E_2} \tag{6.11}$$

$$n_2 = \frac{E_2}{E_2} = 1 \tag{6.12}$$

In accordance with Eurocode 5 [13] and TS TCC [15], the theoretical timber zero-strain axis is chosen as the reference axis for the γ-method (axis $\boxed{2,0}$ in Fig. 6.6). In the investigated TCC structure, the entire timber section will be in tension during states I and II in most cases. This means that the theoretical timber zero-strain axis will normally be positioned above the timber section. The γ-values are calculated as follows:

$$\gamma_{1,\mathrm{I}} = \frac{1}{1 + \frac{\pi^2 E_1 A_{1,\mathrm{I}} s_{\mathrm{ef}}}{K l^2}} \tag{6.13}$$

$$\gamma_2 = 1 \tag{6.14}$$

The effective connector spacing s_{ef} in Eq. 6.13 is estimated according to the recommendations discussed in Chapter 2.2.2. The distance between the centroids of the concrete and timber sections is:

$$e_{\mathrm{I}} = h_0 + \frac{h_1}{2} + \frac{h_2}{2} \tag{6.15}$$

The distances between the theoretical timber zero-strain axis and the centroids of the concrete and timber sections are calculated as follows:

$$a_{1,\mathrm{I}} = \frac{\gamma_2 n_2 A_2}{\gamma_{1,\mathrm{I}} n_1 A_{1,\mathrm{I}} + \gamma_2 n_2 A_2} \cdot e_{\mathrm{I}} \tag{6.16}$$

$$a_{2,\mathrm{I}} = \frac{\gamma_{1,\mathrm{I}} n_1 A_{1,\mathrm{I}}}{\gamma_{1,\mathrm{I}} n_1 A_{1,\mathrm{I}} + \gamma_2 n_2 A_2} \cdot e_{\mathrm{I}} \tag{6.17}$$

The moment of inertia and the bending stiffness of the composite section result as follows:

$$I_{\mathrm{I}} = n_1 I_{1,\mathrm{I}} + n_2 I_2 + \gamma_{1,\mathrm{I}} n_1 A_{1,\mathrm{I}} {a_{1,\mathrm{I}}}^2 + \gamma_2 n_2 A_2 {a_{2,\mathrm{I}}}^2 \tag{6.18}$$

$$EI_{\mathrm{I}} = E_2 I_{\mathrm{I}} \tag{6.19}$$

The curvature of the composite cross-section during state I resulting from a bending moment $M \leq M_{\mathrm{cr}}$ is:

$$\chi = \frac{M}{EI_{\mathrm{I}}} \tag{6.20}$$

The axial strains during state I result as follows:

$$\varepsilon_1 = \begin{pmatrix} \varepsilon_{1,\mathrm{sup}} \\ \varepsilon_{1,\mathrm{m}} \\ \varepsilon_{1,\mathrm{inf}} \end{pmatrix} = \begin{pmatrix} -\gamma_{1,\mathrm{I}} a_{1,\mathrm{I}} - h_1/2 \\ -\gamma_{1,\mathrm{I}} a_{1,\mathrm{I}} \\ -\gamma_{1,\mathrm{I}} a_{1,\mathrm{I}} + h_1/2 \end{pmatrix} \cdot \chi \tag{6.21}$$

$$\varepsilon_2 = \begin{pmatrix} \varepsilon_{2,\mathrm{sup}} \\ \varepsilon_{2,\mathrm{m}} \\ \varepsilon_{2,\mathrm{inf}} \end{pmatrix} = \begin{pmatrix} \gamma_2 a_{2,\mathrm{I}} - h_2/2 \\ \gamma_2 a_{2,\mathrm{I}} \\ \gamma_2 a_{2,\mathrm{I}} + h_2/2 \end{pmatrix} \cdot \chi \tag{6.22}$$

Applying Hooke's law yields the corresponding axial stresses during state I:

$$\sigma_1 = E_1 \cdot \varepsilon_1 = \begin{pmatrix} \sigma_{1,\text{sup}} \\ \sigma_{1,\text{m}} \\ \sigma_{1,\text{inf}} \end{pmatrix} = \begin{pmatrix} -\gamma_{1,\text{I}} a_{1,\text{I}} - h_1/2 \\ -\gamma_{1,\text{I}} a_{1,\text{I}} \\ -\gamma_{1,\text{I}} a_{1,\text{I}} + h_1/2 \end{pmatrix} \cdot n_1 \cdot \frac{M}{I_\text{I}} \tag{6.23}$$

$$\sigma_2 = E_2 \cdot \varepsilon_2 = \begin{pmatrix} \sigma_{2,\text{sup}} \\ \sigma_{2,\text{m}} \\ \sigma_{2,\text{inf}} \end{pmatrix} = \begin{pmatrix} \gamma_2 a_{2,\text{I}} - h_2/2 \\ \gamma_2 a_{2,\text{I}} \\ \gamma_2 a_{2,\text{I}} + h_2/2 \end{pmatrix} \cdot n_2 \cdot \frac{M}{I_\text{I}} \tag{6.24}$$

The internal forces acting on the partial sections are obtained by integration of the axial stresses, leading to the following equations:

$$M_1 = E_1 I_{1,\text{I}} \cdot \chi = \frac{n_1 I_{1,\text{I}}}{I_\text{I}} \cdot M \tag{6.25}$$

$$M_2 = E_2 I_2 \cdot \chi = \frac{n_2 I_2}{I_\text{I}} \cdot M \tag{6.26}$$

$$N = \sigma_{2,\text{m}} \cdot A_2 = -\sigma_{1,\text{m}} \cdot A_{1,\text{I}} \tag{6.27}$$

These fulfil the equilibrium conditions:

$$M = M_1 + M_2 + N \cdot e_\text{I} \tag{6.28}$$

The slip strain is calculated as follows:

$$\Delta\varepsilon = (1 - \gamma_{1,\text{I}}) \cdot a_{1,\text{I}} \cdot \chi \tag{6.29}$$

End of state I: concrete cracking

Setting $\sigma_{1,\text{inf}} = f_{1,\text{t}}$ in Eq. 6.23 yields the external bending moment that leads to concrete cracking

$$M_\text{cr} = \frac{I_\text{I}}{n_1 \cdot (h_1/2 - \gamma_{1,\text{I}} a_{1,\text{I}})} \cdot f_{1,\text{t}} \tag{6.30}$$

And the corresponding curvature

$$\chi_\text{cr} = \frac{M_\text{cr}}{EI_\text{I}} \tag{6.31}$$

The axial strains, stresses and internal forces at the end of state I (concrete cracking) can be calculated using Eq. 6.21–6.27 with $M = M_\text{cr}$ and $\chi = \chi_\text{cr}$

6.2.4 State II: connection elastic, concrete cracked and elastic

During state II, the concrete section is cracked and the connection behaviour remains elastic. Fig. 6.7 illustrates the geometry of the composite cross-section and the axial strains, stresses and internal forces during state II. State II ends when the connection shear capacity is reached.

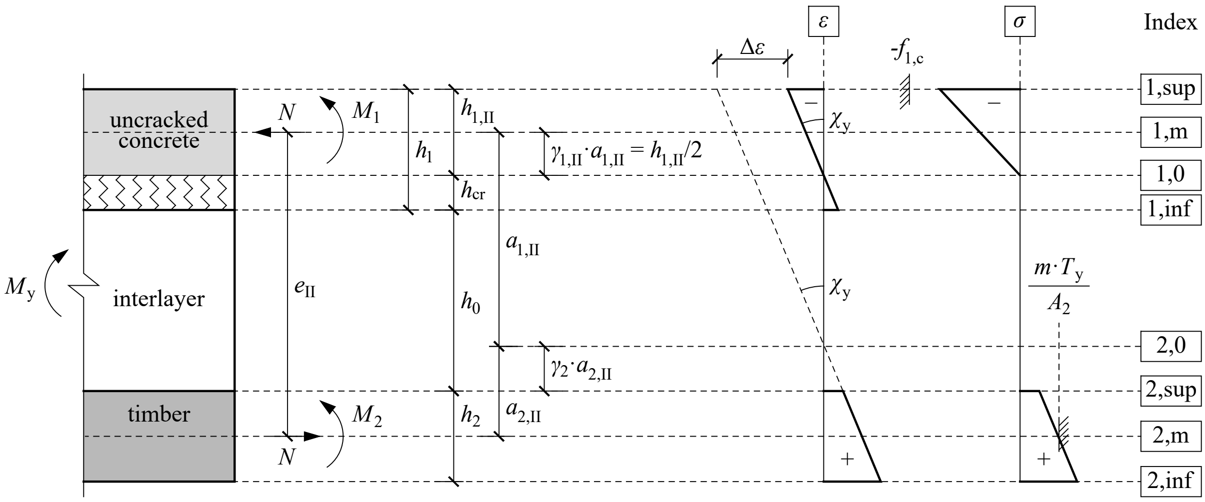

Fig. 6.7: Axial strains, stresses and internal forces at the end of state II (connection shear capacity reached).

After concrete cracking, the model assumes that the concrete section can only carry compressive stresses ($f_{t,1} = 0$). To account for this, the statically active height of the concrete section $h_{1,II}$ is reduced to the part that is subjected to compressive stresses.

$$h_{1,II} = h_1 - h_{cr} \tag{6.32}$$

As the behaviour of the composite member is elastic until the end of state II, the effective concrete height is constant throughout this phase. Once $h_{1,II}$ is determined, the same procedure as described in Chapter 6.2.3 can be applied for this new geometry. $h_{1,II}$ can be found using the following condition, applying Eq. 6.21:

$$\begin{aligned} \varepsilon_{1,0} = (-\gamma_{1,II} \cdot a_{1,II} + h_{1,II}/2) \cdot \chi \overset{!}{=} 0 \\ \Rightarrow \gamma_{1,II} \cdot a_{1,II} = h_{1,II}/2 \end{aligned} \tag{6.33}$$

In Eq. 6.33, both $\gamma_{1,II}$ and $a_{1,II}$ are functions of $h_{1,II}$. Solving this equation for $h_{1,II}$ leads to a fourth degree polynomial. While it is possible to derive a closed-form solution, this procedure results in a very long expression, leaving an iterative solution as the better option to obtain $h_{1,II}$. The mathematical reason for this is the fact that $\gamma_{1,II}$ is a function of $h_{1,II}$. This dependency can be eliminated by using a different definition of the γ-method. If, instead of the theoretical timber zero-strain axis ($\boxed{2,0}$ in Fig. 6.7), the concrete zero-strain axis ($\boxed{1,0}$ in Fig. 6.7) is chosen as the reference axis, the γ-factors read:

$$\gamma_1^* = 1 \tag{6.34}$$

$$\gamma_2^* = \frac{1}{1 + \frac{\pi^2 E_2 A_2 s_{ef}}{K l^2}} \tag{6.35}$$

As Eq. 6.15–6.28 remain valid also for this definition of the γ-method, Eq. 6.33 can be rewritten as follows:

$$\gamma_1^* \cdot a_{1,II} = h_{1,II}/2 \tag{6.36}$$

Solving Eq. 6.36 for $h_{1,\mathrm{II}}$ leads to a quadratic equation. With the condition $h_{1,\mathrm{II}} > 0$ and replacing $\gamma_1^* = 1$ and $n_2 = 1$ for simplicity, the following closed-form expression is derived:

$$h_{1,\mathrm{II}} = \frac{-\gamma_2^* A_2 + \sqrt{\gamma_2^* A_2 \cdot (\gamma_2^* A_2 + n_1 b_1 \cdot (2h_0 + 2h_1 + h_2))}}{n_1 b_1} \tag{6.37}$$

The result obtained from Eq. 6.37 is valid independently from what reference axis is used in the γ-method. In the scope of this thesis, the theoretical timber zero-strain axis is chosen, leading to the γ-factors defined in Eq. 6.13 and 6.14. The values from Eq. 6.34 should be used only in the context of Eq. 6.37.

Using the geometry of the composite cross-section during state II, the same procedure as described in Chapter 6.2.3 can be applied to determine $A_{1,\mathrm{II}}$, $I_{1,\mathrm{II}}$, $\gamma_{1,\mathrm{II}}$, $a_{1,\mathrm{II}}$, $a_{2,\mathrm{II}}$ and I_{II}. The distance between the centroids of the concrete and timber sections during state II is:

$$e_{\mathrm{II}} = h_0 + h_1 - \frac{h_{1,\mathrm{II}}}{2} + \frac{h_2}{2} \tag{6.38}$$

The stresses during state II are:

$$\sigma_{1,\mathrm{sup}} = (-\gamma_{1,\mathrm{II}} a_{1,\mathrm{II}} - h_{1,\mathrm{II}}/2) \cdot n_1 \cdot \frac{M}{I_{\mathrm{II}}} \tag{6.39}$$

$$\sigma_2 = \begin{pmatrix} \sigma_{2,\mathrm{sup}} \\ \sigma_{2,\mathrm{m}} \\ \sigma_{2,\mathrm{inf}} \end{pmatrix} = \begin{pmatrix} \gamma_2 a_{2,\mathrm{II}} - h_2/2 \\ \gamma_2 a_{2,\mathrm{II}} \\ \gamma_2 a_{2,\mathrm{II}} + h_2/2 \end{pmatrix} \cdot n_2 \cdot \frac{M}{I_{\mathrm{II}}} \tag{6.40}$$

The internal forces acting on the partial sections result as follows:

$$M_1 = E_1 I_{1,\mathrm{II}} \cdot \chi = \frac{n_1 I_{1,\mathrm{II}}}{I_{\mathrm{II}}} \cdot M \tag{6.41}$$

$$M_2 = E_2 I_2 \cdot \chi = \frac{n_2 I_2}{I_{\mathrm{II}}} \cdot M \tag{6.42}$$

$$N = \sigma_{2,\mathrm{m}} \cdot A_2 = -\frac{\sigma_{1,\mathrm{sup}}}{2} \cdot A_{1,\mathrm{II}} \tag{6.43}$$

These fulfil the equilibrium conditions:

$$M = M_1 + M_2 + N \cdot e_{\mathrm{II}} \tag{6.44}$$

The slip strain is calculated as follows:

$$\Delta\varepsilon = (1 - \gamma_{1,\mathrm{II}}) \cdot a_{1,\mathrm{II}} \cdot \chi \tag{6.45}$$

End of state II: yielding of all connectors

State II ends when all connectors have reached their shear capacity T_{y}. This also marks the end of the elastic phase of the load-bearing behaviour. The normal force in the partial sections at mid-span can be calculated from the equilibrium of horizontal forces (see Fig. 6.8):

$$N = \sum_{i=1}^{m} T_i = m \cdot T_{\mathrm{y}} \tag{6.46}$$

The model assumes that all connectors reach T_y at the same load level. This can be achieved if the distance between the connectors is chosen such that the resulting elastic shear forces are equal in all connectors. Such a connector layout should always be aimed for, as this also results in the maximum possible bending stiffness for a given number of connectors m. The connection shear forces can be approximated by integrating the theoretic elastic shear stress $\tau_{12}(x)$ at the interface of the composite member. Assuming that $\tau_{12}(x)$ is a linear function of the shear force $V(x)$, the optimal connector positions can be derived as illustrated in Fig. 6.8. For a simply supported beam subjected to uniformly distributed load, the optimal layout with m connectors follows according to Eq. 6.47. Fig. 6.8 shows an example for $m = 4$.

$$x_i = \sqrt{\frac{i}{m}} \cdot \frac{l}{2} \tag{6.47}$$

If a different connector layout is chosen, e. g. with uniform spacing, the connectors subjected to higher elastic shear forces will exhibit plastic deformations already before the end of state II, redistributing shear forces until all connectors reach their shear capacity. In the case of a limited connection deformation capacity, this may affect the load-bearing capacity of the composite member. This influence is further discussed in Chapter 6.4.3.

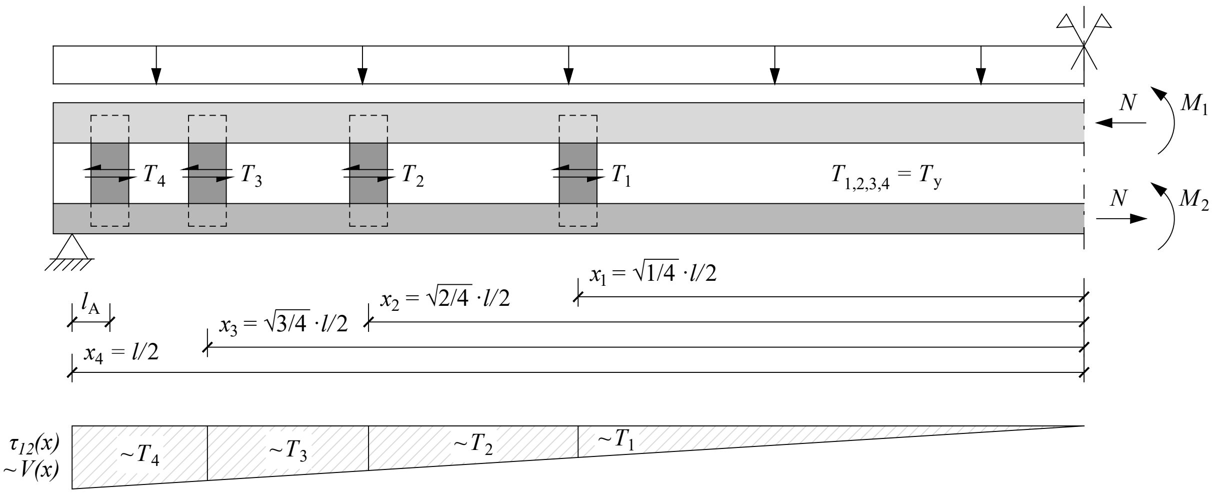

Fig. 6.8: End of state II: composite beam with $m = 4$ connectors per shear area.

Using Eq. 6.40, 6.43 and 6.46, the bending moment leading to yielding of all connectors M_y is calculated:

$$M_y = \underbrace{\frac{m \cdot T_y}{A_2}}_{\sigma_{2,m}} \cdot \frac{I_{II}}{\gamma_2 n_2 \cdot a_{2,II}} \tag{6.48}$$

The corresponding curvature follows:

$$\chi_y = \frac{M_y}{EI_{II}} \tag{6.49}$$

Potential other failures during state II

In order to ensure a ductile failure mode of the composite member, any brittle failures during state II should be avoided, such as:

- $\boxed{\text{II,1c}}$ concrete crushing
- $\boxed{\text{II,2tb}}$ timber tensile-bending failure

Setting $\sigma_{1,\text{sup}} = -f_{1,\text{c}}$ in Eq. 6.39 yields:

$$M_{\text{II,1c}} = \frac{I_{\text{II}} \cdot f_{1,\text{c}}}{(\gamma_{1,\text{II}} a_{1,\text{II}} + h_{1,\text{II}}/2) \cdot n_1} \tag{6.50}$$

This expression delivers a lower limit value for the bending moment at which concrete crushing would occur during state II. The real value would be higher because concrete can exhibit plastic deformations in compression and therefore redistribute stresses. As this is a scenario that should be avoided in any case, a more precise solution is not considered here.
According to Eurocode 5 [13], a combined tensile-bending failure in timber is reached when:

$$\frac{\sigma_{\text{t}}}{f_{\text{t}}} + \frac{\sigma_{\text{m}}}{f_{\text{m}}} = 1 \tag{6.51}$$

Applied to the stress state shown in Fig. 6.7, the failure criterion reads:

$$\frac{\sigma_{2,\text{m}}}{f_{2,\text{t}}} + \frac{\sigma_{2,\text{inf}} - \sigma_{2,\text{m}}}{f_{2,\text{m}}} = 1 \tag{6.52}$$

Using Eq. 6.40, the bending moment leading to a potential timber tensile-bending failure during state II is determined as follows:

$$M_{\text{II,2tb}} = \frac{I_{\text{II}}}{\left(\frac{\gamma_2 a_{2,\text{II}}}{f_{2,\text{t}}} + \frac{h_2}{2 f_{2,\text{m}}}\right) \cdot n_2} \tag{6.53}$$

If $M_{\text{y}} > \min\left(M_{\text{II,1c}}, M_{\text{II,2tb}}\right)$, yielding of all connectors will not be reached. Instead, the load-bearing behaviour ends at the corresponding load level with a brittle failure. Otherwise, the bending moment can be further increased in state III.

6.2.5 State III: connection plastic, concrete cracked and elastic

During state III, the concrete section is cracked and the connection behaviour is plastic. As the sum of the shear forces in the connectors is constant, the normal force N in the partial sections remains constant during state III (Eq. 6.46). The curvature of the composite cross-section χ and consequently the internal bending moments M_1 and M_2 are increased during state III. The normal force in the concrete section can be formulated as follows:

$$N = \underbrace{h_{1,\text{III}} \cdot \chi_{\text{III}} \cdot E_1}_{-\sigma_{1,\text{sup}}} \cdot \frac{1}{2} b_1 h_{1,\text{III}} \tag{6.54}$$

Using Eq. 6.46 and solving for $h_{1,\text{III}}$ reveals the relation between the height of the concrete compression zone and the curvature of the composite cross-section during state III:

$$h_{1,\text{III}} = \sqrt{\frac{2mT_y}{E_1 b_1} \cdot \frac{1}{\chi_{\text{III}}}} \tag{6.55}$$

In contrast to states I and II, the concrete compression zone height is not constant anymore during state III, but gradually decreases with increasing curvature. It is also worth noting that the concrete compression zone height is not dependent on the elastic connection stiffness K anymore.

End of state III: concrete compressive strength reached

Fig. 6.9 illustrates the geometry of the composite cross-section and the axial strains, stresses and internal forces at the end of state III, which is marked by the concrete compressive stress reaching its compressive strength.

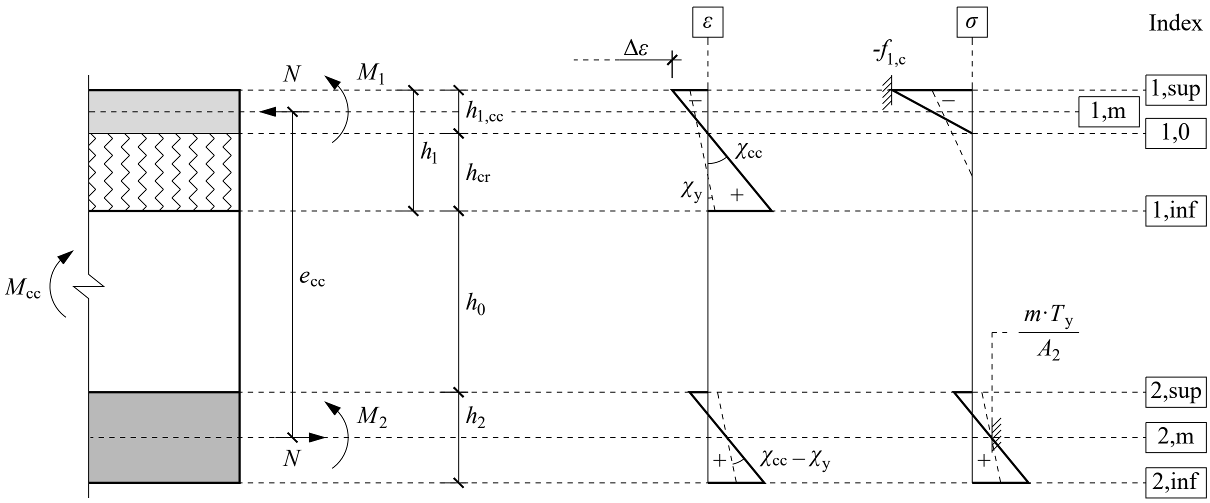

Fig. 6.9: Axial strains, stresses and internal forces at the end of state III (concrete compressive strength reached).

The compressive stress at the top of the concrete section is:

$$\sigma_{1,\text{sup}} = -h_{1,\text{cc}} \cdot \chi_{\text{cc}} \cdot E_1 \overset{!}{=} -f_{1,\text{c}} \tag{6.56}$$

Eq. 6.55 and 6.56 form a 2×2 system of equations leading to the following solutions:

$$h_{1,\text{cc}} = \frac{2mT_y}{b_1 f_{1,\text{c}}} \tag{6.57}$$

$$\chi_{\text{cc}} = \frac{f_{1,\text{c}}}{E_1 h_{1,\text{cc}}} \tag{6.58}$$

As the normal force in the partial sections has not changed since the end of state II, the axial strain and stress in the centroid of the timber section remain unchanged (Fig. 6.9). Using the curvature χ_{cc}, the axial strains and stresses in the timber section at the end of state III are fully defined:

$$\varepsilon_2 = \begin{pmatrix} \varepsilon_{2,sup} \\ \varepsilon_{2,m} \\ \varepsilon_{2,inf} \end{pmatrix} = \frac{mT_y}{E_2 A_2} + \begin{pmatrix} -h_2/2 \\ 0 \\ h_2/2 \end{pmatrix} \cdot \chi_{cc} \tag{6.59}$$

$$\sigma_2 = \begin{pmatrix} \sigma_{2,sup} \\ \sigma_{2,m} \\ \sigma_{2,inf} \end{pmatrix} = \frac{mT_y}{A_2} + \begin{pmatrix} -h_2/2 \\ 0 \\ h_2/2 \end{pmatrix} \cdot E_2 \cdot \chi_{cc} \tag{6.60}$$

The distance between the centroids of the partial sections at the end of state III is calculated as follows:

$$e_{cc} = h_0 + h_1 - \frac{h_{1,cc}}{2} + \frac{h_2}{2} \tag{6.61}$$

The internal forces acting on the partial sections at the end of state III result as follows (with $I_{1,cc}$ from Eq. 6.9 with $h_1 = h_{1,cc}$):

$$M_1 = E_1 I_{1,cc} \cdot \chi_{cc} \tag{6.62}$$

$$M_2 = E_2 I_2 \cdot \chi_{cc} \tag{6.63}$$

$$N = mT_y \tag{6.64}$$

Based on the equilibrium conditions, the bending moment at the end of state III is found:

$$M_{cc} = M_1 + M_2 + N \cdot e_{cc} = (E_1 I_{1,cc} + E_2 I_2) \cdot \chi_{cc} + mT_y \cdot e_{cc} \tag{6.65}$$

The slip strain is calculated as follows:

$$\Delta\varepsilon_{cc} = (h_0 + h_1 - h_{1,cc} + \frac{h_2}{2}) \cdot \chi_{cc} - \frac{mT_y}{E_2 A_2} \tag{6.66}$$

Potential other failures during state III

In order to ensure that the composite member can exhibit large deformations before ultimate failure, any brittle failures should be avoided until the end of state III, such as:

- $\boxed{\text{III,2tb}}$ timber tensile-bending failure
- $\boxed{\text{III,}\Delta\text{u}}$ exceedance of connection deformation capacity (Chapter 6.2.7)

The curvature leading to a potential timber tensile-bending failure $\chi_{III,2tb}$ is derived from Eq. 6.52 and 6.60:

$$\chi_{III,2tb} = \frac{2 f_{2,m}}{E_2 h_2} \cdot \left(1 - \frac{mT_y}{A_2 f_{2,t}}\right) \tag{6.67}$$

If $\chi_{III,2tb} < \chi_{cc}$, the composite member will collapse after small plastic deformations in the connectors. In this case, the corresponding concrete compression zone height $h_{1,III,2tb}$ as well as $e_{III,2tb}$, $I_{1,III,2tb}$ and the corresponding bending moment $M_{III,2tb}$ can be calculated using Eq. 6.55, 6.61, 6.9 and 6.65 using $\chi_{III,2tb}$. If $\chi_{III,2tb} > \chi_{cc}$, curvature and bending moment can be further increased in state IV.

6.2.6 State IV: connection plastic, concrete cracked and plastic

During state IV, the concrete section is cracked and the connection behaviour is plastic. The concrete section exhibits plastic deformations after its compressive strength is reached at the end of state III, leading to a redistribution of stresses. The ultimate failure of the composite member can be caused by:

- $\boxed{\text{u,1c}}$ concrete crushing (i.e. reaching the ultimate compressive strain $\varepsilon_{1,\mathrm{u}} \approx 0.003$)
- $\boxed{\text{u,2tb}}$ timber tensile-bending failure
- $\boxed{\text{u,}\Delta\text{u}}$ exceedance of connection deformation capacity (Chapter 6.2.7)

In the analysis of reinforced concrete sections, various methods are available to consider stress redistributions within the concrete compression zone. One possibility is to assume an analytical nonlinear stress-strain relationship, e. g. as suggested in Eurocode 2 [12]. For simplified analyses, the Swiss standard SIA 262 [76] suggests a rectangular stress block $\sigma = -f_{\mathrm{c}}$ over a height of 85% of the concrete compression zone (Fig. 6.10). This simplification is valid for cases where the reinforced concrete member fails due to concrete crushing while the reinforcement is yielding.

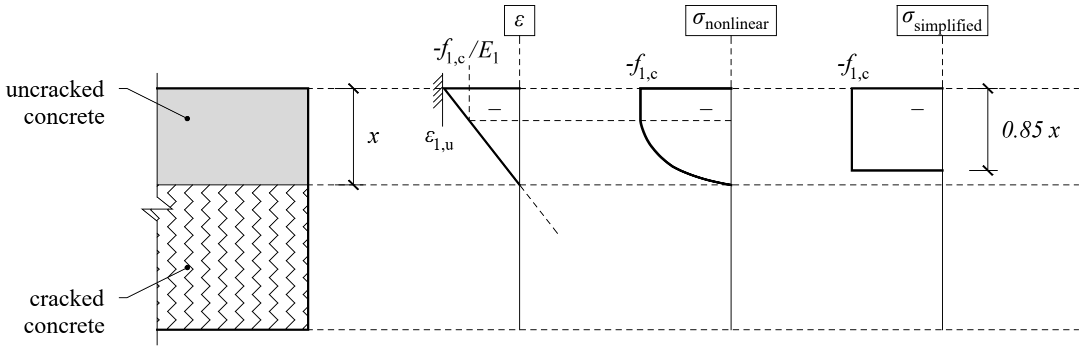

Fig. 6.10: Idealised stress-strain diagrams for concrete, according to SIA 262 [76].

In a TCC structure with a ductile connection system, instead of the steel reinforcement, the connectors yield. The above-mentioned concepts regarding the stress redistributions are applicable also here, if ultimate failure is caused by concrete crushing [4]. If any other failure is decisive, the strain at the top of the concrete section does not reach $\varepsilon_{1,\mathrm{u}}$. As a consequence, assuming a rectangular stress block as depicted in Fig. 6.10 leads to an overestimation of the eccentricity of the resulting concrete compressive force. However, considering the geometry of the investigated structure, this deviation is usually small compared to the distance between the centroids of the partial sections e. Therefore, the stress block simplification is used to obtain an approximation of the failure load also in these cases. Based on these assumptions, the concrete compression zone height during state IV is calculated from the equilibrium of horizontal forces:

$$h_{1,\mathrm{IV}} = \frac{mT_{\mathrm{y}}}{0.85 b_1 f_{1,\mathrm{c}}} \tag{6.68}$$

End of state IV: ultimate failure

The curvature leading to a timber tensile-bending failure at the end of state IV $\chi_{\mathrm{u,2tb}}$ can be calculated with the same formula as during state III (Eq. 6.67). The curvature causing concrete crushing is:

$$\chi_{\mathrm{u,1c}} = \frac{\varepsilon_{1,\mathrm{u}}}{h_{1,\mathrm{IV}}} \tag{6.69}$$

The governing failure mode is determined as follows:

$$\chi_{\mathrm{u}} = \min\left(\chi_{\mathrm{u,1c}}, \chi_{\mathrm{u,2tb}}\right) \tag{6.70}$$

Fig. 6.11 illustrates the geometry of the composite cross-section and the axial strains, stresses and internal forces at the end of state IV, for the case where timber tensile-bending failure is governing.

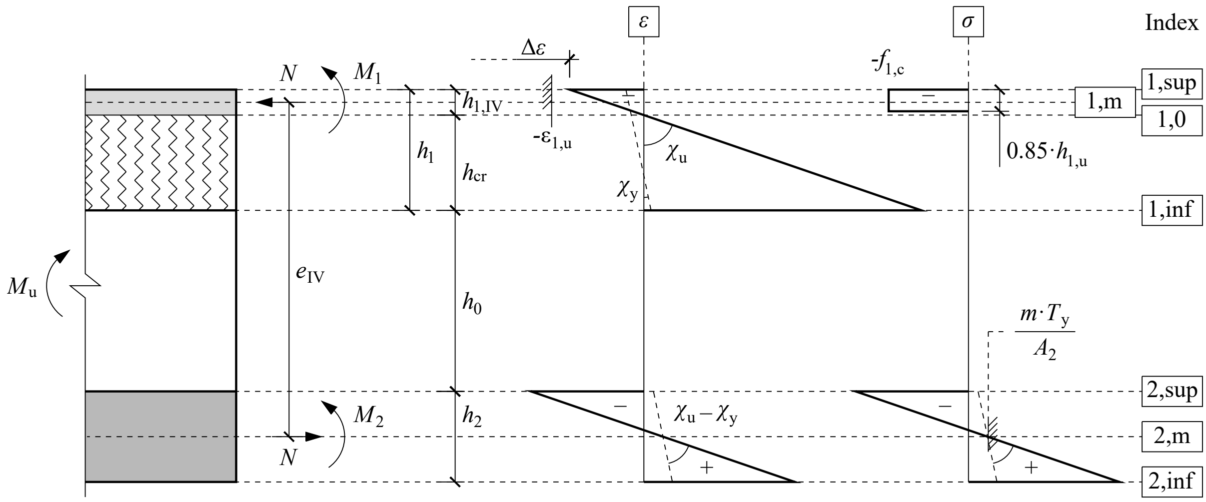

Fig. 6.11: Axial strains, stresses and internal forces at the end of state IV (ultimate failure, here: timber tensile-bending failure).

The axial strains and stresses in the timber section at ultimate failure can be calculated with Eq. 6.59 and 6.60, using χ_{u} instead of χ_{cc}. The distance between the centroids of the partial sections at ultimate failure is calculated as follows:

$$e_{\mathrm{IV}} = h_0 + h_1 - \frac{h_{1,\mathrm{IV}}}{2} + \frac{h_2}{2} \tag{6.71}$$

The internal forces acting on the partial sections at the end of state IV result as follows (with $I_{1,\mathrm{IV}}$ from Eq. 6.9 with $h_1 = h_{1,\mathrm{IV}}$):

$$M_1 = \frac{1 - 0.85}{2} \cdot h_{1,\mathrm{IV}} \cdot mT_{\mathrm{y}} \tag{6.72}$$

$$M_2 = E_2 I_2 \cdot \chi_{\mathrm{u}} \tag{6.73}$$

$$N = mT_{\mathrm{y}} \tag{6.74}$$

Based on the equilibrium conditions, the bending moment at the end of state IV is found:

$$M_{\mathrm{u}} = M_1 + M_2 + N \cdot e_{\mathrm{IV}} = E_2 I_2 \cdot \chi_{\mathrm{u}} + mT_{\mathrm{y}} \cdot \left(e_{\mathrm{IV}} + \frac{1 - 0.85}{2} \cdot h_{1,\mathrm{IV}} \right) \tag{6.75}$$

The slip strain is calculated as follows:

$$\Delta\varepsilon_{\mathrm{u}} = (h_0 + h_1 - h_{1,\mathrm{IV}} + \frac{h_2}{2}) \cdot \chi_{\mathrm{u}} - \frac{mT_{\mathrm{y}}}{E_2 A_2} \tag{6.76}$$

6.2.7 Deflection and slip displacement

The derivation of the curvature χ and the slip strain $\Delta\varepsilon$ for any given bending moment at mid-span is covered in Chapters 6.2.3 – 6.2.6. Fig. 6.12 shows typical results of this part of the analysis. As already discussed in Chapter 6.2.1, the bending stiffness in states I and II are typically almost equal. During states III and IV, the bending stiffness decreases at an approximately constant rate (Fig. 6.12a). Therefore, once the external load leading to yielding of all connectors is exceeded ($q > q_{\mathrm{y}}$), the composite beam does not have a uniform bending stiffness over its entire length anymore. As a consequence, the deflections cannot be calculated accurately based on commonly used formulas for beams with a constant bending stiffness anymore.

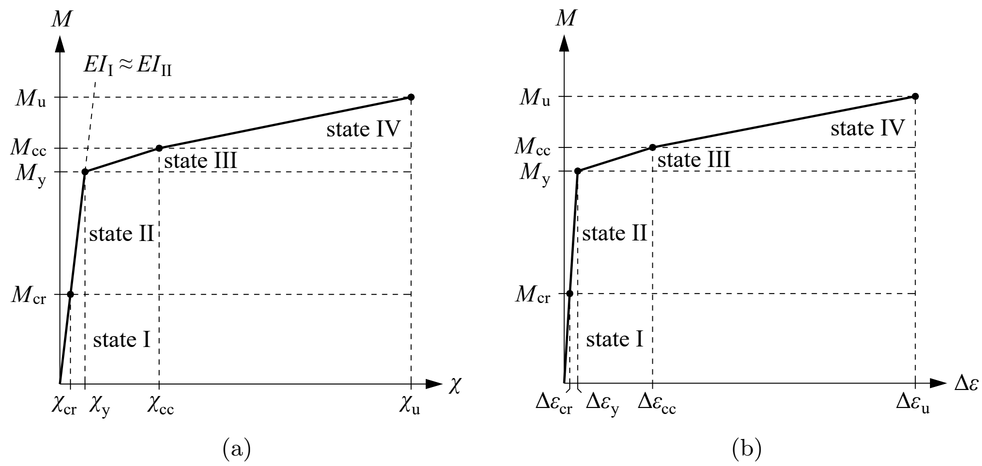

Fig. 6.12: Typical results of the composite cross-section analysis explained in Chapters 6.2.3 – 6.2.6: bending moment vs. (a) curvature and (b) slip strain.

In general, deflections w result from integrating the curvature χ twice along the beam axis, while slip displacements Δu are obtained by integration of the slip strain $\Delta\varepsilon$:

$$w(x) = -\iint \chi(x)\, dx\, dx \tag{6.77}$$

$$\Delta u(x) = \int \Delta\varepsilon(x)\, dx \tag{6.78}$$

As the slip strain $\Delta\varepsilon$ is a function of the curvature χ (Eq. 6.29, 6.66, 6.76), the M-χ and M-$\Delta\varepsilon$ relationships are similar (Fig. 6.12). Considering Eq. 6.77 and 6.78, it can be concluded that the calculation of deflections w and slip displacements Δu are two closely related problems. Thus, it appears reasonable to use a method that allows to calculate w and Δu based on the same principles. As the connectors used in the investigated TCC structure have a limited deformation capacity, the calculation of the slip displacement is an important step in the presented model. Two approaches of how to calculate the deflections due to an external load $q > q_{\mathrm{y}}$ have already been suggested:

(i) For a rough estimation, an upper limit value of the deflections may be obtained by assuming a constant bending stiffness over the entire beam, equal to the secant bending stiffness at the point of maximum bending moment (for instance: $EI_{\mathrm{u}} = M_{\mathrm{u}}/\chi_{\mathrm{u}}$) [4].

(ii) Boccadoro [4] suggested to assume that all deformations induced by loads $\Delta q = q - q_{\mathrm{y}}$ are concentrated in a plastic hinge at the point of maximum bending moment, based on an analogy to reinforced concrete beams. The total deflections are then obtained by superposition $w = w_{\mathrm{y}} + \Delta w_{\mathrm{pl}}$. However, calculation of Δw_{pl} requires an assumption for the plastic hinge length, which is generally unknown [1].

While approach (i) could be used also for an estimation of the slip displacement, the resulting upper limit value may not be close enough to the correct value to be used in the discussed context. Approach (ii) strongly focuses on the calculation of the deflections and does not seem suitable for a calculation of slip displacements. Apart from the fact that the length of the plastic hinge is unknown, it would be difficult to estimate the slip displacements in this plastic zone.

Therefore, a different calculation method is presented below that allows to estimate both deflections and slip displacements using the same principles and without the need to assume a plastic hinge length. Depending on the application, solutions can be obtained based on numerical or analytical integration. The method is applied to the case of a simply supported beam with span l subjected to uniformly distributed load q. However, the same approach may be used to find solutions also for other cases.

The model assumes the M-χ and M-Δu relationships as shown in Fig. 6.12 not only for the cross-section at mid-span, but for the entire beam. Strictly speaking, this is a simplification because during states III and IV, the behaviour depends on the number of connectors between the support and the considered point. In the case of a simply supported beam subjected to uniformly distributed load, this influence is neglected for the following reasons:

- In view of an optimised design, connectors are typically concentrated towards the supports. As a consequence, the size of the areas affected by the described simplification is small.

- The affected areas close to the supports are subjected to relatively small bending moments and mostly remain in state I or II.

Using a numerical integration method such as the Riemann sum (described e. g. by Truc [86]), Eq. 6.77 and 6.78 can be solved with relatively small effort even for nonlinear M-χ and M-Δu relationships. Fig. 6.13 shows results computed in this way for the case of a simply supported beam with span l subjected to uniformly distributed load q.

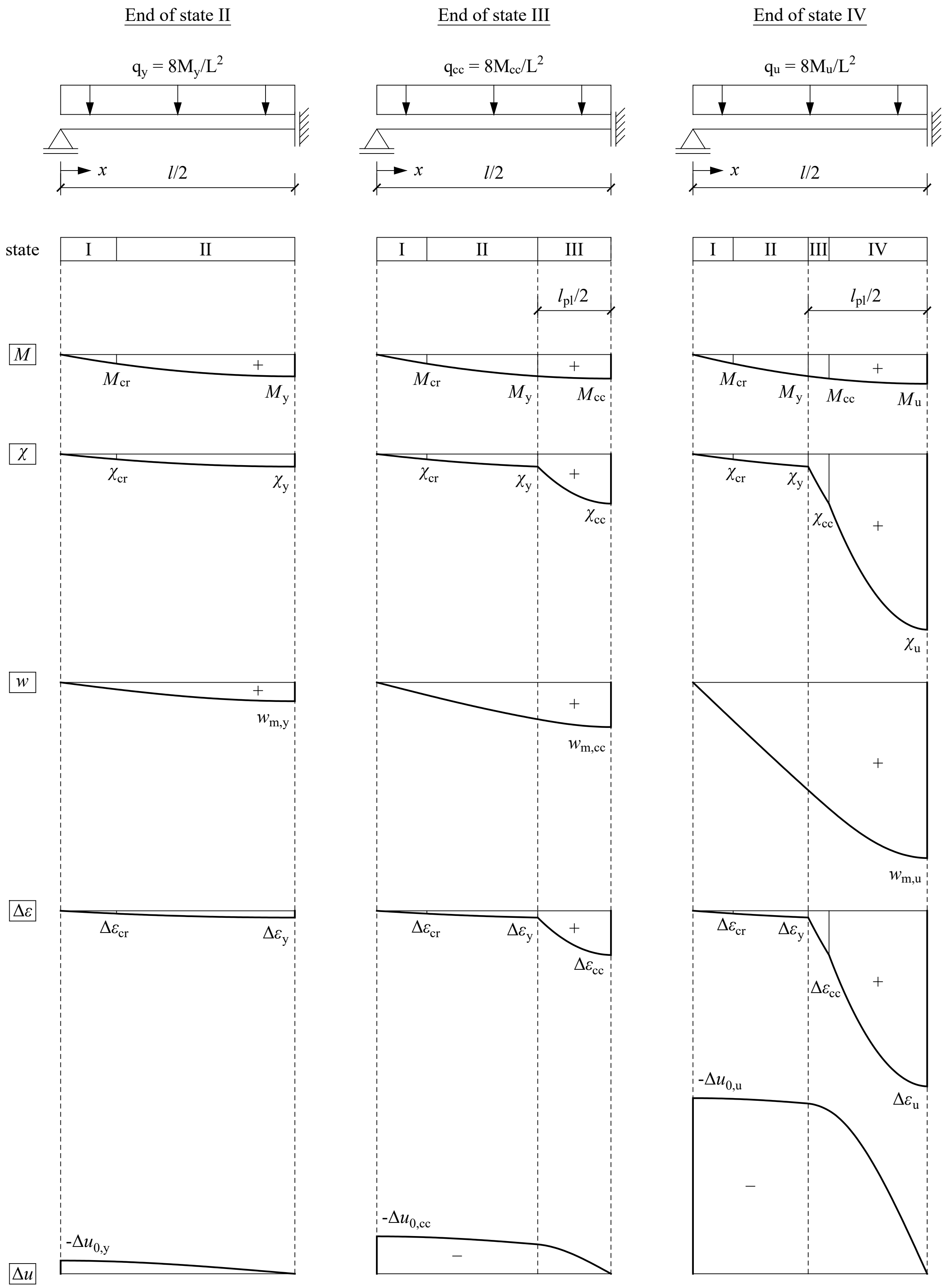

Fig. 6.13: Simply supported beam subjected to uniformly distributed load q: bending moments M, curvature χ, deflections w, slip strains $\Delta\varepsilon$ and slip displacements Δu calculated using numerical integration.

With increasing load, curvature and slip strain start concentrating at mid-span. The length of the area where the composite cross-section is in state III or IV ($M > M_y$) can be calculated as follows:

$$l_{pl} = \begin{cases} 0 & \text{for } q < q_y \\ \sqrt{1 - q_y/q} \cdot l & \text{for } q \geq q_y \end{cases} \tag{6.79}$$

State I

For loads $q < q_{cr}$, the entire beam is in state I. Solving Eq. 6.77 and 6.78, using Eq. 6.20, 6.29 and the boundary conditions $w(0) = 0$, $w'(l/2) = 0$ and $\Delta u(l/2) = 0$ leads to analytical solutions for this case. Solving the indefinite integral in Eq. 6.78 yields a negative value $\Delta u < 0$ for the support at $x = 0$, as depicted in Fig. 6.13, but would be positive for the support at $x = l$. For simplicity, the slip displacement at the supports Δu_0 is defined as a positive value hereinafter.

$$w_{m,I} = \frac{5}{384} \cdot \frac{ql^4}{EI_I} \tag{6.80}$$

$$\Delta u_{0,I} = \frac{1 - \gamma_{1,I}}{24} \cdot \frac{qa_{1,I}l^3}{EI_I} \tag{6.81}$$

State II

In order to simplify the derivation of analytical expressions for loads $q > q_{cr}$, the slightly higher bending stiffness in areas remaining in state I is neglected hereinafter. The cracked stiffness EI_{II} is assumed for both state I and II areas. The same is done also for the M-$\Delta\varepsilon$ relationship (Fig. 6.14a). The following expressions result for loads $q_{cr} < q < q_y$:

$$w_{m,II} = \frac{5}{384} \cdot \frac{ql^4}{EI_{II}} \tag{6.82}$$

$$\Delta u_{0,II} = \frac{1 - \gamma_{1,II}}{24} \cdot \frac{qa_{1,II}l^3}{EI_{II}} \tag{6.83}$$

State III

For loads $q_y < q < q_{cc}$, an analytical expression for $\Delta u_{0,III}$ can be found by solving Eq. 6.78 as a definite integral, dividing the beam into two segments as shown in Fig. 6.14b.

$$\begin{aligned} \Delta u_{0,III} &= \Delta u_0^{(1)} + \Delta u_0^{(2)} = \int_0^{(l-l_{pl})/2} \Delta\varepsilon_{II}(x)\,dx + \int_{(l-l_{pl})/2}^{l_{pl}} \Delta\varepsilon_{III}(x)\,dx \\ &= \frac{(1-\gamma_{1,II}) \cdot a_{1,II}}{EI_{II}} \cdot \int_0^{(l-l_{pl})/2} M(x)\,dx \\ &\quad + \int_{(l-l_{pl})/2}^{l_{pl}} \left(\Delta\varepsilon_y + \frac{\Delta\varepsilon_{cc} - \Delta\varepsilon_y}{M_{cc} - M_y} \cdot (M(x) - M_y) \right) dx \end{aligned} \tag{6.84}$$

Solving the definite integrals in Eq. 6.84 with $M(x) = \frac{q}{2}(lx - x^2)$ leads to the following expression:

$$\Delta u_{0,\mathrm{III}} = \frac{1-\gamma_{1,\mathrm{II}}}{16} \cdot \frac{q a_{1,\mathrm{II}}}{EI_{\mathrm{II}}} \cdot \left[l\,(l-l_{\mathrm{pl}})^2 - \frac{1}{3}(l-l_{\mathrm{pl}})^3 \right] + \frac{1}{2} l_{\mathrm{pl}} \Delta\varepsilon_{\mathrm{y}}$$
$$+ \frac{\Delta\varepsilon_{\mathrm{cc}} - \Delta\varepsilon_{\mathrm{y}}}{M_{\mathrm{cc}} - M_{\mathrm{y}}} \cdot \left[\frac{ql}{16} \cdot l_{\mathrm{pl}}\,(2l - l_{\mathrm{pl}}) - \frac{q}{48}\left(l^3 - (l - l_{\mathrm{pl}})^3 \right) - \frac{1}{2} l_{\mathrm{pl}} M_{\mathrm{y}} \right] \tag{6.85}$$

State IV

In analogy, an analytical solution can be derived also for loads $q_{\mathrm{cc}} < q < q_{\mathrm{u}}$, dividing the beam into three segments corresponding to states I/II, III and IV (Fig. 6.14c). This leads to the following expression:

$$\Delta u_{0,\mathrm{IV}} = \frac{1-\gamma_{1,\mathrm{II}}}{16} \cdot \frac{q a_{1,\mathrm{II}}}{EI_{\mathrm{II}}} \cdot \left[l\,(l-l_{\mathrm{pl}})^2 - \frac{1}{3}(l-l_{\mathrm{pl}})^3 \right] + \frac{1}{2}\left(l_{\mathrm{pl,III}} \Delta\varepsilon_{\mathrm{y}} + l_{\mathrm{pl,IV}} \Delta\varepsilon_{\mathrm{cc}} \right)$$
$$+ \frac{\Delta\varepsilon_{\mathrm{cc}} - \Delta\varepsilon_{\mathrm{y}}}{M_{\mathrm{cc}} - M_{\mathrm{y}}} \cdot \left[\frac{ql}{16} \cdot l_{\mathrm{pl,III}}\,(2l - l_{\mathrm{pl}} - l_{\mathrm{pl,IV}}) - \frac{q}{48}\left((l - l_{\mathrm{pl,IV}})^3 - (l - l_{\mathrm{pl}})^3 \right) - \frac{1}{2} l_{\mathrm{pl,III}} M_{\mathrm{y}} \right]$$
$$+ \frac{\Delta\varepsilon_{\mathrm{u}} - \Delta\varepsilon_{\mathrm{cc}}}{M_{\mathrm{u}} - M_{\mathrm{cc}}} \cdot \left[\frac{ql}{16} \cdot l_{\mathrm{pl,IV}}\,(2l - l_{\mathrm{pl,IV}}) - \frac{q}{48}\left(l^3 - (l - l_{\mathrm{pl,IV}})^3 \right) - \frac{1}{2} l_{\mathrm{pl,IV}} M_{\mathrm{cc}} \right] \tag{6.86}$$

with

$$l_{\mathrm{pl,IV}} = \sqrt{1 - q_{\mathrm{cc}}/q} \cdot l \tag{6.87}$$

$$l_{\mathrm{pl,III}} = l_{\mathrm{pl}} - l_{\mathrm{pl,IV}} \tag{6.88}$$

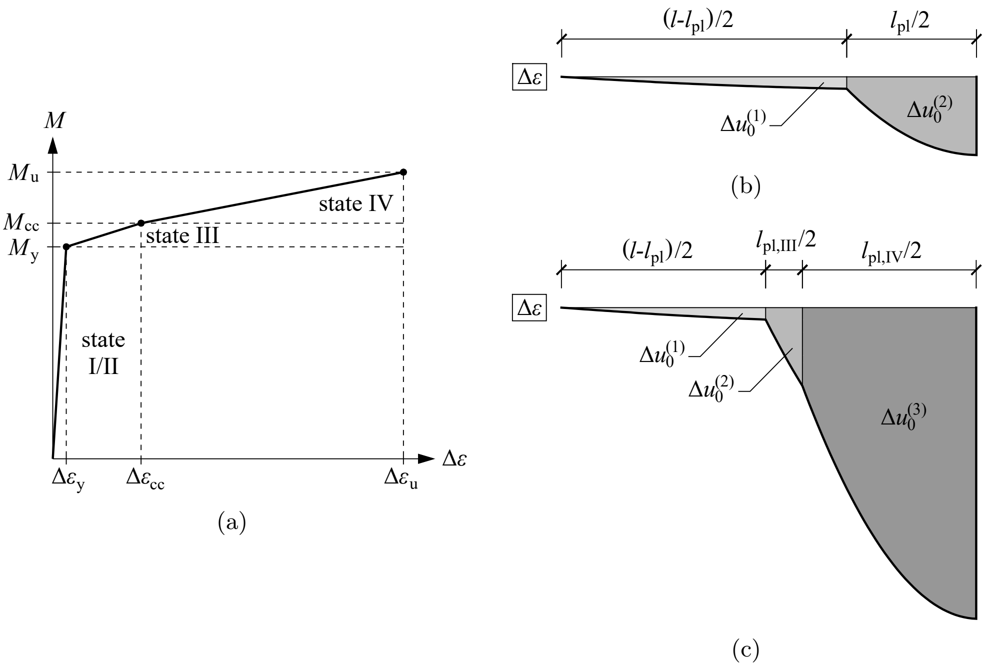

Fig. 6.14: (a) Simplified M-$\Delta\varepsilon$ relationship used in the derivation of analytical expressions for the slip displacement at the supports Δu_0 by integration of $\Delta\varepsilon$, during (b) state III and (c) state IV.

Deriving analytical expressions for $w_{\mathrm{m,III}}$ and $w_{\mathrm{m,IV}}$ would be possible in the same way. Because of the double integral in Eq. 6.77, however, the expressions would become significantly more complicated than in the case of Δu_0. Depending on the assumed connection behaviour, $\Delta u_0 \leq \Delta u_{\max}$ may be the limiting condition for ULS design. Analytical expressions for Δu_0 are therefore valuable in practice as they allow easy parametric design optimisation using spreadsheet calculations. In contrast, estimating the deflections at mid-span for loads $q > q_{\mathrm{y}}$ is mainly of academic interest and can be done using numerical integration methods.

6.3 Strut-and-tie model

6.3.1 Introduction

The strut-and-tie model used in this research project is based on the work published by Grosse et al. [33] and Rautenstrauch et al. [65], described in Chapter 2.2.2. Two main modifications were made to the original strut-and-tie model to better reflect the specific characteristics of the investigated TCC slab with an interlayer. Firstly, instead of using connector beam elements with a fictitious bending stiffness EI^* and a hinge (Fig. 2.7), rotational springs are implemented (Fig. 6.15). This allows for a more direct representation of the connection behaviour, using the rotational stiffness values obtained from the connection shear tests (Chapter 3). The properties of the connector beam itself are derived from the cross-section of the concrete-filled steel tubes (described in Chapter 3.2.4). Secondly, the hinged rigid beam elements representing the vertical contact of the two members may be omitted depending on the stiffness of the interlayer material. If a soft material is used (e. g. cellulose fibers), vertical forces between the two layers are only transmitted via the steel tubes and in the location of the concrete edge beam (Fig. 6.15). Hence, the structural behaviour is represented more accurately if the hinged rigid beam elements are omitted in the model. In the case of the specimens tested in uniaxial bending (Chapter 4), the stiffer stone wool combined with an upper LVL beam provided significant vertical support for the concrete layer and therefore, the respective elements were kept in the model (dashed in Fig. 6.15).

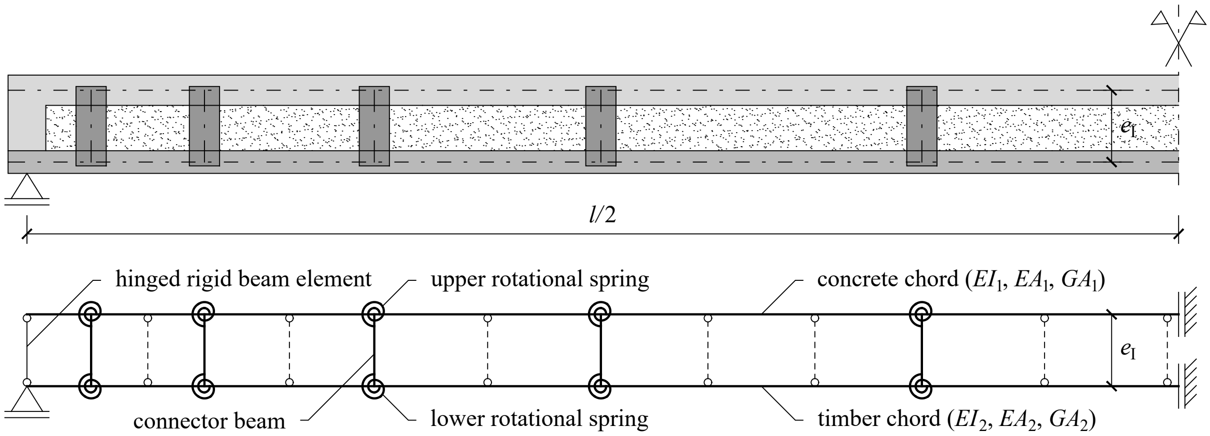

Fig. 6.15: Strut-and-tie model for a single span TCC slab with five steel tubes per shear area and a concrete edge beam.

As mentioned already in Chapter 2.2.2, one of the disadvantages of strut-and-tie models concerns situations where concrete cracking occurs under positive bending moments and significantly influences the structural behaviour. The calculation results show that the investigated TCC slab presents such a case. In the elasto-plastic γ-method (Chapter 6.2), concrete cracking is automatically accounted for. An attempt was made to consider concrete cracking also in the strut-and-tie model to improve the comparability of the calculation results. Furthermore, the model was used with rotational springs either based on linearised stiffness values k_m or on nonlinear $M-\varphi$ curves obtained from the connection shear tests. Therefore, four versions of the strut-and-tie model are presented in the subsequent chapters. An in-depth comparison of the results of these models and the elasto-plastic γ-method with the results obtained from the uniaxial bending tests, follows in Chapter 6.4.

6.3.2 Uncracked concrete and linear connection behaviour

Calculation of modified rotational spring stiffness

The properties of the steel tube connection were determined in push-out tests. Within the scope of the data evaluation, the position of the rotational springs was defined at the base of the steel tube (Chapter 3.2.4). In theory, this definition could be directly implemented also in the strut-and-tie model, as illustrated in Fig. 6.3a. However, this would require additional short rigid beam elements between the connector beams and the timber and concrete chords. For typical geometries ($l_\mathrm{T} > e_\mathrm{I}$), these would overlap the connector beams, affecting the clarity of the model and increasing the probability of errors in the model definition. Therefore, the rotational springs are moved such that the connector beam elements (steel tubes) can be linked directly to the timber and concrete chords as shown in Fig. 6.15. However, changing the position of the rotational springs affects the resulting connection stiffness. To compensate for this influence, modified rotational stiffnesses $k_\mathrm{m,inf,mod}$ and $k_\mathrm{m,sup,mod}$ are calculated.

In general, the eccentricity of the two rotational springs as well as their stiffness values are not equal, which leads to an asymmetric distribution of the bending moment in the steel tube, as shown in Fig. 6.3c. While an individual calculation of $k_\mathrm{m,inf,mod}$ and $k_\mathrm{m,sup,mod}$ considering this asymmetry is theoretically possible, the resulting equations would reach an apparent level of detail that is not anymore in agreement with the precision of the experimentally determined, linearised input values $k_\mathrm{m,inf}$ and $k_\mathrm{m,sup}$. Therefore, the stiffness modification is derived based on a simplified static system illustrated in Fig. 6.16, assuming a symmetric connector with $M = 0$ at half the height of the steel tube. Requiring that T and Δu are equal in both static systems depicted in Fig. 6.16 leads to Eq. 6.89, which can be used for both rotational springs ($k_\mathrm{m,inf} \to k_\mathrm{m,inf,mod}$ and $k_\mathrm{m,sup} \to k_\mathrm{m,sup,mod}$). A further simplification would be to neglect the influence of bending and shear deformations in the steel tube ($EI_\mathrm{T}, GA_\mathrm{T} \to \infty$). In this case, Eq. 6.89 reduces to $k_\mathrm{m,mod} = e_\mathrm{I}^2/l_\mathrm{T}^2 \cdot k_\mathrm{m}$. However, with increasing values of k_m, this simplification may lead to a significant overestimation of the resulting connection stiffness.

$$k_\mathrm{m,mod} = \frac{e_\mathrm{I}^2}{(l_\mathrm{T}^3 - e_\mathrm{I}^3)/6EI_\mathrm{T} + 2(l_\mathrm{T} - e_\mathrm{I})/GA_\mathrm{T} + l_\mathrm{T}^2/k_\mathrm{m}} \tag{6.89}$$

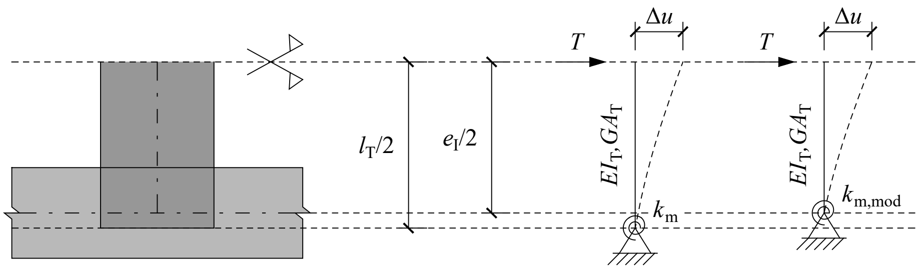

Fig. 6.16: Derivation of modified rotational spring stiffness: geometry of the connection, original spring position and modification for strut-and-tie model.

Failures

With the described modification of the rotational spring stiffnesses, the strut-and-tie model is fully defined and can be implemented in any standard FEM software. The concrete chord is modelled with its uncracked cross-section stiffness. All relevant failure modes can be assessed based on the following results that are obtained directly from the model: internal forces in the concrete (M_1, N_1) and timber section (M_2, N_2) as well as the shear force in the connectors T_i. A connection failure is reached when

$$\max(T_i) = T_\mathrm{y} \tag{6.90}$$

with T_y according to Eq. 6.5. Applying the failure criterion for combined tension and bending in timber according to Eurocode 5 [13] (Eq. 6.51) results in:

$$\frac{N_2}{A_2 \cdot f_{2,\mathrm{t}}} + \frac{M_2 \cdot h_2}{2I_2 \cdot f_{2,\mathrm{m}}} = 1 \tag{6.91}$$

The concrete section remains uncracked if:

$$\frac{N_1}{A_1} + \frac{M_1 \cdot h_1}{2I_1} < f_{1,\mathrm{t}} \tag{6.92}$$

where $N_1 < 0$ (compression). If Eq. 6.92 is valid, concrete compressive failure can be assessed analogously:

$$\left|\frac{N_1}{A_1} - \frac{M_1 \cdot h_1}{2I_1}\right| < f_{1,\mathrm{c}} \tag{6.93}$$

If Eq. 6.92 is not valid, a cracked concrete analysis is necessary. Fig. 6.17 shows the strains and stresses of an unreinforced, cracked concrete cross-section subjected to a bending moment M_1 and a normal force $N_1 < 0$. For small ratios M_1/N_1 the bending moment can be carried by an eccentricity of the resulting internal normal force, without having to activate any reinforcement. The compression zone height x, curvature χ and concrete stress $\sigma_{1,\mathrm{sup}}$ are derived from equilibrium (Eq. 6.94–6.96).

$$x = 3 \cdot (h_1/2 + M_1/N_1) \tag{6.94}$$

$$\chi = -\frac{2N_1}{E_1 b x^2} \tag{6.95}$$

$$\sigma_{1,\mathrm{sup}} = -E_1 \cdot x \cdot \chi \tag{6.96}$$

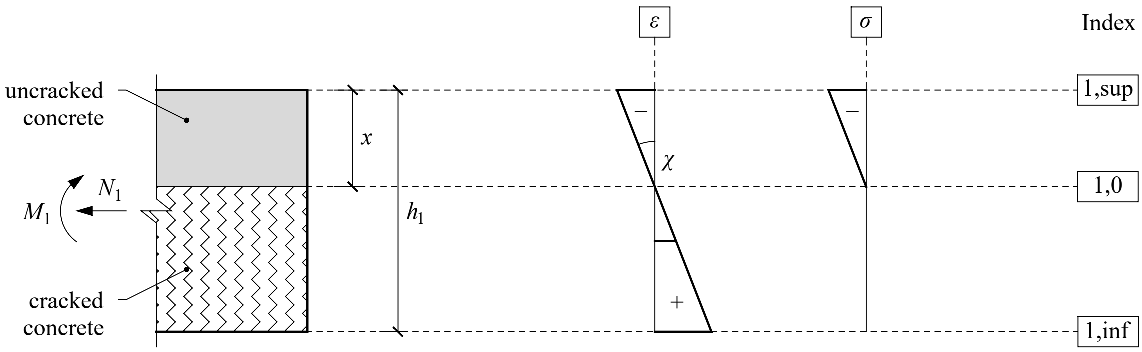

Fig. 6.17: Unreinforced concrete section subjected to a normal force N_1 and a bending moment M_1.

However, this calculation only works if $|M_1/N_1| < h_1/2$, as otherwise Eq. 6.94 delivers a negative value for x. In such a case, the bending moment cannot be carried only by eccentricity of the resulting internal normal force. Therefore, the reinforcement has to be considered in the analysis. This can be done either using suitable software or with an iterative calculation as described below. Fig. 6.18 shows the strains and stresses in the reinforced concrete cross-section. Assuming linear elasticity in both concrete and reinforcement, expressions for the compression zone height x and curvature χ can be derived from equilibrium (Eq. 6.97 and 6.98).

$$\chi = \frac{M_1}{A_s E_s (d - x)(d - h_1/2) + \frac{1}{2} b x^2 E_1 (h_1/2 - x/3)} \tag{6.97}$$

$$x = \frac{1}{b E_1 \chi} \cdot \left(\sqrt{2 A_s E_s E_1 b d \chi^2 + (A_s E_s \chi)^2 - 2 N_1 E_1 b \chi} - A_s E_s \chi \right) \tag{6.98}$$

Eq. 6.97 and 6.98 can be solved iteratively. The stresses in concrete and reinforcement follow according to Eq. 6.96 and 6.99.

$$\sigma_{1,s} = E_s \cdot (d - x) \cdot \chi \tag{6.99}$$

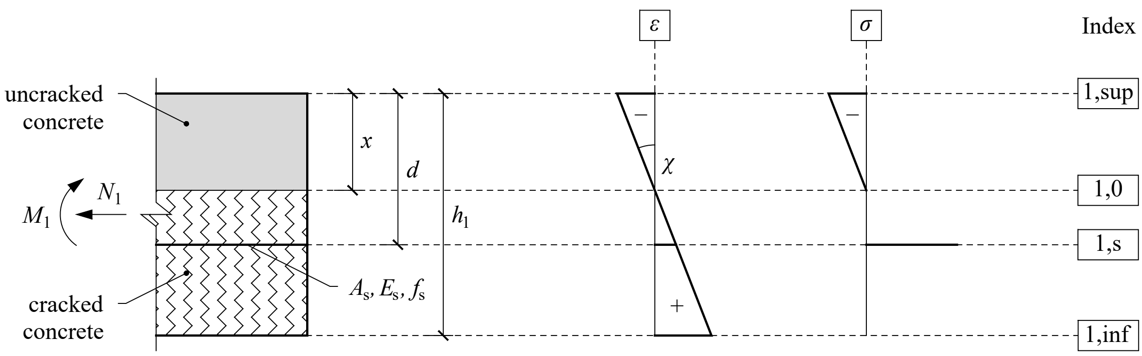

Fig. 6.18: Reinforced concrete section subjected to a normal force N_1 and a bending moment M_1.

If according to Eq. 6.99, $\sigma_{1,\mathrm{s}} \geq f_\mathrm{s}$ (reinforcement yielding), Eq. 6.97 and 6.98 have to be rewritten as follows:

$$\chi = \frac{M_1 - (d - h_1/2) \cdot A_\mathrm{s} f_\mathrm{s}}{\frac{1}{2} b x^2 E_1 \cdot (h_1/2 - x/3)} \tag{6.100}$$

$$x = \sqrt{\frac{A_\mathrm{s} f_\mathrm{s} - N_1}{\frac{1}{2} b E_1 \chi}} \tag{6.101}$$

Compressive failure in concrete occurs when $\sigma_{1,\mathrm{sup}} = -f_{1,\mathrm{c}}$, with $\sigma_{1,\mathrm{sup}}$ according to eg. 6.96.

6.3.3 Uncracked concrete and nonlinear connection behaviour

Calculation of modified connection $M-\varphi$ curves

Instead of characterising the rotational springs with a linearised stiffness k_m, many FEM software packages also allow for nonlinear analyses based on multi-linear $M-\varphi$ curves as an input. Such curves were obtained from the connection shear tests (Chapter 3.3.7). In analogy to the linear springs in Chapter 6.3.2, these curves have to be modified to compensate for the eccentricity with respect to the base of the steel tube. Based on the same assumptions as explained in Chapter 6.3.2 and shown in Fig. 6.16, the following equations can be derived for the modification of both $M-\varphi$ curves describing the lower and upper rotational springs:

$$M_\mathrm{mod} = \frac{e_\mathrm{I}}{l_\mathrm{T}} \cdot M \tag{6.102}$$

$$\varphi_\mathrm{mod} = \frac{l_\mathrm{T}}{e_\mathrm{I}} \varphi + \frac{M_\mathrm{mod}}{6 e_\mathrm{I}^2 E I_\mathrm{T}} (l_\mathrm{T}^3 - e_\mathrm{I}^3) + \frac{2 M_\mathrm{mod}}{e_\mathrm{I}^2 G A_\mathrm{T}} (l_\mathrm{T} - e_\mathrm{I}) \tag{6.103}$$

Failures

All equations derived in Chapter 6.3.2 regarding failures in the timber and concrete sections are valid also for a calculation with nonlinear rotational springs. The connection shear capacity T_y cannot be exceeded in the results of this model as the maximum connection moments $M_{\mathrm{y,inf,mod}}$ and $M_{\mathrm{y,sup,mod}}$ are provided in the nonlinear $M-\varphi$ curves as an input value. Therefore, this failure does not have to be checked in the post-processing.

6.3.4 Cracked concrete and linear connection behaviour

Concrete cracking due to positive bending moments is usually not accounted for in strut-and-tie models predicting the structural behaviour of typical TCC slabs with a small h_1/h_2 ratio. As the uncracked bending stiffness of the concrete section is relatively low in such a case, the strut-and-tie model usually predicts a small ratio M_1/N_1, which is in agreement with the assumption of an uncracked concrete section.

In the investigated TCC structure with a large h_1/h_2 ratio, however, the situation is different. Because of the relatively high bending stiffness of the uncracked concrete section, the strut-and-tie model predicts a large ratio M_1/N_1, which would lead to significant concrete cracking and in some cases even a bending failure. However, concrete cracking leads to a substantial decrease of the bending stiffness and, as a consequence, to a redistribution of the internal forces. In the elasto-plastic γ-method (Chapter 6.2), this redistribution is automatically accounted for in states II, III and IV. In order to improve the comparability of the calculation results, an attempt was made to consider concrete cracking also in the strut-and-tie model, with an iterative procedure described in this chapter.

The basic idea of this procedure is to reduce the concrete height to the resulting compression zone height at mid-span and adjust the position and stiffness of the concrete chord in the model accordingly, as shown in Fig. 6.19. To simplify this iterative process, a dimensionless auxiliary factor η is defined with a value between 0 and 1:

$$h_{1,\mathrm{II}} = \eta \cdot h_1 \tag{6.104}$$

$$EA_{1,\mathrm{II}} = \eta \cdot EA_1 \tag{6.105}$$

$$EI_{1,\mathrm{II}} = \eta^3 \cdot EI_1 \tag{6.106}$$

$$e_{\mathrm{II}} = e_{\mathrm{I}} + \frac{1-\eta}{2} \cdot h_1 \tag{6.107}$$

As the bending stiffness EI is reduced more than the axial stiffness EA, the M_1/N_1 ratio results in a more realistic range where the reinforcement is not needed for equilibrium in the concrete cross-section. Therefore, Eq. 6.94 can be used to derive the condition for the iteration:

$$\eta_{i+1} = \frac{3}{2}\eta_i + \frac{3M_{1,i}}{h_1 N_{1,i}} \tag{6.108}$$

As with the distance between the timber and concrete chords, also the length of the connector beams is changed, the rotational spring stiffnesses have to be updated as well, using Eq. 6.89 with e_{II} instead of e_{I}. In the calculations done within the scope of this project, η typically converged after two to three iterations.

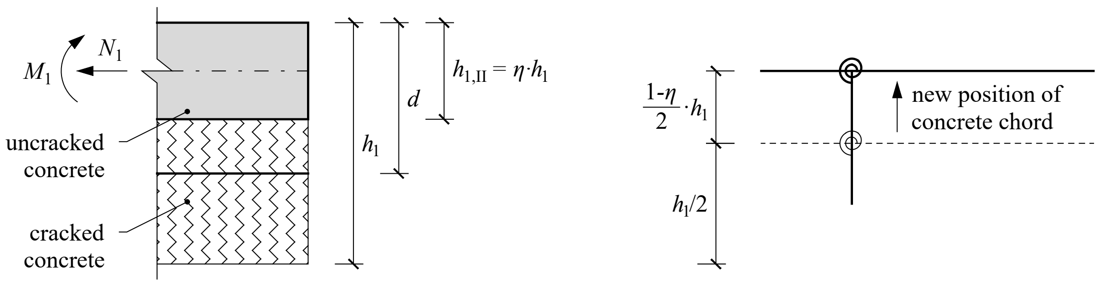

Fig. 6.19: Reduction of the concrete height and new position of the concrete chord.

The failure criteria for the concrete section that were derived in Chapter 6.3.2 are still valid if h_1 is replaced with $h_{1,\mathrm{II}}$ in the respective equations. Either of the two calculation methods without reinforcement (Eq. 6.94 – 6.96) or with reinforcement (Eq. 6.96 – 6.101) may be used. By replacing h_1 with $h_{1,\mathrm{II}}$, the new position of N_1 (Fig. 6.19) is automatically taken into account. Failures in the connection and in the timber section can be assessed with Eq. 6.90 and 6.91.

6.3.5 Cracked concrete and nonlinear connection behaviour

For cases where both nonlinear connection behaviour and concrete cracking are to be considered, the strut-and-tie model reaches its limits of application. In such a case, the resulting M_1/N_1 ratio is dependent on the current connection stiffness and the reduction factor η. Therefore, to account for both influences, the iterative process described in Chapter 6.3.4 would have to be carried out individually for a series of load levels until failure is reached. Doing so would take a considerable effort and lead to results where the concrete chord changes its position with increasing load. Therefore, switching to a more complex FE model (e. g. modelling the concrete section with shell elements instead of beam elements), which is able to solve both nonlinearities, may be the better option.

An approximate result can be obtained if η is assumed to remain constant. In this case, the model does not have to be changed depending on the load level. Using the value of η obtained with linear connection stiffness as described in Chapter 6.3.4 is the most pragmatic approach in this analysis. The $M-\varphi$ curves describing the connection behaviour have to be modified using Eq. 6.102 and 6.103, with e_{II} instead of e_{I}. The failure criteria for the timber and concrete sections remain unchanged with respect to Chapter 6.3.4.

6.4 Comparison of model calculations with test results

6.4.1 Introduction

In this chapter, the measurements from the uniaxial bending tests (Chapter 4) are compared to the predictions obtained from the presented calculation models. Both elasto-plastic γ-method (Chapter 6.2) and strut-and-tie models (Chapter 6.3) were applied for each of the eleven specimens. The measured material properties of both timber and concrete used in the production of the specimens are summarised in Tab. 4.3 and 4.4. The timber MOE and tensile strength were tested on samples from the same LVL board used for the production of the respective bending specimen. These individual results (given in [44]) were used in the calculation models for each specimen. The upper LVL beam was not considered in any of the calculations.

The loading conditions of the experimental setup (10-point bending) was taken into account in the calculation models. In the strut-and-tie model, this was achieved by placing point forces in the respective positions. For the elasto-plastic γ-method, the respective relations between the cylinder forces and the bending moments in the beam had to be derived, as illustrated in Fig. 6.20. The slip displacements were numerically integrated based on these relations, in analogy to Fig. 6.13. In the post-processing of the calculation, an equivalent distributed load q was calculated in analogy to the test data evaluation, using Eq. 4.1.

When comparing nonlinear load-deformation curves from experiments and calculation models, the specimen self-weight and the corresponding deformations have to be considered. This can be done either by deducting the self-weight and the corresponding deformation from the model calculation, or by adding them to the experimental data. The second option was chosen in all subsequent comparison plots because this allows to show the more relevant load q^* including

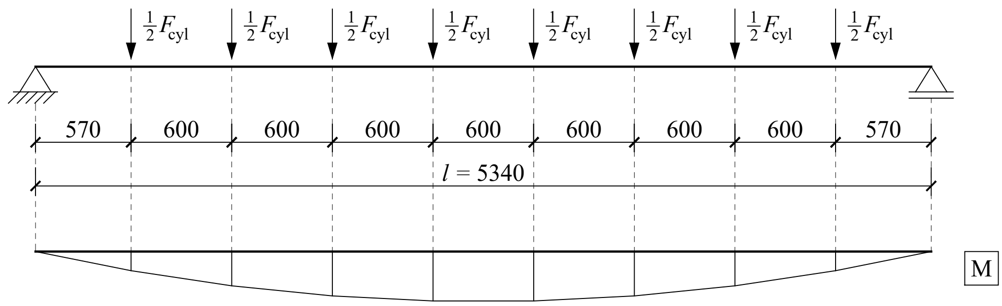

Fig. 6.20: Bending moments acting on the specimen in the test setup of the uniaxial bending tests.

self-weight on the y-axis. The measured load-deformation curve was therefore shifted vertically by applying Eq. 4.2, and horizontally by adding $w_{\mathrm{m}}(q^* - q)$ or $\Delta u_{\mathrm{m}}(q^* - q)$. The latter (deformations due to the specimen self-weight) could not be measured in the experiments. Therefore, they were approximated using the uncracked strut-and-tie model with nonlinear connection behaviour, which delivers accurate deformation predictions (Chapter 6.4.2).

In the subsequent four chapters, the performance of the models is assessed with respect to the prediction of deformations (Chapter 6.4.2), load-bearing capacity (Chapter 6.4.3) and dynamic behaviour (Chapter 6.4.4). The structural behaviour in transversal direction is discussed separately in Chapter 6.4.5.

6.4.2 Deformations

The accuracy of the deformation predictions obtained with the described calculation models is assessed with regard to the mid-span deflection w_{m} and the slip displacement at the supports $\Delta u_{0,\mathrm{L}}$ and $\Delta u_{0,\mathrm{R}}$. For better clarity in the plots, no failure criteria are applied to the model results yet. Fig. 6.21 shows the respective comparison plots for the example of specimens 1.1 and 4. The plots show only the data range that is relevant for the deformation prediction, approximately up to the end of the nonlinear phase, where the mid-span deflection starts increasing substantially.

Out of the five calculation models, the nonlinear strut-and-tie model with uncracked concrete delivers by far the best deformation prediction. Both in the linear and in the nonlinear phase, the predicted w_{m} and Δu_0 are in excellent agreement with the test results.

A comparison of these calculation results with the nonlinear strut-and-tie model with cracked concrete shows that the latter consistently overestimates the deformations. The influence of concrete cracking on the bending stiffness is exaggerated in this model. This conclusion is confirmed by the results of the elasto-plastic γ-method, where concrete cracking is accounted for in a closed-form calculation. No significant change of stiffness occurs between states I and II, which can be explained with the presence of an interlayer between the timber and concrete sections. The visible kink in the load-deformation curve calculated with the elasto-plastic γ-method denotes the point where the shear capacity of all connectors is reached (end of state II).

The elasto-plastic γ-method and the linear strut-and-tie model with uncracked concrete deliver similar predictions of the elastic bending stiffness. This means that for these cases, the choice of s_{ef} in the γ-method according to Eq. 2.1 and Fig. 2.6 was appropriate. While both models deliver good predictions for loads up to around $10\,\text{kN/m}^2$, the deformations are substantially underestimated for higher loads, where the nonlinearity of the connection behaviour starts to play a significant role.

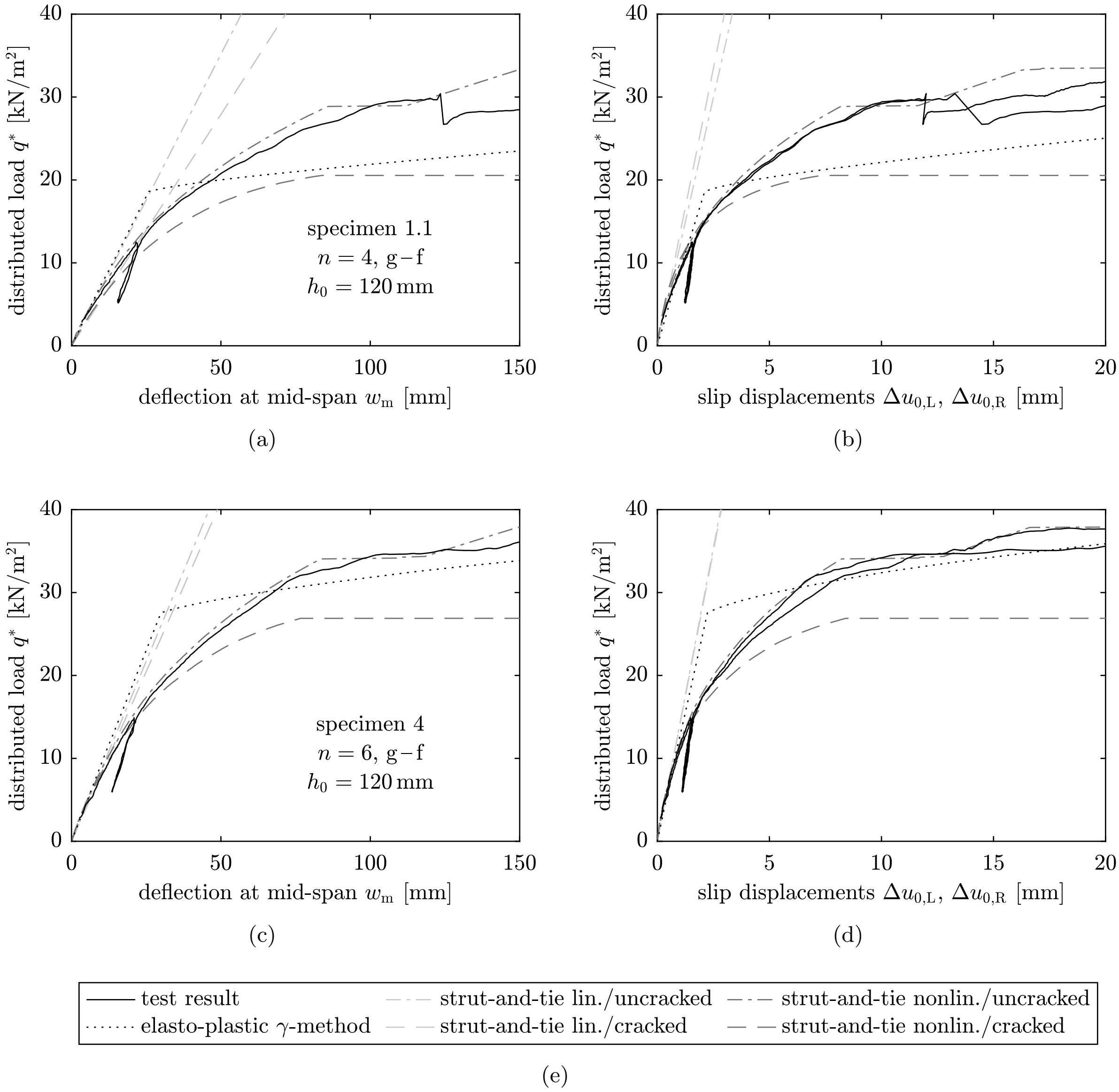

Fig. 6.21: Comparison of test results and calculation models: mid-span deflection w_m and slip displacements at the supports $\Delta u_{0,\text{L}}$ and $\Delta u_{0,\text{R}}$ in the uniaxial bending specimens (a) & (b) 1.1 and (c) & (d) 4; (e) plot legend.

Looking at Fig. 6.21a, the linear strut-and-tie model with cracked concrete seems to deliver a better fit in terms of w_m than the uncracked model. However, the reason for the underestimation of deformations at higher loads in the linear models is not concrete cracking, but the nonlinear connection behaviour. Fig. 6.21b confirms that the linear strut-and-tie model with cracked concrete imposes a stiffness reduction in the wrong place, as it results in lower slip displacements compared to the original model with uncracked concrete.

Tab. 6.2 shows a comparison of the mid-span deflection w_m at $q^* = 10\,\mathrm{kN/m^2}$ from test results and model calculations for all specimens representing the longitudinal load-bearing direction. Both linear calculation methods slightly underestimate w_m. The relative deviations of the nonlinear strut-and-tie model from the test measurements are smaller. This shows that even at this low load level, the nonlinearity of the connection behaviour already has an influence.

Tab. 6.2: Mid-span deflection w_m at load level $q^* = 10\,\mathrm{kN/m^2}$, test results and model calculations, absolute values in [mm] and relative deviation from test result in brackets.

Specimen	Test result	Elasto-plastic γ-method	Strut-and-tie model lin./uncracked	nonlin./uncracked
1.1	16.8	13.8 (−18%)	14.2 (−15%)	15.7 (−6.7%)
1.2	17.8	13.3 (−25%)	13.6 (−23%)	15.2 (−14%)
2	13.2	13.3 (+0.3%)	13.6 (+2.8%)	15.2 (+15%)
3	18.4	15.8 (−14%)	15.7 (−15%)	18.5 (+0.5%)
4	13.2	10.7 (−19%)	11.5 (−12%)	11.9 (−9.6%)
5	18.1	14.1 (−22%)	14.4 (−21%)	15.9 (−12%)
6	14.7	12.1 (−17%)	12.5 (−15%)	14.1 (−3.9%)
7	23.1	22.3 (−3.6%)	19.2 (−17%)	24.7 (+6.8%)
8	33.8	31.6 (−6.7%)	24.4 (−28%)	31.9 (−5.7%)
Average rel. deviation:		−14%	−16%	−3.4%

In conclusion, both the elasto-plastic γ-method and the linear strut-and-tie model with uncracked concrete are suitable for deformation predictions under service loads, which are typically in the range where the connection behaviour remains approximately linear. While the former allows for a fast, parametric calculation, the latter offers more flexibility in the analysis of uneven loading conditions, multi-span beams or in the optimisation of the connector layout. Both linear calculation models slightly underestimate the deflections. Compared to other uncertainties such as the variability of material properties and production tolerances, these deviations are acceptable. However, in cases where high connection shear forces are to be expected, an accurate deformation prediction is possible only with a nonlinear strut-and-tie model. Both linear and nonlinear strut-and-tie models with cracked concrete were found not to be preferable for deformation predictions.

6.4.3 Load-bearing capacity

In the comparison of the different calculation models with the test results, the consideration of (a) concrete cracking and (b) connection deformation capacity and connector layout were found to have a distinct influence on the accuracy of the failure load prediction. Therefore, in the subsequent two subchapters, these influences are explained and discussed separately.

Concrete cracking

In this section, the influence of concrete cracking on the predicted load-bearing capacity in the different calculation models is assessed. As concrete cracking is accounted for in the elasto-plastic γ-method in a closed-form calculation, this model is used as a reference in the comparison. Fig. 6.22a shows the result of this calculation, including the transition points between states I, II, III and IV as described in Chapter 6.2, assuming perfect plasticity in the connectors. In the experiment, the displacement capacity of the hydraulic cylinders was reached at $w_{\mathrm{m}} \approx 300\,\mathrm{mm}$. Therefore, the predicted ultimate failure due to combined bending and tension in timber did not occur in the experiment. However, the predicted failure load q_{u}^{*} is in good agreement with the test result. The load-deflection curves calculated with the strut-and-tie models are plotted in Fig. 6.22a for specimen 1.1 without applying any failure criteria yet. Fig. 6.22b shows the same data as Fig. 6.22a, with all failure criteria applied. Fig. 6.22c shows the equivalent comparison for the example of specimen 4.

For all specimens, both linear and nonlinear strut-and-tie models with uncracked concrete predict a concrete compressive failure that did not occur in the experiments. According to the model calculation, this failure should have happened at a load level of around a third of the maximum load measured in the experiments and before any connectors reached their shear capacity. In order to explain this result, the proportions of internal moments predicted by the different calculation models are analysed, based on the data shown in Fig. 6.22a. In a composite slab with flexible connection, external bending moments are carried by a pair of normal forces $N \cdot e$ and bending moments in the partial sections M_1 and M_2, as illustrated in Fig. 6.23b.

Fig. 6.23a shows the proportions of these three parts in the elasto-plastic γ-method as a function of the external bending moment. After the concrete section cracks at the end of state I, the proportion of M_1 is significantly reduced. As the concrete compression zone height decreases throughout states III and IV, the proportion of M_1 tends towards zero. Fig. 6.23a also shows that after the connectors reach their shear capacity at the end of state II, the proportion of $N \cdot e$ decreases. This is because the absolute value of $N \cdot e$ remains constant during states III and IV while the external bending moment M further increases. Almost the entire additional external bending moment between connection yielding and ultimate failure $M_{\mathrm{u}} - M_{\mathrm{y}}$ is carried by M_2.

The equivalent plots for the strut-and-tie models are shown in Fig. 6.23c – 6.23f. For better comparability, the same range of M is plotted on the x-axis as in Fig. 6.23a, along with the four states from the elasto-plastic γ-method, even though the strut-and-tie models do not directly account for these different states.

Fig. 6.23c shows that the linear strut-and-tie model with uncracked concrete predicts similar internal moments as the elasto-plastic γ-method in state I. However, the proportions remain constant, which means that M_1 increases linearly with the external bending moment also for $M > M_{\mathrm{cr}}$. This leads to a substantial overestimation of M_1 during state II and thus, the prediction of a concrete compressive failure (× in Fig. 6.23c and 6.23e). The proportions of internal moments predicted by this model are not realistic because the concrete section automatically reduces its bending stiffness by cracking and thus evades such large bending moments.

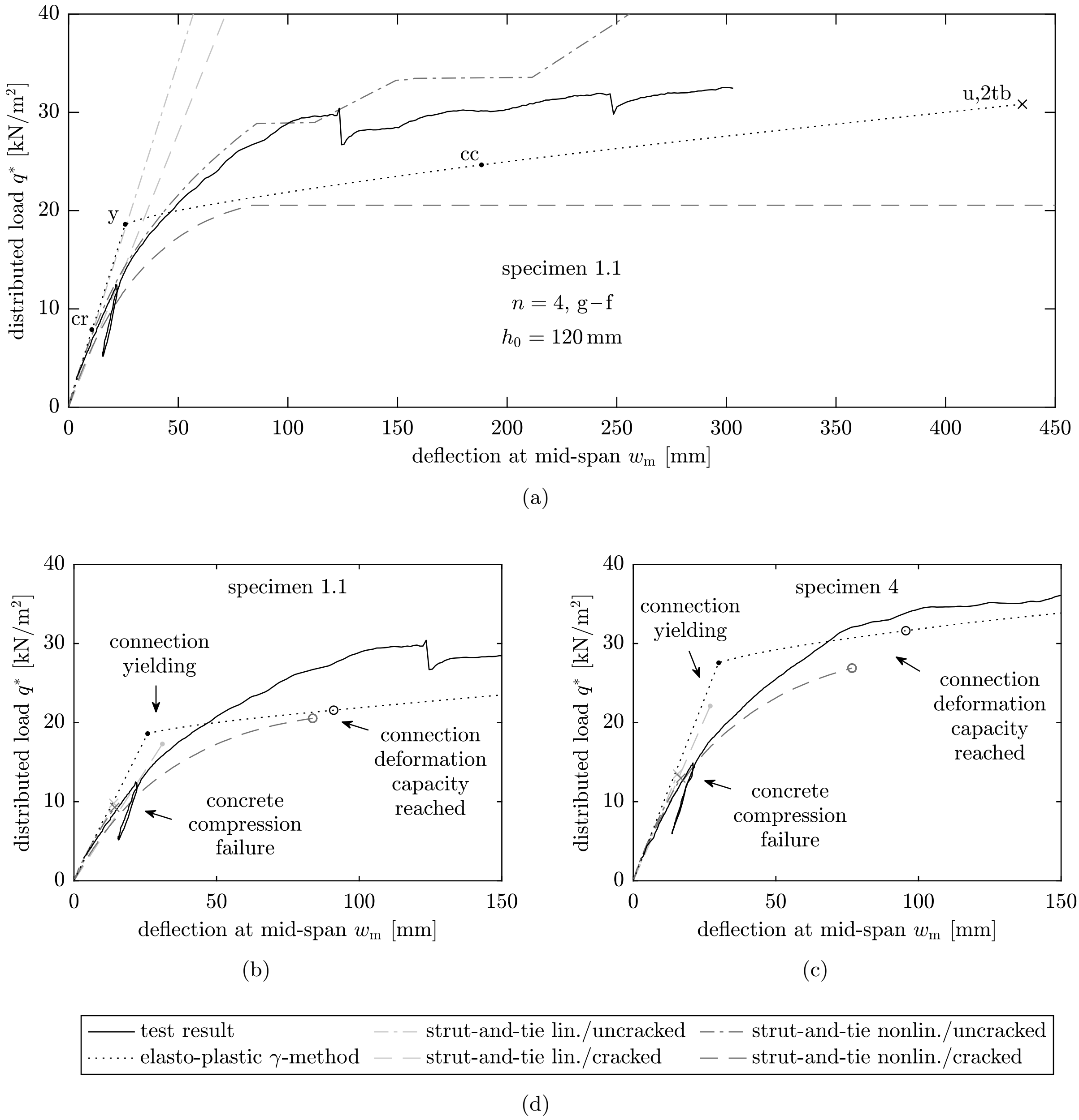

Fig. 6.22: (a) Result of the elasto-plastic γ-method assuming perfect plasticity in the connectors, with transition points between states and ultimate tensile-bending failure in timber, strut-and-tie models without failure points and test result of specimen 1.1, (b) & (c) governing failure criteria in the calculation models with limited connection deformation capacity, specimens 1.1 and 4, (d) plot legend.

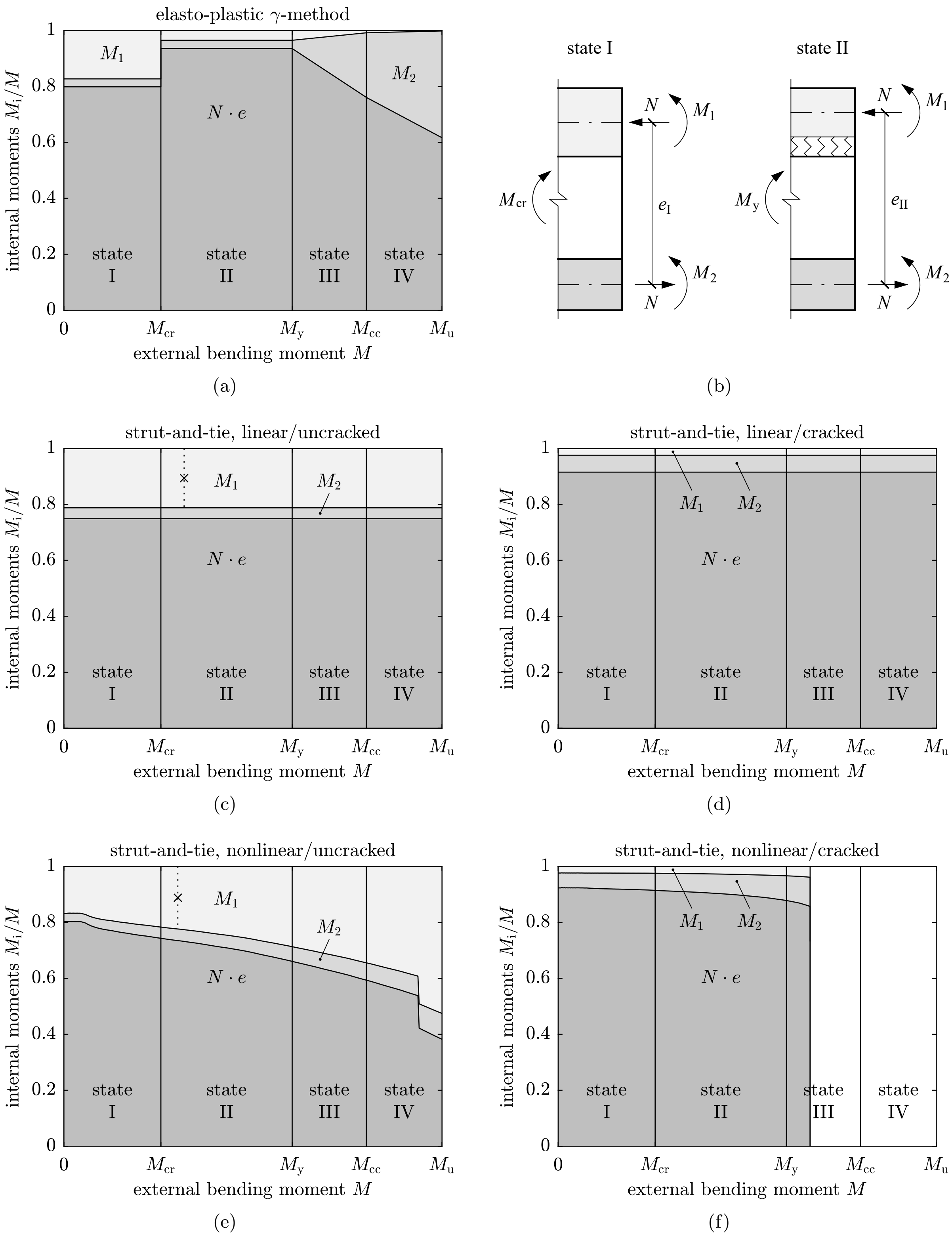

Fig. 6.23: Proportions of internal moments in the different calculation models, based on the data shown in Fig. 6.22a for specimen 1.1.

In the linear strut-and-tie model with cracked concrete (Fig. 6.23d), this issue is mitigated by reducing the bending stiffness of the concrete section EI_1 manually. This leads to more realistic proportions of the internal moments for $M > M_{\mathrm{cr}}$ similar as in the elasto-plastic γ-method in state II. Thus, no premature concrete compressive failure is predicted by this model.

In the nonlinear strut-and-tie models with uncracked (Fig. 6.23e) and cracked concrete (Fig. 6.23f), the proportions of internal moments at low load levels are similar as in the respective linear models. However, the proportions are not constant anymore. With increasing external bending moment, the connection stiffness and thus the proportion of $N \cdot e$ decreases, similar as in states III and IV of the elasto-plastic γ-method. In Fig. 6.23f, M_{u} is not reached because the model assumes a limited connection deformation capacity. This topic is discussed in the following subchapter.

In conclusion, an accurate prediction of the load-bearing capacity of the investigated TCC slab is possible only with a model that accounts for concrete cracking. Strut-and-tie models with uncracked concrete do not perform well because they substantially overestimate M_1, leading to a premature concrete compressive failure.

Connection deformation capacity and connector layout

The main difference between the remaining three models (elasto-plastic γ-method, linear and nonlinear strut-and-tie models with cracked concrete) is the extent to which they allow for plastic force redistributions. In a TCC structure with ductile connection, the slip displacement due to plastic connection deformation can be divided into two parts:

$$\Delta u_{\mathrm{pl}} = \Delta u_{\mathrm{pl,a}} + \Delta u_{\mathrm{pl,b}} \tag{6.109}$$

where $\Delta u_{\mathrm{pl,a}}$ and $\Delta u_{\mathrm{pl,b}}$ denote the slip displacement due to plastic connection deformation occurring (a) before and (b) after all connectors have reached their shear capacity T_{y}. The first part, $\Delta u_{\mathrm{pl,a}}$ mainly depends on the connector layout and the loading conditions. Arranging the connectors in a way that results in equal elastic shear forces in all connectors for a given loading condition leads to $\Delta u_{\mathrm{pl,a}} = 0$, which is one of the assumptions of the elasto-plastic γ-method. However, in any other connector layout, a force redistribution is necessary before all connectors can reach their shear capacity and therefore $\Delta u_{\mathrm{pl,a}} > 0$. The magnitude of $\Delta u_{\mathrm{pl,a}}$ can only be assessed with a calculation model where each connector is considered individually (e. g. strut-and-tie model).

The second part, $\Delta u_{\mathrm{pl,b}}$ occurs after all connectors have yielded and is independent of the connector layout. This part allows for a further increase of the curvature in the composite cross-section. As a consequence, the bending moment in the timber section M_2 increases and large deformations occur. In the elasto-plastic γ-method, only this part is considered.

The structural behaviour observed in the uniaxial bending tests was remarkably ductile. As discussed in Chapter 4.4.1, the experimental results indicate that, after the shear capacity of the connectors was reached, the shear force in the connectors did not significantly decrease throughout the experiment. The connection deformation capacity was not reached in the tests, which means that the connection behaviour could be described with perfect plasticity.

However, these results are not in agreement with the results of the connection shear tests, where a limited deformation capacity was observed. Possible reasons for this discrepancy are discussed in Chapter 4.4.1. Among other factors, the upper LVL beam included in the bending specimens may have had a positive effect on the connection deformation capacity. Therefore, a prediction of the uniaxial load-bearing capacity assuming perfect plasticity in the connectors may not be on the safe side for a version without upper LVL beam, which was chosen as the main concept version by the end of this research project. In conclusion, the connection deformation capacity should be regarded as limited until further experimental results are available on specimens without an upper LVL beam.

Because of the perfectly plastic connection behaviour that was observed in the experiments, the influence of a limited connection deformation capacity and different connector layouts cannot be discussed using only the test results. In the case of perfect plasticity ($\Delta u_{\mathrm{max}} \rightarrow \infty$), the load-bearing capacity is independent of the connector layout. Therefore, the comparison of the test results and model calculations with regard to this influence is performed in two steps:

- In a first step, the test results are compared to the predictions obtained from the elasto-plastic γ-method, assuming perfect plasticity in the connectors ($\Delta u_{\mathrm{max}} \rightarrow \infty$).
- In a second step, the influence of limited connection deformation capacity and different connector layouts is assessed based on a comparison between the remaining three calculation models (elasto-plastic γ-method, linear and nonlinear strut-and-tie models with cracked concrete), assuming a limited connection deformation capacity as described in Chapter 6.2.2.

Tab. 6.3: Comparison of the load-bearing capacity q_{u}^{*} measured in the uniaxial bending tests and predicted with the elasto-plastic γ-method, absolute values in [kN/m^2] and relative deviation in brackets.

Specimen	Connection concept *	Test result	Elasto-plastic γ-method
1.1	g–f	32.5	30.8 (–5.2%)
1.2	g–f	29.6	29.8 (+0.9%)
2	g–g	34.3	29.8 (–13%)
3	g–f	28.4	27.4 (–3.6%)
4	g–f	40.4	40.5 (+0.4%)
5	g–f	32.3	32.8 (+1.4%)
6	g–f	33.7	32.8 (–2.8%)
7	f–f	30.3	29.9 (–1.2%)
8	f–f	26.0	23.3 (–10%)
Average rel. deviation, all specimens:			–3.7%
Specimens with connection type 'g–f':			–1.5%

* g = grouted connection, f = form-fitting connection without grouting

Tab. 6.3 compares the load-bearing capacities measured in the uniaxial bending tests with the predictions based on the elasto-plastic γ-method, assuming perfect plasticity in the connectors. Fig 6.24 shows the corresponding $q^* - w_\mathrm{m}$ and $q^* - \Delta u$ curves for specimens 1.1 and 4. The comparison shows that the predicted load-bearing capacities are in excellent agreement with the test results for specimens with the standard connection concept 'g−f' (grouted type 1 connection and form-fitting type 2 connection, Fig. 3.1), with relative deviations between −5.2% and +1.4%. For the specimens with other connection concepts, which are less relevant for an application in practice, the elasto-plastic γ-method delivers predictions on the safe side (relative deviations between −13% and −1%).

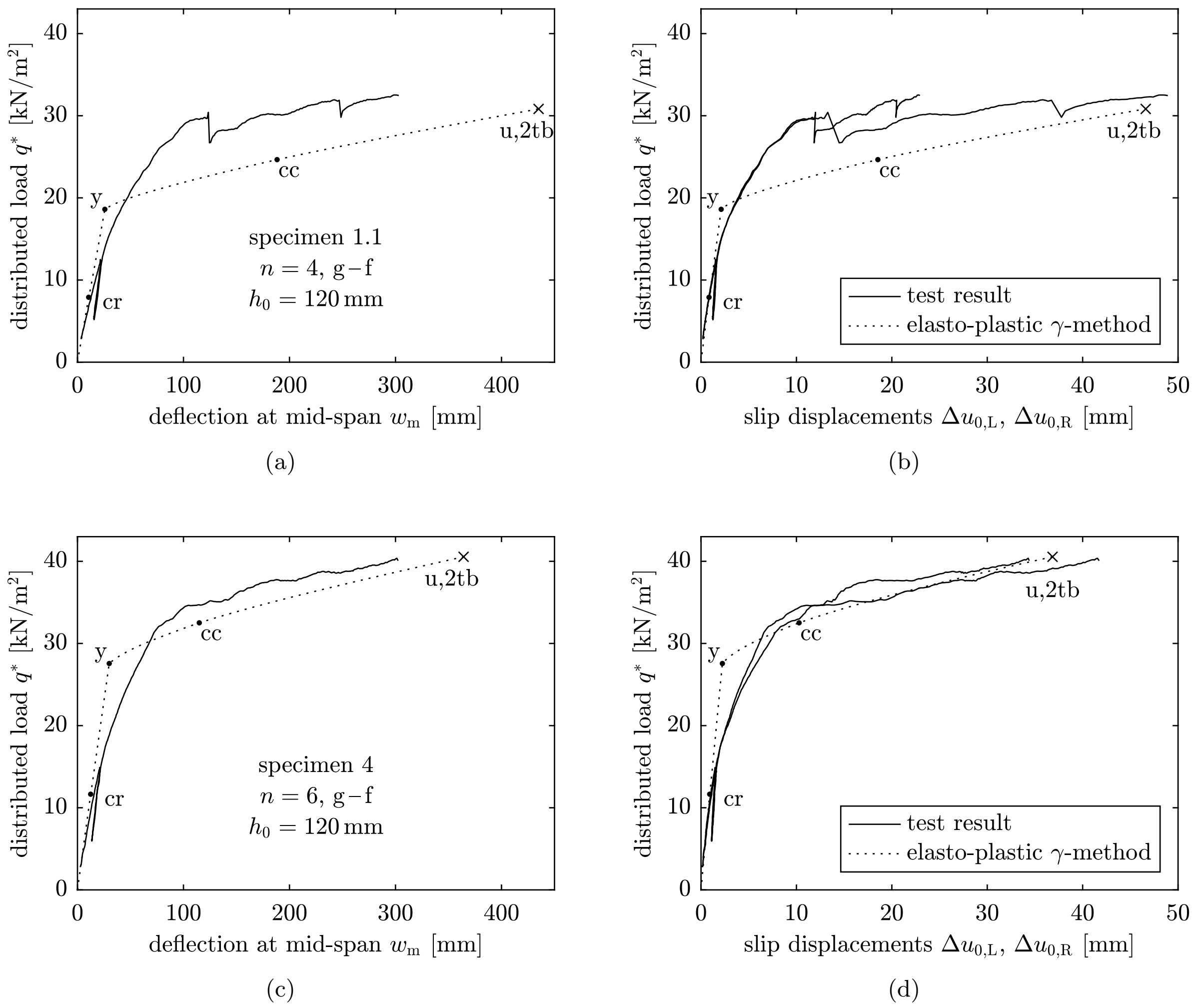

Fig. 6.24: Comparison of test measurements with the results of the elasto-plastic γ-method assuming perfect plasticity in the connectors, with transition points between states and ultimate tensile-bending failure in timber, for the examples of (a) & (b) specimen 1.1 and (c) & (d) specimen 4.

The elasto-plastic γ-method predicts an ultimate tensile-bending failure in timber for all specimens. In the experiments, this failure could not be observed because of the limited displacement capacity of the hydraulic cylinders. Therefore, the comparison should be interpreted with caution. The actual load-bearing capacity may have been higher than the maximum load measured in the experiments. However, given the flat slope of the load-deflection curve at the end of the experiments, a large difference is not to be expected. In any case, it can be concluded that the model did not significantly overestimate the load-bearing capacity of any specimen.

The influence of a limited connection deformation capacity and different connector layouts is assessed based on a comparison of specimens 1.1, 3 and 4. In these specimens, the number of connectors per shear area was varied ($m = 3, 4, 6$). The connector layout was chosen based on a simplified method assuming a uniformly distributed load (linear increase of the connector spacing towards mid-span) and is shown in Fig. 4.2. A more detailed analysis was carried out after the tests, with a strut-and-tie model considering the exact position of the point forces in the test setup as depicted in Fig 6.20. Tab. 6.4 shows the resulting distribution of connection shear forces based on this analysis. While the distribution is relatively even in specimen 3 ($m = 3$), the difference between the elastic connection shear forces is significant in the other specimens.

Tab. 6.4: Distribution of elastic connection shear forces in different connector layouts based on the linear strut-and-tie model with uncracked concrete.

Specimen	$T_1/T_{\max}$	$T_2/T_{\max}$	$T_3/T_{\max}$	$T_4/T_{\max}$	$T_5/T_{\max}$	$T_6/T_{\max}$
1.1	98%	100%	94%	66%	–	–
3	96%	100%	86%	–	–	–
4	100%	99%	94%	82%	62%	34%

Fig. 6.25 shows a comparison of the remaining three calculation models, which differ in the extent to which they allow for plastic force redistributions. The linear strut-and-tie model with cracked concrete predicts failure when the first connector reaches its shear capacity, as no force redistributions are possible. In the other two models, force redistributions are possible and failure occurs when the connection deformation capacity $\Delta u_{\max}$ is reached. As explained in the beginning of this subchapter, a force redistribution and thus plastic connection deformation is necessary before all connectors can reach their shear capacity, if the elastic shear forces are not equal in all connectors. The elasto-plastic γ-method does not account for these deformations as an even connection force distribution is assumed and thus $\Delta u_{\mathrm{pl,a}} = 0$. In contrast, the nonlinear strut-and-tie model with cracked concrete accounts for the entire deformation, including the part that occurs before all connectors reach their shear capacity.

In specimen 3 (Fig 6.25b), the failure points predicted by the nonlinear strut-and-tie model with cracked concrete and the elasto-plastic γ-method coincide. In this case, the elastic shear forces are in the same range (Tab. 6.4) in all connectors and thus, the assumption $u_{\mathrm{pl,a}} = 0$ in the elasto-plastic γ-method is correct. The load-bearing capacity predicted by the linear strut-and-tie model with cracked concrete is very similar to q_{y} (yielding of all connectors) predicted by the elasto-plastic γ-method, which is a direct consequence of the even connection force distribution.

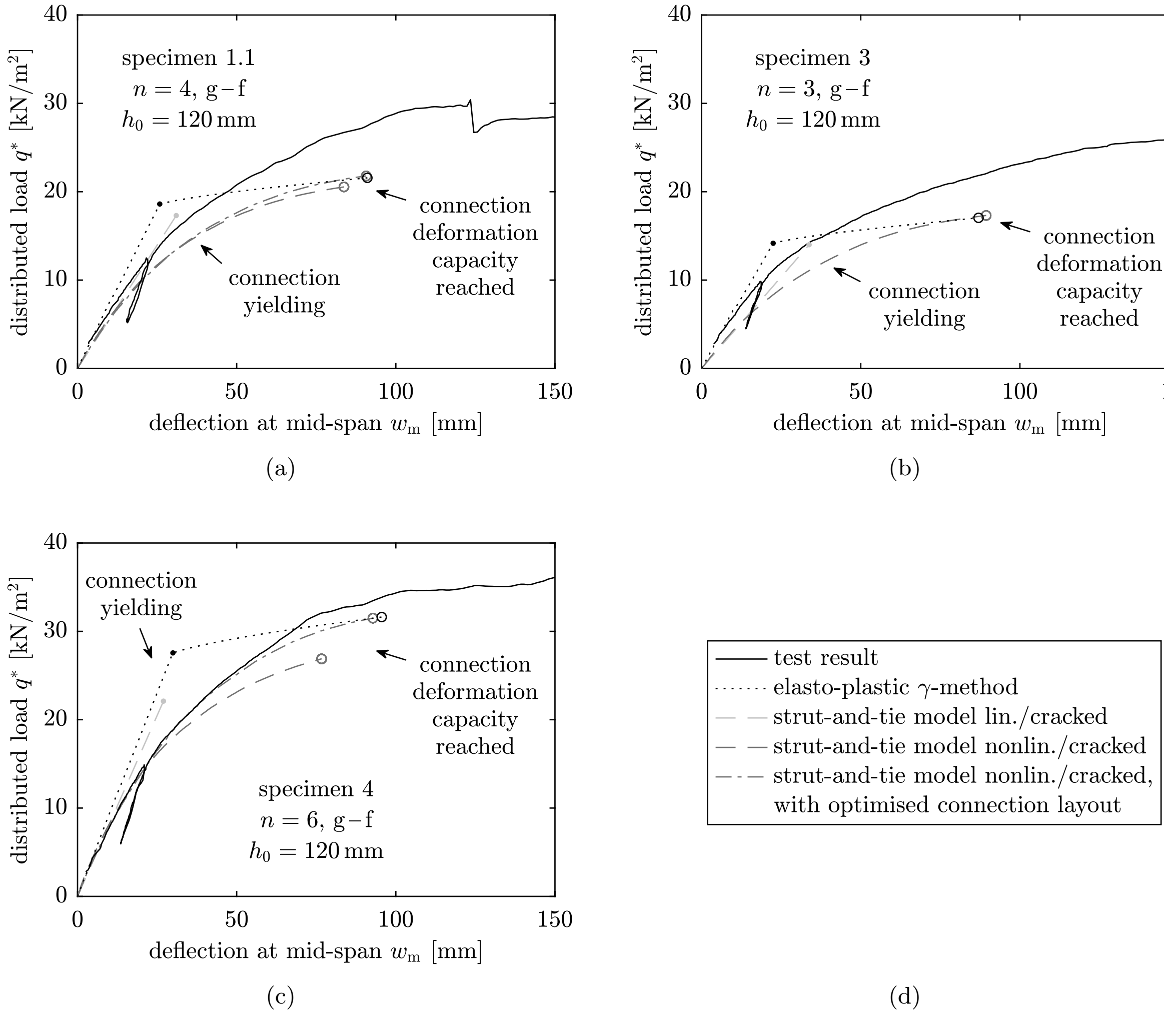

Fig. 6.25: Comparison of the load-bearing behaviour predicted with the elasto-plastic γ-method and with linear and nonlinear strut-and-tie models with cracked concrete, for (a) specimen 1.1, (b) specimen 3 and (c) specimen 4; (d) legend for all plots.

In specimen 4 (Fig 6.25c), the situation is different. The nonlinear strut-and-tie model with cracked concrete reaches only 85% of the load-bearing capacity predicted by the elasto-plastic γ-method. In addition, failure occurs in this model before q_y is reached. This result shows that the assumed connection deformation capacity Δu_max was not sufficient to achieve a full redistribution of the connection forces in this case. To confirm that the observed difference is due to the uneven connection force distribution, a strut-and-tie calculation with an optimised connector layout was performed. Fig 6.25c shows that after this optimisation, the failure point approximately coincides with the prediction of the elasto-plastic γ-method.

Specimen 1.1 presents an intermediate situation between specimens 3 and 4 regarding the connection force distribution (Tab. 6.4). The respective calculation results confirm the findings from specimens 3 and 4. A difference between the predictions of the nonlinear strut-and-tie model with cracked concrete and the elasto-plastic γ-method is visible in Fig. 6.25a but it is not as large as in specimen 4. In analogy to specimen 4, the failure points coincide if the connector layout is optimised.

The comparison of specimens 1.1, 3 and 4 shows that the connector layout has a significant influence on the load-bearing capacity of composite slabs with a limited connection deformation capacity. Arranging the connectors in a way that results in equal elastic shear forces in all connectors allows to activate the maximum possible bending stiffness of the composite slab. As deformation criteria (SLS) often govern the design of TCC slabs, an optimised connector layout should therefore be targeted in any case. The results discussed above show that, if the connector layout is designed accordingly, the elasto-plastic γ-method is applicable to determine the load-bearing capacity of the TCC slab.

However, in cases where such an optimised connector layout is not possible, the elasto-plastic γ-method should not be used. If the chosen connector layout leads to a significantly uneven force distribution among the connectors, and if the deformation capacity is small, this may lead to a premature brittle connection failure before the end of state II. In such a case, a lower limit value of the load-bearing capacity can be determined using a linear strut-and-tie model with cracked concrete. Nonlinear strut-and-tie models with cracked concrete can account for force redistributions even in such cases. However, these models are mainly suitable for use in research as they involve considerable effort.

Further considerations

In a nonlinear strut-and-tie model, the connection behaviour is represented by $M - \varphi$ curves. As both connection stiffness K and shear capacity T_{y} are a function of these curves, K and T_{y} are not independent input parameters. If mean values of all parameters are used, as in this chapter for the comparison with experimental results, this is not a problem. However, if such a model is to be used for design purposes, a characteristic value of the connection shear capacity T_{y} has to be used and partial safety factors have to be applied in agreement with the current design codes. However, reducing T_{y} by modifying the $M - \varphi$ curves would also affect the connection stiffness K and thus the prediction of internal forces in the TCC slab. As a consequence, a nonlinear strut-and-tie model could only be used with a global safety factor, which is not in agreement with the current design codes. In contrast, the connection stiffness K and shear capacity T_{y} are two independent input parameters in the elasto-plastic γ-method. Therefore, using a partial safety factor on T_{y} does not affect the connection stiffness K in this model.

The elasto-plastic γ-method with limited connection deformation capacity is based entirely on analytical calculations, which means that a parametric design using spreadsheets is possible. Therefore, this method is especially valuable during the early stages of the design process, allowing for an efficient derivation of the most important parameters of the TCC slab (cross-section geometry and number of steel tubes). In a later stage of the design process, it is advisable to include analyses based on a strut-and-tie model. This allows to address issues such as defining the final connector layout, or other analyses that exceed the limitations of the elasto-plastic γ-method, for example in the case of concentrated loads or in multi-span situations.

6.4.4 Dynamic behaviour

The free vibration response of the investigated TCC slab to an impulse excitation was measured in all uniaxial bending specimens before the static loading tests. In this chapter, the experimentally determined fundamental frequencies are compared to the respective results of the model calculations. As discussed in Chapter 3.3.5, the reloading stiffness $k_{\mathrm{m},2}$ is relevant for the dynamic behaviour of the investigated TCC slab rather than the first loading stiffness $k_{\mathrm{m},1}$. As the observed behaviour during reloading was approximately linear in all connection shear tests, nonlinear calculation models are not necessary. Concrete cracking is not expected to have an influence on the dynamic behaviour of the TCC slab. Thus, the γ-method (state I) and the linear strut-and-tie model with uncracked concrete were used to predict the fundamental frequency. The dynamic bending stiffness of the composite slab EI_{dyn} according to the γ-method was calculated with Eq. 6.1 – 6.19, using $k_{\mathrm{m},2}$. The fundamental frequency follows:

$$f_1 = \frac{\pi}{2l^2} \cdot \sqrt{\frac{EI_{\mathrm{dyn}}/b}{m_{\mathrm{s}}/(bl)}} = \frac{\pi}{2l^2} \cdot \sqrt{\frac{EI_{\mathrm{dyn}} \cdot l}{m_{\mathrm{s}}}} \tag{6.110}$$

In Eq. 6.110, m_{s} is the specimen mass as measured in the experiments (Tab. 4.5) and l is the span. As a comparison, f_1 was also calculated using the first loading stiffness $k_{\mathrm{m},1}$.

The same linear strut-and-tie models with uncracked concrete as in Chapters 6.4.2 and 6.4.3 were used, replacing $k_{\mathrm{m},1}$ with $k_{\mathrm{m},2}$ accordingly. The specimen mass m_{s} was specified in the models, allowing for a calculation of the fundamental frequency. Most modern FEM software packages offer such a function. Alternatively, a static analysis could be performed to determine EI_{dyn} for a corresponding calculation of f_1 with Eq. 6.110.

Tab. 6.5 shows all test measurements and the respective results of the calculation models. The predictions using the static (first loading) stiffness $k_{\mathrm{m},1}$ consistently underestimate the

Tab. 6.5: Fundamental frequency f_1 of the uniaxial bending specimens, test results and model calculations, absolute values in [Hz] and relative deviation from test result in brackets.

Specimen	Test result	γ-method with $k_{\mathrm{m},1}$	γ-method with $k_{\mathrm{m},2}$	Strut-and-tie model lin./uncracked
1.1	12.0	9.6 (−20%)	10.6 (−12%)	10.5 (−13%)
1.2	11.6	10.0 (−13%)	11.0 (−4.7%)	11.0 (−5.3%)
2	13.0	10.0 (−23%)	11.0 (−15%)	10.9 (−16%)
3	11.6	9.2 (−21%)	10.1 (−13%)	10.2 (−12%)
4	12.8	10.8 (−15%)	11.8 (−7.5%)	11.6 (−9.0%)
5	11.4	9.9 (−13%)	10.8 (−5.5%)	10.8 (−5.0%)
6	12.0	10.1 (−16%)	11.3 (−6.2%)	11.3 (−6.2%)
7	11.2	7.9 (−30%)	9.7 (−13%)	10.0 (−11%)
8	10.0	7.0 (−30%)	8.4 (−16%)	8.8 (−12%)
Average rel. deviation:		−20%	−10%	−10%

fundamental frequency. Using $k_{\mathrm{m},2}$ significantly improves the results, although the predictions are still 10% below the test measurements. Both γ-method and linear strut-and-tie model with uncracked concrete produce very similar results. This means that the choice of s_{ef} in the γ-method according to Eq. 2.1 and Fig. 2.6 was appropriate.

In conclusion, the results show that both the γ-method and the linear strut-and-tie model with uncracked concrete deliver sufficiently accurate estimations of the fundamental frequency, if the reloading connection stiffness $k_{\mathrm{m},2}$ is used. In a practical design process, the former is preferable in most cases as it allows for a fast, analytical calculation. Using the first loading connection stiffness $k_{\mathrm{m},1}$ is not recommended as this may lead to a significant underestimation of the fundamental frequency.

6.4.5 Uniaxial bending in transversal direction

The models described in this chapter are mainly intended for predicting the load-bearing behaviour of the one-way spanning version of the investigated TCC slab. However, the same models can also be used to separately assess the longitudinal and transversal load-bearing directions in a two-way spanning version of the slab. In the uniaxial bending tests, two specimens focused on the transversal load-bearing direction in such a slab. The measurements obtained from these two tests are compared to results from corresponding calculation models in this chapter.

No push-out tests on type 1 connections (steel tube in beech LVL) perpendicular to the grain have been carried out within the scope of this research project. Therefore, the connection stiffness was estimated based on the corresponding stiffness value parallel to the grain as follows:

$$k_{\mathrm{m,inf,90}} = \frac{E_{2,90,\mathrm{mean}}}{E_{2,0,\mathrm{mean}}} \cdot k_{\mathrm{m,inf,0}} \approx 0.32 \cdot k_{\mathrm{m,inf,0}} \tag{6.111}$$

with the MOE values $E_{2,0,\mathrm{mean}}$ and $E_{2,90,\mathrm{mean}}$ as determined in the material tests (Tab. 4.3 and 4.4). The yield moment in the connection perpendicular to the grain was estimated as follows:

$$M_{\mathrm{inf,y,90}} = \frac{f_{2,\mathrm{c},90,\mathrm{mean}}}{f_{2,\mathrm{c},0,\mathrm{mean}}} \cdot M_{\mathrm{inf,y,0}} \approx 0.42 \cdot M_{\mathrm{inf,y,0}} \tag{6.112}$$

As no compression tests were performed on the LVL boards used in the uniaxial bending specimens, the respective strength values from van de Kuilen & Knorz [88] were used. The stiffness and yield moment values obtained from Eq. 6.111 and 6.112 are rough estimations. Push-out tests perpendicular to the grain should be performed in order to provide a more reliable data basis.

An estimation of nonlinear $M-\varphi$ curves in analogy to Eq. 6.111 and 6.112 is not feasible in a consistent way because stiffness and yield moment are not independent parameters in these curves. Therefore, only the elasto-plastic γ-method and a linear strut-and-tie model with uncracked concrete were used in the comparison with the test results.

In the strut-and-tie model, the influence of the side connections (i.e. the two GIR connections located at 1/3 and 2/3 of the span) was considered as shown in Fig. 6.26. Hunger et al. [37] experimentally determined $k_{\mathrm{GIR}} \approx 130\,\mathrm{kN/mm}$ for GIR M12 in beech LVL parallel to the grain.

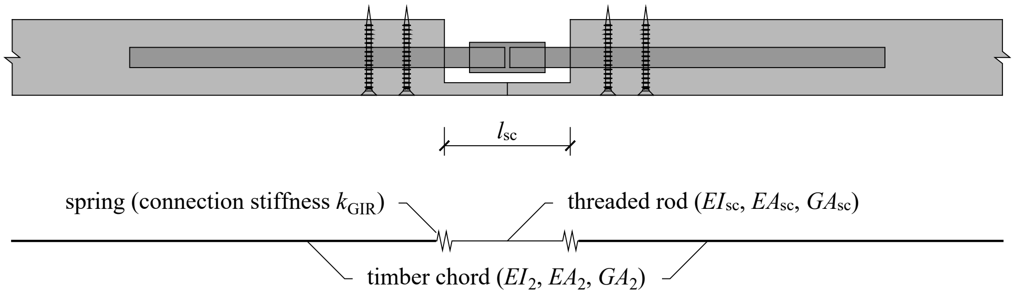

Fig. 6.26: Side connection with glued-in rods in specimens T1 and T2 and consideration of local connection stiffness in the strut-and-tie model.

The GIR in specimens T1 and T2 have a larger diameter (M16) and are oriented perpendicular to the grain. However, as an approximation, this value is used without modification.

In the γ-method, local weaknesses such as the side connections cannot be considered explicitly. Therefore, the loss of stiffness in the timber section due to the side connections is distributed along the entire span l, by reducing the respective MOE as follows:

$$E_{2,\text{red}} = \frac{l/A_2}{(l - n_{sc} l_{sc})/EA_2 + n_{sc} l_{sc}/EA_{sc} + 2n_{sc}/k_{\text{GIR}}} \tag{6.113}$$

In Eq. 6.113, n_{sc} is the number of side connections along the span and l_{sc}, EA_{sc}, k_{GIR} are parameters characterising the side connection as depicted in Fig. 6.26.

Fig. 6.27 compares the test measurements with the results of the described two models. In terms of stiffness, the predictions of both models are in good agreement with the test results. At higher loads, the deflections are underestimated, which is due to the nonlinear connection behaviour. As expected based on the findings of Chapter 6.4.3, the strut-and-tie model substantially underestimates the load-bearing capacity because of a premature concrete compressive

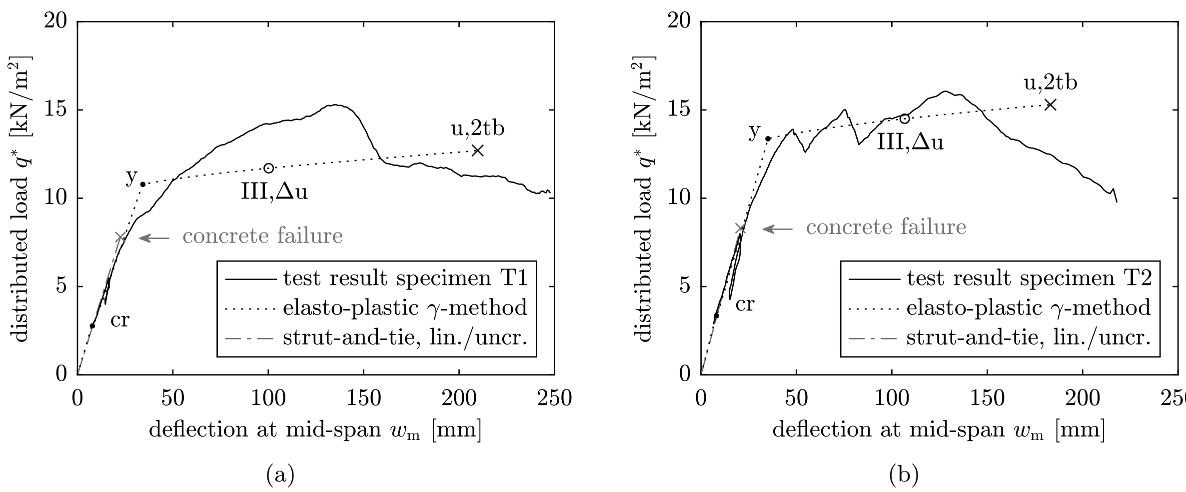

Fig. 6.27: Comparison of test measurements with the results of the elasto-plastic γ-method and the linear strut-and-tie model with uncracked concrete, with consideration of the stiffness reduction due to the side connections.

failure. The elasto-plastic γ-method delivers a good prediction of the load-bearing capacity. Failure is predicted due to exceedance of the connection deformation capacity during state III. If perfect plasticity is assumed in the connectors, failure is predicted due to bending and tension in timber, at an only slightly higher load but significantly larger deflection. Both failure modes are marked in Fig. 6.27 (III,Δu and u,2tb). In the experiments, the maximum measured load was determined by the connection behaviour, not by a cross-sectional failure in timber.

As both stiffness $k_{\mathrm{m,inf,90}}$ and yield moment $M_{\mathrm{inf,y,90}}$ in the connection perpendicular to the grain are subject to uncertainty, these parameters were varied in the elasto-plastic γ-method by $\pm 25\%$ and $\pm 50\%$ to investigate the respective influence on the predicted load-bearing behaviour. The results in Fig. 6.28 show that $M_{\mathrm{inf,y,90}}$ has a significant influence on the predicted load-bearing capacity. Therefore, the respective model results should be interpreted with caution until reliable experimental data regarding this parameter are available. The stiffness $k_{\mathrm{m,inf,90}}$

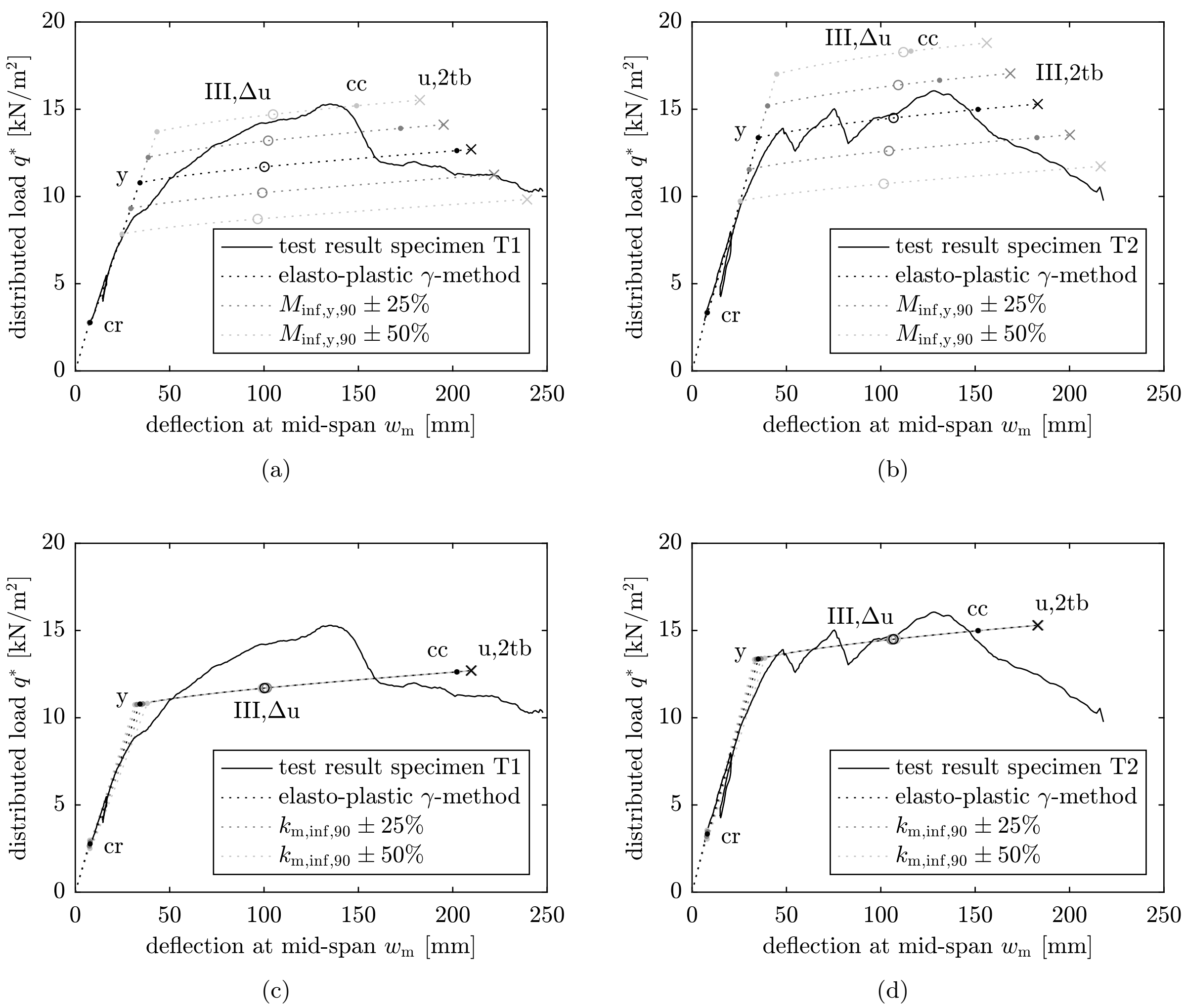

Fig. 6.28: Comparison of test measurements with the results of the elasto-plastic γ-method and sensitivity of the predicted load-bearing capacity with regard to (a) & (b) $M_{\mathrm{inf,y,90}}$ and (c) & (d) $k_{\mathrm{m,inf,90}}$.

has no influence on the load-bearing capacity and only a limited influence on the stiffness. Increasing this parameter by 50% leads to an only 7% smaller mid-span deflection.

The influence of the side connections was assessed with a comparison of calculation results. For this purpose, the side connections were neglected in both strut-and-tie model and elasto-plastic γ-method, assuming the timber chord as continuous. This led to an underestimation of the mid-span deflections by approximately 20% in both models and in both specimens. This result shows that the side connection has a significant influence on the stiffness and should therefore be considered in the calculation model.

In conclusion, the elasto-plastic γ-method with a reduced timber MOE according to Eq. 6.113 is able to accurately predict both deflections and load-bearing capacity of the two test specimens in transversal direction. As the load-bearing capacity strongly depends on the yield moment in the connection perpendicular to the grain $M_{\mathrm{inf,y,90}}$, this parameter should be further investigated in push-out tests to provide a more reliable data basis. In analogy to the findings of Chapters 6.4.2 and 6.4.3, the linear strut-and-tie model with uncracked concrete delivers good deformation predictions but is not suitable for an accurate failure prediction.

6.5 Conclusions

In this chapter, two models were presented that can be used to describe the uniaxial load-bearing behaviour of the investigated TCC slab: the elasto-plastic γ-method and the strut-and-tie model. The latter can be implemented either with an uncracked or cracked concrete section and with linear or nonlinear connection behaviour, which leads to four versions of this model. The accuracy of the model predictions was assessed by means of a comparison with the results of the uniaxial bending tests. Tab. 6.6 summarises the main conclusions regarding the applicability of the different models for the prediction of deformations, load-bearing capacity and dynamic behaviour.

Tab. 6.6 shows that the elasto-plastic γ-method is the only model that performs well in all three mentioned analysis types. As it is entirely based on analytical calculations, it allows for a fast, parametric design process. Furthermore, the model can be implemented with design values of the connection shear capacity according to the current design codes. Therefore, this method is recommended to be used as the main model in the design process of TCC slabs with steel tube connection.

Compared to the elasto-plastic γ-method, strut-and-tie models cannot account for concrete cracking in a closed-form calculation. As a consequence, their application for the prediction of the load-bearing capacity involves an iterative procedure. However, strut-and-tie models are a valuable complementary tool for all analyses requiring the specific consideration of a given connector layout or loading situation.

The prediction of the load-bearing capacity obtained from the elasto-plastic γ-method is valid only in cases where yielding of all connectors occurs before the connection deformation capacity is reached. This can be ensured by choosing a connector layout that leads to approximately equal elastic shear forces in all connectors. Such a connector layout also allows to activate the

Tab. 6.6: Applicability of the assessed calculation models describing the uniaxial load-bearing behaviour of the TCC slab with steel tube connection.

Prediction of	Elasto-plastic	Strut-and-tie model			
	γ-method	lin./uncr.	lin./cr.	nonlin./uncr.	nonlin./cr.
Deformations under service loads	✓	✓	×	✓	×
Deformations under loads inducing high connection shear forces	×	×	×	✓	×
Load-bearing capacity in case of even connection force distribution	✓	×	✓ (LLV)	×	✓
Load-bearing capacity in case of uneven connection force distribution	×	×	✓ (LLV)	×	✓
Fundamental frequency	✓	✓	–	–	–

Symbol legend: ✓ model applicable, × model not applicable, – applicability not assessed
LLV = lower limit value

maximum possible bending stiffness of the composite slab. The most efficient way of optimising the connector layout for any given loading situation is by using a linear strut-and-tie model with uncracked concrete.

In practice, there may be cases where such an optimised connector layout is not possible. In such cases, the elasto-plastic γ-method may overestimate the load-bearing capacity and should therefore not be used for this purpose. Instead, a lower limit value should be determined using a linear strut-and-tie model with cracked concrete. An estimation closer to the actual load-bearing capacity in such a case is possible with a nonlinear strut-and-tie model with cracked concrete. However, this model involves a considerable time effort and is therefore mainly suitable for academic purposes.

With respect to the prediction of deformations, the elasto-plastic γ-method performs well under service loads, which are typically in the range where the connection behaviour remains approximately linear. However, in cases where high connection shear forces are to be expected, an accurate deformation prediction is possible only with a nonlinear strut-and-tie model.

Both elasto-plastic γ-method and the linear strut-and-tie model with uncracked concrete deliver good estimations of the fundamental frequency, if the reloading connection stiffness $k_{\mathrm{m},2}$ is used. Dynamic calculations based on the first loading stiffness $k_{\mathrm{m},1}$ lead to a significant underestimation of the fundamental frequency and are therefore not recommended.

The models described in this chapter are mainly intended for predicting the load-bearing behaviour of the one-way spanning version of the investigated TCC slab. However, the same models can also be used to separately assess the longitudinal and transversal load-bearing directions in a two-way spanning version of the slab. In this context, the conclusions summarised in Tab. 6.6 are valid also for the transversal load-bearing direction, if the stiffness of the side connections is considered as described in Chapter 6.4.5.

Chapter 7

Models for biaxial bending

7.1 Introduction

In Chapter 6, two models were presented that can be used to predict the load-bearing behaviour of the investigated TCC slab in uniaxial bending. These two models are extended in this chapter to represent the biaxial bending behaviour of the novel two-way spanning TCC slab.

The elasto-plastic γ-method (Chapter 6.2) is based on Bernoulli beam theory with an implicit consideration of the connection flexibility using an effective bending stiffness. The extension of this simplified method for a two-way spanning slab consequently leads to an orthotropic plate model based on Kirchhoff-Love plate theory. This model is described in Chapter 7.2.

The strut-and-tie model (Chapter 6.3) is an FE based method that allows for an explicit consideration of each single TCC connector in the slab. The concrete and timber chords are modelled as horizontal beams, linked with vertical beams and springs that represent the connectors in their exact position. Extending this model for the biaxial case leads to a three-dimensional FE model where the timber and concrete layers are represented by shells. The two shells are linked with the same connector beams as in the uniaxial case. This 'coupled shell model' is described in Chapter 7.3.

Both models are applied to the boundary conditions of the biaxial bending test performed within the scope of this research project. This allows for a comparison of the respective predictions with the test results. On this basis, the accuracy of the models is assessed with regard to the prediction of deformations, load-bearing capacity and dynamic behaviour.

7.2 Orthotropic plate model

7.2.1 Introduction

This chapter describes an approach to predict the load-bearing behaviour of two-way spanning TCC slabs using orthotropic plate theory. FE based plate calculations are typically based either on Kirchhoff-Love plate theory [39; 51] or on Reissner-Mindlin plate theory [55; 66]. The former is derived from the hypothesis that plane sections remain plane after deformation and is the two-dimensional equivalent of Bernoulli beam theory. Shear deformations are not considered in Kirchhoff-Love plates. The latter, Reissner-Mindlin plate theory, is the two-dimensional equivalent of Timoshenko beam theory and takes into consideration both bending and shear deformations.

In TCC slabs, the flexibility of the connection leads to slip strains between the timber and concrete sections. As a consequence, the hypothesis that plane sections remain plane after deformation is generally not valid. In the γ-method, the most widely used calculation model for one-way spanning TCC slabs, this is taken into account with a calculation process in two stages. In a first step, a reduced, effective bending stiffness is calculated. In this effective bending stiffness, the shear deformations in the connection are implicitly considered. Therefore, all subsequent analyses (second step of the process, e. g. calculation of deformations or vibrations) are based on Bernoulli beam theory, not on Timoshenko beam theory.

Transferring this concept to a two-way spanning TCC slab leads to an orthotropic plate model based on Kirchhoff-Love plate theory. The corresponding calculation process in two stages is illustrated in Fig. 7.1. In a first step, the three orthotropic stiffness parameters are calculated:

- Bending stiffness in x-direction EI_{x} (often referred to as D_{11} in FEM software)
- Bending stiffness in y-direction EI_{y} (D_{22})
- Torsional stiffness EI_{xy} (D_{33})

The parameters EI_{x} and EI_{y} can be calculated e. g. based on the γ-method, applying the procedures explained in Chapters 6.2 and 6.4.5. Alternatively, strut-and-tie models can be used as described in Chapters 6.3.2 and 6.4.5. In this case, EI_{x} and EI_{y} are backcalculated e. g. from the mid-span deflection in the model under a chosen load.

Up to date, no models are available for an analytical calculation of the torsional stiffness EI_{xy} of a TCC slab with partial composite action. A lower limit value may be calculated according

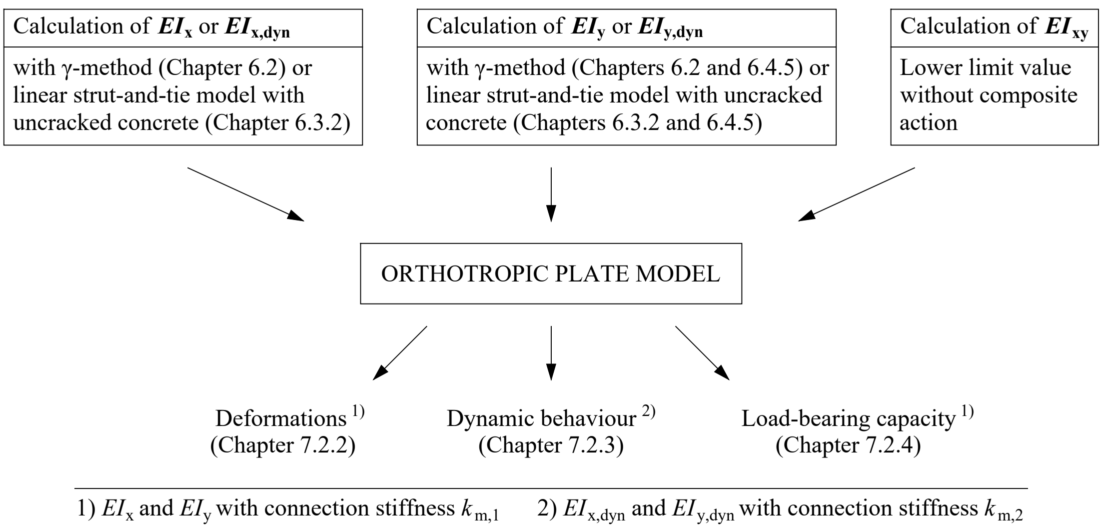

Fig. 7.1: Overview of the orthotropic plate model with input parameters and results.

to Eq. 7.1, neglecting any composite action in torsion. The contribution of the timber section is typically negligible because $G_2 \ll G_1$. Using a lower limit value for EI_{xy} in the design analysis leads to conservative results in terms of deformations and vibrations.

$$EI_{\mathrm{xy}} = \frac{G_1 h_1^3 + G_2 h_2^3}{12} \approx \frac{G_1 h_1^3}{12} \tag{7.1}$$

As discussed in Chapters 3.3.5 and 6.4.4, the reloading connection stiffness $k_{\mathrm{m,2}}$ is relevant for the dynamic behaviour of the investigated TCC slab rather than the first loading stiffness $k_{\mathrm{m,1}}$. Therefore, the input values EI_{x}, $EI_{\mathrm{x,dyn}}$, EI_{y} and $EI_{\mathrm{y,dyn}}$ are calculated using the respective connection stiffness depending on the type of analysis, as indicated in Fig. 7.1.

7.2.2 Deformations

The biaxial bending test campaign (Chapter 5) comprised four static loading tests as shown in Fig. 5.2. The idea behind this concept was to measure all three input parameters of the orthotropic plate model EI_{x}, EI_{y} and EI_{xy} and the resulting load-bearing behaviour in biaxial support conditions. This allowed for a specific assessment of the performance of the orthotropic plate model in this case, as all input and output values were known from the experiment. The model was calculated using the software *RFEM 5* from *Dlubal*. The four line supports were modelled such that only compressive support reactions are transferred. The orthotropic stiffness parameters were $EI_{\mathrm{x}} = 5\text{'}310\,\mathrm{kNm^2/m}$, $EI_{\mathrm{y}} = 2\text{'}380\,\mathrm{kNm^2/m}$ and $EI_{\mathrm{xy}} = 3\text{'}030\,\mathrm{kNm^2/m}$.

Fig. 7.2a shows that the prediction of deflections is accurate in the linear range up to 40% of the failure load. At higher loads, the nonlinear connection behaviour starts to play a significant role and thus, the deflections are underestimated, similar as in the linear models for uniaxial bending (Chapter 6.4.2). Fig. 7.2b shows that also regarding the ratio of the support forces in x- and y-direction, the model prediction is in good agreement with the test results.

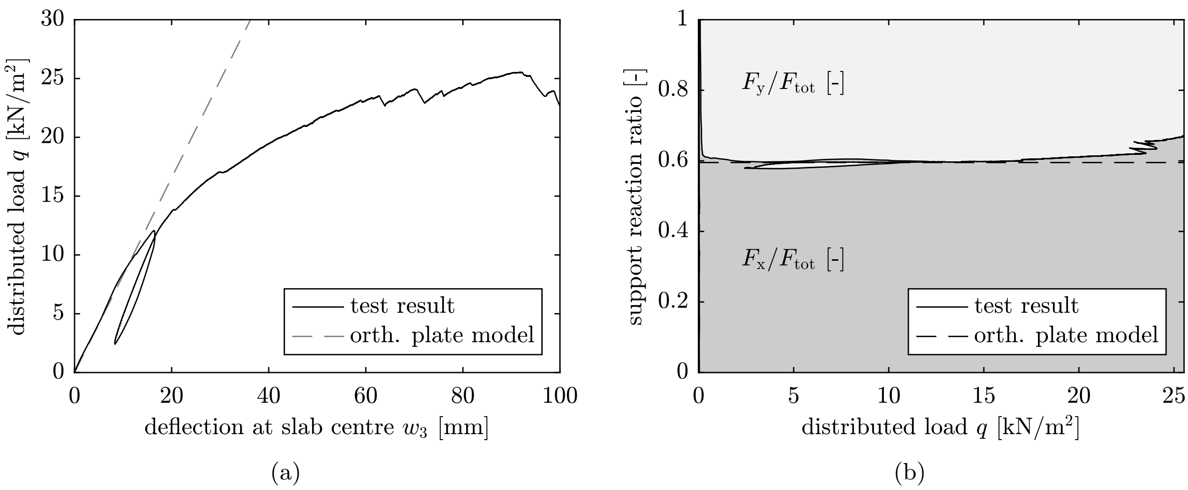

Fig. 7.2: Comparison of the test measurements from the biaxial bending test with the results from the orthotropic plate model: (a) deflections and (b) ratio of the support forces in x- and y-direction.

As a comparison, the same calculation was performed with a lower limit value of the torsional stiffness $EI_{xy} = 660\,\text{kNm}^2/\text{m}$ according to Eq. 7.1, which led to an overestimation of the mid-span deflections by 35%. This result is on the safe side for practical design applications. However, given the distinct influence of this parameter, further research should be conducted in order to allow for a better estimation of EI_{xy} considering partial composite action.

7.2.3 Dynamic behaviour

Dynamic tests were performed on the biaxial test specimen in four different support conditions as illustrated in Fig. 5.2. For a prediction of the respective fundamental frequencies with the orthotropic plate model, the experimentally determined reloading stiffness values (loading cycles 2/3 in Tab. 5.3) were used. Apart from these stiffness values, the FE model was identical to the one described in Chapter 7.2.2. Tab. 7.1 shows that the resulting predictions of the fundamental frequency f_1 are within ±11% of the measurement values for all configurations with line supports. In the case of point supports in the corners, the model underestimates f_1 by 17%. In the specimen, concrete edge beams were included (Fig. 5.3). In the orthotropic plate model, these edge beams are not explicitly considered. It is likely that this edge beam had a stiffening effect especially in the situation with point supports in the corners. This may explain at least a part of the difference in this case.

If the static bending stiffness values are used in the model as in Chapter 7.2.2, the fundamental frequencies are significantly underestimated in all cases, on average by 30%. A similar observation was made already in the comparison of test measurements and model results in uniaxial bending (Chapter 6.4.4). These results confirm the need to distinguish between static and dynamic stiffness values in the investigated TCC slab with steel tube connection.

Tab. 7.1: Fundamental frequency f_1 in [Hz], measurement values before the respective static loading tests and results from the orthotropic plate model.

Support conditions	$f_{1,\text{test}}$	$f_{1,\text{model}}$ *	Rel. difference
Uniaxial bending in x-direction	10.1	9.0	−11%
Uniaxial bending in y-direction	6.3	5.8	−8%
Point supports in the slab corners	5.9	4.9	−17%
Biaxial bending	14.4	15.0	+4%

* Input parameters: $EI_x \,/\, EI_y \,/\, EI_{xy} = 9'860 \,/\, 4'110 \,/\, 3'620\,\text{kNm}^2/\text{m}$

7.2.4 Load-bearing capacity

The uniaxial bending tests (Chapter 4) showed that the load-bearing capacity of the investigated TCC slab is governed by a ductile connection failure. Based on this observation, several calculation models were presented in Chapter 6 that are able to account for a limited plastic redistribution of internal forces in a one-way spanning TCC slab.

The biaxial bending test (Chapter 5) showed that the same ductile connection failure mechanisms develop also in a two-way spanning TCC slab with steel tube connection. However, accounting for a limited plastic redistribution of internal forces is much more complex in a two-way spanning system.

Two approaches for the calculation of the load-bearing capacity based on the orthotropic plate model are presented in this chapter. The first approach aims at a direct calculation of the maximum connection shear force from the elastic plate shear forces. The second approach is based on the lower limit theorem of plasticity and uses the elasto-plastic γ-method.

Calculation of connection shear forces from elastic plate shear forces

One-way spanning TCC slabs with linear-elastic, brittle connection behaviour are usually designed based on a linear-elastic analysis. Connection failure is predicted by these models when the first connector reaches its shear capacity, assuming that no internal force redistributions are possible. If the γ-method is used, the respective calculation procedure is identical to the one described in Chapters 6.2.3 and 6.2.4 (states I and II). The maximum connection shear force during state I is calculated with Eq. 7.2 based on the maximum shear force $V_{\max}$. S_{12} is the static moment at the interface of the partial cross-sections and all other parameters are calculated according to Chapter 6.2.3.

$$T_{\max} = \frac{S_{12} s_{\mathrm{ef}}}{I_{\mathrm{I}}} \cdot V_{\max} = \frac{\gamma_1 E_1 A_1 a_1 s_{\mathrm{ef}}}{EI_{\mathrm{I}}} \cdot V_{\max} \tag{7.2}$$

In theory, the same concept can also be used to calculate the elastic connection shear forces in a two-way spanning TCC slab, based on the plate shear forces v_{x} and v_{y} that result from the orthotropic plate analysis. This approach was applied to the orthotropic plate model described in Chapter 7.2.2 with the same stiffness parameters. Fig. 7.3 shows why a direct calculation based on the plate shear forces can be problematic. Depending on the torsional stiffness EI_{xy}, the FE model predicts a strong concentration of shear forces towards the centre of the line supports. Strictly applying Eq. 7.2 to obtain an elastic connection shear force would therefore

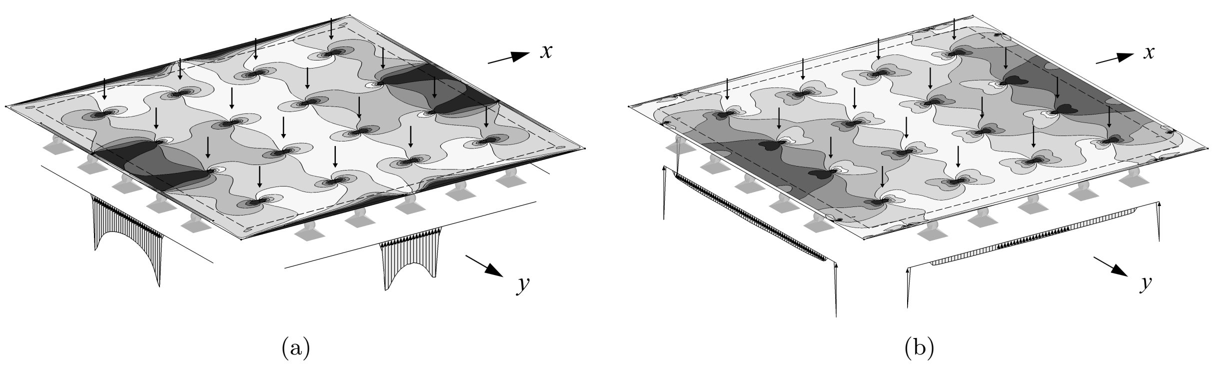

Fig. 7.3: Qualitative distribution of plate shear force v_{x} and support forces resulting from a calculation with different torsional stiffness values: (a) $EI_{\mathrm{xy}} = 3'030\,\mathrm{kNm^2/m}$ and (b) $EI_{\mathrm{xy}} = 10\,\mathrm{kNm^2/m}$, same colour scale in both plots with dark areas corresponding to high values of v_{x}.

lead to a highly unstable result with regard to EI_{xy}. As EI_{xy} is an input parameter that is difficult to estimate, such a strong dependency is not desirable.

This does not mean that it is impossible to obtain an estimation of the load-bearing capacity based on the elastic plate shear forces resulting from an orthotropic plate model. However, a post-processing of the results is necessary that involves a redistribution of the shear forces. As a consequence, the results no longer correspond to an elastic solution. An example for such a post-processing would be to manually distribute the total support force according to Eq. 7.3. The widths $b_{\mathrm{v,x}}$ and $b_{\mathrm{v,y}}$ have to be chosen based on engineering judgement.

$$v_{\mathrm{x,max}} = F_{\mathrm{x}}/b_{\mathrm{v,x}} \qquad \text{and} \qquad v_{\mathrm{y,max}} = F_{\mathrm{y}}/b_{\mathrm{v,y}} \tag{7.3}$$

This approach is applied to the biaxial bending specimen. Based on the ductile connection behaviour, the support forces are distributed along the entire specimen width ($b_{\mathrm{v,x}} = b_{\mathrm{v,y}} = 5.46\,\mathrm{m}$). Eq. 7.2 is applied accordingly to calculate the resulting connection shear forces in x- and y-direction. Fig. 7.4 shows that this procedure leads to a good estimation of the load-bearing capacity in this example. Connection failure in x-direction is predicted at a distributed load of $q^*_{\mathrm{u,x}} = 24.4\,\mathrm{kN/m^2}$, which is 11% lower than the load at which the first significant load drop due to a visible connection failure occurred in the experiment. However, this result is a linear function of the chosen values of $b_{\mathrm{v,x}}$ and $b_{\mathrm{v,y}}$ and should thus be interpreted with caution.

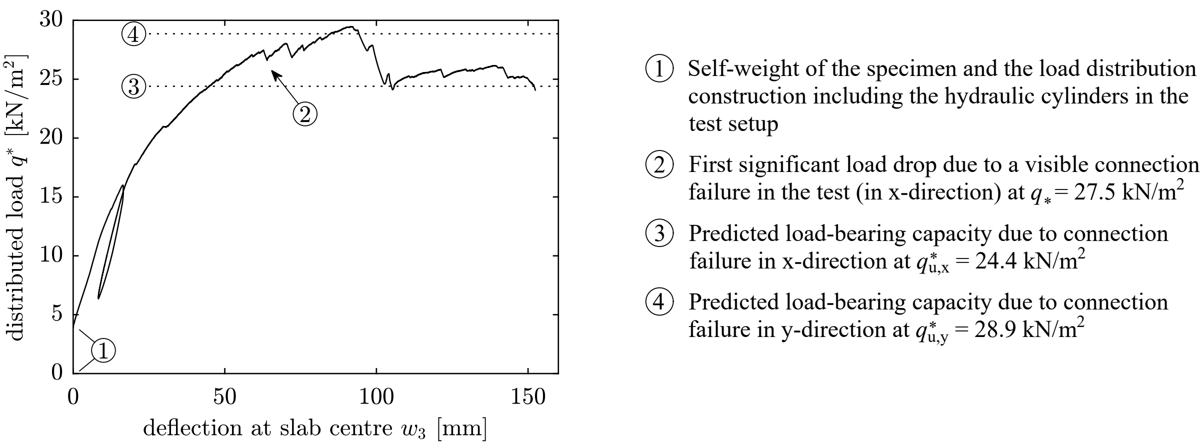

Fig. 7.4: Load-deflection curve from the biaxial loading test and prediction of the load-bearing capacity based on a calculation of the connection shear forces with $b_{\mathrm{v,x}} = b_{\mathrm{v,y}} = 5.46\,\mathrm{m}$.

Calculation based on the strip method and the elasto-plastic γ-method

Reinforced concrete slabs can be designed based on the lower limit theorem of plasticity. The strip method is an application of this theorem for slabs [36]. Its main assumption is that the torsional moments $m_{\mathrm{xy}} = 0$ and therefore, the equilibrium conditions are fulfilled with the bending moments m_{x} and m_{y} only. This method is applicable for slabs with a perfectly plastic behaviour, which is typically assumed in the case of reinforced concrete slabs. Examples for the application of the strip method are discussed e. g. by Marti et al. [53].

In theory, as kinematic compatibility is neglected in the strip method, the distribution of forces in x- and y-direction can be freely chosen. However, if a load distribution is chosen that substantially differs from the elastic solution, a large plastic deformation capacity is necessary to allow the assumed stress state to develop. Therefore, if the deformation capacity is limited (as in the investigated two-way spanning TCC slab), the load distribution should be chosen as close as possible to the elastic solution. Otherwise, the strip method may lead to results on the unsafe side, as a brittle failure could occur before the assumed stress state has developed.

Fig. 7.5 presents an application of the strip method for a quadratic, orthotropic slab with hinged line supports on all four sides. For $\lambda = 0.5$, this is a well-known solution of the isotropic case, e. g. covered in [53]. For a slab with $EI_x > EI_y$, the parameter λ can take values between 0.5 and 1. As discussed above, λ should not be chosen without any consideration of kinematic compatibility if this solution is applied to a slab with limited plastic deformation capacity.

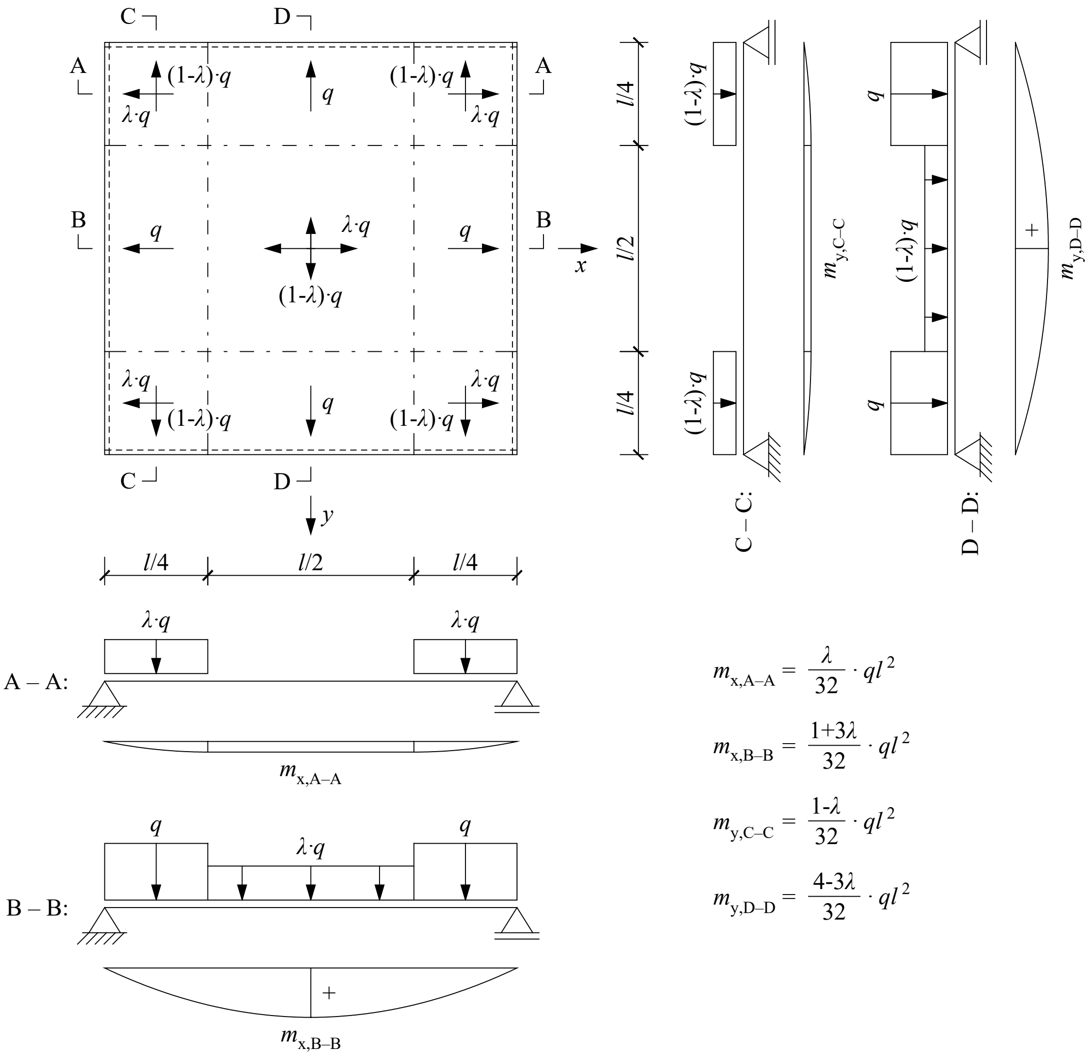

Fig. 7.5: Application of the strip method for a quadratic, orthotropic slab with hinged line supports on all four sides.

Based on the static systems depicted in Fig. 7.5, sections B – B and D – D, the following two expressions for the elastic mid-span deflection can be derived:

$$w_{\mathrm{m,B-B}} = \frac{23 + 57\lambda}{6144} \cdot \frac{ql^4}{EI_{\mathrm{x}}} \qquad \text{and} \qquad w_{\mathrm{m,D-D}} = \frac{80 - 57\lambda}{6144} \cdot \frac{ql^4}{EI_{\mathrm{y}}} \tag{7.4}$$

Kinematic compatibility can be achieved at mid-span by requiring $w_{\mathrm{m,B-B}} = w_{\mathrm{m,D-D}}$, which leads to the following expression for λ:

$$\lambda = \frac{80 \cdot EI_{\mathrm{x}}/EI_{\mathrm{y}} - 23}{57 \cdot (1 + EI_{\mathrm{x}}/EI_{\mathrm{y}})} \tag{7.5}$$

The ratio of support forces reads:

$$\frac{F_{\mathrm{x}}}{F_{\mathrm{tot}}} = \frac{1 + 2\lambda}{4} \qquad \text{and} \qquad \frac{F_{\mathrm{y}}}{F_{\mathrm{tot}}} = \frac{3 - 2\lambda}{4} \tag{7.6}$$

The strip method presented in Fig. 7.5 with λ according to Eq. 7.5 allows for an estimation of the load-bearing capacity of a quadratic, orthotropic slab with a limited plastic deformation capacity, based on an analytical calculation procedure.

Alternatively, an estimation of the load-bearing capacity following the same principles can be obtained from the FE based orthotropic plate model used in the previous section. Setting the torsional stiffness to a low value leads to a solution with $m_{\mathrm{xy}} \approx 0$ and delivers values for m_{x} and m_{y} that satisfy kinematic compatibility.

Both procedures were applied to the boundary conditions of the biaxial bending test. In the FE model, point forces were positioned in the same locations as in the test setup. The strip method (Fig. 7.5) assumes an equivalent distributed load, which leads to a lower bending moment at mid-span as shown in Fig. 7.6. The bending moments m_{x} and m_{y} resulting from the strip method were therefore multiplied with the respective ratio 294/267 to account for this influence. Eq. 7.5 returns a value of $\lambda = 0.84$ for the experimentally determined parameters EI_{x} and EI_{y}. This value corresponds to $F_{\mathrm{x}}/F_{\mathrm{tot}} = 67\%$, which is in a similar range as the respective test measurement. The elasto-plastic γ-method predicts a uniaxial bending moment resistance that is limited by exceedance of the connection deformation capacity during state III in both directions, at $m_{\mathrm{x,III,\Delta u}} = 92.5\,\mathrm{kNm/m}$ and $m_{\mathrm{y,III,\Delta u}} = 58.4\,\mathrm{kNm/m}$. Failure of the slab is defined when either $m_{\mathrm{x}} = m_{\mathrm{x,III,\Delta u}}$ or $m_{\mathrm{y}} = m_{\mathrm{y,III,\Delta u}}$ is reached at mid-span.

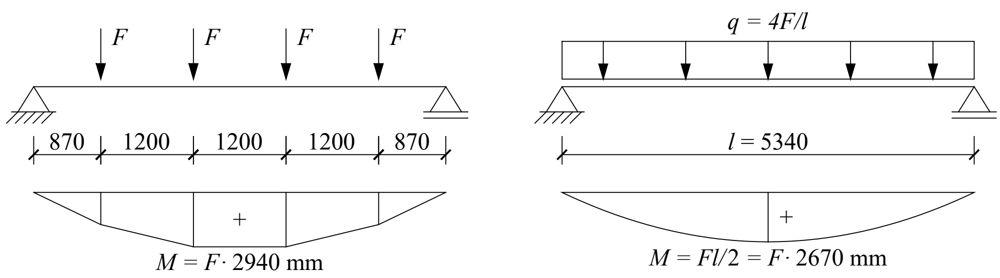

Fig. 7.6: Bending moments resulting from four point loads F as in the test setup and from an equivalent distributed load $q = 4F/l$.

Fig. 7.7 shows the load-deflection curve from the biaxial loading test and the results of both calculation procedures. In the experiment, the first significant load drop due to a visible connection failure was observed in x-direction at $q^* = 27.5\,\mathrm{kN/m^2}$. Both calculation methods predict a failure due to exceedance of the connection deformation capacity in x-direction. The corresponding failure loads are in good agreement with the test results, 3% (strip method) and 13% (FE based calculation) below the mentioned load level in the experiment.

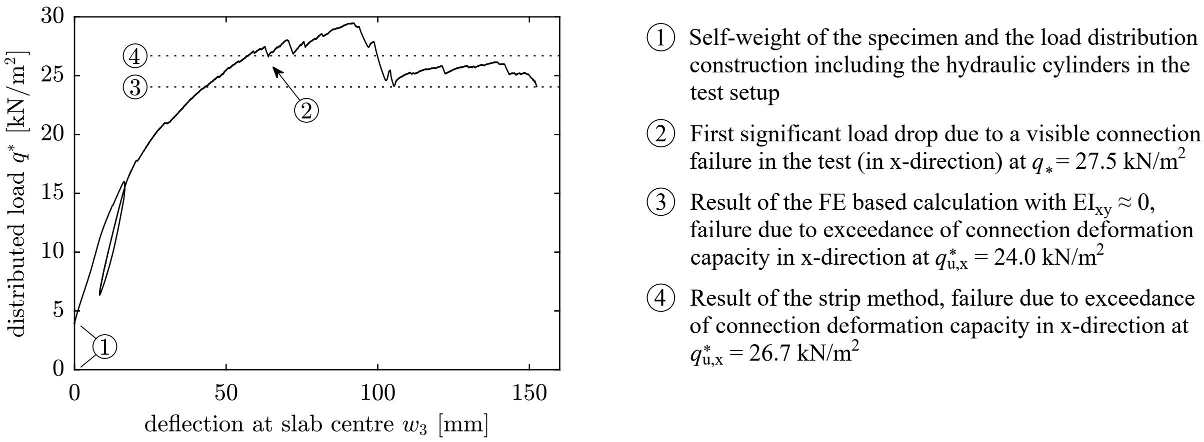

Fig. 7.7: Load-deflection curve from the biaxial loading test and prediction of the load-bearing capacity based on the strip method and the elasto-plastic γ-method.

Fig. 7.8 shows the influence of λ on the predicted load-bearing capacity q^*_u with the described strip method. The maximum load-bearing capacity would result with a value of $\lambda = 0.69$, leading to simultaneous failure in x- and y-direction. In a slab with perfect plasticity, this highest lower limit value would be the best estimation of the true load-bearing capacity that can be obtained from the described strip method.

Calculating λ according to Eq. 7.5 leads to a lower q^*_u as it considers the elastic deflection at mid-span. The resulting utilisation ratio in y-direction at failure is $m_\mathrm{y}/m_{\mathrm{y,III},\Delta\mathrm{u}} = 66\%$. This result implies that, with a sufficient plastic deformation capacity, the load could be increased with a redistribution of internal forces towards the y-direction.

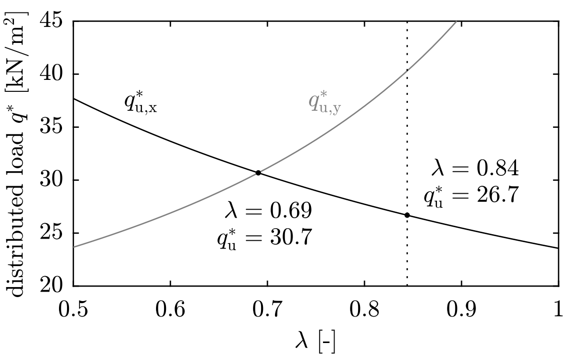

Fig. 7.8: Prediction of the load-bearing capacity with the strip method as a function of λ.

In the experiment, a brittle failure of the side connections (i.e. the GIR connections in the timber layer in y-direction) occurred at $q_u^* = 29.5\,\mathrm{kN/m^2}$, which limited the deformation capacity of the slab. A redistribution of forces towards the y-direction may have been possible if this failure had not occurred. However, the deformation capacity of the slab is also limited by the steel tube connection system. Therefore, in the context of the investigated TCC slab, the strip method should not be applied without any consideration of the elastic deformations.

Comparison of the two calculation approaches

Two different approaches for the estimation of the load-bearing capacity of the two-way spanning TCC slab were investigated in this chapter.

The first approach showed that a consistent calculation of elastic connection shear forces from the results of the FE based orthotropic plate model is not possible. Nevertheless, a rough estimation of the load-bearing capacity can be obtained based on a manual distribution of the support forces across a chosen width. This approach may be useful during early design phases as it can be easily applied to more complex slab geometries and support conditions. The design of TCC slabs in practice is typically governed by SLS criteria. Therefore, a rough estimation of the load-bearing capacity based on conservative assumptions may be sufficient during an early project phase.

The second approach is based on the lower limit theorem of plasticity and allows for a more consistent calculation of the load-bearing capacity. Two alternative procedures based on an analytical calculation and an FE based calculation of the bending moments at mid-span were assessed. Both procedures allow for an accurate prediction of the load-bearing capacity. In contrast to the first approach, no parameters have to be chosen that directly influence the result. However, the application of this method may be more challenging for complex slab geometries and support conditions.

Both calculation approaches were investigated only with regard to the boundary conditions of the biaxial bending test performed within the scope of this research project. Further investigations are necessary to assess the performance of these models in the case of other slab geometries and support conditions.

7.3 Coupled shell model

This chapter describes an approach to predict the load-bearing behaviour of two-way spanning TCC slabs using a coupled shell model. This model is an adaptation of the strut-and-tie model described in Chapter 6.3 and allows to explicitly consider each connector in its exact position in the slab. The complexity of such a model is substantial and is therefore mainly intended for academic purposes. The application of this model was investigated in a master thesis that was carried out as a part of this research project [47]. Fig. 7.9 illustrates the model and its components. A special detail is required in the connection of the shells with the connector beams. Introducing a bending moment into a shell in a single node leads to a mesh size dependency

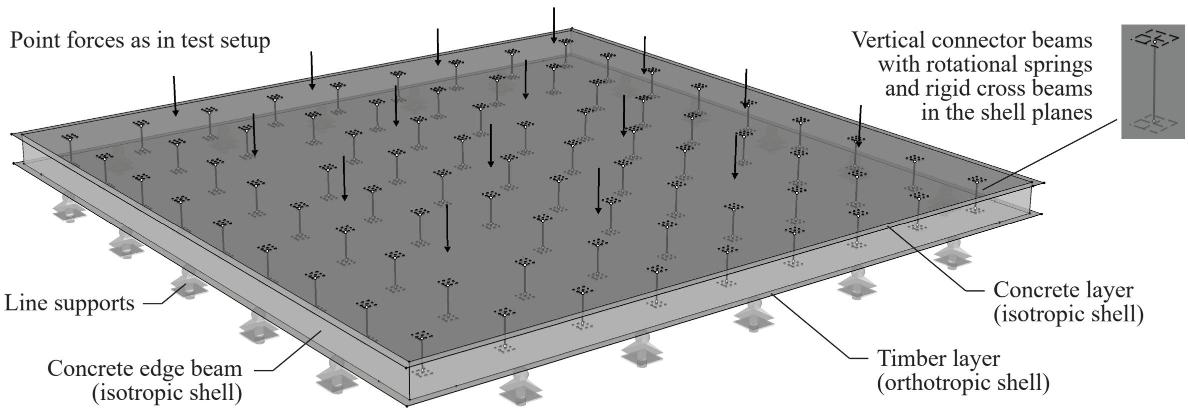

Fig. 7.9: Coupled shell model applied to the boundary conditions of the biaxial bending test.

that affects the model results. This problem can be mitigated by adding a set of rigid cross beams in the shell plane (Fig. 7.9), which allows for an introduction of the bending moment as a pair of shear forces into the shell. The length of these rigid beams corresponds to the steel tube diameter. A convergence study with regard to the mentioned mesh size dependency is described in [47]. Aside from this detail, the model is built in analogy to the uniaxial strut-and-tie model as described in Chapter 6.3. This includes the modification of the rotational spring behaviour to account for their shifted vertical position in the model.

The coupled shell model is characterised by the same advantages and disadvantages as the uniaxial strut-and-tie model. The main disadvantage compared to the elasto-plastic γ-method is the fact that concrete cracking can only be accounted for by iteratively adjusting the stiffness and position of the concrete shell. Given the complexity of the described model, this iterative process requires a substantial time effort. Nevertheless, this model allows to investigate a range of aspects that cannot be assessed using a simplified orthotropic plate model, such as:

- Influence of different connector layouts on the biaxial load-bearing behaviour
- Possible interactions of the shear forces in the connectors in both directions
- Torsional stiffness of the composite slab

Not all of these aspects were investigated in detail within the scope of this study. In analogy to the uniaxial strut-and-tie model, four versions of the shell model are possible. The rotational springs can be modelled as linear or nonlinear and concrete cracking can be considered or neglected. A coupled shell model with nonlinear rotational springs (Chapter 3.3.7) and cracked concrete was applied to the boundary conditions of the biaxial bending test using the software *RFEM 5* from *Dlubal*. Fig. 7.10 shows the result of the obtained model prediction compared to the test measurements. The starting point of the experimentally determined load-deflection curve is shifted to account for the self-weight of the specimen and the load distribution construction. Failure is predicted when the first connectors reach their deformation capacity. The first connectors reaching their deformation capacity according to the coupled shell model are

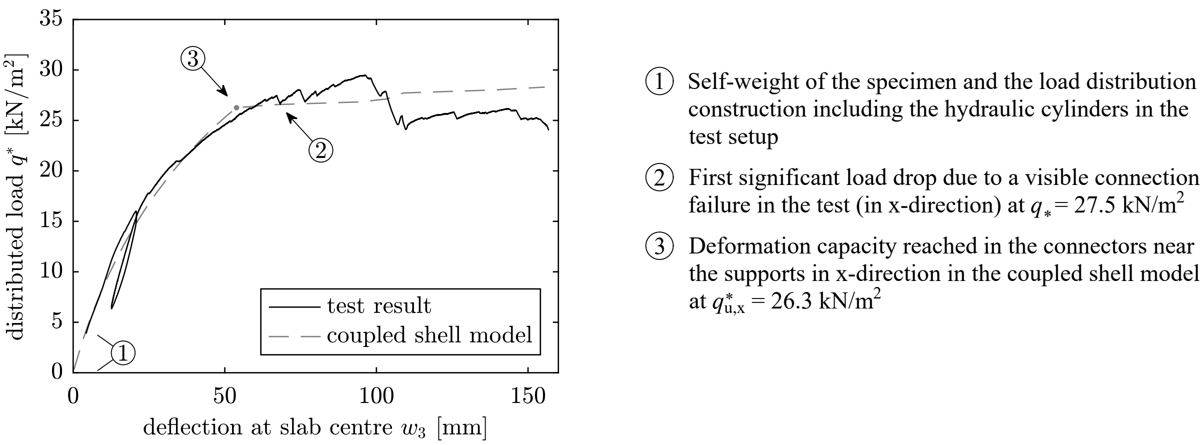

Fig. 7.10: Load-deflection curve from the biaxial loading test and prediction with the coupled shell model with nonlinear rotational springs and cracked concrete.

located close to the line supports in x-direction. These are the same connectors where the first failures were observed during the experiment. The corresponding load level in the model is only 4% below the measured load in the experiment. This result shows the great potential of coupled shell models for the detailed analysis of two-way spanning TCC slabs. Furthermore, the prediction of the load-bearing capacity that was obtained with the simplified models in the previous chapter is validated with this result for the given boundary conditions.

The coupled shell model should be further developed with the aim to facilitate the consideration of concrete cracking, ideally without the need for an iterative procedure. Such an improved version of this model would be a valuable tool to investigate more complex slab geometries, support conditions and connector layouts. As an alternative to costly large-scale experiments, the respective model results could then serve as a basis to further validate the simplified methods using orthotropic plate theory.

7.4 Conclusions

In this chapter, two models were presented that can be used to predict the biaxial load-bearing behaviour of the novel TCC slab with steel tube connection. Both models were applied to the boundary conditions of the biaxial bending test (Chapter 5), which allowed for a comparison of the test results with the corresponding predictions. Below, the main conclusions are summarised:

- The orthotropic plate model delivers accurate predictions of the deformations under service loads and the fundamental frequency of the slab.

- The torsional stiffness EI_{xy} has a distinct influence on the deformation predictions of the orthotropic plate model. Results on the safe side can be obtained using a lower limit value. However, given that the design of TCC slabs is typically governed by deformation criteria, this assumption prevents full exploitation of the advantages of a two-way spanning slab compared to a one-way spanning alternative. Therefore, further research is necessary to allow for a better estimation of the torsional stiffness EI_{xy} of TCC slabs with partial composite action.

- For the boundary conditions of the biaxial bending test, several model approaches based on orthotropic plate theory delivered accurate predictions of the load-bearing capacity. The strip method was found to be applicable if the load distribution in x- and y-direction is chosen based on the uniaxial bending stiffness ratio $EI_{\mathrm{x}}/EI_{\mathrm{y}}$.

- The results of the coupled shell model demonstrate its great potential for the detailed analysis of two-way spanning TCC slabs. However, the iterative procedure that is needed to account for concrete cracking requires a considerable time effort. The model should be further developed to allow for a more efficient analysis. An improved version of this model would be a valuable tool to investigate more complex slab geometries, support conditions and connector layouts.

Chapter 8

Conclusions and outlook

8.1 Conclusions

In this thesis, a novel two-way spanning TCC slab was developed and investigated. It was found that an optimised stiffness-to-mass ratio can be achieved if the core of the slab between the timber and concrete layers is filled with a light-weight material such as cellulose fibres or stone wool. As a direct consequence of this concept choice, TCC connectors with a high bending stiffness have to be used. Therefore, a solution using steel tubes as connectors was developed. In order to achieve a biaxial load-bearing behaviour, the beech LVL plates have to be connected along their side edges. A concept for this side connection was developed using glued-in rods.

The load-bearing behaviour of the novel TCC slab was investigated on three levels, focusing on the local connection behaviour and the global behaviour in uniaxial and biaxial bending. Several experimental campaigns as well as analytical and numerical investigations were conducted for this purpose. The conclusions corresponding to the mentioned three levels are summarised in the following sections.

Connection behaviour

The connection system with steel tubes was investigated in three series of push-out tests. The experiments allowed for a separate assessment of the steel tube-timber and the steel tube-concrete connection, which led to the conclusions summarised below.

Steel tube-timber connection:

- The results showed that a sufficient connection stiffness can only be achieved if the gap between the steel tube and the timber cutout is filled with a grouting system.
- The shear capacity of the steel tube-timber connection is governed by inelastic compression deformation in timber, which leads to a ductile behaviour. The deformation capacity is limited by the shear capacity of the timber.

Steel tube-concrete connection:

- The embedment depth a and steel tube diameter D were identified as the main parameters influencing the connection behaviour.
- A ductile failure is achieved through force redistribution and eventually reinforcement yielding. The deformation capacity is limited by concrete crushing close to the steel tube.
- A significant influence of pre-loading on the connection stiffness was observed. The first loading curve should be the basis for calculations regarding deformations (SLS) and load-bearing capacity (ULS). The higher reloading stiffness is relevant for dynamic analyses. This conclusion was confirmed by the results of dynamic tests in both uniaxial and biaxial support conditions and a comparison with the corresponding prediction of the calculation models.

Uniaxial bending behaviour

The load-bearing behaviour of the one-way spanning version of the novel TCC slab was investigated in a series of uniaxial bending tests. Two calculation models were developed that can be used to predict the uniaxial load-bearing behaviour. The analysis and comparison of the respective results led to the following conclusions:

- The efficiency of the chosen connection concept with a grouted steel tube-timber connection for TCC slabs with an interlayer was confirmed.
- The results show that the connection behaviour governs the global load-bearing behaviour. Cross-sectional failures in timber or concrete were not observed. A ductile failure in the connectors leads to a remarkably ductile behaviour of the TCC slab in uniaxial bending.
- The results consistently show that a higher number of connectors leads to a significant increase in bending stiffness and load-bearing capacity.
- Increasing the interlayer height h_0 does not generally lead to a higher bending stiffness or load-bearing capacity. The positive effect of a larger static height of the composite beam is partly or fully compensated by a reduced connection stiffness K due to the larger lever arm of the steel tubes. Whether the load-bearing behaviour can be improved by increasing h_0 mainly depends on the span l and the number of connectors m.
- The elasto-plastic γ-method delivers accurate predictions of the deformations under service loads, fundamental frequency and load-bearing capacity of the investigated TCC slab. This analytical method is based entirely on analytical calculations and thus allows for a fast, parametric design process.
- The connector layout should be chosen such that similar elastic shear forces result in all connectors. This allows to activate the maximum possible bending stiffness of the

composite slab. In addition, such a connector layout ensures that the prediction of the load-bearing capacity obtained from the elasto-plastic γ-method is on the safe side.

- In the investigated TCC slab, applying strut-and-tie models without considering concrete cracking leads to a substantial overestimation of the concrete bending moment M_1. An iterative procedure was developed to take this issue into account.
- Strut-and-tie models are a valuable complementary tool for all analyses requiring the specific consideration of a given connector layout, loading situation or the nonlinearity of the connection behaviour. They are especially useful for the optimisation of the connector layout, analysis of multi-span situations or the prediction of deformations under loads inducing high connection shear forces.

Biaxial bending behaviour

The load-bearing behaviour of the novel two-way spanning TCC slab was investigated in an extensive experimental campaign. A test setup was developed that allowed to perform static and dynamic tests on the same large-scale specimen in different support conditions. Two calculation models were developed that can be used to predict the biaxial load-bearing behaviour. The analysis and comparison of both experimental and model results led to the following conclusions:

- The tested quadratic specimen showed a 34% higher stiffness and 43% higher fundamental frequency in biaxial versus uniaxial support conditions. 60% of the total load was carried in the longitudinal direction and 40% in the transversal direction of the slab. These results confirm the great potential of two-way spanning TCC slabs for the application in practice.
- After experiencing problems with the assembly of the specimen, an alternative solution for the side connections was chosen using an epoxy adhesive anchoring system. The global load-bearing behaviour was not as ductile as in the uniaxial bending tests due to a brittle failure of these glued side connections. However, a redistribution of internal forces allowed for large deformations at 80% of the maximum load during a post-peak phase. The final side connection concept was developed on the basis of the practical experience gained during the assembly of this specimen.
- The orthotropic plate model, combined with the elasto-plastic γ-method, delivers accurate predictions of the deformations under service loads, fundamental frequency and load-bearing capacity of the investigated two-way spanning TCC slab. The strip method was found to be applicable if the load distribution in x- and y-direction is chosen based on the uniaxial bending stiffness ratio $EI_{\mathrm{x}}/EI_{\mathrm{y}}$.
- The torsional stiffness EI_{xy} has a distinct influence on the deformation predictions of the orthotropic plate model and should therefore be further investigated.
- The results of the coupled shell model demonstrate its great potential for the detailed analysis of two-way spanning TCC slabs.

8.2 Limitations

All results and conclusions of this research project are limited to the short-term behaviour of the investigated TCC slab. A preliminary creep test in biaxial bending showed a significant increase of deformations after three days under a constant load. This result confirms that long-term effects have to be considered in the design, which is typical for TCC slabs.

The findings of this research project are further limited to the use of beech LVL with cross-layers in the timber section of the described TCC slab. None of the results presented in this thesis should be transferred to other engineered wood products without conducting further specific experimental investigations.

The calculation models presented in this thesis were only applied to the boundary conditions of the conducted experiments. Mean values of all mechanical properties were used in all calculations. This allowed for a comparison of the model results with the test measurements. For practical applications, reduced design values of all mechanical properties have to be used in accordance with the current design codes.

8.3 Outlook

In this research project, the concept of a novel two-way spanning TCC slab was developed and the most relevant aspects of its structural behaviour were investigated and described. As part of this research and development process, several ideas have emerged on how to further improve the system and which aspects of the structural behaviour should be investigated in more detail. This chapter addresses these points and provides a brief overview of the studies already launched regarding these issues.

Further experimental and analytical investigation of the current concept

A substantial part of the **connection shear tests** conducted within this research project focused on the respective concept development. Many parameters were varied in the tests, resulting in small sample sizes for each configuration. Therefore, the current experimental data basis regarding the connection behaviour does not necessarily satisfy statistical relevance. The results of this thesis show that profound knowledge regarding the connection behaviour is the basis for accurate predictions of the uniaxial and biaxial bending behaviour of the novel TCC slab. Further connection shear tests should thus be performed to broaden the respective data basis. In particular, the steel tube connection in timber perpendicular to the grain should be investigated experimentally to review the respective assumptions that were made in this thesis.

The final concept of the **side connection** as depicted in Fig. 1.3 was developed after the last experimental campaign of this research project. Therefore, no experimental data are available yet concerning the stiffness and load-bearing capacity of this connection. The biaxial bending tests showed that the combination of tensile and shear forces in the side connection may play a significant role. This aspect should be investigated in further studies.

The **torsional stiffness** EI_{xy} of the two-way spanning TCC slab was identified to have a significant influence on the deformation predictions of the orthotropic plate model. Currently, a lower limit value has to be assumed, which delivers results on the safe side. However, given that the design of TCC slabs is typically governed by deformation criteria, this assumption prevents full exploitation of the advantages of a two-way spanning slab compared to a one-way spanning alternative. Further studies should focus on the development of a method to calculate EI_{xy} considering partial composite action. The coupled shell model may present a valuable tool in this process.

Further development of the current concept

The stiffness of the steel tube-concrete connection showed a distinct **pre-loading dependency** in all experiments. This effect is likely caused by small cracks developing around the steel tube as a consequence of concrete shrinkage. Reducing this influence would allow for a substantial improvement of the connection efficiency, especially regarding the deflections of the slab. One possible approach would be to increase the surface roughness of the steel tubes, e. g. with an epoxy-glued sand coating. Ideally, this would lead to some adhesion with the surrounding concrete and reduce the development of concentrated cracks at the interface with the steel tube.

In the biaxial bending test, **local punching failures** occurred in the concrete cover above several steel tubes. A possible concept to improve the respective punching resistance is discussed in Chapter 5.4.

In the past years, **new engineered wood products** have become available on the market such as cross laminated timber made of beech or birch. A possible application of these materials in TCC slabs with an interlayer and steel tube connection should be investigated as this would allow to broaden the application field in practice. Exploring this possibility is one of the objectives of a follow-up research project that has been launched at the Institute of Structural Engineering (IBK) of ETH Zurich. As a first step, the local connection behaviour in these alternative materials will be investigated.

Long-term behaviour

The main objective of the mentioned follow-up project concerns the investigation of the long-term behaviour of the presented TCC slab concept. Within the scope of this thesis, only a preliminary 3-day creep test in biaxial bending was conducted. The results showed a significant increase of deformations, confirming the need for further research on this topic. Guidelines for the design of conventional TCC structures considering the long-term behaviour are given in the TS TCC [15]. The applicability of the respective calculation models in this specific case has to be assessed.

Practical application in projects

A first application of the novel two-way spanning TCC slab in practice is planned in the tallest timber building in Switzerland. The partner companies involved in this research project *Implenia*

Schweiz AG and *WaltGalmarini AG* won the respective project competition in 2019 [87]. The novel TCC slab system made a significant contribution to this success, as its low construction height allows better use of the total building volume. Compared to the solutions suggested by the competitors, two additional floors can be realised in this 80 m tall building. In addition, the low self-weight of the slabs allows for significant material savings in the vertical load-bearing members such as the columns and the foundation.

A real-scale mock-up including a 12×10 m segment of the two-way spanning TCC slab was built in October 2020. The TCC slab spans 9.1 m at a total construction height of 320 mm ($h_1/h_0/h_2 = 60/170/90$ mm). This mock-up is built inside an old factory and presents a unique opportunity to investigate the long-term behaviour of the slab as it is planned to remain installed for at least two years. Measurement equipment has already been installed in order to record displacements in several locations as well as the climatic conditions. The construction works on the real building are planned to start in 2023.

Nomenclature

Abbreviations

CLT	Cross laminated timber
COV	Coefficient of variation
FBS	Front block shear failure
FEM	Finite Element Method
FFT	Fast Fourier Transform
GIR	Glued-in rod
LDC	Load distribution construction
LFS	Local front shear failure
LLV	Lower limit value
LVDT	Linear variable differential transformer
LVL	Laminated veneer lumber
MOE	Modulus of elasticity
RST	Rear shear/tensile failure
SLS	Serviceability limit state
TCC	Timber-concrete composite
TS	Technical Specification
ULS	Ultimate limit state

Upper-case roman letters

A_1	Cross-sectional area of the concrete section
A_2	Cross-sectional area of the timber section
A_{v}	Shear area

D	Diameter
E_1	Concrete modulus of elasticity
E_2	Timber modulus of elasticity
EI_{I}	Bending stiffness of the composite cross-section during state I
EI_{II}	Bending stiffness of the composite cross-section during state II
EI_{T}	Bending stiffness of the (concrete filled) steel tube
EI_{x}	Bending stiffness in x-direction
EI_{xy}	Torsional stiffness
EI_{y}	Bending stiffness in y-direction
F_{cyl}	Cylinder force
F_{x}	Support reaction in x-direction
F_{y}	Support reaction in y-direction
G_1	Concrete shear modulus
G_2	Timber shear modulus
GA_{T}	Shear stiffness of the (concrete filled) steel tube
H	Normal force in the steel tube
H_{S}	Bottom horizontal support reaction in the push-out test
I_1	Moment of inertia of the concrete section
I_2	Moment of inertia area of the timber section
I_{I}	Moment of inertia of the composite cross-section during state I
I_{II}	Moment of inertia of the composite cross-section during state II
K	Elastic connection stiffness
M	External bending moment or connection moment
M_1	Internal bending moment acting on the concrete section
M_2	Internal bending moment acting on the timber section
M_{cc}	External bending moment at the end of state III (concrete compressive strength reached)
M_{cr}	External bending moment at the end of state I (concrete cracking)
$M_{\mathrm{II,1c}}$	External bending moment leading to concrete crushing during state II
$M_{\mathrm{II,2tb}}$	External bending moment leading to timber tensile-bending failure during state II
M_{inf}	Moment in the steel tube-timber connection

$M_{\mathrm{inf,y}}$	Yield moment in the steel tube-timber connection
M_{sup}	Moment in the steel tube-concrete connection
$M_{\mathrm{sup,y}}$	Yield moment in the steel tube-concrete connection
M_{u}	External bending moment at ultimate failure, or maximum connection moment in push-out tests
M_{y}	External bending moment at the end of state II (yielding of all connectors), or yield moment in the steel tube-timber or steel tube-concrete connection
N	Normal force
S_{12}	Static moment at the interface of the partial cross-sections
T	Connection shear force
T_{u}	Maximum shear force in push-out tests
T_{y}	Connection shear capacity
V	Shear force

Lower-case roman letters

a	Embedment depth of steel tube in timber or concrete
a_1	Distance between the theoretical timber zero-strain axis and the centroid of the concrete section
a_2	Distance between the theoretical timber zero-strain axis and the centroid of the timber section
a_{inf}	Embedment depth in the steel tube-timber connection
a_{sup}	Embedment depth in the steel tube-concrete connection
b_1	Width of the concrete section
b_2	Width of the timber section
$b_{\mathrm{v,x}}$	Width for the calculation of the plate shear force v_{x} from the support force in x-direction
$b_{\mathrm{v,y}}$	Width for the calculation of the plate shear force v_{y} from the support force in y-direction
e	Distance between the centroids of the concrete and timber sections
$f_{1,\mathrm{c}}$	Concrete compressive strength
$f_{1,\mathrm{t}}$	Concrete tensile strength
$f_{2,\mathrm{c}}$	Timber compressive strength

$f_{2,\mathrm{m}}$	Timber bending strength
$f_{2,\mathrm{t}}$	Timber tensile strength
g	Standard acceleration due to gravity, $g = 9.81\,\mathrm{m/s^2}$
h_0	Height of interlayer between timber and concrete
h_1	Concrete height
h_2	Timber height
h_{cr}	Crack height
k_{GIR}	Axial connection stiffness of glued-in rod
$k_{\mathrm{m,1}}$	Rotational spring stiffness during 1st loading
$k_{\mathrm{m,2}}$	Rotational spring stiffness during reloading
$k_{\mathrm{m,inf}}$	Rotational spring stiffness representing the steel tube-timber connection
$k_{\mathrm{m,mod}}$	Modified rotational spring stiffness for strut-and-tie model
$k_{\mathrm{m,sup}}$	Rotational spring stiffness representing the steel tube-concrete connection
$k_{\mathrm{s,1}}$	Global connection stiffness during 1st loading
$k_{\mathrm{s,2}}$	Global connection stiffness during reloading
l	Span
l_{A}	Distance of the first connector from the support
l_{pl}	Length of the region where the composite cross-section is in state III or IV
$l_{\mathrm{pl,IV}}$	Length of the region where the composite cross-section is in state IV
l_{sc}	Length of the side connection
l_{T}	Length of the steel tube
m	Number of connectors per shear area
m_{cyl}	Mass of the hydraulic cylinders in the biaxial bending tests
m_{LDC}	Mass of the load distribution construction in the uniaxial and biaxial bending tests
m_{s}	Specimen mass
m_{x}	Bending moment in x-direction
m_{xy}	Torsional moment
m_{y}	Bending moment in y-direction
n_{90}	Number of cross-layers in *BauBuche Q*
n_i	Ratio of MOE of material i to reference MOE
n_{sc}	Number of side connections along the span

n_{tot}	Total number of veneers in *BauBuche Q*
q	External uniformly distributed load
q^*	Uniformly distributed load including the self-weight of the specimen and the respective load distribution construction in the uniaxial and biaxial bending tests
q_{cc}	External uniformly distributed load at the end of state III (concrete compressive strength reached)
q_{cr}	External uniformly distributed load at the end of state I (concrete cracking)
q_{u}	External uniformly distributed load at ultimate failure
q_{y}	External uniformly distributed load at the end of state II (yielding of all connectors)
s_{ef}	Effective connector spacing
s_i	Relative horizontal displacement perpendicular to the element interfaces at position i in the biaxial bending test
t	Thickness or time
v_{x}	Plate shear force in x-direction
v_{y}	Plate shear force in y-direction
w	Deflection
w_{cyl}	Cylinder displacement
w_{m}	Mid-span deflection
x	Concrete compression zone height

Upper-case greek letters

Δu	Relative displacement $\parallel$ to beam axis or in x-direction of the slab (slip displacement)
Δu_0	Slip displacement at the supports
$\Delta u_{\max}$	Connection deformation capacity
Δu_{pl}	Plastic slip displacement
Δv	Relative displacement $\parallel$ to beam axis or in y-direction of the slab (slip displacement)
Δw	Relative displacement $\perp$ to beam axis or slab plane (in z-direction)
$\Delta\varepsilon$	Slip strain
$\Delta\varepsilon_{\mathrm{cc}}$	Slip strain at the end of state III (concrete compressive strength reached)
$\Delta\varepsilon_{\mathrm{cr}}$	Slip strain at the end of state I (concrete cracking)
$\Delta\varepsilon_{\mathrm{u}}$	Slip strain at ultimate failure

$\Delta\varepsilon_{\mathrm{y}}$	Slip strain at the end of state II (yielding of all connectors)
$\Delta\vartheta$	Difference of the bending line inclination at the side connections

Lower-case greek letters

γ	Model factor accounting for the flexibility of the composite connection
ε	Strain
ε_1	Concrete strain
$\varepsilon_{1,\mathrm{u}}$	Concrete ultimate compressive strain
ε_2	Timber strain
ζ	Factor depending on the embedment depth a as well as the ratio between shear force T and bending moment M in type 3 connections
η	Dimensionless auxiliary factor for iterative strut-and-tie model with cracked concrete
ϑ	Inclination of the bending line
λ	Parameter for the load distribution in the strip method
σ	Stress
σ_1	Concrete stress
σ_2	Timber stress
φ	Rotation
$\varphi_{\mathrm{sup,max}}$	Maximum rotation in the steel tube-concrete connection before a brittle failure occurs
χ	Curvature
χ_{cc}	Curvature at the end of state III (concrete compressive strength reached)
χ_{cr}	Curvature at the end of state I (concrete cracking)
$\chi_{\mathrm{III,2tb}}$	Curvature leading to timber tensile-bending failure during state III
χ_{u}	Curvature at ultimate failure
χ_{y}	Curvature at the end of state II (yielding of all connectors)

Bibliography

[1] Bachmann, H. *Zur plastizitätstheoretischen Berechnung statisch unbestimmter Stahlbetonbalken.* PhD Thesis No. 4069, Institute of Structural Engineering, ETH Zurich, 1967.

[2] BAFU Bundesamt für Umwelt. Jahrbuch Wald und Holz 2019. *Umwelt-Zustand Nr. 1914* (2019).

[3] Blass, H. J., Ehlbeck, J., van der Linden, M., and Schlager, M. *Trag- und Verformungsverhalten von Holz-Beton-Verbundkonstruktionen.* Universität Karlsruhe, 1995.

[4] Boccadoro, L. *Timber-concrete composite slabs made of beech laminated veneer lumber with notched connection.* PhD Thesis No. 23577, Institute of Structural Engineering, ETH Zurich, 2016.

[5] Boccadoro, L., Steiger, R., Zweidler, S., and Frangi, A. Analysis of shear transfer and gap opening in timber-concrete composite members with notched connections. *Materials and Structures 50*, 5 (2017).

[6] Boccadoro, L., Zweidler, S., Steiger, R., and Frangi, A. Bending tests on timber-concrete composite members made of beech laminated veneer lumber with notched connection. *Engineering Structures 132* (2017), 14–28.

[7] Boccadoro, L., Zweidler, S., Steiger, R., and Frangi, A. Calculation model to assess the structural behavior of LVL-concrete composite members with ductile notched connection. *Engineering Structures 153* (2017), 106–117.

[8] Brunner, M., Romer, M., and Schnüriger, M. Timber-concrete-composite with an adhesive connector (wet on wet process). *Materials and Structures 40*, 1 (2007), 119–126.

[9] CCFAT Commission chargée de formuler des Avis Techniques et Documents D'Application. Avis Technique 3.1/15-940_V1: Plancher mixte bois-béton "Sylvabat", 2018.

[10] CEN European Committee for Standardisation. EN 26891, Timber structures – joints made with mechanical fasteners – general principles for the determination of strength and deformation characteristics, 1991.

[11] CEN European Committee for Standardisation. EN 12390-3, Testing hardened concrete – Part 3: Compressive strength of test specimens, 2001.

[12] CEN European Committee for Standardisation. EN 1992-1-1, Eurocode 2: Design of concrete structures – Part 1-1: General rules and rules for buildings, 2004.

[13] CEN European Committee for Standardisation. EN 1995-1-1, Eurocode 5: Design of timber structures – Part 1-1: General – Common rules and rules for buildings, 2004.

[14] CEN European Committee for Standardisation. EN 1993-1-1, Eurocode 3: Design of steel structures – Part 1-1: General rules and rules for buildings, 2005.

[15] CEN/TC250/SC5 European Committee for Standardisation. TS TCC: Design of Timber Structures – Structural design of timber-concrete composite structures – Common rules and rules for buildings. Final draft, 2020.

[16] Chen, W. F. Double Punch Test for Tensile Strength of Concrete. *ACI Journal 67*, 12 (1970), 993–995.

[17] Dias, A. M. P. G. *Mechanical behaviour of timber-concrete joints*. PhD Thesis, TU Delft, 2005.

[18] Dias, A. M. P. G. Analysis of the Nonlinear Behavior of Timber-Concrete Connections. *Journal of Structural Engineering 138*, 9 (2012), 1128–1137.

[19] Dias, A. M. P. G., Cruz, H. M. P., Lopes, S. M. R., and van de Kuilen, J.-W. Stiffness of dowel-type fasteners in timber-concrete joints. *Structures and Buildings 163*, 4 (2010), 257–266.

[20] Dias, A. M. P. G., Lopes, S. M., van de Kuilen, J.-W., and Cruz, H. M. P. Load-Carrying Capacity of Timber-Concrete Joints with Dowel-Type Fasteners. *Journal of Structural Engineering 133*, 5 (2007), 720–727.

[21] Dias, A. M. P. G., Schänzlin, J., and Dietsch, P. *Design of timber-concrete composite structures – A state-of-the-art report by COST Action FP1402 / WG 4*. Shaker Verlag, 2018.

[22] DIBT Deutsches Institut für Bautechnik. Zulassung Z-9.1-837: Brettschichtholz aus Buchen-Furnierschichtholz, 2013.

[23] DIBT Deutsches Institut für Bautechnik. Zulassung Z-9.1-705: 2K-EP-Klebstoff WEVO-Spezialharz EP 32 S mit WEVO-Härter B 22 TS zum Einkleben von Stahlstäben in Holzbaustoffe, 2018.

[24] DIBT Deutsches Institut für Bautechnik. Zulassung Z-9.1-838: Furnierschichtholz aus Buche zur Ausbildung stabförmiger und flächiger Tragwerke "Platte BauBuche S" und "Platte BauBuche Q", 2018.

[25] Ehlbeck, J., and Colling, F. *Ermittlung fehlender Festigkeitswerte von Buchenfurnierplatten.* Universität Karlsruhe, 1983.

[26] Ehlbeck, J., and Colling, F. Determination of panel shear strength and panel shear modulus of beech plywoood in structural sizes. In *CIB W18 – Meeting seventeen* (Rapperswil, 1984).

[27] Ehlbeck, J., and Colling, F. Scherfestigkeit rechtwinklig zur Plattenebene und Schubmodul von Bau-Furniersperrholz aus Buche. *Holz als Roh- und Werkstoff 43*, 4 (1985), 143–147.

[28] Ehrhart, T. *European Beech Glued Laminated Timber.* PhD Thesis No. 26173, Institute of Structural Engineering, ETH Zurich, 2019.

[29] Foschi, R. O. Load-Slip Characteristics of Nails. *Wood Science 7*, 1 (1974), 69–77.

[30] Frangi, A. *Brandverhalten von Holz-Beton-Verbunddecken.* PhD Thesis No. 14328, Institute of Structural Engineering, ETH Zurich, 2001.

[31] Frangi, A., and Fontana, M. Elasto-Plastic Model for Timber-Concrete Composite Beams with Ductile Connection. *Structural Engineering International 13*, 1 (2003), 47–57.

[32] Gelfi, P., Giuriani, E., and Marini, A. Stud Shear Connection Design for Composite Concrete Slab and Wood Beams. *Journal of Structural Engineering 128*, 12 (2002), 1544–1550.

[33] Grosse, M., Hartnack, R., Lehmann, S., and Rautenstrauch, K. Modellierung von diskontinuierlich verbundenen Holz-Beton-Verbundkonstruktionen / Teil 1: Kurzzeittragverhalten. *Bautechnik 80*, 8 (2003), 534–541.

[34] Hassan, J., and Eisele, M. BauBuche – Der nachhaltige Hochleistungswerkstoff. *Bautechnik 92*, 1 (2015), 40–45.

[35] Higgins, C., Barbosa, A. R., and Blank, C. *Structural Tests of Concrete Composite-Cross-Laminated Timber Floors.* Report No. 17-01, Oregon State University, 2017.

[36] Hillerborg, A. *Strip Method of Design.* Viewpoint Publications, London, 1975.

[37] Hunger, F., Stepinac, M., Rajčić, V., and van de Kuilen, J.-W. Pull-compression tests on glued-in metric thread rods parallel to grain in glulam and laminated veneer lumber of different timber species. *European Journal of Wood and Wood Products 74*, 3 (2016), 379–391.

[38] Johnson, B., Horos, D., and Baker, W. Timber Tower Research Project. *Structure Magazine*, 3 (2014), 22–23.

[39] Kirchhoff, G. Über das Gleichgewicht und die Bewegung einer elastischen Scheibe. *Journal für reine und angewandte Mathematik 40* (1850), 51–88.

[40] Kolb, H. Biegeversuche und Prüfung des Brandverhaltens an Trägern aus verleimten Buchenschälfurnieren – Tests on the Bending Strength and Fire Tests with Glulam-Girders of Beech Veneers. *Holz als Roh-und Werkstoff 26*, 8 (1968), 277–283.

[41] Kostic, S., Merk, V., Berg, J. K., Hass, P., Burgert, I., and Cabane, E. Timber-mortar composites: The effect of sol-gel surface modification on the wood-adhesive interface. *Composite Structures 201* (2018), 828–833.

[42] Krackler, V., and Niemz, P. Schwierigkeiten und Chancen in der Laubholzverarbeitung – Teil 1: Bestandssituation, Eigenschaften und Verarbeitung von Laubholz am Beispiel der Schweiz. *Holztechnologie 52*, 2 (2011), 5–11.

[43] Krackler, V., and Niemz, P. Schwierigkeiten und Chancen in der Laubholzverarbeitung – Teil 2: Verwendungsmöglichkeiten von sägefähigem Laubholz. *Holztechnologie 52*, 3 (2011), 5–10.

[44] Kreis, B., and Frangi, A. *Experimental Investigations on Two-Way Spanning Timber-Concrete Composite Slabs made of Beech Laminated Veneer Lumber with Steel Tube Connection.* Report 2021-01, Institute of Structural Engineering – Timber Structures, ETH Zurich, 2021.

[45] Kreuzinger, H. Flächentragwerke: Platten, Scheiben, Schalen, Berechnungsmethoden und Beispiele. *Informationsdienst Holz: Brücken aus Holz* (1999), 43–60.

[46] Kudla, K. *Kerven als Verbindungsmittel für Holz-Beton-Verbundstraßenbrücken.* PhD Thesis, Universität Stuttgart, 2017.

[47] Laube, C. *Grossversuch an einer zweiachsig tragenden Holz-Beton-Verbunddecke.* Master Thesis, Institute of Structural Engineering, ETH Zurich, 2019.

[48] Lehmann, S. *Untersuchungen zur Bewertung von Verbundbauteilen aus Brettstapelelementen im Flächenverbund mit mineralischen Deckschichten.* PhD Thesis, Bauhaus-Universität Weimar, 2004.

[49] Loebus, S., Dietsch, P., and Winter, S. Two-way Spanning CLT-Concrete-Composite-Slabs, Paper 50-12-7. In *International Network on Timber Engineering Research (INTER) - Meeting fifty* (Kyoto, 2017).

[50] Loebus, S., and Winter, S. *Zweiachsige Tragwirkung bei Holz-Beton-Verbundkonstruktionen – Entwicklung von Bemessungsverfahren und Konstruktionsdetails für zweiachsige Lastabtragung bei der Holz-Beton-Verbundbauweise.* Stuttgart, 2017.

[51] Love, A. E. H. The small free vibrations and deformation of a thin elastic shell. *Philosophical Transactions of the Royal Society of London 179* (1888), 491–546.

[52] Lukaszewska, E., Johnsson, H., and Fragiacomo, M. Performance of connections for prefabricated timber-concrete composite floors. *Materials and Structures 41*, 9 (2008), 1533–1550.

[53] Marti, P., Alvarez, M., Kaufmann, W., and Sigrist, V. *Tragverhalten von Stahlbeton.* Institut für Baustatik und Konstruktion, ETH Zürich, 1999.

[54] Michelfelder, B. *Trag- und Verformungsverhalten von Kerven bei Brettstapel-Beton-Verbunddecken.* PhD Thesis, Universität Stuttgart, 2006.

[55] Mindlin, R. D. Influence of Rotatory Inertia and Shear on Flexural Motions of Isotropic, Elastic Plates. *Journal of Applied Mechanics 18* (1951), 1031–1038.

[56] Möhler, K. *Über das Tragverhalten von Biegeträgern und Druckstäben mit zusammengesetztem Querschnitt und nachgiebigen Verbindungsmitteln.* Habilitation, TU Karlsruhe, 1956.

[57] Mönch, S. Untersuchung von HBV-Trägern aus Buchen-FSH mit Kerven. In *Doktorandenkolloquium Holzbau Forschung + Praxis* (Stuttgart, 2016), pp. 145–152.

[58] Monteiro, S., Dias, A. M. P. G., and Negrão, J. Experimental and Numerical Evaluation of Notched Timber-Concrete Joints Mechanical Behaviour. In *World Conference on Timber Engineering* (Riva del Garda, 2010).

[59] Müller, K. *Timber-concrete composite slabs with micro-notches.* PhD Thesis No. 27083, Institute of Structural Engineering, ETH Zurich, 2020.

[60] Natterer, J., and Hoeft, M. *Zum Tragverhalten von Holz-Beton-Verbundkonstruktionen.* Forschungsbericht CERS Nr. 1345, EPF Lausanne, 1987.

[61] OIB Österreichisches Institut für Bautechnik. Europäische Technische Bewertung ETA-14/0354: Brettschichtholz aus Laubholz – Buchenfurnierschichtholz für tragende Zwecke, 2015.

[62] OIB Österreichisches Institut für Bautechnik. Europäische Technische Bewertung ETA-19/0194: Hilti HIT-RE 500 V3, 2019.

[63] Pollmeier GmbH. Leistungserklärung PM-005-2018: Furnierschichtholz aus Buche, 2018.

[64] Ramberg, W., and Osgood, W. R. Description of Stress-Strain Curves by Three Parameters. *Technical Note No. 902, National Advisory Committee for Aeronautics* (1943).

[65] Rautenstrauch, K., Grosse, M., Lehmann, S., and Hartnack, R. Baupraktische Dimensionierung von Holz-Beton-Verbunddecken. In *6. Informationstag des IKI* (2003), Bauhaus-Universität Weimar.

[66] Reissner, E. On a mixed variational theorem and on shear deformable plate theory. *International Journal for Numerical Methods in Engineering 23*, 2 (1986), 193–198.

[67] Richard, R. M., and Abbott, B. J. Versatile Elastic-Plastic Stress-Strain Formula. *Journal of the Engineering Mechanics Division 101*, 4 (1975), 511–515.

[68] Sarrazin, O., and Schäfer, K. Die Verwendung des Buchenholzes zu Bauzwecken. *Centralblatt der Bauverwaltung 4*, 47 (1884), 483–484.

[69] Sauter, U. H., and Breinig, L. European hardwoods for the building sector: Reality of today – possibilities for tomorrow, WP 1 – Hardwood resources in Europe: Standing stock and resource forecasts. In *Workshop Garmisch-Partenkirchen* (2016).

[70] Schäfers, M., and Seim, W. Investigation on bonding between timber and ultra-high performance concrete (UHPC). *Construction and Building Materials 25*, 7 (2011), 3078–3088.

[71] Scholz, A. *Ein Beitrag zur Berechnung von Flächentragwerken aus Holz.* PhD Thesis, TU München, 2003.

[72] Schuler, P. Neue, zweiachsig tragende HBV-Konstruktion ohne Bewehrung. In *50. Fortbildungskurs S-WIN* (Weinfelden, 2018), pp. 65–70.

[73] Sebastian, W. M., Mudie, J., Cox, G., Piazza, M., Tomasi, R., and Giongo, I. Insight into mechanics of externally indeterminate hardwood-concrete composite beams. *Construction and Building Materials 102* (2016), 1029–1048.

[74] Sebastian, W. M., Piazza, M., Harvey, T., and Webster, T. Forward and Reverse shear transfer in beech LVL-concrete composites with singly inclined coach screw connectors. *Engineering Structures 175* (2018), 231–244.

[75] Seim, W., Eisenhut, L., and Kühlborn, S. Adhesive-Bonded Timber-Concrete Composites - Experimental Investigation of Thermal-Hygric Effects. In *World Conference on Timber Engineering* (2016).

[76] SIA Swiss Society of Engineers and Architects. SIA 262: Concrete Structures, 2013.

[77] SIA Swiss Society of Engineers and Architects. SIA 262/1: Concrete Structures – Supplementary Specifications, 2013.

[78] Sika. Sikadur-12 Pronto, Product Data Sheet, Version 01.01, 2019.

[79] Sika. Sikadur-42 HE, Product Data Sheet, Version 02.01, 2019.

[80] Skidmore Owings & Merrill. Timber Tower Research Project: System Report #1 – Gravity Framing Developement of Concrete Jointed Timber Frame System, 2014.

[81] Skidmore Owings & Merrill. Timber Tower Research Project: Physical Testing Report #1 – Composite Timber Floor Testing at Oregon State University, 2017.

[82] Smith, A., Schänzlin, J., Piazza, M., Lawrence, A., and Bell, O. Formulaic Design Methods for TCC floors, Paper 51-10-1. In *International Network on Timber Engineering Research (INTER) – Meeting fifty-one* (Tallinn, 2018).

[83] Stüssi, F. Ueber den verdübelten Balken. *Schweizerische Bauzeitung 122*, 21 (1943), 271–274.

[84] Stüssi, F. Zusammengesetzte Vollwandträger. *IABSE publications 8* (1947), 249–269.

[85] Tannert, T., Endacott, B., Brunner, M., and Vallée, T. Long-term performance of adhesively bonded timber-concrete composites. *International Journal of Adhesion and Adhesives 72* (2017).

[86] Truc, J.-P. Riemann Sums for Generalized Integrals. *The College Mathematics Journal 50*, 2 (2019), 123–132.

[87] V-ZUG Immobilien AG. *Projekt Pi – Gesamtleistungsstudie für ein Wohnhochhaus in Zug – Schlussbericht.* 2019.

[88] van de Kuilen, J.-W., and Knorz, M. *Ergebnisse der Zulassungsversuche für eine 'allgemeine bauaufsichtliche Zulassung' (abZ) von Furnierschichtholz aus Buche.* Prüfbericht Nr. 10511, TU München, 2012.

[89] van de Kuilen, J.-W., Knorz, M., and Xia, Z. *Ergebnisse der Zulassungsversuche für eine Erweiterung der beantragten 'allgemeinen bauaufsichtlichen Zulassung' (abZ) von Furnierschichtholz aus Buche.* Prüfbericht Nr. 11513, TU München, 2013.

[90] van der Linden, M. *Timber-Concrete Composite Floor Systems.* PhD Thesis, TU Delft, 1999.

[91] Yeoh, D., Fragiacomo, M., De Franceschi, M., and Boon, K. H. State of the Art on Timber-Concrete Composite Structures: Literature Review. *Journal of Structural Engineering 137*, 10 (2011), 1085–1095.

[92] Yeoh, D., Fragiacomo, M., De Franceschi, M., and Buchanan, A. H. Experimental Tests of Notched and Plate Connectors for LVL-Concrete Composite Beams. *Journal of Structural Engineering 137*, February (2011), 261–269.

[93] Yeoh, D., Fragiacomo, M., and Deam, B. Experimental behaviour of LVL-concrete composite floor beams at strength limit state. *Engineering Structures 33*, 9 (2011), 2697–2707.